X-ray Flare-Driven Chemistry in Protoplanetary Disks

Abygail R. Waggoner
Converse, Indiana

B.S. Chemistry, Ball State University, 2018

A Dissertation Presented to the
Graduate Faculty of the

University of Virginia

in Candidacy for the Degree of

Doctor of Philosophy

Department of Chemistry

University of Virginia
May 2024

Committee Members:
L. Ilsedore Cleeves
Eric Herbst
Rob Garrod
Zhi-Yun Li

Abstract

The gas and dust of protoplanetary disks surrounding solar-mass, T Tauri stars are a window into the history of the Solar System and extrasolar planetary systems. The central star plays an important role in shaping disk chemistry and physics, as its UV and X-ray radiation are strong ionizing agents. However, T Tauri stars are also highly variable, as X-ray flaring events temporarily increase disk ionization rates from a few to hundreds of factors times the quiescent rates. My thesis provides the first deep dive into the theoretical and observational consequences of time-variable flare-driven chemistry within protoplanetary disks. I use a combination of disk chemical models and radio observations to determine how individual flares impact molecules on short time scales (∼weeks) and how flares cumulatively impact the molecules available during planet formation. ALMA (Cleeves et al., 2017) and SMA (PI: A. Waggoner) observations of $H^{13}CO^+$ $3-2$ in the IM Lup protoplanetary disk showed that the line flux approximately doubled for a short period of time while continuum flux remained constant. Enhancement duration is unknown, since observations were spread out over a six-year period, but an X-ray flaring event is the most likely source of $H^{13}CO^+$ enhancement. I have also identified tentative HCO^+ $1-0$ spectral variability in the Molecules with ALMA at Planet forming Scales (MAPS) protoplanetary disks, which may be evidence of flare-driven spatial variability. While a single flare is unlikely to have a long lasting (> 1 month) effect on disk chemistry, the cumulative impact of

flares over relatively short astrophysical timescales (hundreds of years) could drive chemistry to a new 'steady state.' I wrote a stochastic X-ray flare model, XGEN, motivated by observed flare frequency and energy distribution for T Tauri stars. When I incorporated XGEN into the chemical disk model, I found that flares push chemistry to a slightly more complex state, which could help explain two chemical puzzles in disks: the high O_2 seen in comets and the low degree of sulfur bearing molecules. Incorporating flare chemistry slightly enhances O_2 and tends to form organosulfides in our models. Together, my observational and theoretical work support flares playing a key role in shaping the chemical inventory available to forming planets.

Acknowledgements

I always thought that acknowledgement sections that started, "Where do I begin?" were too cliche, yet here I am. Staring at a blank page, trying to decide who to thank first. There are countless people who have supported me in more ways than I can begin to capture. Family who encouraged me to start this path and have patiently listened as I've droned on. Friends who held me up during my darkest moments. Colleagues who spent hours teaching me basic astronomy and answering my questions over slack. Professors who lengthened office hours to explain course material to me over and over until it finally clicked. If you've been in my life these last six years, know that you have impacted it, and it's thanks to you that I had the strength to get where I am today.

First I would like to thank Ilse, who I first worked with as an undergraduate REU student. I was a chemist with no background in physics, astronomy, or computers, and yet she took a chance on me to do a summer research project. Little did either of us realize, that seven years later I would be writing a dissertation that started with that summer project. Over the years Ilse has taught me confidence in my scientific abilities and my personal life, and her influence will continue to guide me in life well after my PhD is complete.

I would also like to thank our research group and all the other amazing people in our slack channel. Most everything I know about radio astronomy came from Ryan

Loomis and Brett McGuire answering my highly specific questions on slack. Jon Ramsey and Christian Eistrup would sit in the lounge with me after meetings in my first years of graduate school, answering the questions I was too nervous to ask the group. Dana Anderson and Jeroen Terwisscha van Scheltinga for helping me learn confidence and to be proud of the work I do. Nick Ballering and Michael Küffmeier remind me to look for connections in topics that may not seem related. Yao-Lun Yang, Charles Law, and Jamila Pegues taught me to pursue projects I am passionate about and not hold back on my ideas. Finally, I'd like to thank Amanda, Amina, Deryl, Rachel, and Richard for being a supportive group.

My mother deserves more than thanks. When I enrolled for college in 2014, I was convinced I would never succeed in STEM. Her encouragement is the only reason I pursued chemistry, and her constant motivating words have pushed me to be the best version of myself.

Lastly, I would like to thank the friends who have been by my side. Jillian, for reminding me that I am a person, and not just an academic. Fridays will always be wine nights, and I will forever crave a burger after a hike because of you. Molly, for reminding me that I don't have to be a perfect person to be a decent person. Jordan, for being the Paula to my Rebecca (or vice versa?). Rachel, for never letting me forget all the hard work I do and the many *unplanned yet matching* faces we make at each other. Hannah, for always having something positive to say when I complain and for bringing joy with groundhog sightings. The sports crew, including Nick, Deven, Samer, Daniel, Conner, Mark, and Renato for helping me realize that mistakes are a part of the fun. Whitney, for reminding that everything I do should be for joy. Everyone who has passed through our DnD group, because you all gave me a constant joy to look forward to.

For my brother, Dillon, for ~~tolerating~~ supporting me through this journey and reminding me that the most important step to take is the next one

Table of Contents

List of Figures

List of Tables

Chapter 1

Introduction

"I'm certain some will feel threatened by this record. Some few may feel liberated. Most will simply feel that it should not exist. I needed to write it anyway."

Brandon Sanderson, *Oathbringer*

1.1 Astrochemistry: What is it?

While we traditionally give Dmitri Mendelev credit for inventing the modern periodic table, decades of research and ingenuity from chemists and physicists from around the world contributed to the final product we recognize today.[1] Some of the earliest versions of the periodic table were quite ingenuitive, for example G. D. Henrich developed a spiral periodic table (Figure 1.1). While the Mendelev periodic table's predecessors have faded to a historical fascination, today there exists a plethora of 'joke' periodic tables intended to poke fun of the organization of elements.

One such 'joke' table is the astronomer's periodic table, which is meant to represent the mass of each element contained in the universe. The take-away message: the universe is filled with hydrogen, helium and metals; metals being every other element (an example table is shown in Figure 1.1). For many sub-fields in astronomy, this assumption is mostly true. Hydrogen and helium make up approximately 74% and 24% of mass in the universe, while all other elements make up less than 2% of the total mass.

So, why would I begin a thesis on astrochemistry with the astronomer's periodic table? To emphasize how incredible it is that the earth, our oceans, plant and animal life, and every human who has ever lived and ever will live are are made up of the elements categorized as metals. We are the 'everything else.' We exist in a universe where less than two percent of total material comes together in such a way that planets and life can form. But, how do planets and life form? What chemical and physical processes does material undergo that leads to our existence? These two questions are the backbone of astrochemistry.

[1]Notably, Lothar Meyer independently created a periodic table very similar to Mendelev five years before him, but Lothar is not given the same credit as Mendelev. See Scerri (2007) Chapters 3 and 4 for a full history on the development of the periodic table.

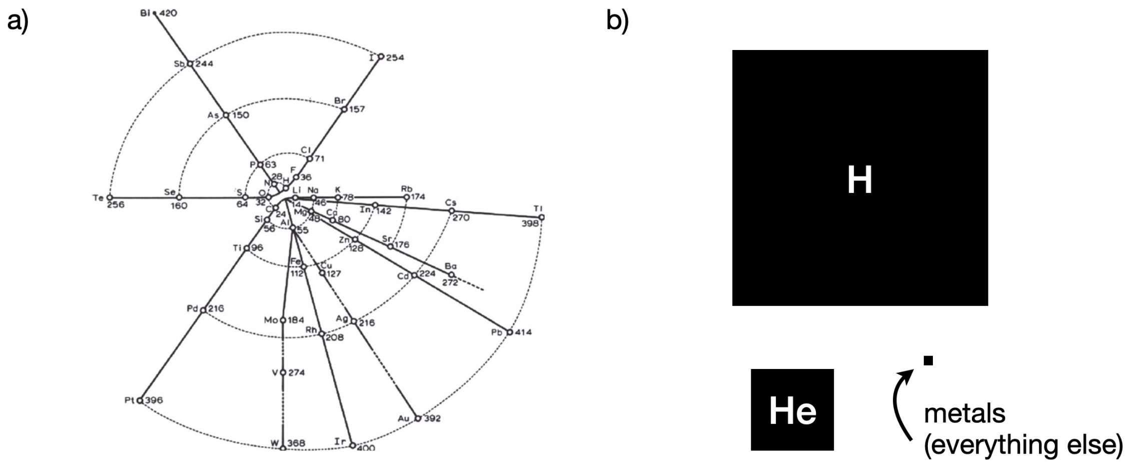

Figure 1.1 *a)* Spiral periodic table produced by G. D. Henrich (taken from Scerri, 2015). *b)* Example of the astronomer's periodic table that I made, where the size of the box represents the total mass that element has in the universe (assuming that H and He make up 74% and 24% of all mass, respectively).

In this chapter, I will first introduce the astronomical environments involved in the planet formation process. Next, tools used in astrochemical research will be discussed, including chemical disk models and how astronomers use radio observations to detect molecules. Next, I highlight some of my accomplishments in scientific outreach and communication. This chapter will conclude with an overview of several outreach initiatives I have taken part in and an overview of the thesis.

1.2 Star and Planet Formation

Planet formation begins in massive clouds composed of dust and gas known as dense molecular clouds. Over time (up to millions of years), these clouds collapse in on themselves to form pre-stellar cores (Class 0), where star formation begins. As material collapses (accretes), a gaseous and dusty disk forms around the young protostar (Class I). At this stage, the disk is quite 'fluffy,' and over time material settles out into a more compact disk. Remaining material from the original molecular cloud

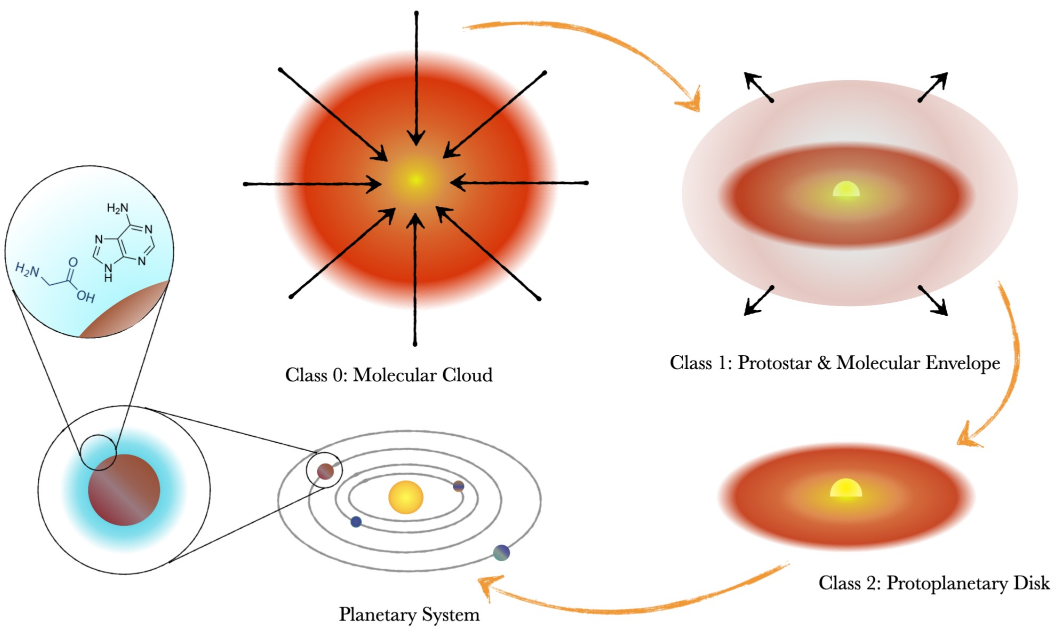

Figure 1.2 A simple graphic representing the planet forming process, as described in Section 1.2. Graphics are not to scale. To understand the origins of biologically relevant molecules, we must study the evolution of atoms and molecules throughout the star and planet forming process.

dissipates, leaving behind a (relatively) isolated system known as a protoplanetary disk (Class II). The proto-star at the center of the disk has fully formed into a pre-main sequence star (meaning that it is not yet burning hydrogen). Protoplanetary disks are complex environments, with densities ranging from $\sim 10^{-9}$ to $\sim 10^{-18}$ g cm^3, and temperatures ranging from thousands to 20K Reviews by Henning & Semenov (2013) and Öberg & Bergin (2021) provide a more comprehensive overview of the star and planet formation process and disk substructure. Disks are classified by three layers: the photon dissociative region, the warm molecular layer, and the mid-plane.[2]

- Photon Dissociative Region (PDR, also known as the Proton Dissociative Region): This layer corresponds to the outermost layer of the disk, where densities are lowest and temperatures are highest. The dominant ionization process in this layer is from UV photons emitted by the central star, and the layer is composed of ions and atoms. See Wolfire et al. (2022) for a detailed review of PDRs.

- Warm Molecular Layer: This layer corresponds to the middle layer in the disk, where the majority of chemical species are in the form of gas-phase molecules and radicals. UV photons still dominate a large portion of the ionization in this region, but density levels become high enough to scatter UV photons. X-ray photons emitted by the central star become the dominant ionizing agent within inner regions of this layer.

- Mid-plane: This layer is the innermost layer of the disk, where densities are highest and temperatures are lowest. This layer is primarily composed of dust particles, where ices (and planets) form. Water ice is the most abundant solid

[2]This overview is specific for low mass star and disk formation. High mass stars tend to follow slightly different formation pathways.

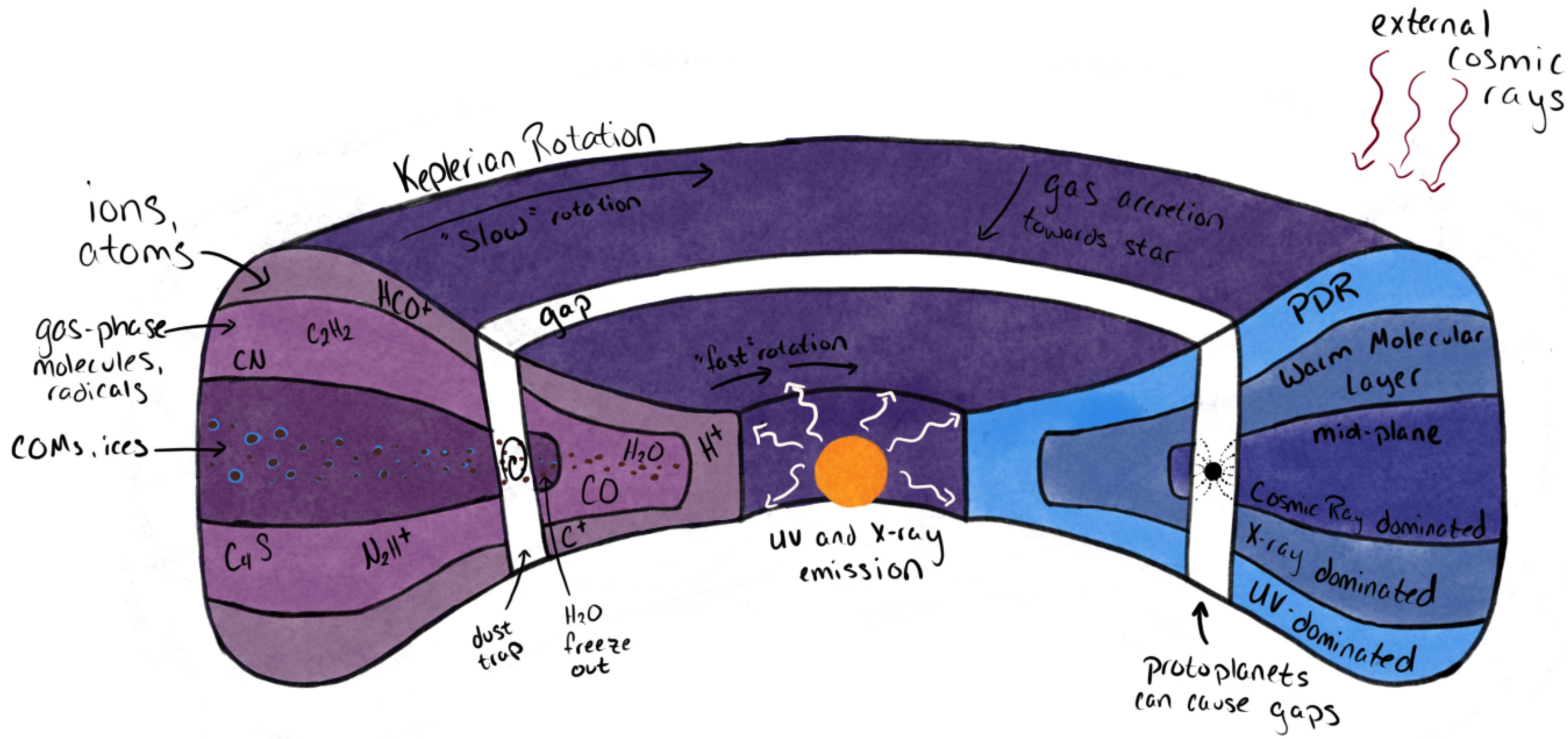

Figure 1.3 This graphic demonstrates the structure and chemical composition of a protoplanetary disk with a protoplanet. See Henning & Semenov (2013) and Öberg & Bergin (2021) for a more comprehensive overview of disk structure.

state species, but larger complex organic molecules (COMs) are also thought to form here. The dominant ionizing agents in this region are external cosmic rays.

Sometime between the Class I and Class II stages planet formation begins in the disk mid-plane.[3] Planets are believed to cause the presence of disk substructure in the form of rings, gaps, and spiral arms. Notably, substructure can be explained by a number of other factors, so in recent years there has been a campaign to model and observe disk substructure and better understand what causes it.

Two of the largest programs to do so are the Disk Substructures at High Angular Resolution Project (DSHARP) and Molecules at ALMA at Planet forming Scales (MAPS) large programs (Figure 1.4). Both programs have led to dozens of publications, and the program overviews are reported in Andrews et al. (2018) and Öberg et al. (2021). The MWC 480, HD 163296, GM Aur, AS 209, and IM Lup protoplanetary disks were observed by DSHARP and MAPS, and these five disks are covered in this thesis. For more information on the physical parameters of the disks, see the previously mentioned overview papers.

Eventually the remaining dust in protoplanetary disks settles into the mid-plane, and the gas fully dissipates leaving behind a fully formed planetary system (after $\sim$ 40Myr Carrol & Ostlie, 2007). Astrochemists study chemical evolution across all of these stages to understand how material necessary for life is incorporated into planets. The work in this thesis focuses specifically on the Class II protoplanetary disk stage and how radiation from the young central star impacts the molecular species that are incorporated into forming planets.

[3] The exact timing of when planet formation can begin is disputed, but planets and protoplanets have been detected in both Class I and Class II systems.

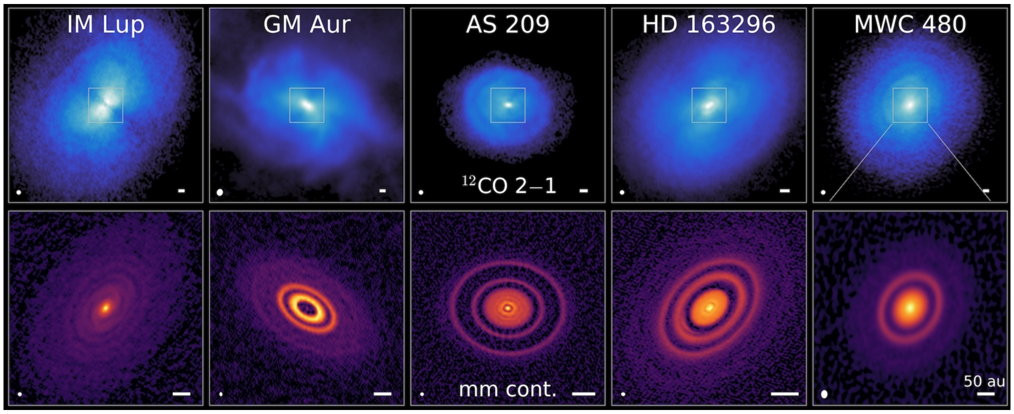

Figure 1.4 Top: CO $2-1$ moment zero maps for the five disks observed by MAPS (Öberg et al., 2021; Law et al., 2021). Bottom: Continuum emission for the same five disks. The IM Lup, AS 209, and HD 163296 continuum images are from the DSHARP survey (Andrews et al., 2011). The GM Aur continuum image is from Huang et al. (2020). The MWC 480 continuum image is from the MAPS data. Image beams are shown in the bottom left corner. This image was taken from the MAPS webpage and adapted from Law et al. (2021)

1.2.1 T Tauri Stars

T Tauri stars are a specific type of star that are particularly relevant for studying the origins of the Solar System, as they are essentially 'baby' versions of the Sun. These stars are approximately solar mass pre-main sequence stars (i.e., they do not yet burn hydrogen), and they are exceptionally more dynamic and X-ray bright than the modern Sun. For example, the typical X-ray luminosity of a T Tauri star is $L_{\mathrm{XR}} \approx 2 \times 10^{30}$ erg s^{-1} (Flaccomio et al., 2003; Wolk et al., 2005), about 10^4 times brighter than the modern day Sun (Peres et al., 2000). Additionally, T Tauri stars commonly undergo flaring events that temporarily increase light emission across the electromagnetic spectrum. Flare statistics by Wolk et al. (2005) suggest that T Tauri stars experience flares on an approximately weekly basis.

While the exact mechanism behind flaring events is still debated, one theory suggests this variability occurs because T Tauri stars do not yet have stabilized stellar

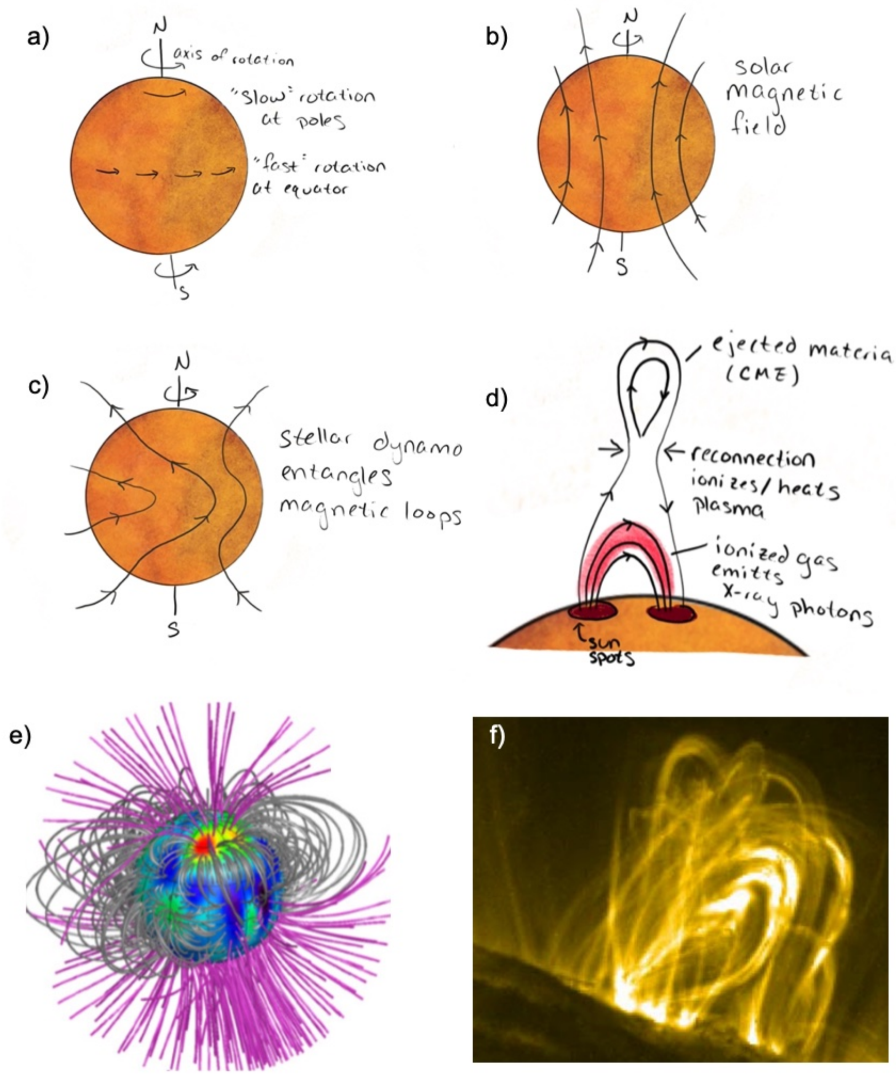

Figure 1.5 This graphic represents how X-ray flares occur in solar mass stars. The stellar equator rotates more quickly than the poles (a), which causes magnetic field lines that trace the star's magnetic field (b) to become twisted (c). The twisted field lines can connect with each other or 'pinch' in a re-connection event (d). This processes dramatically heats and ionizes gas/plasma resulting in X-ray photon emission. Figure (e) is an example of the complex flare structure in solar mass stars. Grey lines indicate closed magnetic fields, and purple lines indicate open magnetic fields. This particular example represents the magnetic field topology of the star II Peg from Rosén et al. (2015). Figure (f) is an image of a flare on the Sun (observation by the Transition Regions and Coronal Explorer, TRACE, at 171 A). Note that the brightest emission comes from the hot gas trapped in the field lines, as indicated in (d). Image is taken from Güdel (2004).

dynamo, which is a phenomenon caused by differential rotation. The poles of a star rotate much more slowly than the equator, which entangles magnetic field lines. These field lines then 'snap,' or reconnect, releasing large amounts of heat and energy in the form of X-ray light. See Figure 1.5 for an illustration of the dynamo or Carrol & Ostlie (2007) and Shu (1982) for more on flare energetics and physics.

The Sun also experiences flares, notably the source of the auroras, but the flares are exceptionally less bright and less frequent than in T Tauri stars. Additionally, the Earth's magnetic field protects us from weaker modern flares, but the building blocks of Earth were unprotected from the harsh radiation fields associated with the protostellar environment.

1.3 Chemical Reactions in Space

At first glance, chemical processes in space seem to break all the rules of chemistry on the earth, but chemistry obeys the same laws of physics no matter the environment. Temperatures and densities in star and planet forming regions are so dramatically different than on Earth, that reactions and processes common in space would be challenging or impossible on Earth and vice versa. There are no liquids in space (excluding terrestrial bodies, but we are only considering the planet formation stages here), so chemistry must evolve in either the gas-phase or in interstellar ices. Planet forming regions are incredibly dynamic, where species can freeze out, desorb, then freeze out again throughout the entire star and planet formation process. To gain a comprehensive view of chemical evolution, we must consider both gas and ice and how the two are connected.

Photodissociation	$AB + h\nu$	$\rightarrow$	$A + B$
Neutral-neutral	$A + B$	$\rightarrow$	$C + D$
Ion-molecule	$A^+ + B$	$\rightarrow$	$C^+ + D$
Charge-transfer	$A^+ + B$	$\rightarrow$	$A + B^+$
Radiative Association	$A + B$	$\rightarrow$	$AB + h\nu$
Dissociative Recombination	$A^+ + e^-$	$\rightarrow$	$C + D$
Collisional Association	$A + B + M$	$\rightarrow$	$AB + B$
Associative Detachment	$A^- + B$	$\rightarrow$	$AB + e^-$

Table 1.1 A generalized list of reactions and products that are considered in gas-phase chemical reaction networks. Adapted from Tielens (2005) Table 4.1.

1.3.1 Gas-phase Chemistry

In general, the majority of gas-phase chemical processes in space can be summarized as

$$A + B \rightarrow C + D, \tag{1.1}$$

where the A, B, C, and D include molecules, atoms, ions, phtons, dust grains, and electrons. For example, in the photoionization of water,

$$\mathrm{H_2O} + \gamma_{\mathrm{UV}} \rightarrow \mathrm{H_2O^+} + \mathrm{e^-}, \tag{1.2}$$

A and B are the water molecule and UV photon, and C and D are ionized water and an electron. A list of chemical and physical processes commonly considered in astrochemical reaction networks is summarized in Table 1.1.

Three-body reactions (or higher) are incredibly rare, since density and pressure levels in space are so low that the rate of successful three-body collisions is negligible compared to the rate of successful two-body reactions. Additionally, the low temperatures in space make reactions with barriers practically impossible.[4]

[4]Unless we want to start talking about tunneling, but tunneling dominantly occurs in interstellar ices, and it is not relevant for the topics covered in this thesis.

In general, reactions that include a photon and/or charged reactant occur more readily than reactions with only neutral species. For example, neutral association reactions are less likely to be successful due to the conservation of energy. For two reactants to successfully create a new bond the following must occur. 1) the new bond must be at a lower energy state than the independent reactants, and 2) energy must be emitted in some way, otherwise the reactants will dissociate. Williams & Hartquist (2013) fully describes this concept with respect to the formation of H_2. Reactions with ions are also faster, since they typically have higher collisional cross sections, thus increasing the probability that a collision between two reactants will occur at all. See Draine (1947) for further information on the mathematics of collisional cross sections.

1.3.2 Chemistry in Interstellar Ices

Within protoplanetary disks, molecules begin to freeze out beyond the snow-line, which is the radial location where densities are high enough and temperatures are low enough for a species to stick to dust grains, forming ice layers. A single disk will have several snow-lines, where water freezes out first, then CO_2, then CO, and so on based on the vapor pressure of the species.

Once a chemical species freezes out onto a dust grain, they can react with neighboring species in neutral-neutral reactions that are inefficient in the gas. Additionally, atoms and some molecules can migrate, or hop, across the ice, which allows for further reactions (mostly hydrogen, since the more mass a species has the slower it migrates). For example, methanol (CH_3OH) forms dominantly in the ice via a series of neutral-neutral protonation reactions of CO (Watanabe & Kouchi, 2002). Many organic molecular species, particular complex organic molecules[5] (COMs), are thought

[5]Complex organic molecules (COMs) are defined as any carbon bearing species with six or more atoms; methanol being the simplest COM. To methanol's credit, it once *was* considered a complex

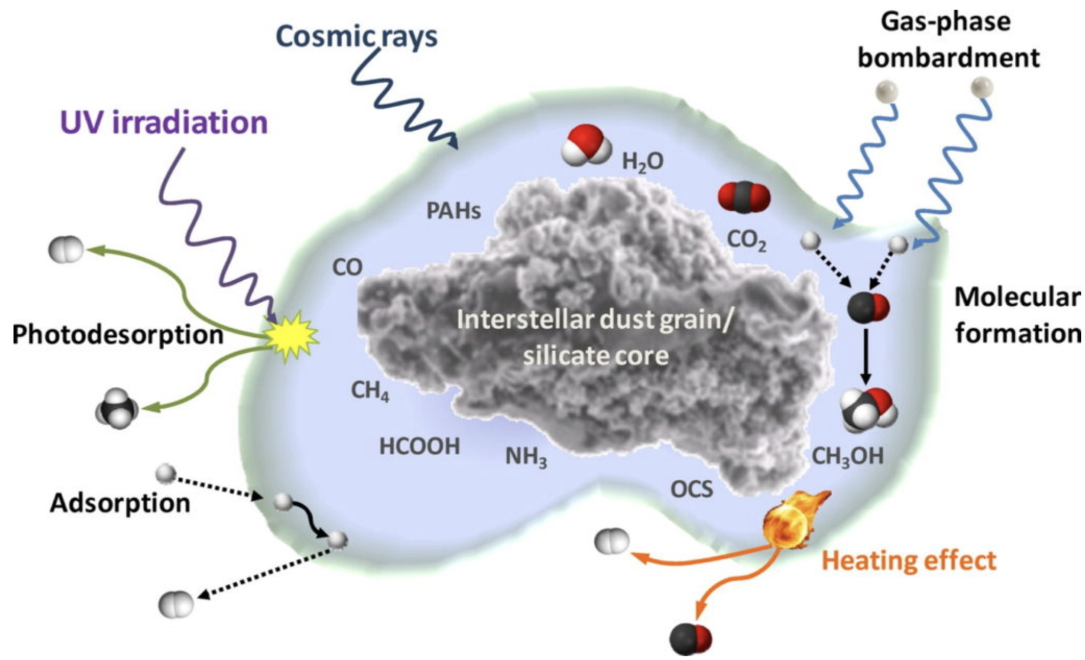

Figure 1.6 Examples of chemical and physical processes that occur in ices on dust grains. UV radiation and cosmic rays can ionize and desorb ices. Exothermic reactions can give reaction products enough energy chemically desorb. Taken from Meinert et al. (2011).

to form almost exclusively in the ice. See Figure 1.6 for further examples of processes that occur on ices.

1.3.3 Chemical Modeling: the Rate Equation Method

There are many different types of chemical and astrochemical models, but for the purpose of this work we focus on models based on the rate equation method (Wakelam et al., 2013). These types of models are created to monitor how chemistry evolves over time using reaction kinetics. Essentially, the change in the abundance of molecule A at one moment in time compared to a previous moment in time can be

species in space, but in recent years larger molecules like aromatic rings have been discovered at an increasing rate (e.g. McGuire et al., 2020; Burkhardt et al., 2021). This has spurred a debate amongst astrochemists on what 'complex' means and if we need to revise our terminology.

defined as the sum of the amount of A created minus the amount of A destroyed at a moment in time.

Assuming that all reactions can be summarized as Equation 1.1, then the rate of destruction of reactants A and B is defined as

$$\frac{d[\mathrm{A}]}{dt} = \frac{d[\mathrm{B}]}{dt} = -k[\mathrm{A}][\mathrm{B}], \tag{1.3}$$

where k is a reaction rate constant. Similarly, the rate of formation of products C and D defined by

$$\frac{d[\mathrm{C}]}{dt} = \frac{d[\mathrm{D}]}{dt} = k[\mathrm{C}][\mathrm{D}]. \tag{1.4}$$

The rate coefficient, $k = \sigma\nu$, is determined by collisional cross section between the reactants, σ, and the velocity of a particle, ν. The collisional cross section is the minimum distance required for two particles to collide. This is also the reason charged particles tend to have faster reactions rates, since they tend to have higher attractions to other species, so the two reactants do not need to get as close to each for a successful collision to occur. A particle's velocity is defined as

$$<\nu>= (\frac{8K_BT}{\pi\mu})^{0.5}, \tag{1.5}$$

where μ is the species mean molecular weight, K_B is the Boltzmann constant, and T is the system temperature. Therefore, the warmer a system is the higher the rate coefficient is.

Based on the reaction kinetics in Equations 1.3 and 1.4, the rate at which a reaction occurs is dependent on three factors. 1) The amount of reactant in the system. 2) How likely two particles are to successfully collide. 3) The temperature of the system. Yamamoto (2017) and Draine (1947) include a more comprehensive overview of reaction kinetics, and I recommend referring to them for further details.

The rate equation methods utilizes these ideas to determine the abundance of a species A by

$$d[\mathrm{A}] = \sum_{i=1}^{n} k_i[\mathrm{A}][\mathrm{B}_i] - \sum_{j=1}^{m} k_j[\mathrm{A}][\mathrm{B}_j], \tag{1.6}$$

assuming i total reactions that form A and j total reactions that consume A. The models presented in Chapters 2 and 3 utilize the rate equation method to model the chemical evolution of a protoplanetary disk. The specific models are covered in further detail in those chapters.

1.4 Observational Astrochemistry

1.4.1 Radio Interferometers

Protoplanetary disks are relatively small and dim in our night sky, so it is incredibly difficult (if not impossible) to observe them by with single dish radio telescopes. Protoplanetary disks need interferometers that are not constrained by the size of a single dish.[6] Instead, they use the collective power of several to dozens of individual antennas to create a single 'giant' telescope. Together, many antennas can effectively create a telescope the size of the Earth, as has been done by the Event Horizon Telescope (EHT) which directly observed a black hole for the first time ever (Event Horizon Telescope Collaboration et al., 2022). Notably, the EHT is a combination of radio facilities from around the world, whereas the 'typical' interferometer uses a single observing facility/telescope. The Atacama Large Millimeter/submillimeter Array (ALMA) in Chile and the Sub-Millimeter Array (SMA) in Hawaii are two such

[6] I would like to note that single dish telescopes are powerful tools in the field of astrochemistry, but not as much for protoplanetary disk chemistry, since they are so faint. Single dish telescopes have been used to detect some of the most complex molecular species in space to date (e.g. the GOTHAM and ARKHAM collaborations, McGuire et al., 2020), but for the purpose of this thesis we are focusing on interferometers.

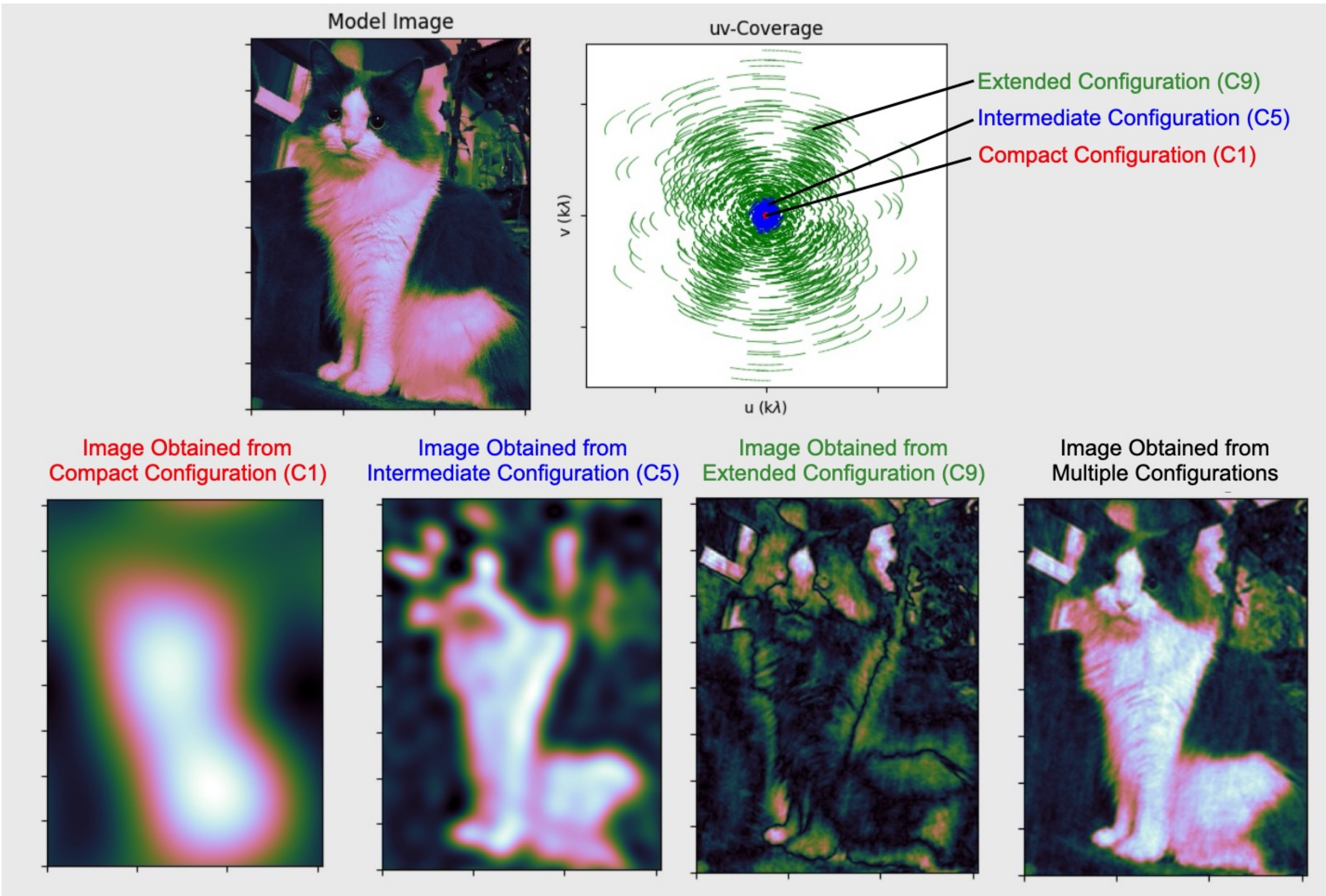

Figure 1.7 This figure demonstrates how an interferometer 'sees' an image, based on it's configuration. In this case, the model image is of a cat (named Dancer), and synthesized ALMA images were made in compact (C1), intermediate (C5), extended (C9) configurations, and combined data from the C1, C5, and C9 configurations. The compact configuration (C1, low baseline coverage) is able to accurately measure flux, but is not able to resolve the image. In the C1 configuration, we can clearly see the brightest parts of the image, but we cannot tell that the image is of a cat. The extended configuration (C9, long baseline coverage) is able to resolve that the image is a cat, but we not able to tell what parts of the cat are brightest. This figure was produced using the friendlyVRI software produced by Cormac R. Purcell and Roy Truelove and is available at https://crpurcell.github.io/friendlyVRI/. Credit also goes to Dancer for posing for this photograph.

facilities.

Observations from the SMA led to some of the earliest detections of molecular gasses in disks (e.g. Öberg et al., 2010), while ALMA observations have revolutionized the field by providing such high spatial resolution images that we can even indirectly observe planets.

However, the spatial resolution and flux sensitivity associated with interferometers come at a price. The 'giant' telescope that is created by combining antennas does not 'see' the sky the same that a single dish antenna (or even your eyes) can. Instead, an interferometer can be thought of as a single dish with holes in it. The interferometer 'sees' the sky, but the configuration of the antennas determines how sensitive the telescope is to the emitted light (flux) and how well the image can be resolved (spatial sensitivity). Antennas close to each other (i.e., short baselines) are significantly more sensitive to flux, while antennas further apart (i.e., long baselines) have much higher spatial resolution (see Figure 1.7 for an example). The most powerful images use a combination of short and long baseline data to utilize the full range of interferometers. If the reader desires a further explanation of interferometry, I recommend the text books Shu (1982) and Thompson (2017) for further reading.

1.4.2 Radio Spectroscopy

All light traces and interacts differently with matter. For example, optical and UV light typically corresponds with electronic excitation in atoms, IR light traces molecular vibrations, and radio and microwave light trace molecular rotations. Radio spectroscopy is a particularly powerful tool to study the gas-phase composition of astronomical environments, since each and every molecule has a unique spectrum[7]

[7]This is true except for symmetrical molecules, like H_2. These species do not have rotational spectra due to their lack of dipole moment. I recommend Steinfeld (1974) and Bernath (2016) for more information on spectroscopy.

or 'fingerprint.' Each unique spectrum can be measured in a laboratory vacuum chamber and then compared to line detections from observations. Laboratory experiments combined with observations allows for the robust detection and identification of molecular species in space.[8]

Radio spectroscopy can also be used to measure disk temperature using rotational diagrams, molecular abundances and column densities using radiative transfer models (see Kwok (2007) for details on radiative transfer), and to trace the velocity structure of objects in space, such as protoplanetary disks.

Protoplanetary disks rotate around the central star, where material closest to the star rotates the fastest, and material furthest from the star rotates the slowest. The rotation of the majority of disks can be defined as Keplerian rotation, and the velocity (ν_0) at a radius r can be defined as

$$\nu_0 = \sqrt{\frac{GM}{r}} = 30(\frac{r}{1\mathrm{au}})^{-0.5}(\frac{M}{1M_{\mathrm{sun}}})^{0.5}\mathrm{kms}^{-1}, \tag{1.7}$$

where M is the mass at radius r and assuming $M_{\mathrm{star}} >> M_{\mathrm{disk}}$ (Yamamoto, 2017). This velocity gradient causes lines to have a 'double horn' shape, instead of a single peak like would be measured in a stationary environment (see Figure 1.8).

In this thesis, I use radio spectroscopy to search for variations in line flux, and therefore molecular abundance. Additionally, I search for variations in the spectral shape of HCO^+ and $H^{13}CO^+$, which would correspond to changes in molecular abundance at different radial locations.

[8] This process can actually be very complicated, and I've just described a 'best case scenario' detection.

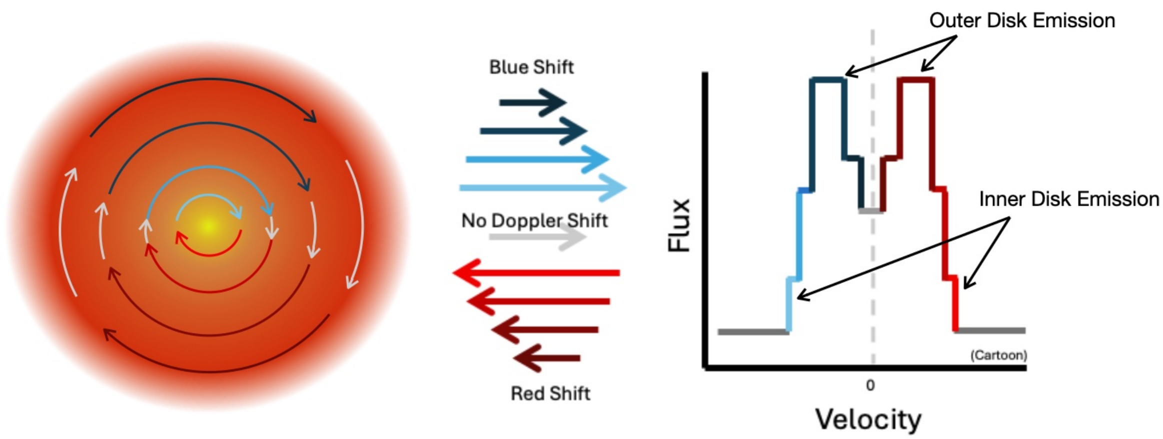

Figure 1.8 This graphic demonstrates line broadening due to the Keplerian rotation of a protoplanetary disk, assuming that the disk is being viewed edge on from the position of Doppler shift arrows. The inner disk, which rotates the fastest, has the highest velocity shift, while the outer disk, which rotates the slowest, is closest to the line's true transition frequency.

1.5 Science Communication

Communication is one of the most important aspects of science. To fully disseminate our work with the world, we must be able to convey our our knowledge to experts in the field, young scientists, students, and even the general public. I would argue that scientific communication is not only an essential part of being a scientist, but it is our responsibility to ensure that science is accessible to all.

I have over nine years of experience in scientific outreach towards children; I am an active member of the Astrobites collaboration; I am currently advising an undergraduate student on their senior thesis; I participate in public nights at telescope facilities such as McCormick Observatory and Fan Mountain; I have presented at several Astronomy on Tap events. These are but a few examples of the scientific outreach and communication skills I have gained during my scientific career. In the following sections I go into further detail on some of the advising and outreach initiatives I have participated in.

1.5.1 A Guide for CASA Imaging Disk Continuum and Lines

During the 2023-2024 academic year I advised Claire Thilenius for her undergraduate senior thesis. During this time, Claire completed an imaging guide using the interferometry imaging software CASA (Common Astronomy Software Applications). Her guide is intended to walk the user through the basics of interferometry, continuum imaging, and line imaging; it includes examples on how robust values, mask shape/size, signal to noise ratio, and other important factors impact an image.

Intended for individuals with little to no experience with radio astronomy, the guide runs through an online Jupyter notebook on GitHub, and it utilizes the software MyBinder so that users do not need to create a local python environment to use the guide. This guide will be open access, and we hope to share it with undergraduate astronomy classes and early career scientists who are newer to the field. At the current moment, we are preparing to send the code out for beta testing. The guide will be complete publicly available on GitHub once complete.

Additionally, I worked with Claire during the 2022 Fall semester, where she used the models presented in Chapter 3. A brief summary of her results are included there.

1.5.2 Dark Skies, Bright Kids!

I'd like to ask that you take a second and imagine a scientist. What do they look like? What are they wearing? What are they doing? What makes them a scientist?

Everyone who answers those questions will answer them differently, but the sad reality is that the majority of people will imagine the same thing. White men in lab coats (just try google image searching the word "scientist"). And unfortunately, the demographics of astronomers in the United States[9] reflects this stereotype. Today,

[9]Motivated by the DATA USA 2021 survey: linked here.

Figure 1.9 Volunteers for Dark Skies, Bright Kids after our annual Star Party in September 2022.

many scientists are striving to remove said stereotypes and make astronomy more accessible to under-represented groups. I decided to include an adapted version of an Astrobites article I wrote [10] in this thesis, as it encompasses much of the effort I have put into astronomy accessibility and Diversity, Equity, and Inclusion (DEI), particularly towards children. The majority of text in this section was originally published in an Astrobites article I wrote, entitled "Beyond: Making Astronomy DIY During a Pandemic."

There are many ways for scientists to be more inclusive, but one graduate-student lead organization aims to aid in DEI is by working directly with children to remove these stereotypes. Dark Skies, Bright Kids! (DSBK[11]) is a non-profit volunteer organization lead by the University of Virginia astronomy graduate students. Our mission statement: “Enhance science education and literacy in Virginia elementary schools, primarily in under-served areas.” DSBK hosts weekly after school clubs, summer

[10]Original article can be found here: https://astrobites.org/2020/11/20/template-post-2-3/
[11]Check out the DSBK website: https://www.darkskiesbrightkids.com/

clubs, and one-off events such as an annual Star Party. Each club covers a different science topic (e.g. the Solar System, astrobiology, galaxies and stars). Each club is designed to foster a natural curiosity in children using hands on activities that introduce astronomy and the scientific process.

How do we know if DSBK is challenging preconceived notions of who can be a scientist? We ask the children to do the very same thing I asked you to do. Imagine a scientist. We ask children to "draw a scientist" before and after numerous weekly activities during semester club, and our assessments team analyzed our success in removing stereotypes in science. (Hayes et al., 2020) found that our hands-on activities have a positive influence on children's perspective of science.

1.5.3 Astrobites

Astrobites is a graduate student run organization with members from around the world. Astrobites' mission is to make astronomy accessible to early career scientists. As a member of the Astrobites collaboration, I have written research summaries (bites), attended AAS 236 and 237 for press-coverage, chaired the hiring committee for three years, and I am a Co-PI on an education study, where we measured the efficacy of Astrobites lesson plans in an undergraduate classroom setting (see Chapter 6). I have included some of this work in my thesis. Through Astrobites, I have learned to approach the role of astronomer from the perspective of an educator, rather than a student. These experiences will continue to influence and motivate my future work just as much as my scientific research. Below are a list of my Astrobite articles. The titles are hyperlinked in the online version of this thesis.

- Outreach for Astronomers; Skype a Scientist and Dark Skies, Bright Kids (written with Briley Lewis).
- Beyond: Making Astronomy DIY During a Pandemic.

- Bio-signatures with Flare, a summary of Chen et al. (2021).
- How do Imines Form in Space Clouds? a summary of Lupi et al. (2020).
- Pencil Lead in Space, a summary of Rahul et al. (2020).
- There "Where's Waldo?" of Astrochemistry, a summary of Shingledecker et al. (2019).
- Baby Stars, X-rays, and Planets: How are they Related? a summary of Dupuy et al. (2018).
- Dynamic Desorption: A Tale of Cosmic Rays, a summary of Sipilä et al. (2021).

1.6 What's in this Thesis

While there are decades of research investigating X-ray flares and how they impact temperature, magnetic activity, and accretion in protoplanetary disks, there is relatively little work on the impact of flares on gas and ice composition, even though the atomic and molecular species in gas and ice are the sources of pre-biotic species in planets. This thesis aims to do just that.

Traditionally, light from the Sun and Sun-like stars is considered relatively stable in astrochemical models, even though X-ray flares have been seen to increase disk ionization levels by up to several hundred factors. Since ionization reactions are some of the strongest driving forces of gas-phase chemistry, could flares temporarily cause chemistry to progress more rapidly? And if so, would this effect be permanent or short lived with respect to the disk's life time? For example, HCO^+ is one of the most abundant gas-phase cations in disks and is known to be highly sensitive to ionization rates (Figure 1.10). My research uses techniques explained in this chapter to determine if flares impact the building blocks of Earth and life, and if so, to what extent?

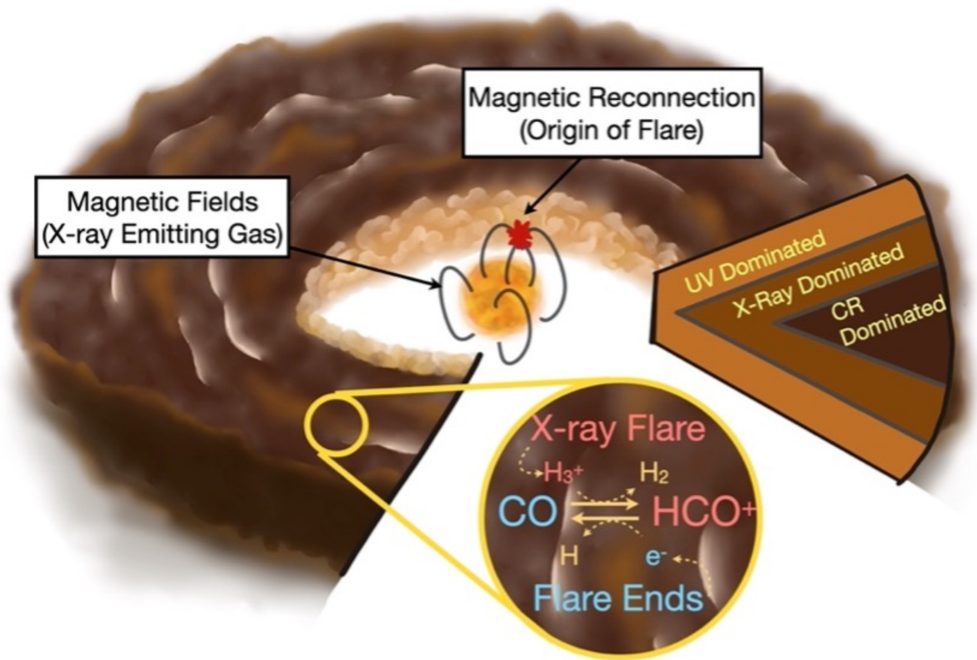

Figure 1.10 Magnetic reconnection events on the surface of T Tauri stars results in an X-ray flare. Flares then increase X-ray ionization rates in the surrounding protoplanetary disk, which causes a temporary enhancement of some gas-phase cations, like HCO^+. Flares are particularly powerful in the 'mid' disk, as UV photons and cosmic rays tend to dominate ionization in the disk surface and mid-plane, respectively.

Chapters 2 and 3 utilize chemical disk models to gain an in-depth perspective of flare-driven chemistry. Chapters 4 and 5 present observational evidence of X-ray flare driven chemistry. Additionally, Chapter 6 discusses an outreach initiative I co-lead through Astrobites. These five chapters are further summarized below. Chapter 6.6 provides an overview of this thesis, further applications to the field, and future work.

Chapter 2: Modeling Time Dependent Water Due to Powerful X-ray Flares from T Tauri Stars. Originally published in Waggoner & Cleeves (2019), this Chapter uses chemical models to explore how a single and powerful X-ray flare impacts the abundance of gas-phase water in a protoplanetary disk.

Chapter 3: Classification of X-ray Flare Driven Chemical Variability in Protoplanetary Disks. Originally published in Waggoner & Cleeves (2022), this Chapter present a new X-ray flare model, XGEN, which was then incorporated in to the chemical disk model used in Chapter 2. In this chapter, I performed a comprehensive study on flare driven chemistry throughout the entire disk.

Chapter 4: Variable $H^{13}CO^+$ Emission in the IM Lup Disk: Further Evidence for X-ray Driven Time-dependent Chemistry. This chapter is in preparation to be published, and presents SMA observations of $H^{13}CO^+$ $3-2$ in the IM Lup protoplanetary disk. This chapter is a follow-up to (Cleeves et al., 2017), who first identified variability in this line in this disk.

Chapter 5: MAPS: Constraining Serendipitous Time Variability in Protoplanetary Disk Molecular Ion Emission. This chapter is originally published in Waggoner et al. (2023) and uses data taken as a part of the MAPS large program. I imaged HCO^+ $1-0$ data for each unique observation epoch for each disk to search for variations in the line spectra.

Chapter 6: Improving Undergraduate Astronomy Students' Skills with Research Literature via Accessible Summaries: A Case Study with Astrobites Based Lesson Plans. This Chapter is a part of collaborative project through Astrobites. It is available on ArVix (Lewis et al., 2024) and is currently in peer review with Physical Review Physics Education Research. I was a co-principal investigator with Briley Lewis on this project, and I am second author. We implemented Astrobites lesson plans in undergraduate classrooms to determine if the lessons have an impact on students' perspective of understanding and belonging in astronomy.

Chapter 2

Modeling Time Dependent Water Chemistry Due to Powerful X-ray Flares from T-Tauri Stars

"Each experiment done, each step on the path of knowledge, is achieved by striking out into the darkness. You can't know what you will find, or that you will find anything at all."

Brandon Sanderson, *The Sunlit Man*

2.1 Abstract

The work presented in this chapter has been published in the Astrophysical Journal with L. Ilsedore Cleeves as a coauthor (Waggoner & Cleeves, 2019).

Abstract: Young stars emit strong flares of X-ray radiation that penetrate the surface layers of their associated protoplanetary disks. It is still an open question as to whether flares create significant changes in disk chemical composition. We present models of the time-evolving chemistry of gas-phase H_2O during X-ray flaring events. The chemistry is modeled at point locations in the disk between 1 and 50 au at vertical heights ranging from the midplane to the surface. We find that strong, rare flares, i.e., those that increase the unattenuated X-ray ionization rate by a factor of 100 every few years, can temporarily increase the gas-phase H_2O abundance relative to H by more than a factor of $\sim 3-5$ along the disk surface ($Z/R \geq 0.3$). We report that a "typical" flare, i.e., those that increase the unattenuated X-ray ionization rate by a factor of a few every few weeks, will not lead to significant, observable changes. Dissociative recombination of H_3O^+, H_2O adsorption and desorption onto dust grains, and ultraviolet photolysis of H_2O and related species are found to be the three dominant processes regulating the gas-phase H_2O abundance. While the changes are found to be significant, we find that the effect on gas-phase water abundances throughout the disk is short-lived (days). Even though we do not see a substantial increase in long-term water (gas and ice) production, the flares' large effects may be detectable as time-varying inner disk water "bursts" at radii between 5 and 30 au with future far-infrared observations.

2.2 Introduction

The composition of planets is likely affected by the physical and chemical processes that occur during their formation in the protoplanetary disk stage. It is therefore necessary to understand these processes in order to create accurate models of planetary system formation. Observations have shown that protoplanetary disks are flared dust and gas rich disks with radii as large as hundreds of au (Ardila et al., 2002). Disks are composed of three layers: *i.* the photon-dominated region (PDR), which is rich in atomic and ionic species, *ii.* the warm molecular layer, where molecular and radical species can exist (Aikawa et al., 2002), and *iii.* the mid-plane, where molecular and atomic ices can form on dust grains (Bergin et al., 2007). Photons can easily penetrate the surface layers of the disk since it is a low density area with little shielding. Some UV and X-ray photons can penetrate the warm molecular layer, fostering active chemistry, but few photons reach the dense mid-plane due to the high levels of extinction in this region (Bethell & Bergin, 2011b; Fogel et al., 2011).

The presence of these high energy photons influences the chemistry of the disk, which is thought to evolve slowly over the disk lifetime of $\sim 3-10$ Myr (Strom et al., 1989; Glassgold et al., 1997; Haisch et al., 2001; Fedele et al., 2010). Chemical species observed in disks are primarily small and simple molecules like CO, HCO^+, CN, H_2O, OH, CO_2, HCN, CS, C_2H, and N_2H^+, and some complex molecules, such as formaldehyde, methanol, and methyl cyanide (Dutrey et al., 1997, 2007; Aikawa et al., 2003; Öberg et al., 2015; Walsh et al., 2016). The chemistry of many of these species is directly or indirectly related to the presence or absence of energetic photons or particles from the star and/or environment.

The stellar radiation environment is not constant in time. In fact, short-term X-ray flaring is common in young solar mass stars (e.g., Montmerle & Casanova, 1996), and can produce enough X-rays to dynamically affect the chemical and physical properties of the disk (Glassgold et al., 2005). There is some possibility that short-term X-ray activity can impact the chemical composition of the disk. Ilgner & Nelson (2006c) considered the theoretical impact of flares on the disk ionization fraction by computing electron abundances using a full chemical model. They found flares could play a significant role in the ionization fraction of the disk, which directly impacted the extent of disk "dead zones." Cleeves et al. (2017) found evidence for variations in the disk molecular ion abundances based on multi-epoch submillimeter wavelength data of $H^{13}CO^+$ emission in the IM Lup protoplanetary disk. Since this molecule is directly and efficiently formed from H_3^+, one possible explanation for the observed time variability is chemistry induced by an X-ray flare.

Among molecules detected in disks, H_2O is one of the most important, owing to its role in the formation of habitable planets like Earth. In addition H_2O ice, referred to here as $H_2O_{(gr)}$, may enable grains to more efficiently stick together when they collide (Wang et al., 2005). For planets formed by core accretion, it is believed that both terrestrial and gas giants' rocky inner cores are formed from such inelastic grain collisions (e.g., Pollack et al., 1996). Without an ice coating, the grains are more likely to bounce off each other in an elastic collision, which suggests that planet formation can be impacted by the presence of water-rich ice.

Like HCO^+, H_2O is sensitive to the ionization state of gas, as most processes that form water involve the initial ionization of H_2 (Cleeves et al., 2014b). We present a theoretical study of how water chemistry can be impacted by X-ray flares emitted from a T Tauri star, a star similar to the Sun in the early stages of its life. We adapt a model based on the physical structure of a disk where variability has previously been detected, IM Lup (Cleeves et al., 2017), a solar mass T Tauri star (Panić et al., 2009). The present paper aims to understand how a dynamic X-ray radiation field affects

Table 2.1 Initial Chemical Abundances

H_2	5.0×10^{-1}	Grain	6.0×10^{-12}
$H_2O_{(gr)}$	8.0×10^{-5}	CO	1.3×10^{-4}
O	1.0×10^{-8}	C	5.0×10^{-9}
O_2	1.0×10^{-8}	NH_3	8.0×10^{-8}
He	1.4×10^{-1}	HCN	1.0×10^{-8}
N_2	3.75×10^{-5}	C^+	1.0×10^{-9}
CN	6.0×10^{-8}	HCO^+	9.0×10^{-9}
$H_3{}^+$	1.0×10^{-8}	C_2H	8.0×10^{-9}
S^+	1.0×10^{-11}	CS	4.0×10^{-9}
Si^+	1.0×10^{-11}	SO	5.0×10^{-9}
Mg^+	1.0×10^{-11}	Fe^+	1.0×10^{-11}

both instantaneous (∼days) and long-term (∼Myr) H_2O abundances in protoplanetary disks, and to identify key species and processes contributing to H_2O abundance changes during energetic flares.

2.3 Model

2.3.1 Disk Model

To model the chemistry in a dynamic X-ray environment we adopt the model from Fogel et al. (2011), updated in Cleeves et al. (2014b), which includes 647 species and 5944 reactions and processes. The code adopts the rate equation method and calculates the non-equilibrium chemistry as a function of time.

The code begins with the initial chemical abundances motivated by interstellar cloud models (Table 2.1), which are designed to be representative of molecular cloud abundances. The code runs for 0.5 Myr to reach a pseudo steady state equilibrium at the time of the flare, where 0.5 Myr is redefined as $t = 0$. The code then slows down to calculate the chemistry during the event with fine resolution (30 minute time steps). All chemical abundances are presented with respect to total number of

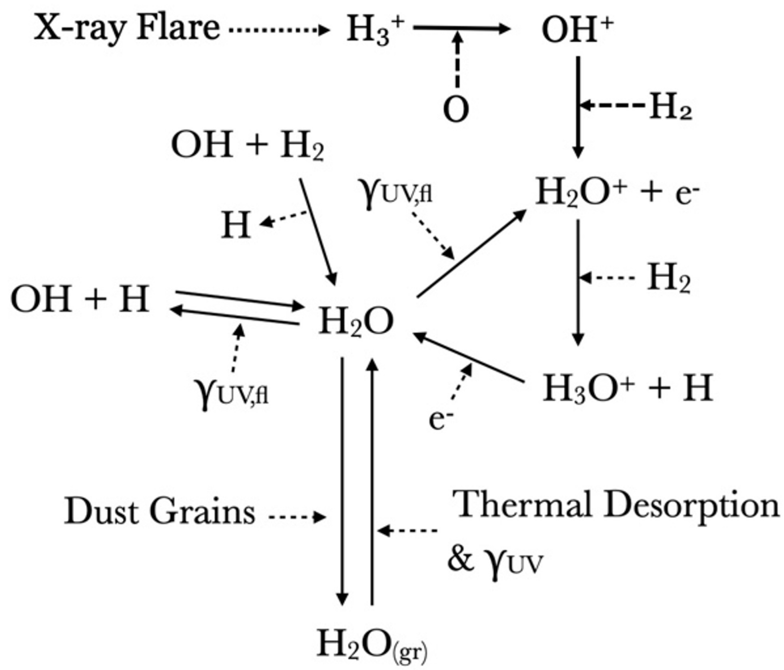

Figure 2.1 This figure is not a part of the original publication, but has been included to demonstrate the dominant processes and how they are connected. See Table 2.2 for additional reactions.

Table 2.2 H_2O Related Processes

	Dissociative Recombination		
1.	$H_3O^+ + e^-$	$\rightarrow$	$H_2O + H$
2.	$H_3O^+ + \mathrm{Grain}^-$	$\rightarrow$	$H_2O + H + \mathrm{Grain}$
	Photo-Chemistry		
3.	$H_2O + \gamma_{UV}$	$\rightarrow$	$H_2O^+ + e^-$
4.	$H_2O + \gamma_{UV}$	$\rightarrow$	$OH + H$
5.	$H_2O + \gamma_{UV,fl}$	$\rightarrow$	$OH + H$
6.	$H_2O + \gamma_{UV,fl}$	$\rightarrow$	$O + H_2$
	Neutral + Neutral		
7.	$H + OH$	$\rightarrow$	H_2O
8.	$H_2 + OH$	$\rightarrow$	$H_2O + H$
9.	$OH + OH$	$\rightarrow$	$H_2O + O$
10.	$H + H_2O$	$\rightarrow$	$OH + H_2$
	Ion + Neutral		
11.	$O^- + H_2$	$\rightarrow$	$H_2O + e^-$
12.	$OH^- + H$	$\rightarrow$	$H_2O + e^-$
13.	$H^+ + H_2O$	$\rightarrow$	$H_2O^+ + H$
14.	$C^+ + H_2O$	$\rightarrow$	$HOC^+ + H$
15.	$C^+ + H_2O$	$\rightarrow$	$HCO^+ + H$
16.	$HCO^+ + H_2O$	$\rightarrow$	$H_3O^+ + CO$
	Adsorption and Desorption		
17.	$H_2O_{(gr)} + \mathrm{Heat}$	$\rightarrow$	H_2O
18.	$H_2O_{(gr)} + \gamma_{Ly\alpha}$	$\rightarrow$	H_2O
19.	$H_2O_{(gr)} + \gamma_{UV}$	$\rightarrow$	H_2O
20.	$H_2O + \mathrm{Grain}$	$\rightarrow$	$H_2O_{(gr)} + \mathrm{Grain}$

hydrogen atoms.

Physical parameters of the IM Lup protoplanetary disk were used in this model, the first source to show significant chemical variability (Cleeves et al., 2017). The model inputs include gas density (ρ), gas temperature (T_{gas}), dust temperature (T_{dust}), UV flux, and X-ray ionization rate, and are sampled from the Cleeves et al. (2016) IM Lup disk model. The simulations were run at discrete points labeled by their radial distance from the star (R) and vertical height from the mid-plane (Z/R), see Appendix A.1. The disk is assumed to be azimuthally symmetric and reflected about the mid-plane. The model treats the point locations independently and does not take into account interactions between horizontal zones.

Parameters for the central star are as follows: effective temperature of $T_{\rm eff} = 3900$ K, stellar radius of 2.5 $R_\odot$ (Pinte et al., 2008), stellar mass of 1 $M_\odot$ (Panić et al., 2009), which is held fixed as was done in Cleeves et al. (2016).

The Smith et al. (2004) Ohio State University (OSU) gas-phase chemical network was used as a basis for the chemical network, and the method of Hasegawa et al. (1992) was used to model grain-surface chemistry. The six types of chemical and physical processes most relevant for the present paper include:

1. dissociative recombination reactions, where a molecular ion accepts a negative charge and dissociates (Table 2.2, Reactions 1 and 2),

2. photolysis, where high energy photons dissociate or ionize species (Table 2.2, Reactions 3-6),

3. neutral + neutral association reactions, defined as
   $A + B \rightarrow C + D$ (Table 2.2, Reactions 7-10),

4. neutral + ion association reactions, defined as
   $A + B^{+/-} \rightarrow C + D^{+/-}$ (Table 2.2, Reactions 11-16),

5. gas-grain adsorption and desorption (Table 2.2, Processes 17-20),

6. grain surface chemistry, such as $A_{(gr)} + B_{(gr)} \rightarrow AB_{(gr)}$ (not shown in Table 2.2).

Four types of photons were included in the model for photolysis reactions. UV Photons ($\gamma_{\rm UV}$) produced by the star's accretion shock (Gullbring et al., 1998); Lyα photons ($\gamma_{{\rm Ly}\alpha}$), which can carry up to 85% of the UV flux (Herczeg et al., 2004);

X-ray photons produced by the central star; UV photons ($\gamma_{\mathrm{UV,fl}}$) produced when electrons are ejected during X-ray ionization of H_2, that impact H_2 and create a fluorescent UV field that can dissociate and ionize chemical species (Maloney et al., 1996).

2.3.2 Chemical Analysis During Flares

The chemical response to X-ray flares was examined at a total of 35 points with radii of $R = 1, 5, 10, 20, 30, 40,$ and $50\,\mathrm{au}$ and normalized vertical heights of $Z/R = 0.0, 0.1, 0.2, 0.3,$ and 0.4 (Appendix A.1, Figure A.1). These points were chosen since they are are relatively close to the star, and the vertical heights allow us to examine chemical responses in the different regions of the disk. We additionally explored models beyond 50 au and saw relatively little change as discussed below in Section §2.4. The cosmic ray rate was held constant at a low value of 2.0×10^{-20} ionizations per H_2 per second. However, Cleeves et al. (2013) determined that cosmic rays are energetically negligible compared to X-rays at the disk surface, the region focused on in this paper, and so the specific value of this input parameter does not impact our findings. See Table A.1 for physical values at all twenty points. Changes in chemical abundance per H atom are determined by plotting $\Delta\chi$, which represents the relative change in abundance compared to a model with no X-ray flares, versus time and is defined as:

$$\Delta\chi = \frac{\Delta\chi_{\text{with flare}}}{\Delta\chi_{\text{without flare}}}$$

It should be noted that for a given flare, highly abundant ($\geq 10^{-5}$) molecules do not show relative change as strongly as those with low abundances (e.g., $\lesssim 10^{-20}$ per H). Individually, these models show H_2O responses at specific locations in the disk, but together they create a 2D model mapping out H_2O flare responses in radius and height, as shown in Figure 2.3.1.

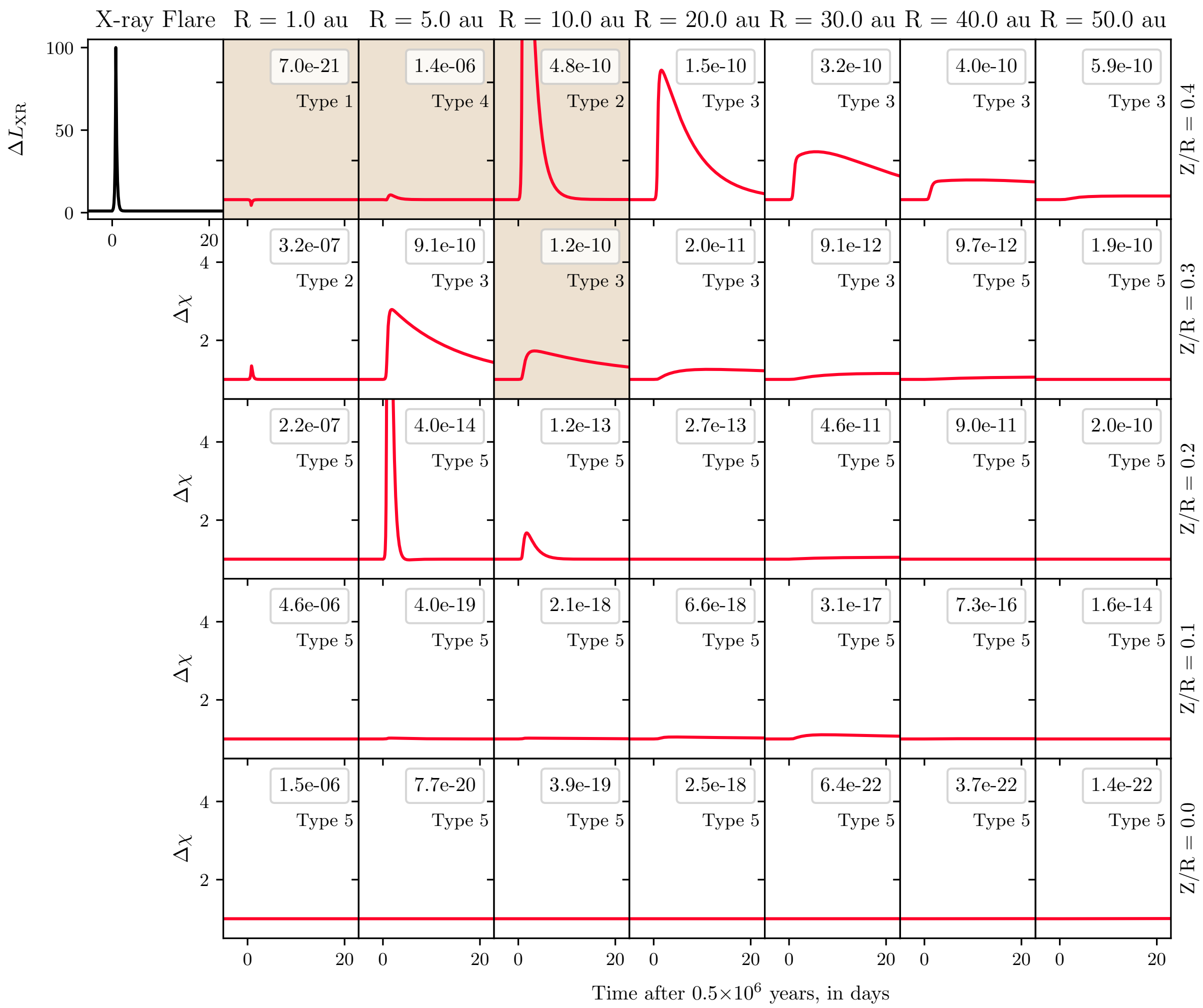

Figure 2.2 H_2O response grid from Test 1. See §2.3.2 for test parameters. Initial H_2O abundances appear at the top of each plot and correspond to $\Delta\chi = 1$. Curve types are described in §2.4.2, and represent the five different response curves seen in the model.
For the points where the maximum abundance is not visible on the plot, the maxima occur: 1. $(\mathrm{R}, \mathrm{Z/R}) = (10\,\mathrm{au}, 0.4)$ at $t = 1.3$ days, $\Delta\chi = 13.4$, 2. $(R, Z/R) = (5\,au, 0.2)$ at $t = 1.1$ days, $\Delta\chi = 15.5$. Analyzed points representing Curves 1-4 are highlighted in tan. Detailed analysis is presented in §2.4.2.

The peak X-ray flare strength used in our fiducial model is 100 times the magnitude of the baseline X-ray luminosity, which was $L_{\mathrm{XR}} = 4 \times 10^{30}$ erg s^{-1}. This high flare value was chosen to show the maximum impact on water abundance due to X-ray flares. The flare rise time is 3 hours, and the exponential decay time is 5 hours. These timescales are chosen to be typical of observed X-ray flares from T-Tauri stars (e.g., Preibisch & Feigelson, 2005). We additionally ran models for both single flare and multi-flare events. Test 1 was run with a single flare initiated at 0.5 Myr ($t = 0$ days). We define the beginning of the flare as six e-folding times prior to the flare peak, effectively setting the flare strength equal to zero at $t = 0$. Test 2 was run with two flares in rapid succession at 0 days and 5 days. Each test was modeled for approximately 23 days after $t = 0$. Note that the timescales presented in §2.4 do not include light travel time, so it assumed that the X-ray ionization rate at each time step reaches each location in the disk instantaneously.

2.4 Results

To guide the discussion in the following sections, Table 2.2 lists the key reactions and processes at the twenty points of the disk considered here. The following sections will refer back to these processes.

2.4.1 General Trends Throughout the Disk

The model revealed that H_2O responses beyond 50 au are insignificant compared to distances interior to 50 au. At distances greater than 50 au there are X-ray flare responses, but responses are typically $\leq 10\%$, and the H_2O abundance is $\leq 10^{-10}$ at most points. As such, we focus the remainder of our analysis on radii ≤ 50 au.

Figure 2.3.1 shows H_2O responses at 35 points across the disk inside of 50 au. Several trends are seen in the responses both vertically and radially. The mid-plane is along $Z/R = 0$, and has no flare response. This behavior is expected because photons are absorbed in the PDR and warm molecular layer before reaching the mid-plane. Likewise, response strength decreases radially from the inner disk atmosphere to the outer disk atmosphere as X-rays become geometrically diluted with distance from the star.

The effect of the snow line, the point at which H_2O exists primarily in the solid rather than gas-phase state, can also be seen as drops in H_2O abundances across the disk. Generally, any points where gas-phase H_2O abundance is less than 10^{-5} are exterior to the snow line, where $H_2O_{(gr)}$ is the dominant phase of H_2O. The surface, such as the point $(R, Z/R) = (1.0\,\mathrm{au}, 0.4)$ is an exception, since this region is strongly impacted by UV radiation from the star and neither gas-phase nor ice-phase H_2O exist in high abundance due to the high levels of photodissociation.

2.4.2 Analysis of Different H_2O Response Curves

Five types of time-varying abundance curves of H_2O are observed in the disk. All 35 positions are labeled with their closest response curve type in Figure 2.3.1, alongside the adopted X-ray light curve. The responses include:

1. abundance decrease, such as at $(R, Z/R) = (1.0\,\mathrm{au}, 0.4)$, where the response curve is a narrow negative spike,

2. production with a fast exponential rise and decay ($t < 10\,\mathrm{days}$), such as $(R, Z/R) = (10.0\,\mathrm{au}, 0.4)$, where the response curve is a positive sharp rise,

3. initial production with a slow decay ($t > 10\,\mathrm{days}$), such as $(R, Z/R) = (10.0\,\mathrm{au}, 0.3)$, where the curve increases and experiences little to no decay,

4. hybrid, such as $(R, Z/R) = (5.0\,\mathrm{au}, 0.4)$, where the curve decreases to a minimum below the initial abundance then increases to a maximum spike,

5. and no observable flare response, such as $(R, Z/R) = (1.0\,\mathrm{au}, 0.0)$, where $\Delta\chi = 0$ or $\Delta\chi \leq \pm 0.05$ and abundance $< 10^{-13}$ with respect to H atom.

These curve types are further analyzed in the following sections. Moreover, the seven fastest processes involved in the production and destruction of gas-phase H_2O were analyzed for each response type using Table 2.2 for reference.

Type 1: Short-term Destruction

Only one point in the disk shows a net destruction curve, $(R, Z/R) = (1.0\,\mathrm{au}, 0.4)$, shown in Figure 2.4.2. Water abundance drops by 15% after 0.75 days, then quickly increases to approximately its initial abundance.

Detailed rates for reactions and processes involving H_2O are evaluated at three representative times, before the flare ($t = 0$ days), at the peak H_2O response ($t = 0.75$ days), and after the peak H_2O response ($t = 3$ days). Of all the disk points modeled, this one is the closest to the star and at the disk surface. This point is more strongly irradiated than other points in the disk, and the increase in X-ray photons during the flare tends to enhance the H_2O photodissociation rate. This behavior can be seen by the appearance of Reactions 5 and 6 at $t = 0.75$ days. These two reactions involve H_2O destruction by UV photons that arise from X-ray photon induced H_2 fluorescence ($\gamma_{\mathrm{UV,fl}}$). At $t = 0$ days and $t = 3$ days Reactions 5 and 6 are not among the seven fastest processes and only appear during the time of the flare. After the flare ends H_2O is reformed by Reactions 7 and 8 to return to its initial abundance.

The abundance of OH was expected to increase since it is a product of Reactions 4 and 5: however, Figure 2.4.2 shows that OH abundance decreases. There are two explanations as to why. First, Reactions 4 and 5 are not among the seven fastest OH reactions, so it is likely that these are not the dominant OH production mechanisms. In addition, OH experiences multiple destructive photolysis reactions, including OH ionization and dissociation to form O and H.

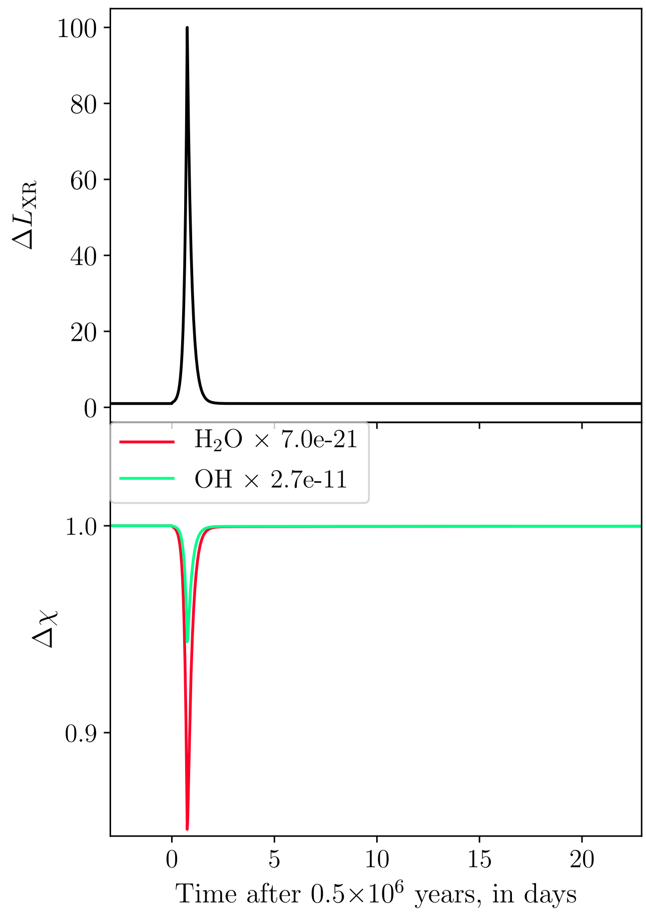

Figure 2.3 Type 1 Reaction Curve: Destruction, $(R, Z/R) = (1.0\,\mathrm{au}, 0.4)$. H_2O is temporarily destroyed through photolysis to produce OH (Reaction 4), but H_2O is reformed by Reactions 7 and 8 to return to its initial abundance. OH abundance decreases due to rapid photolysis.

Type 2: Rapid Production with Fast Decay (< 10 days)

Type 2 responses, i.e., a rapid production with fast rise and decay, occur commonly in the disk grid (Figure 2.3.1). The strongest response is at $(R, Z/R) = (10.0\,\mathrm{au}, 0.4)$, shown in Figure 2.4.2. At this point H_2O abundance increases $\sim 1340\%$ at 1.3 days, then returns back to its initial abundance after 10 days.

Detailed rates are evaluated at four representative times, before the flare ($t = 0$ days), at the peak H_2O response ($t = 1.25$ days and $t = 4.35$ days), and after the peak H_2O response ($t = 8$ days). This point is both on the surface layer of the disk and radially close enough to feel a strong impact from the X-ray flare, but not so strong that the flare is solely destructive like in Type 1. Because of this, neutral and ionic atoms and some molecules, such as C^+ and H_3O^+ are abundant enough to be significant in chemical reactions.

Figure 2.4.2 reveals that the H_3O^+ abundance increases by over 1500% in direct response to the flare, which then speeds up the dissociative recombination of H_3O^+, which in turn drastically increases the production of H_2O (Reactions 1 and 2). There is a flare response delay from H_2O because it takes time for H_3O^+ to find electrons to dissociatively recombine to form H_2O. Reaction 8 also contributes to the production of H_2O due to an increase of 1230% of OH due to the flare. Reaction 8 is an order of magnitude slower than dissociative recombination, and thus does not impact the increase of H_2O abundance as strongly as Reaction 1.

Once the X-ray flare ends, H_3O^+ returns back to its initial abundance, Reaction 1 rate significantly drops at $t = 4.35$ days, which decreases H_2O production. Consumption is much faster than production since H_3O^+ is no longer overly abundant to produce H_2O. The main destructive process is an ion-neutral reaction between H_2O

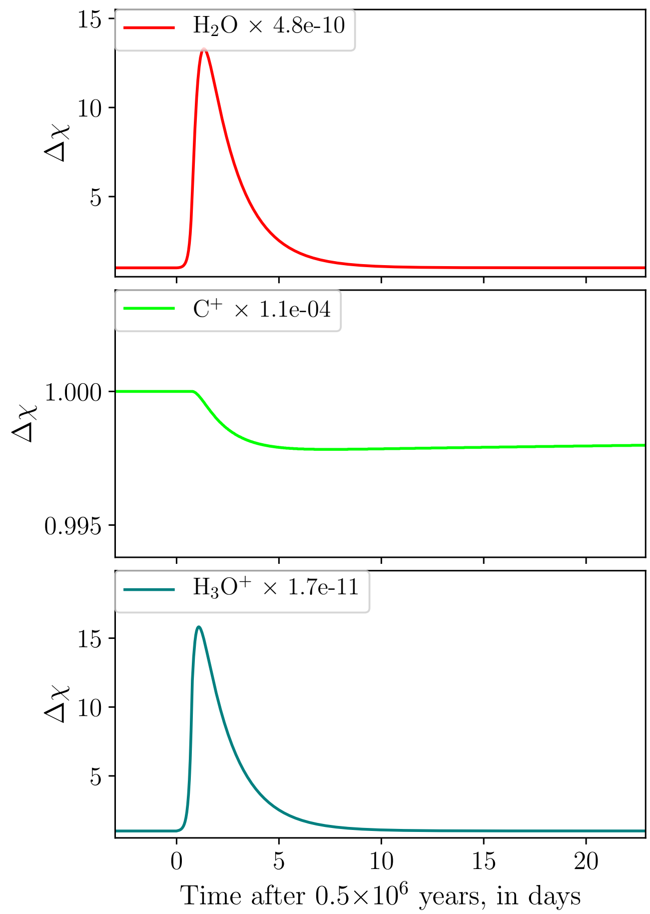

Figure 2.4 Type 2: Production with fast rise and decay ($<$ 10 days), $(R, Z/R) = (10.0\,\mathrm{au}, 0.4)$. Dominant H_2O production is dissociative recombination of H_3O^+ (Process 1). Dominant H_2O consumption is ion-neutral reaction with C^+. Refer to Figure 2.4.2 for change in X-ray ionization rate.

and C^+ (Reactions 14 and 15), with some contribution from UV photolysis (Process 4). C^+ is produced directly from the UV flux, thus H_2O is primarily consumed from photolysis and photolysis dependent processes at this location. Once H_2O abundance has returned to its initial abundance the pseudo steady state equilibrium is reached and further changes in abundance do not occur.

Type 3: "Long-lived" Enhancement (> 10 days)

Response curves that experience an initial enhancement with a slow decay over the course of the simulation ($>$ 10 days) are observed along the $Z/R = 0.4$ and $Z/R = 0.3$ vertical heights (Figure 2.3.1). The point $(R, Z/R) = (10.0\,\mathrm{au}, 0.3)$ was chosen to represent this trend, and whose evolution in plotted in more detail in Figure 2.4.2. After a 0.2 day delay, H_2O increases 73% at 3.3 days, then steadily decreases until the end of the simulation. Detailed rates are evaluated at four representative times, before the flare ($t = 0$ days), after the flare and before/at the peak H_2O response ($t = 1.25$ days/$t = 4.35$ days), and after the peak H_2O response ($t = 8$ days)

Like a Type 2 response (§2.4.2), the initial increase in H_2O abundance is caused by a sharp increase in H_3O^+ abundance (Figure 2.4.2 shows that H_3O^+ abundance increases over 2000%). H_3O^+ undergoes dissociative recombination via Reactions 1 and 2 to produce H_2O faster than H_2O is consumed. While photolysis does occur, this point is not as strongly exposed to the destructive photons, so the fastest gas-phase removal process of excess gas-phase H_2O is adsorption onto grains, creating a slower tail of H_2O removal from the gas. Figure 2.4.2 shows that $H_2O_{(gr)}$ is steadily increasing (to $\sim$4%) as H_2O is steadily decreasing. It is to be noted that H_2O decline appears greater than $H_2O_{(gr)}$ increase for two reasons. First, $H_2O_{(gr)}$ is more abundant than H_2O, so the change in abundance is smaller, and second, H_2O is also being consumed via multiple processes including slow UV destruction, so not all gas-phase H_2O is being converted to ice. Longer simulations are required to determine if the water ice abundance remains permanently elevated or returns back to its initial abundance.

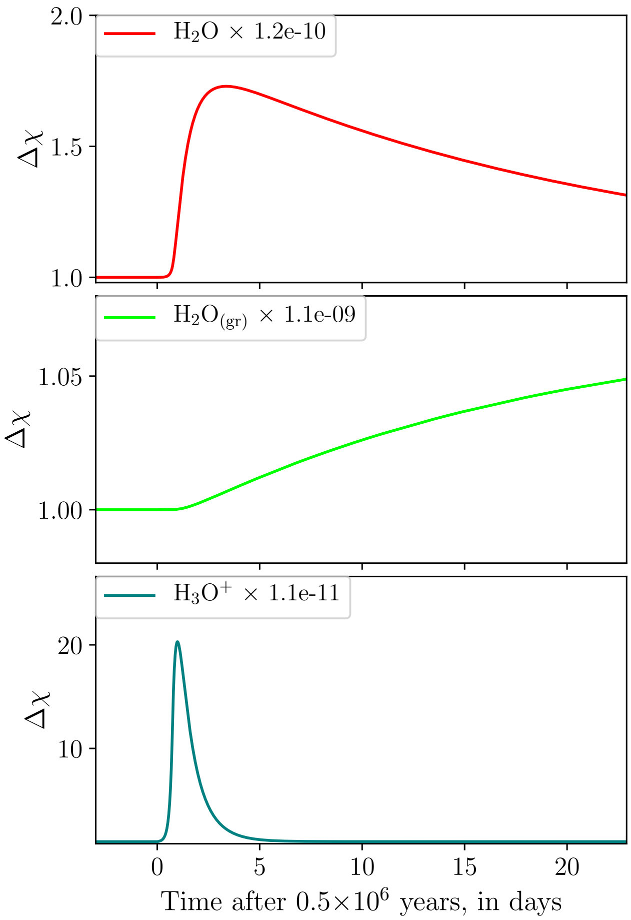

Figure 2.5 Type 3: Long-lived enhancement (> 10 days) $(R, Z/R) = (10.0\,\mathrm{au}, 0.3)$. Main H_2O production is dissociative recombination of H_3O^+ (Reactions 1 and 2). Main H_2O consumption is adsorption (Process 20). Refer to Figure 2.4.2 for change in X-ray ionization rate.

Type 4: Hybrid

Unlike the other curve types, the hybridized response experiences both an absolute minimum and an absolution maximum. $(R, Z/R) = (5.0\,\text{au}, 0.4)$ is the only hybrid response observed in this model (Figure 2.4.2). H_2O abundance initially decreases $\sim$1% at $t = 0.5$ days, then increases $\sim$12% above initial abundance at $t = 1.6$ days, then returns back to its initial abundance for the duration of the run (15 days). Detailed rates are evaluated at four representative times, before the flare ($t = 0$ days), at the absolute minimum H_2O response, ($t = 0.5$ days), at the absolute maximum H_2O response ($t = 1.7$ days), and after the peak H_2O responses ($t = 5$ days).

Similar to the Type 1 response at $(R, Z/R) = (1.0\,\text{au}, 0.4)$ (§2.4.2), this point is strongly impacted by the flare since it is at a close distance to the star (5.0 au) and on the disk surface. However, it is far enough away from the star to have a high abundance of gas-phase molecules and ions, such as H_2O and H_3O^+($\geq 10^{-8}$ per H). Because of its proximity to the star and high abundance of gas-phase precursors, the response of H_2O is a combination of Type 1 (§2.4.2) and Type 2 (§2.4.2) curves. During the initial flare impact, H_2O abundance decreases due to an increase photodissociation (Processes 5 and 6), similar to Type 1. After the initial impact, H_2O is then produced via the normal gas-phase channels followed by dissociative recombination of H_3O^+, similar to Type 2. An initial decrease in H_2O abundance is only observed at $(R, Z/R) = (5.0\,\text{au}, 0.4)$ due to the initial enhanced photodissociation by X-ray induced UV fluorescence. At the end of the flare H_2O is no longer being produced by Process 1 as quickly, since H_3O^+ abundance decreases (Figure 2.4.2). H_2O then returns to its initial abundance due to a combination of photolysis and charge exchange by H^+ (Process 13) followed by dissociative recombination of H_2O^+.

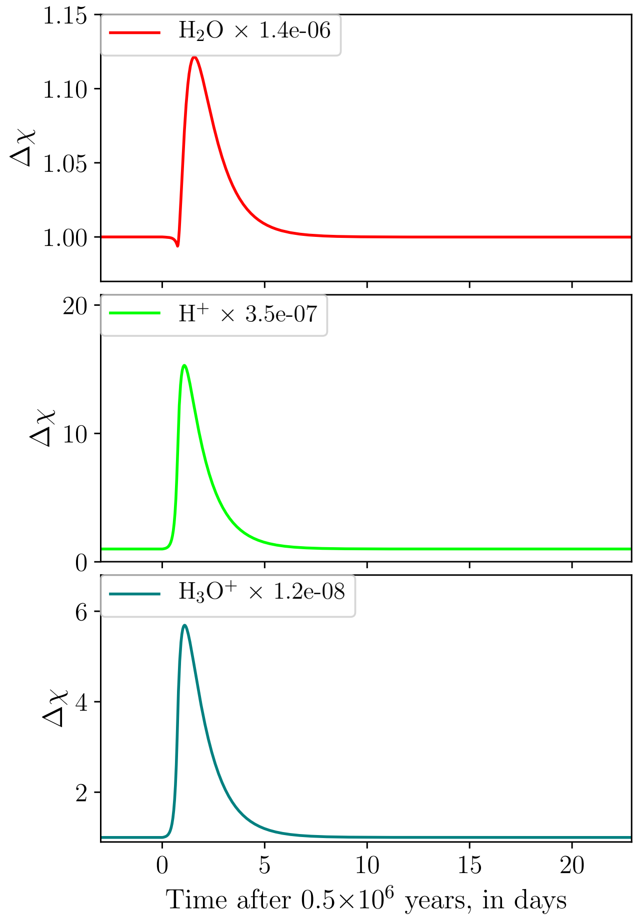

Figure 2.6 Type 4: Hybrid, $(R, Z/R) = (5.0\,\mathrm{au}, 0.4)$. Initially, H_2O is consumed by an increase in photolysis reactions (Processes 5 and 6), then is produced by dissociative recombination of H_3O^+ (Process 1), then it is consumed by a combination of photolysis (Processes 4, 5, and 6) and ionization (Process 13) to return to its initial abundance. Refer to Figure 2.4.2 for change in X-ray ionization rate.

Type 5: No Observable Response

Observable flare responses do not occur at the most dense regions of the disk ($\rho \geq 10^{-12}\,\mathrm{g\,cm^{-3}}$) or along the mid-plane for one of two reasons. In regions where there is a large abundance of gas-phase H_2O ($\geq 10^{-7}$ per H) H_2O is not as sensitive to change. In regions where there is a low X-ray ionization rate (essentially zero) there are not enough photons present to initiate chemistry.

2.4.3 Flare Strength Variation

All previous analyses were performed with X-ray flare strengths equal to 100 times the background X-ray ionization rate, which is considered an extremely strong and rare flaring event (Wolk et al., 2005). We found that weaker flares (a few times X-ray ionization rate), which are much more common, produced similar time-varying abundance profiles in this model, but with smaller amplitude.

Figure 2.4.3 shows H_2O responses to flare strengths of 5, 10, 25, 50 and 100 at $(R, Z/R) = (10\,\mathrm{au}, 0.4)$. Figure 2.4.3 presents a relationship between the maximum change in H_2O abundance that occurs and flare strength, for values of 100, 50, 25, 10, and 5 times the baseline X-ray luminosity. Both $(R, Z/R) = (10\,\mathrm{au}, 0.4)$ and $(20\,\mathrm{au}, 0.4)$ were found to have a linear dependence on change in H_2O abundance compared to the change in flare strength (Figure 2.4.3). The maximum change in the H_2O abundance in response to a flare follows the following relationships: at $(R, Z/R) = (10\,\mathrm{au}, 0.4)$, $\Delta\chi = 0.12 \times \Delta L_{XR} + 0.88$, and at $(R, Z/R) = (20\,\mathrm{au}, 0.4)$, $\Delta\chi = 0.034 \times \Delta L_{XR} + 0.97$, where ΔL_{XR} is the peak change in X-ray ionization rate.

2.4.4 Impacts of Muliflare Events

In addition to the single flare analysis (Test 1, Figure 2.3.1), we investigate a model that has multiple flaring events (Test 2, Figure 2.4.4) discussed qualitatively here. Between Tests 1 and 2 only slight variations occurred. As seen by comparing Figures 2.3.1 and 2.4.4 the plots have similar response patterns. Figure 2.4.4 shows that a response to two flares behaves in a similar pattern to a response to one flare, only the responses “stack up" on each other. This behavior suggests that multiple flares will have a similar effect as a single flare, and their cumulative effect will be related to the timing between flares.

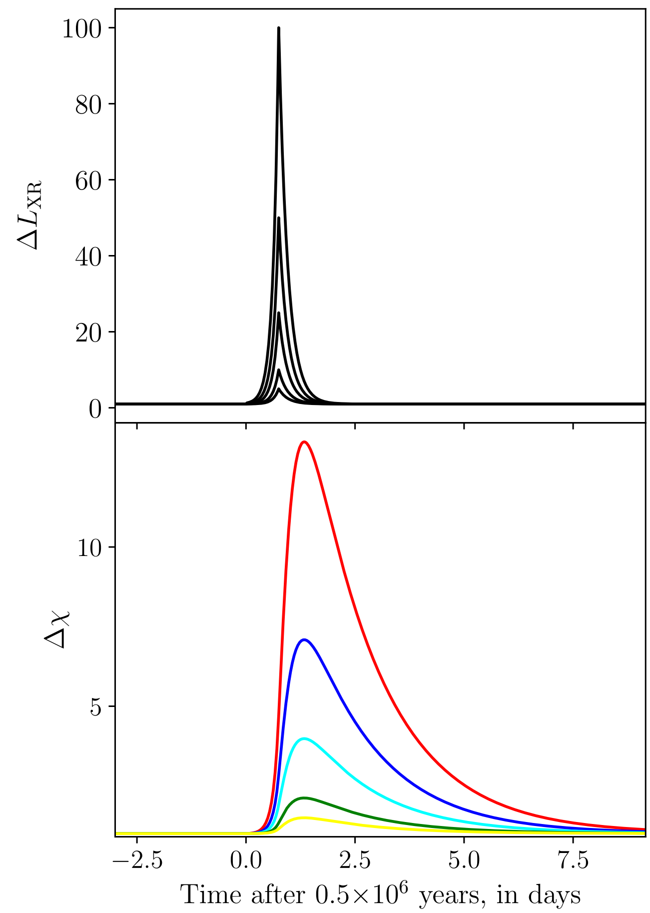

Figure 2.7 H_2O responses to flares of different peak magnitudes at R = 10au Z/R = 0.4. Red indicates flare strength 100, blue indicates 50, cyan indicates 25, green indicates 10, and yellow indicates 5 times the background X-ray ionization rate. Note that the overall abundance profile stays similar while the peak H_2O abundance changes with respect to the X-ray flare strength.

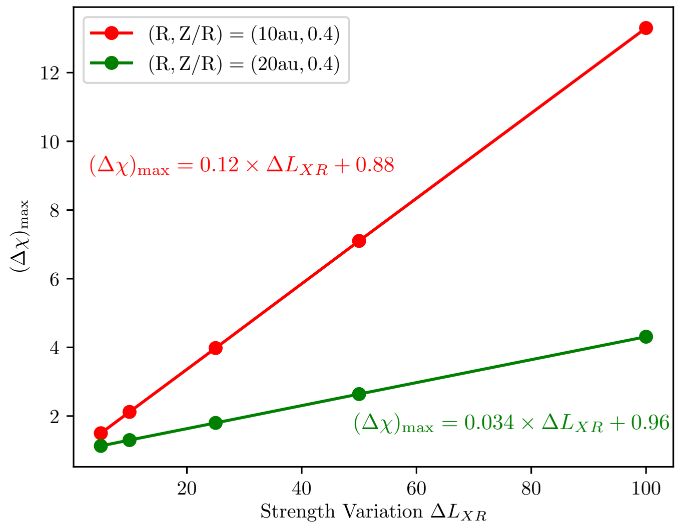

Figure 2.8 The maximum change in H_2O abundance that occurs due to peak flare strengths of 100, 50, 25, 10, and 5 times the relative background X-ray ionization rate , along with linear fits as indicated.

2.4.5 H_2O Ice Responses

In the following section, we quantify how much of the gas-phase response is imparted into the ice. $H_2O_{(gr)}$ responses discussed in this section are obtained from the fiducial strong X-ray flare model. The results of the runs for $H_2O_{(gr)}$ are shown in Figure 2.4.4.

Interior to the snow line there is little $H_2O_{(gr)}$, and the small amount that exists has the same flare response as the gas. When the dust temperature decreases to below the desorption temperature of H_2O, $\lesssim 170\,\mathrm{K}$, $H_2O_{(gr)}$ responses start to deviate from gas-phase H_2O. Finally, in colder regions ($\sim 20 - 100\,\mathrm{K}$), ice and gas-phase responses show little to no correlation.

This suggests that as excess H_2O is produced in hot regions by flares, H_2O rapidly adsorbs onto grains to form $H_2O_{(gr)}$. As the excess gas-phase H_2O returns back to

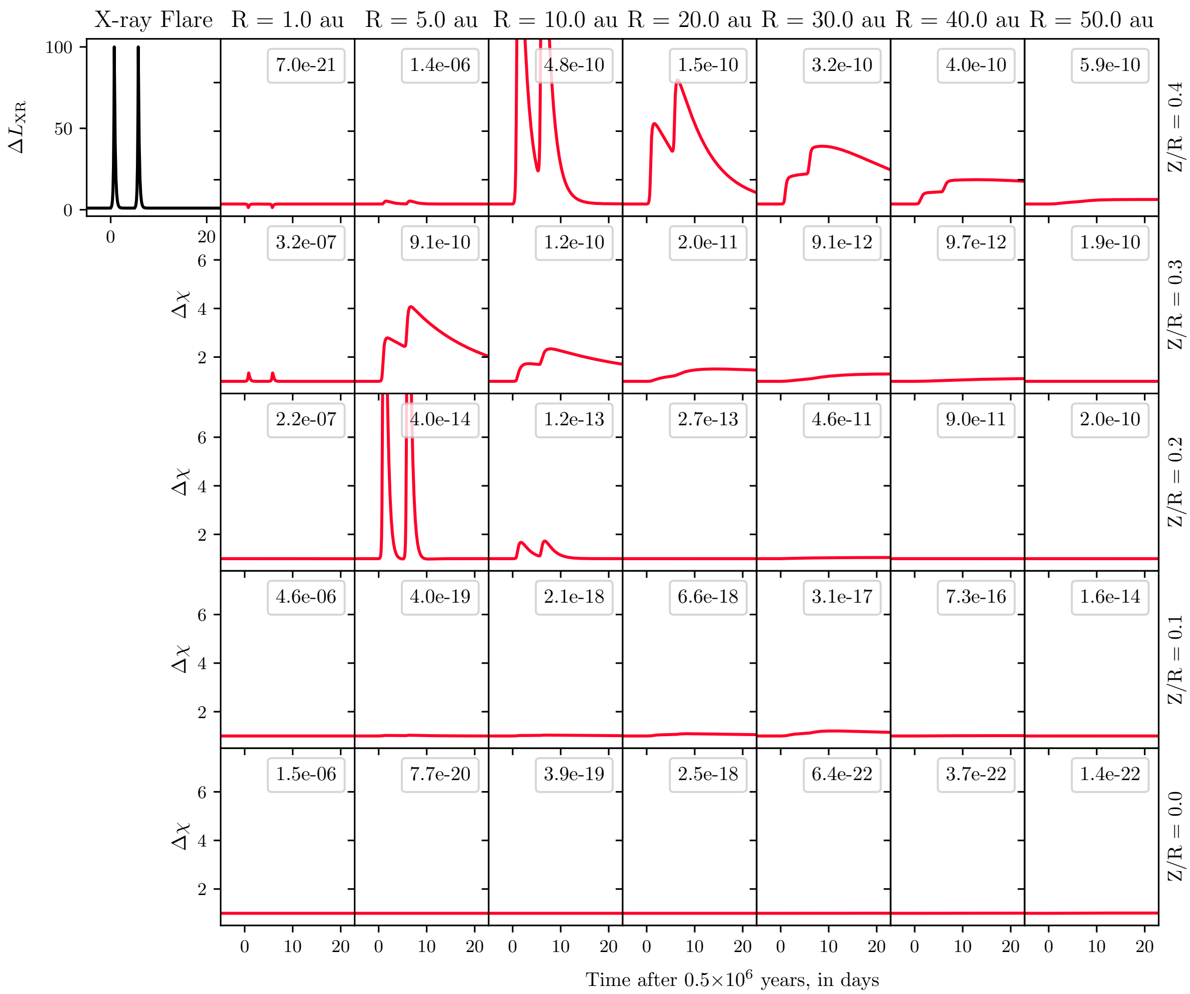

Figure 2.9 H_2O response grid from Test 2. See §2.3.2 for test parameters. Flares occur at $t = 0$ days and $t = 5$ days. Maximums at $(R, Z/R) = (10, 0.4)$ occurs at $\Delta\chi = 12.6, t = 1.7$ days and $\Delta\chi = 13.4, t = 6.6$ days. Second maximum at $(R, Z/R) = (20, 0.4)$ occurs at $\Delta\chi = 5.8, t = 7.5$ days.

its initial pre-flare abundance, $H_2O_{(gr)}$ desorbs and does so as well (Processes 17-19, Table 2.2). At temperatures just below H_2O freeze-out ($\lesssim 170\,K$), desorption is a much slower process, resulting in the observed "longer-lived" response in $H_2O_{(gr)}$ compared to gas-phase H_2O.

The cold, shielded regions, including the points from 5 to 30 au at $Z/R = 0.3$,

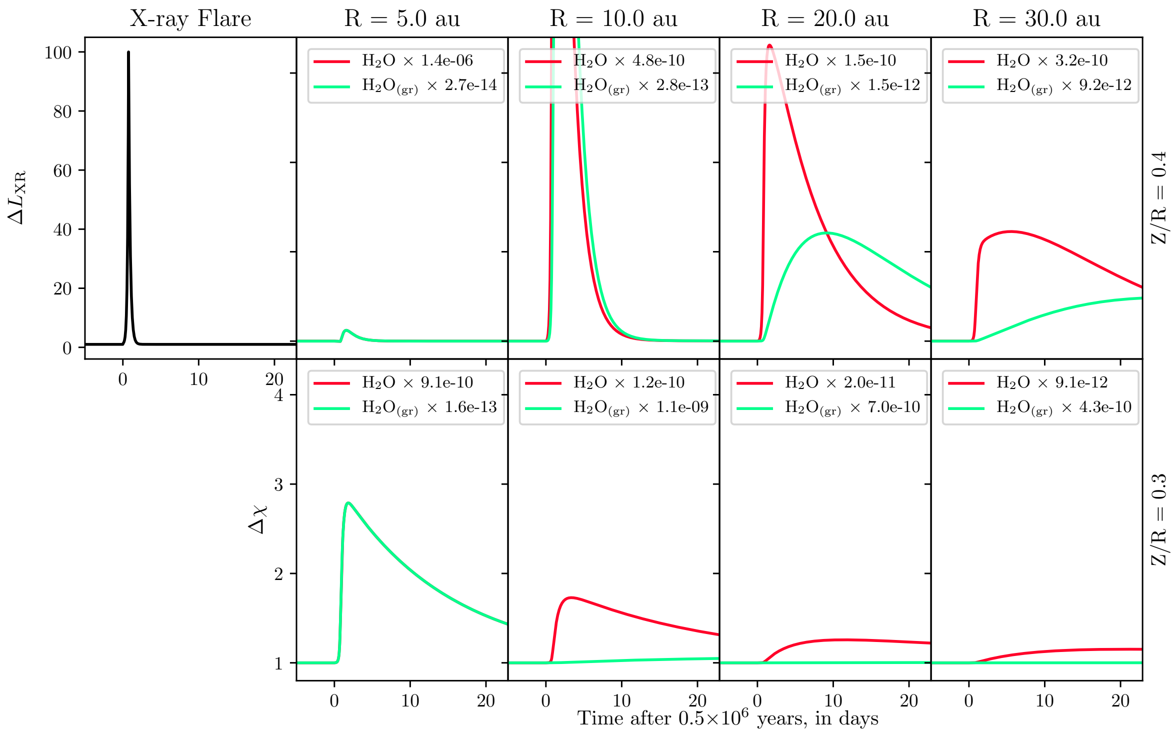

Figure 2.10 Gas-phase H_2O and $H_2O_{(gr)}$ responses radially along the vertical heights of $Z/R = 0.4$ and 0.3, between $R = 5\,\mathrm{au}$ and $30\,\mathrm{au}$. For the point $(\mathrm{R}, \mathrm{Z/R}) = (10\,\mathrm{au}, 0.4)$, where the maximum abundance is not visible on the plot, the $H_2O_{(gr)}$ maximum occurs at $t = 2.3$ days and $\Delta\chi = 10.8$ and the gas-phase H_2O maximum occurs at $t = 1.3$ days, $\Delta\chi = 13.4$.

there is a small but persistent amount $H_2O_{(gr)}$ for the duration of the simulation. At $(R, Z/R) = (30.0\,\mathrm{au}, 0.4)$ the increase is much more significant, about 50%, and does not decrease within the duration of the simulation.

We note that changes to $H_2O_{(gr)}$ from discrete flaring events do not strongly impact the total amount of $H_2O_{(gr)}$ the disk, since the majority of $H_2O_{(gr)}$ lies near the midplane and long term surface changes are minimal (up to 3%) but may have cumulative effects that will be explored in future work.

2.5 Discussion

2.5.1 Response Trends in the Disk

General reaction trends across the disk can be found by comparing the vertical and radial response trends in the disk with the five curve types discussed in the previous Section (§2.4.2) and the physical conditions of the gas as summarized in Table A.1. A Type 1 response is rare and only occurs in regions along the surface of the disk and close (~1 au) to the central star, where the X-ray ionization rate is highest.

Along the vertical height traced by $Z/R = 0.3$, response curves behave primarily with a radially fading Type 3 to Type 5 (no response) pattern. The region closest to the star at $(R, Z/R) = (1.0\,\mathrm{au}, 3)$ is an exception to this trend, since it has a much greater H_2O abundance (three orders of magnitude) and is located in a region with a high UV flux.

A second trend occurs along the $Z/R = 0.3$ vertical height: as radial distance increases, the response curves begin to develop a more prominent lagging tail (Type 3). This feature is likely because photon intensity decreases as distance from the star increases, so after the initial H_2O production, the weaker radiation field decreases the rate of photodissociation. Thus, the dominant gas-phase H_2O consumption process transitions to adsorption onto grains. These Type 3 responses show that H_2O abundance can increase for tens of days, or more. However, additional longer simulations show that each Type 3 response does eventually return to its initial abundance within a year.

Along the vertical heights traced by $Z/R = 0$, and 1 no significant response is observed. This height is along and near the mid-plane, and it is very difficult for photons to penetrate since they are absorbed in the upper layers, so the X-ray ionization rate is very low ($\leq 10^{-27}\,\mathrm{s}^{-1}\ \mathrm{H}_2^{-1}$).

2.5.2 Potential Observability

The ideal conditions to observe X-ray driven variability on H_2O requires both H_2O to be sufficiently abundant ($> 10^{-10}$ per H) and a sufficiently large response in magnitude, at the very least 5% or greater. In addition, having a moderate-long lasting effect can help confirm an abundance change. If the change in abundance occurs for too short of a time, one would have to be very lucky to catch it. Alternatively, if the changes are too gradual, they may go unnoticed.

The regions that show the greatest magnitude of change in water abundance are those with X-ray ionization rates $\geq 10^{-17}\,\mathrm{s}^{-1}\ \mathrm{H}_2^{-1}$ and densities of $\leq 10^{-12}\,\mathrm{g\,cm}^{-3}$. When X-ray ionization rates exceed $\geq 10^{-10}\,\mathrm{s}^{-1}\ \mathrm{H}_2^{-1}$ Type 1 (destructive) response curves are observed. Correspondingly, the significantly changed regions that are potentially observable lie near the surface of the disk ($Z/R \geq 0.3$) and between 10 au and 40 au distance from the star. These regions can be observed using the ground state transitions of water in the far infrared at 557 GHz ($1_{11} - 0_{00}$) and 1113 GHz ($1_{10} - 1_{01}$).

Figure 2.5.2 shows the vertical column density of gas phase water at different times after our fiducial strong flare model. Changes in radial column density presented in Figure 2.5.2 incorporate light travel time. The times are plotted such that $t = 0$ is defined as six e-folding times prior to the peak flare at the star's location. The high column density of water close to the star comes from the water snow line. The intermediate dip and radial rise from 20 to 30 au is caused by increased photo-destruction of water at these intermediate radii. Between 5 and 30 au the greatest change in overall column density of gas-phase H_2O is seen, varying by just over a factor of two in column density. Note that even though the change in H_2O abundance at individual

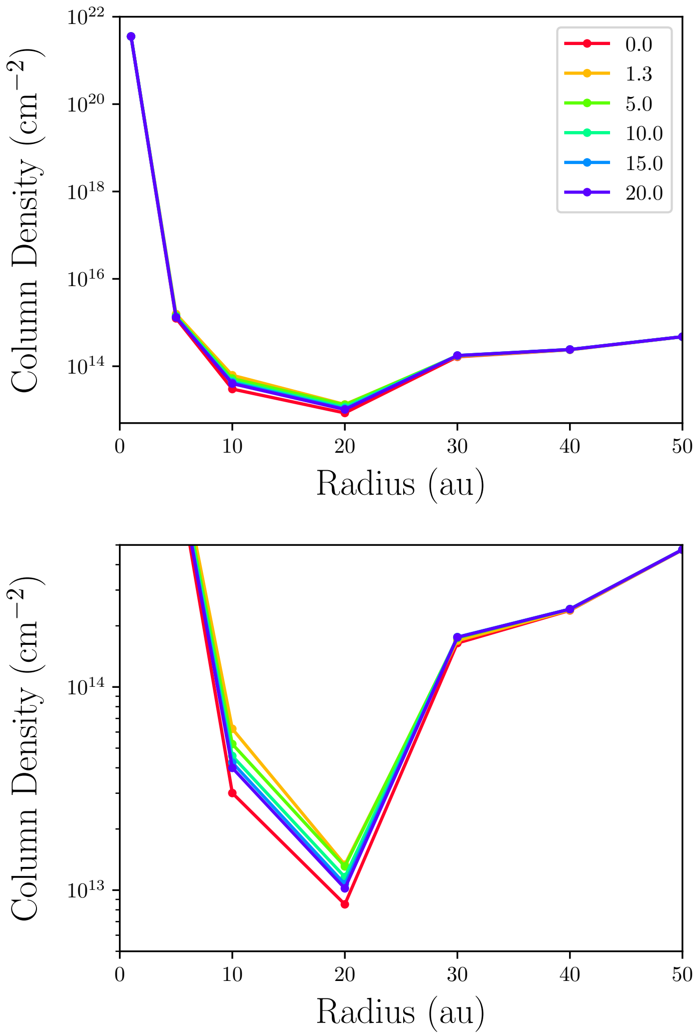

Figure 2.11 H_2O column densities, N(H_2O), are shown at times before flare impact (t=0.0 days), at maximum N(H_2O) increase (t=1.3 days), and as N(H_2O) returns to pseudo steady-state. The right panel shows a zoom-in of the maximally changed region of the left panel, highlighting the factor of ~ 2 change in column density.

heights can be much greater, but the higher densities in the deeper layers, $Z/R = 0.3$ and below, more strongly impacts the overall change in column density.

Within this radial range, H_2O responses have potential observability up to 10 days after flare impact, when there is still a 53% and 36% increase in N(H_2O) at $R = 10$ au and 20 au. H_2O ice variability is unlikely to be observed with little to no variation in column density.

Choice of Disk Model

It is to be noted that IM Lup is extremely massive compared to a "typical" disk, with 0.17 $M_\odot$ (Cleeves et al., 2016). A typical disk has a mass of $\sim 0.04\,M_\odot$ (Williams & Cieza, 2011). A lower gas mass results in higher photon penetration due to less absorption along the disk surface. Therefore, more of the disk volume will be exposed to X-ray flares.

IM Lup also lacks strong disk substructure, with only weak spiral arms and rings in the millimeter emission (Huang et al., 2018b) and rings in the infrared scattered light (Avenhaus et al., 2018). We surmise that if such features are associated with low disk surface density (such as gaps), they will allow for further X-ray penetration into the disk. The resulting chemical responses will be more intense and extend closer to the mid-plane than the responses modeled in IM Lup. In addition, IM Lup is vertically flared, which intercepts more stellar radiation. X-ray flares may not impact a flat disk as strongly.

2.6 Summary

We have conducted a theoretical study of protoplanetary disk water chemistry exposed to strong X-ray flaring events. Our models show that the gas-phase H_2O abundance at the surface responds to X-ray flares in many ways, but the effects are typically short term, lasting a few days or weeks. Analyzing the chemical reaction rates in detail reveals that H_2O production occurs dominantly by dissociative recombination of H_3O^+, and gas-phase H_2O destruction occurs dominantly by photolysis, adsorption onto grains, or ion-neutral reactions with C^+. Photolysis is dominant in the warmer ($T_g > 200$ K) upper layers of the disk, whereas adsorption is dominant in cooler ($T_d < 170$ K) deeper layers of the disk. Reactions with C^+ were only observed in an ion-rich region along the disk surface.

Overall the dominant production mechanisms for water formation during X-ray flares are the gas-phase channels. Grain surface chemistry is included in the model, but it appears to be too slow of a process to impact the short term H_2O abundance changes.

The magnitude of the response is dependent on the local X-ray ionization rate and gas density. Regions with low gas density have high X-ray ionization rates, which tend to have large and flare responses, while regions with higher density and low X-ray ionization rates tend to have no observable flare response. Between these extremes, we find the largest response on water abundances to flares.

We emphasize, this work focuses on strong X-ray flares to understand the maximum effect of these phenomena on H_2O. However, these are rare events and occur every few years. We find that more common flares, i.e., those that increase X-ray luminosity by factors of a few, do not significantly impact H_2O in the disk.

It is possible that any observations done during major flaring events would lead to a higher observed abundance of H_2O than would typically be in the present disk. This type of time-dependent chemical variability has already been observed and reported by Cleeves et al. (2017) with $H^{13}CO^+$ in the IM Lup protoplanetary disk.

Short-term chemical variability could occur in a range of astronomical objects, other than protoplanetary disks, that are exposed to X-ray flaring. Recently, Mackey et al. (2019) modeled non-equilibrium chemistry in molecular clouds caused by X-ray flaring from active galactic nuclei. While conditions used in this model differ greatly from protoplanetary disk environments, it lends further support to the idea that astronomical environments are far more chemically dynamic than previously assumed.

It should also be noted that these simulations are focused on discrete flaring events. Additional work is needed to examine how the full stochastic behavior of flaring from a young star might accumulate water over time, thereby influencing the proclivity for a given disk to form potentially habitable planets.

2.7 Chapter Acknowledgements

The authors are grateful for support from the 2017 Smithsonian Astrophysical Observatory REU program funded by the National Science Foundation REU and Department of Defense ASSURE programs under NSF Grant AST-1659473, and by the Smithsonian Institution. This material is based upon work supported by the National Science Foundation Graduate Research Fellowship Program under Grant No. 1842490. Any opinions, findings, and conclusions or recommendations expressed in this material are those of the author(s) and do not necessarily reflect the views of the National Science Foundation.

Chapter 3

Classification of X-ray Flare Driven Chemical Variability in Protoplanetary Disks

"Sometimes, you have to destroy something in order to build something better."

Brandon Sanderson, *Hero of Ages*

3.1 Background and Motivation

The work presented in this chapter has been published in the Astrophysical Journal with L. Ilsedore Cleeves as a coauthor (Waggoner & Cleeves, 2022). During the Fall 2022 semester I advised Claire Thilinius for a project where she used this model to explore sulphur bearing species. A brief summary of her results are included at the end of this chapter, which was not a part of the original publication.

Abstract: Young stars are highly variable in the X-ray regime. In particular, bright X-ray flares can substantially enhance ionization in the surrounding protoplanetary disk. Since disk chemical evolution is impacted by ionization, X-ray flares have the potential to fundamentally alter the chemistry of planet-forming regions. We present two-dimensional disk chemical models that incorporate a stochastic X-ray flaring module, named XGEN, and examine the flares' overall chemical impact compared to models that assume a constant X-ray flux. We examine the impact of 500 yr of flaring events and find global chemical changes on both short timescales (days) in response to discrete flaring events and long timescales (centuries) in response to the cumulative impact of many flares. Individual X-ray flares most strongly affect small gas-phase cations, where a single flare can temporarily enhance the abundance of species such as H_3^+ , HCO^+, CH_3^+, and C^+. We find that flares can also drive chemistry out of "steady state" over longer time periods, where the disk-integrated abundance of some species, such as O and O_2, changes by a few percent over the 500 yr model. We also explore whether the specific history of X-ray flaring events (randomly drawn but from the same energy distribution) impacts the chemical evolution and find that it does not. Finally, we examine the impact of X-ray flares on the electron fraction. While most molecules modeled are not highly sensitive to flares, certain species, including observable molecules, are very reactive to the dynamic environment of a

young star.

3.2 Introduction

The young central star in a protoplanetary disk plays an important role in shaping the disk's physical and chemical evolution. Solar mass pre-main sequence stars, i.e., T Tauri stars, are X-ray bright due to emission from hot ionized gas trapped in magnetic loops on the stellar surface (e.g., Feigelson & Montmerle, 1999; Favata et al., 2005; Feigelson et al., 2007). The typical X-ray luminosity of a T Tauri star is $L_{\rm XR} \approx 2{\times}10^{30}$ erg s^{-1} (Flaccomio et al., 2003; Wolk et al., 2005), about 10^4 times brighter than the modern day Sun (Peres et al., 2000). In addition to being generally X-ray bright, T Tauri stars are also highly variable in X-rays. This variability arises at least in part due to X-ray flaring produced by magnetic reconnection events (e.g., Getman et al., 2008a,b). The most powerful flares rapidly increase the star's X-ray luminosity by several orders of magnitude within a few hours, followed by exponentially decay over the course of days (e.g., Getman et al., 2021).

As a star ages, the stellar dynamo stabilizes and magnetic fields are thought to weaken, thus X-ray luminosity and variability becomes less intense and frequent (see review of Güdel, 2004, and references therein). Therefore, to best understand how high energy processes impact planet formation, we must understand how the highly variable X-ray radiation field of T Tauri stars affects the protoplanetary disk environment.

In general, high energy ionization, including from X-rays, drives disk chemistry at low ($<$ 100 K) temperatures through ion-neutral reactions (Strom et al., 1989; Glassgold et al., 1997; Haisch et al., 2001; Fedele et al., 2010; Cleeves et al., 2014a). X-ray ionization occurs primarily via the ionization of H_2 and He (Maloney et al., 1996). Specifically, the ionization of H_2 results in the formation of H and H_3^+, both of which are essential in the formation of more complex molecules in both the gas and ice phases (e.g., McCall, 2006). X-rays also have the potential to drive chemistry close to the disk mid-plane, since high energy ($\gtrsim$ 5 keV) X-ray photons are capable of penetrating denser gas ($N_H = 9 \times 10^{23}$ cm^{-2}; Bethell & Bergin, 2011a). Less energetic photons, like UV, are absorbed closer to the disk surface (Glassgold et al., 2005; Bethell & Bergin, 2011c).

Astrochemical codes typically include X-ray related processes often as a single value or as a single spectrum constant in time that are representative of a "characteristic" ionization rate. However, there is increasing theoretical and observational evidence that this simplification may not always be valid. Ilgner & Nelson (2006d) were first to model how periodic flares impact the ionization fraction of a disk both using a simplified network and a full chemical network. They found the size of a disk's "dead zone" was impacted by flares, but the extent of the variation was sensitive to the distribution and size of dust grains.

More recently, potential observational evidence of flares was reported in Cleeves et al. (2017). Specifically, significant (20 σ) changes in the emission of a known X-ray sensitive molecule, $H^{13}CO^+$, was discovered in the IM Lup protoplanetary disk. With simple chemical models, they found that X-ray flares were a viable explanation for this variability. Since $H^{13}CO^+$ is not the only X-ray sensitive molecule, Waggoner & Cleeves (2019) carried out a theoretical study and found that gas-phase H_2O can also experience a short-lived enhancement in abundance in response to a single, strong flaring event that enhances the X-ray luminosity by a factor of 100. Chemical evolution in planet-forming disks driven by X-ray flares has otherwise been relatively unexplored.

We present a comprehensive study on 2D disk chemical responses (radius and height) to 500 years of stochastic X-ray flaring events. Section 3.3.1 introduces a new, flexible X-ray flare model, XGEN, which is used to model a stochastic X-ray light curve for a T Tauri star. The light curve is incorporated into a chemical disk model described in Section 3.3.2. The results from the model are presented in Section 3.4, where chemical responses are categorized and relevant reactions discussed in depth. In Section 3.5, we discuss the results, such as the short- and long-term impact of flares on disk chemistry and electron abundances, along with their observational implications. Lastly, in Section 3.7 a summary of the results and concluding remarks are provided.

3.3 Model

3.3.1 X-ray Light Curve Generator: XGEN

We present a flexible code for generating randomized light curves drawing from known stellar X-ray flare statistics. The code, called the X-ray Light Curve Generator (XGEN), models a stochastic light curve based on a user-provided flare frequency, flare energy distribution, and rise/decay time. Literature has shown that the energy distribution of stellar flares in an X-ray light curve can be defined by a power-law distribution:

$$\frac{dN}{dE} = \beta log(E_{\rm tot})^{1.0-\alpha}, \tag{3.1}$$

where the power-law defines the total number of flares (dN) that occur over an energy range dE (e.g., Hudson, 1991; Caramazza et al., 2007). $E_{\rm tot}$ signifies the total energy output of a single flare. β is a normalization factor that controls the total number of flares the model produces. As described below, the time evolution of individual flares is represented by a sharp exponential rise followed by a slower exponential decay. While the present paper applies the code to the case of T Tauri-like stellar parameters, we note that XGEN is not limited to any particular type of star. Instead, XGEN can create any light curve based on a power law energy distribution, including

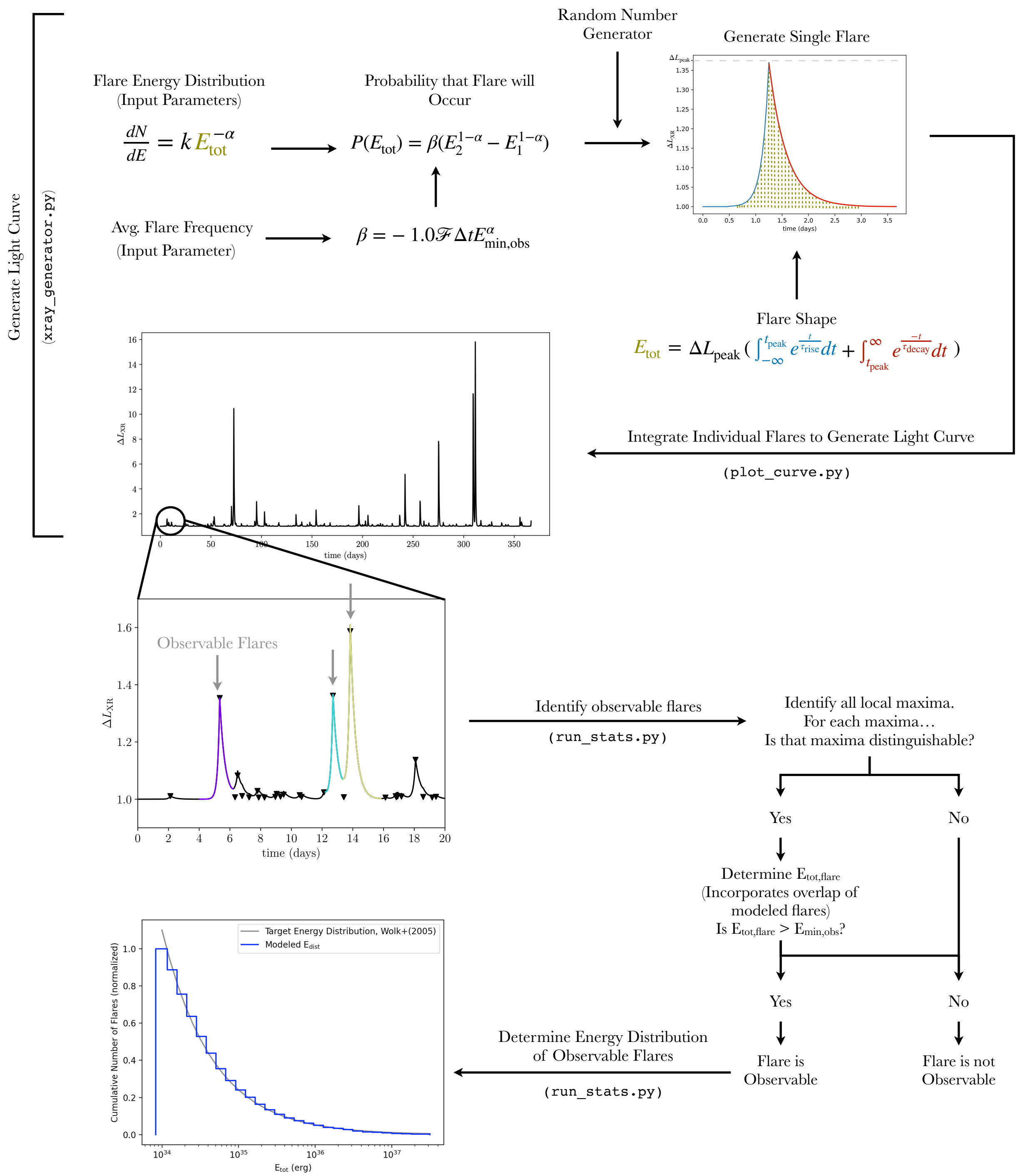

Figure 3.1 This figure is not a part of the original publication, but is available as an additional resource for XGEN on github.

but not limited to flares from main sequence stars or active galactic nuclei.

Overview of Model

XGEN uses a random number generator to determine the probability that a flare with total energy $E_{\rm tot}$ will occur. $E_{\rm tot}$ is spectrally integrated from 1 - 20 keV. The spectrum used in this work is considered a typical X-ray emission spectrum for a T-Tauri star, as was observed by *Swift* in the IM Lup protoplanetary disk (Cleeves et al., 2017, Figure 2). XGEN simulates flares by uniformly scaling the X-ray spectrum based on the flare magnitude. In reality, flares change the X-ray spectrum by producing proportionally more high-energy, or 'hard,' photons relative to low-energy, or 'soft,' photons. This work uses a simplified model, where hard and soft photons are equivalently increased, and the spectral energy distribution remains constant. X-ray hardening will be incorporated into future versions of XGEN.

$E_{\rm tot}$ is discretized into energy "bins" within a specific range, so that a finite number of flare energies are considered possible. The lower and upper boundaries for each energy bin $E_{\rm tot}$ are defined as $E_{\rm low}$ and $E_{\rm up}$, respectively. The spread of $E_{\rm tot}$ per energy bin is defined as ΔE, where $\Delta E = E_{\rm up} - E_{\rm low}$. In this work, the energy bins are spaced evenly with $\Delta E = 10^{0.01}$ erg. Note that $E_{\rm low}$ and $E_{\rm up}$ span the total energy range considered flares, from $E_{\rm min}$ to $E_{\rm max}$ and all energy values in between at a resolution of ΔE. The random number generator uses the python 2.7 numpy.random package, version 1.16.6 and build py27hbc911f0_0.

The probability of a flare with energy $E_{\rm tot}$ occurring is defined by

$$P(E_{\rm tot}) = \beta\,(E_{\rm up}^{-\alpha+1} - E_{\rm low}^{-\alpha+1}) \tag{3.2}$$

$$\beta = -\mathcal{F}\;E_{min}^{\alpha-1}\;\Delta t \tag{3.3}$$

where β is a normalization constant, Δt is the time step resolution ran in XGEN, and $\mathcal{F}$ is the target flare frequency. Multiple flares are allowed to occur within the same time step, which represents flares occurring simultaneously on different parts of the star. Model parameters and their symbols are provided in Table 3.1.

All flares are assumed to have an exponential rise ($\tau_{\rm rise}$) and decay ($\tau_{\rm decay}$) time profile. XGEN is written such that $\tau_{\rm rise}$ and $\tau_{\rm decay}$ can be variable based on a probability distribution, but for simplicity, we assume a uniform $\tau_{\rm rise} = 3\,{\rm hr}$ and $\tau_{\rm decay} = 8\,{\rm hr}$ for all flares. Given these timescales and a total flare energy, $E_{\rm tot}$, one can use the following to solve for useful parameters such as the peak change in luminosity, $\Delta L_{\rm peak}$, and the X-ray luminosity at a given time:

$$E_{tot} = \Delta L_{\rm peak} \int_{-\infty}^{t_{peak}} e^{t/\tau_{\rm rise}} dt + \Delta L_{\rm peak} \int_{t_{peak}}^{\infty} e^{-t/\tau_{\rm decay}} dt \tag{3.4}$$

The cumulative light curve is constructed by adding the luminosity of all individual flares at every time step, then adding in a "baseline" or characteristic luminosity ($L_{\rm char}$). For the purpose of this study, light curves are also normalized with respect to $L_{\rm char}$ and represented by $\Delta L_{\rm XR}$.

$$\Delta L_{\rm XR} = \frac{L_{\rm char} + \sum L_{\rm flare}}{L_{\rm char}} \tag{3.5}$$

XGEN includes flares that are lower than presently detectable, e.g., microflaring and nanoflaring events. Therefore many of the individually modeled flares overlap or are below a realistic detection limit. As a result, we define 'observable flares' as those that satisfy two criteria. First, the flare peak must be distinguishable. XGEN identifies individual flare peaks as any point were the slope is effectively zero (for practical purposes, where $|dL_{\rm XR}/dt| < 0.015$). Once individual flare peaks are identified, the beginning and end of each flare is determined by a location where the slope either returns to zero or switches signs. This process constructs each distinguishable flare. Second, the distinguishable flare must have a total energy greater than a predetermined minimum energy value ($E_{\rm min,obs}$) to be considered observable (Figure 3.2). XGEN can then determine energy distribution and frequency of observable and distinguishable flares, which can then be compared to an observed statistical distribution (Figure 3.3).

X-ray Light Curve for a T Tauri Star

The light curves presented in this work are modeled after the statistical analysis of solar type young stars presented in Wolk et al. (2005) from the *Chandra Orion Ultra-deep Project* (*COUP*). The *COUP* survey is the longest, continuous observation of stars in the X-ray regime, thus making it the most comprehensive study of X-ray flaring events in solar mass stars to date (Getman et al., 2005). The energy distribution of flares observed by Wolk et al. (2005) are best fit by

$$N = 1.1 \log(E_{\rm tot})^{-0.66} \tag{3.6}$$

where N is the cumulative number of flares observed with total energy $E_{\rm tot}$ or greater and, when re-cast in dN/dE, representative of $\alpha = 1.66$.

The observed average flare frequency by Wolk et al. (2005) is approximately 1 flare every 650 ks, with an uncertainty of 10%, or ~ 50 flares per year. The modeled light curves are in agreement with an average of $\mathcal{F} \sim 64 \mathrm{yr}^{-1}$. This is a slightly higher flare frequency than the target frequency, but it is only natural that the modelled flare count is higher than the observed flare count. Since the modelled flare count comes from a direct comparison to the observed data, the excess flares are attributed

Quantity	Symbol	Value
	Parameters motivated by observations	
Max Flare Energy*	$E_{\rm max}$	$10^{37.57}$ erg
Min. Flare Energy*	$E_{\rm min,obs}$	$10^{34.0}$ erg
Target Flare Frequency*	$\mathcal{F}$	48.5 $\rm yr^{-1}$
Characteristic Luminosity	$\rm L_{char}$	$10^{30.25}$ $\rm ergs^{-1}$
Flare rise time	$\tau_{\rm rise}$	3 hrs
Flare decay time	$\tau_{\rm decay}$	8 hrs
	Parameters quantitatively fit	
Power-law index	α	1.64
Min. modeled flare energy	$E_{\rm min,model}$	$10^{32.50}$ erg
Energy Step Resolution	ΔE	$10^{0.01}$ erg

Table 3.1 Input parameters used to generate an X-ray flare light curve for a T Tauri star. * parameters based on a statistical analysis of young solar mass stars presented in Wolk et al. (2005). ** parameters found to produce the best fit energy distribution (Figure 3.3).

to smaller low energy flares that would not be distinguishable due to observational limitations.

Flares modeled by XGEN range from $E_{\rm min} = 10^{32.50}$ erg to $E_{\rm max} = 10^{37.57}$ erg. Flares with $E_{\rm tot} < 10^{32.50}$ erg corresponded to $\Delta L_{\rm XR}$ values less than 1.004, and are considered negligible for the purpose of this model. While $10^{32.50}$ erg also corresponds to a negligible flare peak ($\Delta L_{\rm XR} \sim 1.005$), we found that larger $E_{\rm min}$ values were unable to fit the desired energy distribution as well. The minimum total energy for an observable flare was set to $E_{\rm tot}$ of the weakest flare reported in Wolk et al. (2005), $E_{\rm min,obs} = 10^{34.0}$ erg. The maximum allowed flare energy in the model is consistent with the largest flare energy detected in Wolk et al. (2005) ($E_{tot} = 10^{37.57}$ erg), and is in agreement with the 'super-flares' detected in Getman & Feigelson (2021). The characteristic luminosity is set to $L_{\rm char} = 10^{30.25}$ $\rm ergs^{-1}$ (e.g., Flaccomio et al., 2003). The maximum flare energy considered is thus equal to the amount of energy output by the star at quiescence for a period of 8 months.

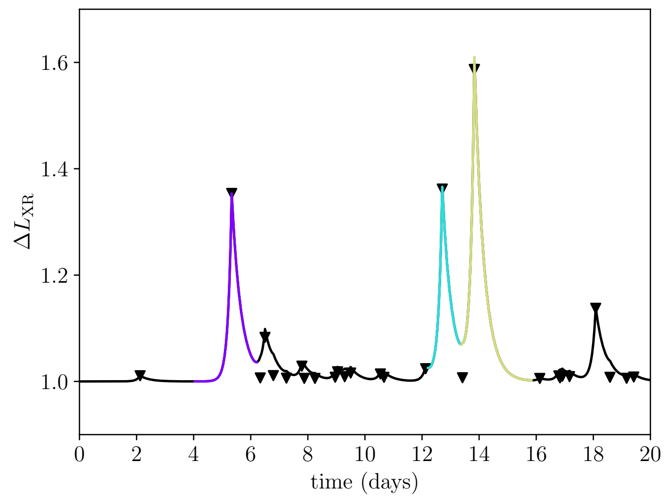

Figure 3.2 A simulated light curve for a T Tauri star. Individual modeled flare peaks, including unobservable flares, are represented by triangles. Individual observable flares (distinguishable peak and $E_{tot} > 10^{34}$ erg) are highlighted as purple, blue, and yellow. Note there are 27 modeled flares but only 3 observable flares based on our criteria.

To best match the Wolk et al. (2005) distribution, a series of different power laws were tested with α values ranging from 1.5 to 3.0. For each value of α, 100 one-year curves were produced and analyzed at one hour time step resolution. The energy distribution of observable flares is sensitive to the chosen α value, as shown in Figure 3.3. We find that $\alpha = 1.64$ yielded the best overall fit to the observed energy distribution of solar mass YSOs with $\chi^2 = 0.15$, where χ^2 measures the goodness of fit. This power law index is consistent with the best fit of $\alpha = 1.66$ reported in Wolk et al. (2005, Equation 3.6). It should be noted that $\alpha = 1.50$ appears to better fit the observed distribution below $E_{\rm tot} \sim 10^{34.5}$ erg. However, α values less than 1.64 fail to fit the high energy flares and have higher χ^2 values. For example, $\chi^2 = 0.91$ for $\alpha = 1.50$. Refitting the light curve to the best fit α value, rather than using $\alpha = 1.66$, was necessary since Wolk et al. (2005) empirically derived alpha from data. However, the synthetic light curves in this work include microflaring and flare blending, neither

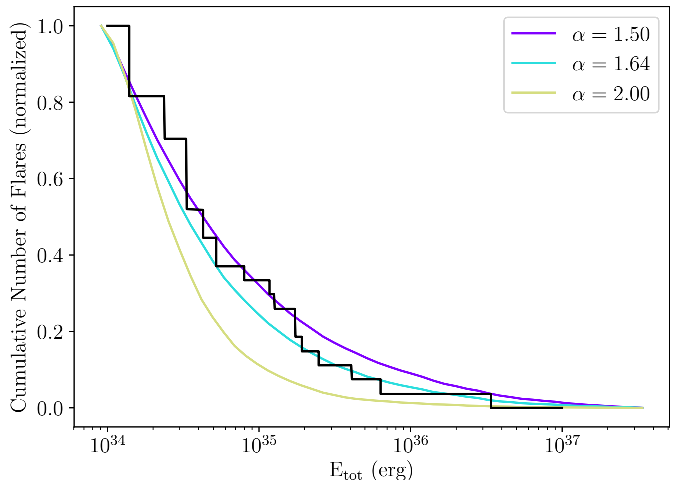

Figure 3.3 Energy distribution of flares from a T Tauri star compared to the observations of Wolk et al. (2005) shown in black (see their Figure 9). Over-plotted are the simulated flare energy distributions for $\alpha = 1.50$, 1.64, and 2.00 tabulated for a 100 year light curve. A power law index of $\alpha = 1.64$ was found to yield the best match to the observations.

of which can be identified in observations.

Incorporating all of the effects described above and adopting the observationally motivated X-ray flaring statistics, Figure 3.4 shows a one year subsection of our model light curve. As can be seen, moderate flares (changes greater than 10 times L_{char}) happen a few times (in this case 3 times) over the course of a year, while weaker flares (changes of 2 to 3 times L_{char}) are far more frequent.

3.3.2 Disk Chemical Model

The chemical disk model used in this work is modeled after Fogel et al. (2011), which adopts the rate equation method and includes 644 chemical species and 5944 types of chemical and physical processes. The physical environment is modeled after the IM Lup protoplanetary disk system, the original source observed to experience variability (Cleeves et al., 2017). The disk and stellar physical parameters are repre-

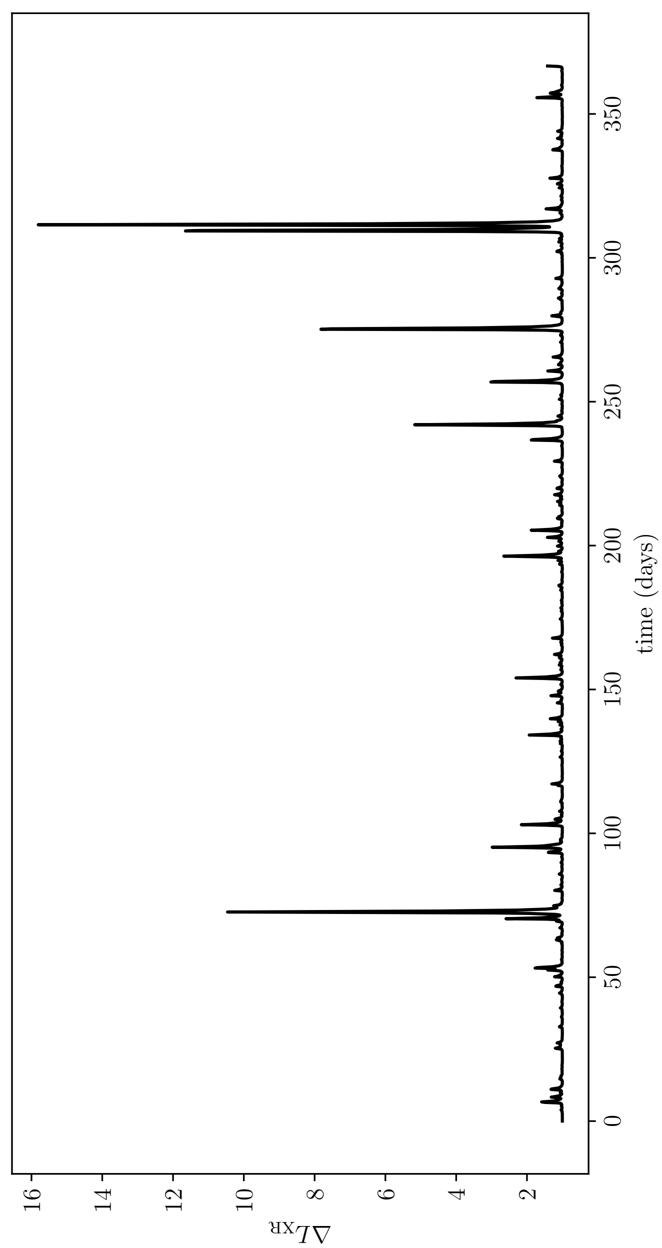

Figure 3.4 Year one of a 500 year X-ray light curve produced by XGEN for T Tauri-like stellar parameters. $\Delta L_{\rm XR}$ is the relative (multiplicative) change in luminosity when there is a flare compared to the characteristic luminosity (Equation 3.5).

Table 3.2 Initial chemical abundances with respect to H for volatile species. These values are representative of molecular cloud abundances (Aikawa et al., 1999).

H_2	5.0×10^{-1}	C	5.0×10^{-9}	CS	4.0×10^{-9}
H_3^+	1.0×10^{-8}	C^+	1.0×10^{-9}	SO	5.0×10^{-9}
He	1.4×10^{-1}	C_2H	8.0×10^{-9}	S^+	1.0×10^{-11}
O	1.0×10^{-8}	N_2	3.51×10^{-5}	Si^+	1.0×10^{-11}
O_2	1.0×10^{-8}	NH_3	8.0×10^{-8}	Fe^+	1.0×10^{-11}
CO	1.2×10^{-4}	HCN	1.0×10^{-8}		
HCO^+	9.0×10^{-9}	CN	6.0×10^{-8}		
H_2O_{ice}	8.0×10^{-5}	Mg^+	1.0×10^{-11}		

sentative of a solar mass star between $0.5 - 1$ Myr old (Cleeves et al., 2016).

A two dimensional disk is simulated by running a series of point locations at various radial distances (R) and vertical heights (Z). We model the chemistry at radii of $R = 1$, 5, 10, 20, 30, 40, 60, 80, and 100 au from the central star. We note that the gas in IM Lup extends to $R \sim 1000$ au, but we only model the inner disk because we find that chemical responses to flares beyond 100 au are generally negligible. Modeled vertical heights (in cylindrical coordinates) range from the disk mid-plane to the disk surface with vertical height ratios of $Z/R = 0.0$, 0.1, 0.2, 0.3, 0.4, 0.5, and 0.6 at each radii.

The model begins with chemical abundances considered typical for a molecular cloud (motivated by Aikawa et al., 1999, see Table 3.2). We run the model for 0.5 Myr to achieve a pseudo steady state, then the X-ray flaring events produced by XGEN are initiated. Once flaring begins, defined as $t = 0.0$ years in the Figures below, the model takes linear, four hour time steps for 500 years. Small time steps were necessary to ensure individual flares in the light curve were not 'missed' in the model. We tested a range of time steps from 1 minute to 2 days, and found that four hours allowed us to obtain sufficiently long duration models without losing time resolution. We note that four hours means that we only have 2-3 time steps crossing the flare; however, based on our tests of shorter time steps, the chemical results were not significantly impacted by this. The implication of these tests is that the total flare energy is more important than the details of the shape of an individual flare. We found that a 500 year model was long enough to probe the diverse range of modeled flare energies while balancing the computational limits of the model. A 500 year model was long enough to ensure that at least one of the strongest possible flares occurred ($\Delta L_{\rm XR} > 800$), and the chemical responses to such a flare, could be modeled. In our fiducial model, two such flares occurred.

Disk density, temperature, UV ionization, and X-ray ionization are extracted similarly as was done in Waggoner & Cleeves (2019) and are based off of the Cleeves et al. (2016) physical structure. To summarize, the energy-dependent X-ray (and UV) radiative transfer is computed using Bethell & Bergin (2011c). The spectra are used to compute a local spectrally integrated UV flux, and for the X-rays, to compute a local H_2 and He ionization rate at every (R, Z) position in the disk. The model uses an incident cosmic ray ionization rate of $\zeta = 2 \times 10^{-20}$ s^{-1} (Cleeves et al., 2015). We note this value is lower than typical ionization rates of $\zeta \approx 10^{-17}$ s^{-1}; however, there is increasing evidence of low cosmic ray ionization rates within molecular gas disks (e.g. Seifert et al., 2021). Figure 3.5 demonstrates regions of the disk where the X-ray ionization rate dominates the cosmic ray ionization rate.

X-ray flares are incorporated into the chemical disk network by uniformly increasing the X-ray ionization rate, and by extension the X-ray flux, by ΔL_{XR} during flaring events. We emphasize that this assumption does not incorporate X-ray hardening, which will be explored in future work. The chemical disk model assumes that flares do not have a directional preference, i.e., a flare propagates uniformly throughout the disk and is only attenuated. This assumption is valid if the X-ray illumination is both azimuthally symmetric and symmetric about the mid-plane. This simplification is valid to first order because the size of X-ray emitting coronal loops on T Tauri stars is expected to be large compared to the size of the star, allowing the disk to be more uniformly illuminated. Directional flares will be explored in future work. The observed increase in $H^{13}CO^+$ in IM Lup supports this theory, as enhancement was the same in both blue- and red-shifted gas (Cleeves et al., 2017).

In this model X-rays interact with the disk by ionizing H_2 and He. While previous work has found that additional noble gasses, such as Ne and Ar, and metals have been seen to be sensitive to flares, we do not include these species in our network. However, there is no evidence that these species contribute to the formation of molecules (e.g., Ádámkovics et al., 2011), and they are not considered a main source of electrons in the disk when compared to, e.g., ionization of H_2 and He, as well as carbon ionization by UV. Therefore, omitting these species will not strongly impact our results. We do note that the metal abundances used in this model (10^{-11} w.r.t. H_{tot}) are considered to be a low metal abundance compared to a typical metal abundance in disks (e.g., Fogel et al., 2011; Aikawa et al., 1999). In future work we will explore increasing the abundances of these species, which can act as sources of electrons especially in regions of the disk where there is little atomic carbon, closer to the midplane.

3.3.3 Assessment of Chemical Variability

To best understand the impact of flares on chemistry in the disk, the column density, $N(R)$, and disk-integrated number, designated by $\mathcal{N}$, of each species was calculated at one day resolution. The integrated number of each species is found by assuming azimuthal symmetry, i.e., $\mathcal{N} = 2\pi \int RN(R)dR$. Since it takes time for light to propagate from the central star to the disk, the affects of a flare do not occur instantaneously at all radial distances. For example, when a flare occurs it takes 8.32 minutes to reach $R = 1\,\mathrm{au}$ and 13.86 hours to reach $R = 100\,\mathrm{au}$. To

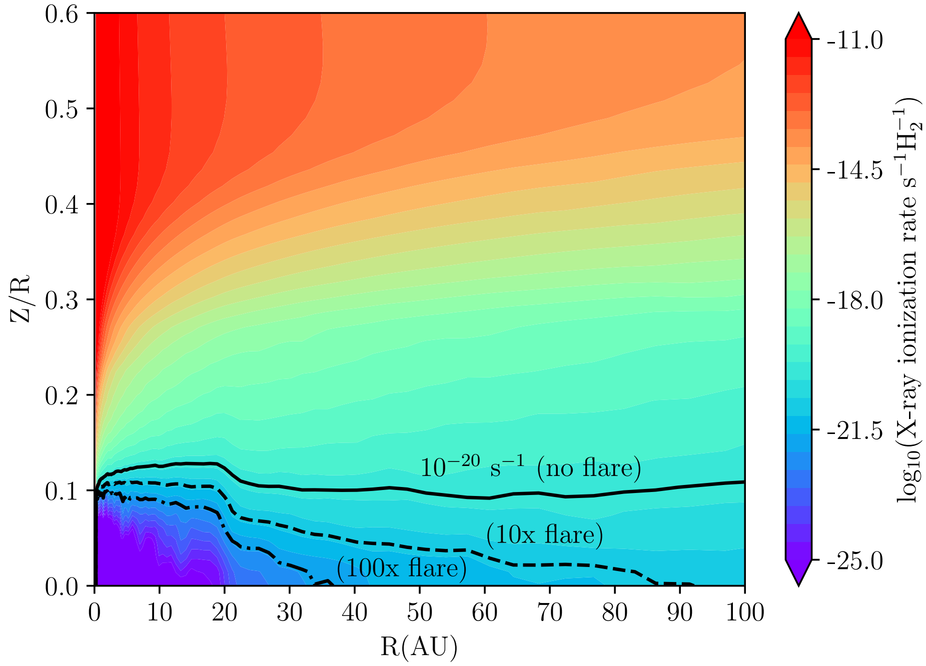

Figure 3.5 Comparison of the X-ray ionization rate to the CR ionization rate. The background color contours show the non-flaring X-ray ionization rate in the disk. Overlaid are lines indicating where the X-ray ionization rate is $10^{-20}\mathrm{s}^{-1}$ for cases where ΔL_{XR}= 1, 10, 100, and 1000. Outside of 10 au, the CRs are unattenuated, and therefore these values can be directly compared to an assumed CR ionization rate (here $2 \times 10^{-20}\mathrm{s}^{-1}$). Depending on flaring state, X-rays dominate above the contours and CRs below.

accurately model the chemical impact of flares and simulate light propagation through the disk, both $N(R)$ and $\mathcal{N}$ incorporate light travel time as the flare propagates radially outward. As a reference, the disk integrated number of hydrogen atoms (in H and H_2) is $\mathcal{N}_{\rm hydrogen} = 9.46 \times 10^{55}$. Species with $\mathcal{N} < 10^{25}$ (approximately a fractional abundance 10^{-30} w.r.t. $H_{\rm tot}$) are considered below the numerical error of the model are are omitted from the following analysis.

Species' level of susceptibility to individual flares is quantified by the standard deviation, σ, of the relative change in $\mathcal{N}$, $\Delta\mathcal{N}$, over the 500 year simulation time. A large standard deviation is indicative of a highly variable species, and a small (≈ 0) standard deviation indicates that species is not significantly impacted by individual flares. The cumulative impact of many flares, i.e., the long-term (centuries) impact, is quantified by a relative change in the total number of a particular species, $\mathcal{C}$, at the end of the chemical model ($\mathcal{N}_{\rm final}$) compared to the start ($\mathcal{N}_0$) and is defined as:

$$\mathcal{C} = \frac{\mathcal{N}_{\rm final}}{\mathcal{N}_0}. \tag{3.7}$$

$\mathcal{N}_{\rm final}$ and $\mathcal{N}_0$ are averaged from the first and final 20 time steps (3.3 days) of the model to ensure flares at the end or beginning of the model do not cause an artificially large $\mathcal{C}$. In this model, no flares were seen at the end of the 500 year model. $\mathcal{C} > 1$ indicates a net increase and $\mathcal{C} < 1$ indicates a decrease in abundance as a result of the cumulative impact of flares. $\mathcal{C} \approx 1$ suggests that species are unaffected by 500 years of stochastic flares.

To test the validity of using a fixed time at 0.5 Myr to compute σ and $\mathcal{C}$, we ran an additional 500 year model with a constant X-ray ionization rate (no flares). For the sake of computational efficiency, we ran the evolution after 0.5 Myr in five 100-year time steps rather than the 4-hour time steps in the fiducial model. We find the

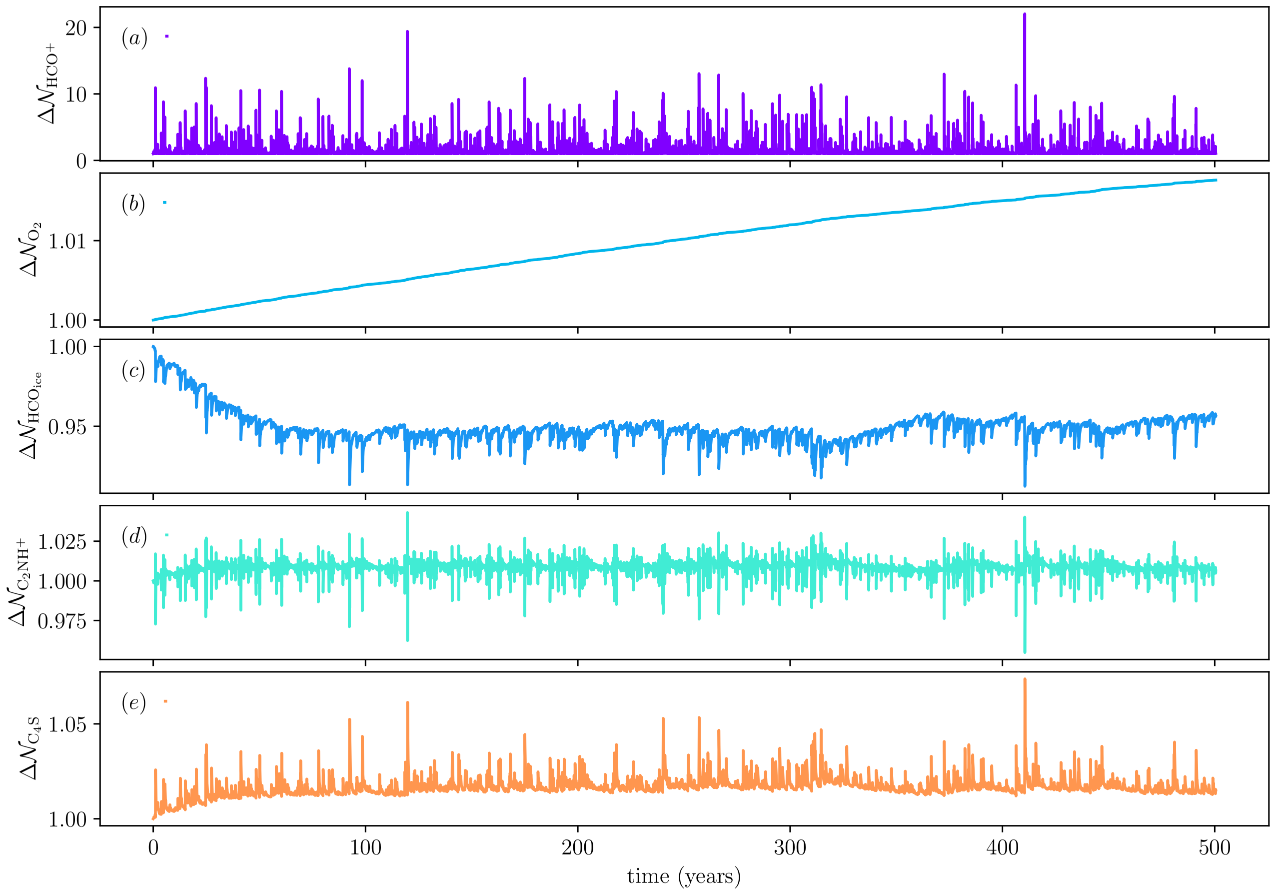

Figure 3.6 Examples of the types of changes seen in disk integrated number, $\Delta\mathcal{N}$, over the model duration. (*a*) Certain species, like HCO^+, vary in response to individual flares. (*b*) Species, such as O_2, are not impacted by individual flares, but exhibit a slow and gradual change in abundance over the course of the model. (*c*,*e*) Species, such as HCO_{ice} and C_4S, are responsive to individual flares and have a shifted baseline abundance (*d*) Species, such as C_2NH^+ exhibit both enhancement and destruction as a result of flares

relative change in a given species's abundance in the non-flare model over 500 years is very small, with $\mathcal{N}$ changing by less than 1%. This confirms that the chemical model had indeed reached steady state prior to flare initiation and that changes in chemical abundance are caused by variations in the X-ray ionization rate.

3.4 Results

Given the large number of locations, species, and timesteps considered in the simulations, we have aimed to focus the results by grouping them into types of responses as well as into chemical families. Furthermore, we define here several key terms used throughout the Results and Discussion sections of this work. The disk mid-plane corresponds to temperatures < 20K, where CO freeze out occurs. The molecular layer corresponds to regions where CO can be in the gas-phase (> 20K). The photodissociation or photon-dominated region is defined as regions where CO is dissociated to C and C^+. For more on the physical and chemical structure of disks see the review of Öberg & Bergin (2021), and references therein.

3.4.1 General Findings

Chemical responses to X-ray flaring events fall into three categories, as demonstrated in Figure 3.6. While the following percentages are highly model dependent, they give the reader a baseline to compare which species are more changed compared to other species. First are flare sensitive species, which are defined as species with an abundance that varies as a direct result of an individual flare. Flare sensitivity is measured by standard deviation ($\sigma > 0.05$), where the most sensitive species have large σ values. Second are species with altered 'steady-states,' meaning that their average abundance over time has consistently changed over the duration of the model. An altered steady state is measured by the relative change in abundance that is at least

$\mathcal{C} > 5\%$. While a 5% change may sound like a small percentage, it is possible that over much longer - astrophysically relevant - time scales these species could continue to trend either upwards or downwards. Third are species that are non-responsive to flares. These species have $\sigma \leq 0.05$ and $\mathcal{C} \leq 5\%$.

The majority of species in the model are unaffected by flares. 27% of species are considered significantly variable ($\sigma > 0.05$), and 8% have an altered steady state ($\mathcal{C} > 5\%$). Even though a relatively small percent of the total species in the network appear to be impacted by flares, a large fraction of gas-phase species, especially gas-phase cations, are susceptible to flares. Average standard deviations and percent changes of each chemical family are shown in Table 3.3. We note that species bearing phosphorus, chlorine, or metals (e.g., Mg, Fe) are excluded from this analysis due to their low gas phase abundances, under the expectation that they primarily take refractory form.

The chemical species used in this model can be categorized into chemical families, where families are defined as a group of gas-phase species containing oxygen, carbon, nitrogen, sulphur, or silicon. Additional families include gas-phase anions, cations, and neutrals in addition to ices frozen out on dust grains. A single species can belong to multiple families. Table 3.3 summarizes the standard deviation and relative change of each of these families.

3.4.2 Cations: The Most Responsive Species

Cations are the most flare-responsive group of species in the model. Cations are more likely to experience both an immediate response to flares and are more likely to be impacted on longer time scales ($\gtrsim$ months) as a result of a single, strong flaring event. Gas-phase cations make up 39% of the chemical network. 23% of the modeled cations have $\sigma > 0.05$, and 19% have $\mathcal{C} > 5\%$.

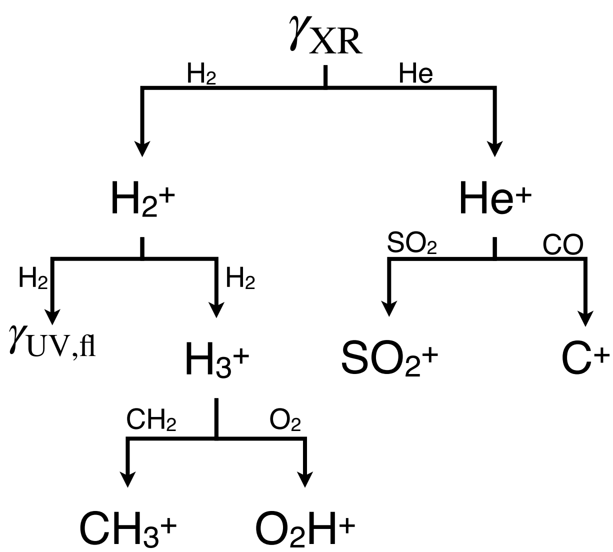

Figure 3.7 Initial products of X-ray ionization in the disk. $\gamma_{\rm XR}$ indicates X-ray photons and $\gamma_{\rm UV,fl}$ are fluoresced UV photons. When a flare occurs, the X-ray flux increases, then increasing the ionization rates of H_2 and He and causing a temporary enhancement in gas-phase cations. This reaction network is the main driver in all other flare driven chemistry seen in the model.

Among the flare sensitive cations, H_3^+, H_2^+, SO_2^+, and O_2H^+ are significantly more variable than any other species, including ionized and neutral gas-phase species and ices, in the network. These four species are seen to increase by up to 500% in $\mathcal{N}$ in response to the strongest flares ($\Delta L_{\rm XR} \geq 600$). The flare enhanced X-ray ionization rate drives a direct enhancement in H_2^+. H_2^+ drives further reactions, leading to the enhancement in H_3^+ and O_2H^+ by

$$\mathrm{H_2} + \gamma_{\rm XR} \rightarrow \mathrm{H_2^+} + \mathrm{e^-} \tag{3.8}$$

$$\mathrm{H_2^+} + \mathrm{H_2} \rightarrow \mathrm{H_3^+} + \mathrm{H} \tag{3.9}$$

$$\mathrm{H_3^+} + \mathrm{O_2} \rightarrow \mathrm{O_2H^+} + \mathrm{H_2}. \tag{3.10}$$

Enhancement of SO_2^+ is a result of X-ray ionization of helium, rather than H_2:

$$\mathrm{He^+} + \mathrm{SO_2} \rightarrow \mathrm{SO_2^+} + \mathrm{He}. \tag{3.11}$$

An example reaction network of these four species and their immediate products is shown in Figure 3.7. In general, most flare responses can be traced back to the ionization of H_2 and He or UV photons ($\gamma_{\rm fl,UV}$) produced by collisional de-excitation of H_2^+. After ionized H_2 and He, the dominant chemical drivers are CH_3^+ produced through

$$\mathrm{CH_2} + \mathrm{H_3^+} \rightarrow \mathrm{CH_3^+} + \mathrm{H_2}, \tag{3.12}$$

and C^+ from CO:

$$\mathrm{He^+} + \mathrm{CO} \rightarrow \mathrm{C^+} + \mathrm{O} + \mathrm{He}. \tag{3.13}$$

Of the family of cations impacted by flares, HCO^+ and N_2H^+ are of of primary interest, as they are commonly observed species in disks. Both of these species are temporarily enhanced by flares. Enhancement is a product of protonation from H_3^+, where HCO^+ is formed by

$$H_3^+ + CO \rightarrow HCO^+ + H_2, \tag{3.14}$$

and N_2H^+ is formed by

$$H_3^+ + N_2 \rightarrow N_2H^+ + H_2 \tag{3.15}$$

Dissociative recombination with electrons is the primary destruction mechanism for both species. N_2H^+ and HCO^+ experience a nearly instantaneous enhancement, but the HCO^+ enhancement is sustained for longer periods of time. Figure 3.8 shows how the radial column density of HCO^+ and N_2H^+ vary as a function of time during a strong flare. HCO^+ stays elevated at all radii for longer ($\sim$ 1 week) than N_2H^+, which returns to its pre-flare abundance after a few days. The reason for this difference is that the N_2H^+ traces gas closer to the midplane where the densities are generally higher, which speeds up the dissociative recombination.

3.4.3 Neutral Species

Neutral species (both gas and ice-phase) make up 59% of the chemical network, and the vast majority are unaffected by flaring events. Only 0.6% of the neutral species have $\sigma > 0.05$, and only 0.9% have $\mathcal{C} > 5\%$. The most variable neutral species are H, HCO, O_2H, C_3O, C_2H_4, and C_3H_4. In this section, we highlight the chemical and physical processes that drive variability in these species.

Variability in neutral species is driven by an enhancement in H_3^+. For example, H_3^+ enhances HCO^+ (see Reaction 3.14), which then accepts an electron from a neutral

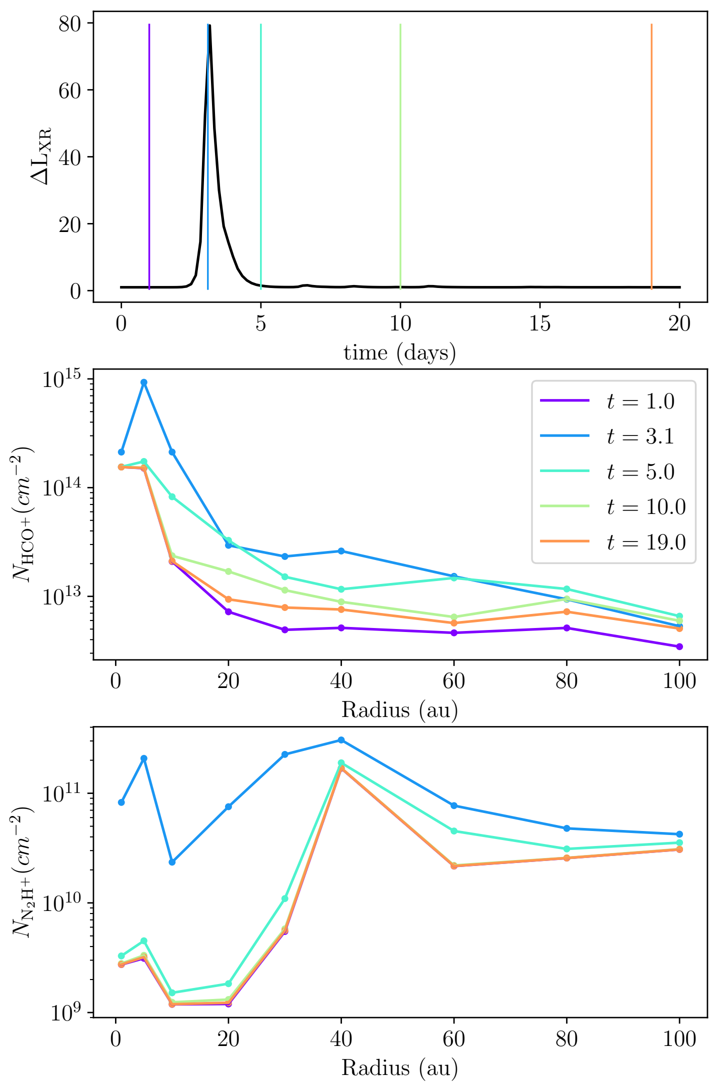

Figure 3.8 *Top:* X-ray flare with a strength of $\Delta L_{\mathrm{XR,peak}} = 80$ (Equation 3.5). The colored lines correspond to the time steps HCO^+ and N_2H^+ column density if plotted below. *Middle and Bottom:* Column density (N) of HCO^+ and N_2H^+ before the flare ($t = 1.0$ day), at the flare peak ($t = 3.1$ day), and after the flare ($t = 5.0, 10.0, 19.0$ days). Note that both species are enhanced more at shorter radii, and HCO^+ is enhanced for a longer time (~ 20 days) than N_2H^+ (~ 5 days). N_2H^+ has the same column density at $t = 1.0$, 10.0, and 19.0 days.

donor (represented by M),

$$HCO^+ + M \rightarrow HCO + M^+, \tag{3.16}$$

to enhance HCO abundance. HCO variability occurs primarily beyond $R = 5\,\mathrm{au}$ and within the vertical heights $Z/R = 0.2$ and 0.3. HCO is relatively constant in the disk surface, where UV photolysis and destruction reactions with cations are significantly faster than the neutralization of HCO^+. Between $Z/R = 0.2$ and 0.3 HCO enhancement closely follows HCO^+ enhancement. Below $Z/R = 0.2$ HCO is not significantly abundant due to the reduced ionization rates.

Additionally, H_3^+ leads to an enhancement in CH_3^+ by Reaction 3.12. CH_3^+ then can either react with small oxygen bearing species, such as OH,

$$CH_3^+ + OH \rightarrow H_2CO^+ + H_2, \tag{3.17}$$

or be converted to CH_4 through a radiative association step:

$$CH_3^+ + H_2 \rightarrow CH_5^+, \tag{3.18}$$

followed by a dissociative recombination step:

$$CH_5^+ + CO \rightarrow HCO^+ + CH_4. \tag{3.19}$$

These reactions and products branch off to drive enhancement in species such as O_2H, C_3O, C_2H_4, and C_3H_4. CH_3^+ enhancement also plays an important role in carbon, oxygen, and silicon variability as discussed in later sections.

We note that H_3^+ indirectly leads to a 0.5% increase in the amount of free hydrogen

Table 3.3 Average standard deviation ($\bar{\sigma}$) and average change ($|1-\bar{\mathcal{C}}|$) for the defined chemical families. Note: H_3^+, H_2^+, SO_2^+, and O_2H^+ were excluded from the O and S families in these values, as they are significantly more variable than any other species in the network and skewed σ and $\mathcal{C}$ values. Additionally, phosphorus, chlorine, or metals (e.g., Mg, Fe) are excluded, as they have abundances below the computational limit of the model..

Family	$\bar{\sigma}_{\mathrm{all}}$	$\bar{\sigma}_{\mathrm{cations}}$	$\lvert 1-\bar{\mathcal{C}}_{\mathrm{all}}\rvert$	$\lvert 1-\bar{\mathcal{C}}_{\mathrm{cations}}\rvert$
Cations	—	0.13	—	0.03
Anions	0.02	—	0.01	—
Neutrals	0.00	—	0.00	—
O	0.06	0.10	0.03	0.05
S	0.05	0.08	0.04	0.06
C	0.02	0.03	0.01	0.02
N	0.02	0.04	0.01	0.02
Si	0.01	0.2	0.01	0.02
Ices	0.00	—	0.00	—

atoms. However, given the large uncertainties on H_2 reformation on grains (including H-binding energies), we do not expect this to significantly change the chemistry.

3.4.4 Chemical Families

Oxygen Bearing Species

Oxygen bearing species are the most variable chemical family, where 29% of gas-phase O-bearing species have $\sigma > 0.05$, and 22% have $\mathcal{C} > 5\%$. Variability among these species tends to occur in warmer disk regions, i.e., dominantly near the disk surface ($Z/R > 0.3$) and close to the star ($R < 40\,\mathrm{au}$). For the most part, changes in O bearing species can be traced to two pathways originating from enhancement of H_3^+, as summarized by Figure 3.9.

One chemical pathway is driven by enhancement of CH_3^+ (Reaction 3.12). CH_3^+ reacts with small species, such as OH, to form larger C and O bearing species, such as H_2CO^+. This reaction branch drives short-term variability in larger O bearing

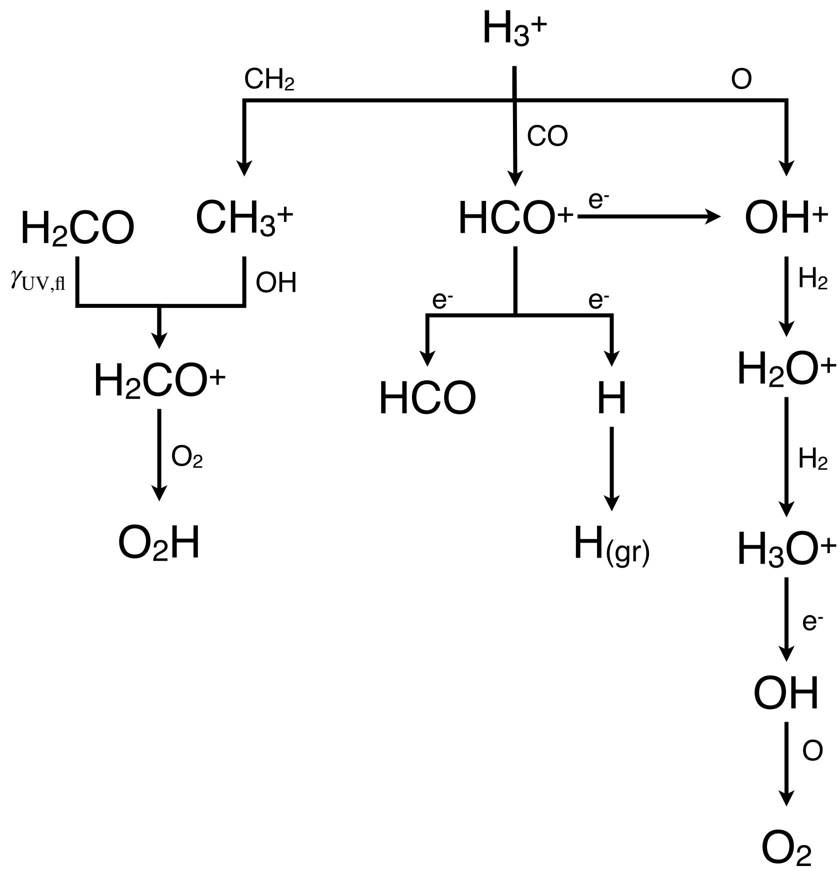

Figure 3.9 Example flare-driven reaction network of oxygen bearing species. O-bearing species are the most flare susceptible chemical family in the network. The strongest responses occur in regions of the disk near the star and disk surface. X-ray flares enhance H_3^+ in the disk, which then protonates small gas-phase neutral species, such as CO, O, and CH_2. Some O-bearing species, such as O_2H and HCO^+ are variable on short time scales (days-weeks), whereas others, such as O and O_2, are gradually impacted over the 500 year model.

species, including O bearing carbon chains. Additionally, oxygen chemistry is driven by H_3^+, which directly protonates small O bearing species, such as CO and O. This reaction branch is interesting, as protonation drives both short-term variability and long-term changes in abundance. Temporary enhancement of HCO^+, as discussed in Section 3.4.3, is an example of H_3^+ driven short-term variability.

Flares are also seen to slowly convert atomic O to O_2 over the 500 year model. The dominate process occurs via a series of gas-phase protonation reactions to form H_3O^+:

$$H_3^+ + O \rightarrow H_2 + OH^+ \tag{3.20}$$

$$OH^+ + H_2 \rightarrow H_2O^+ + H \tag{3.21}$$

$$H_2O^+ + H_2 \rightarrow H_3O^+ + H. \tag{3.22}$$

H_3O^+ then undergoes dissociative recombination to form OH,

$$H_3O^+ + e^- \rightarrow OH + H_2. \tag{3.23}$$

Additionally, H_3O^+ can form H_2O, as discussed in Waggoner & Cleeves (2019). OH can then undergo a substitution reaction with O to form O_2

$$OH + O \rightarrow O_2 + H. \tag{3.24}$$

$\mathcal{N}_{\mathrm{O,atomic}}$ decreases by 0.2%, and $\mathcal{N}_{\mathrm{O_2}}$ increases 1.2% over the 500 year model. While these changes may seem insignificant, atomic O and O_2 are both abundant species in the disk (O and O_2 abundances are 1.96×10^{-6} and 1.31×10^{-7} with respect to H, respectively). Since $\mathcal{C}$ is a relative change in disk integrated abundance abundant species, such as O_2 and especially O, are less likely to exhibit a large change

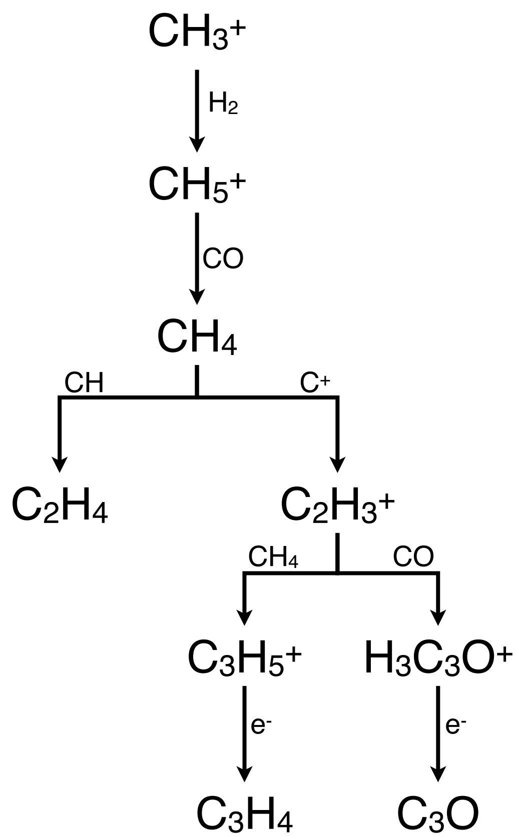

Figure 3.10 Example flare-driven reaction network of carbon bearing species. C-bearing species are the second most flare susceptible chemical family in the model, where the strongest responses occur in colder regions of disk. Variability in C-bearing species, especially carbon chains, dominantly come from flare enhanced production of CH_4 and C^+.

in $\mathcal{N}$. Therefore, these seemingly small fractional changes are indicative of a non-insignificant conversion of O to O_2, as further discussed in Section 3.5.4 and shown in Figure 3.6b.

Carbon Bearing Species

Gas-phase carbon bearing species are the third most variable species, behind sulphur bearing species. While S-bearing species have higher σ and $\mathcal{C}$ values than C-bearing species on average, it should be noted that S-bearing species are generally less abundant and are therefore more susceptible to small changes in abundance than C-bearing species. Gas-phase C-bearing species make up 52% of the chemical network, where 9% of gas-phase C-bearing species have $\sigma > 0.05$, and 8% have $\mathcal{C} > 5\%$.

As discussed in Section 3.4.3, carbon chain chemistry can be traced to enhancement of C^+ and CH_3^+. While enhanced, C^+ and CH_3^+ drive carbon protonation reactions and neutral-neutral and neutral-ion combination reactions between different carbon bearing species, as demonstrated in the enhancement of C_3H_4 and C_2H_4 (Figure 3.10). Typically, C^+ tends to drive variability closer to star and along the disk surface. CH_3^+ tends to drive variability in carbon chemistry along the warm molecular layer. As a whole, the cumulative impact of flares tends to produce larger neutral and ionized carbon chains.

Sulphur Bearing Species

Gas-phase sulphur bearing species make up 8% of the chemical network, where 18% have $\sigma > 0.05$ and 16% have $\mathcal{C} > 5\%$. Variability in S-bearing species is directly tied to flare driven carbon chain chemistry, as demonstrated in Figure 3.11. C^+ and CH_3^+ lead to variability in carbon chains, which react with atomic sulphur and other small S-bearing species, such as H_2S_2, H_2S, OCS, and S_2^+, to form S-bearing organics. These smaller S-bearing species are slowly and gradually converted to organosulphur species, most notably C_4S, over the 500 year model at the few percent level (e.g., $\mathcal{C}_{\mathrm{S}} = 0.99$ and $\mathcal{C}_{\mathrm{C_4S}} = 1.02$).

Nitrogen Bearing Species

The majority of species containing nitrogen are impacted on smaller scales than the other chemical families. Most of the nitrogen in the model is in the form of N_2, with fractional amounts in species like N, CN, HCN, and NH_3. While the average σ and $\mathcal{C}$ values for N-bearing species (see Table 3.3) suggest that N-bearing species

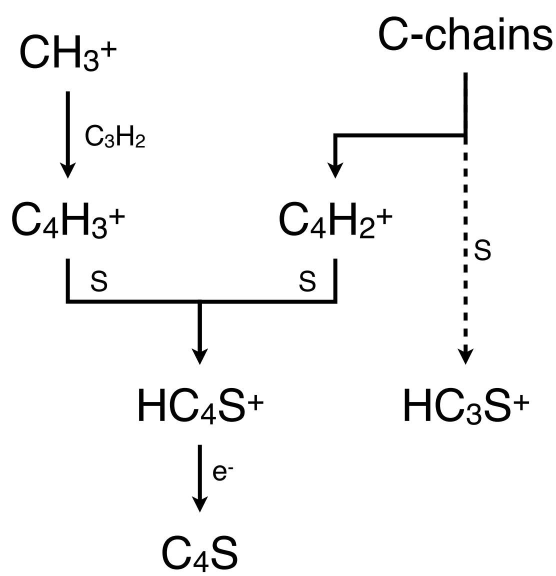

Figure 3.11 Example flare driven reaction network for sulphur bearing species. Variability in S-bearing species is tied to the carbon chain chemistry (Figure 3.10), where carbon chain cations can react with small S-bearing species (such as S) to form larger organosulphur species.

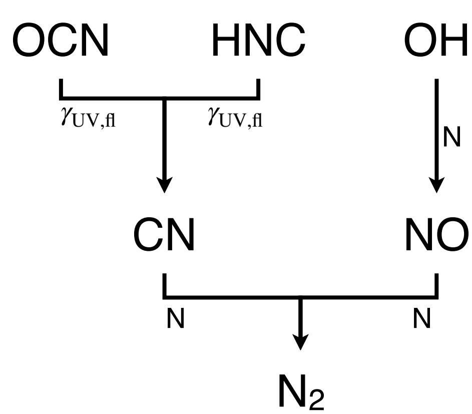

Figure 3.12 Example flare driven reaction network for nitrogen bearing species. N-bearing species are among the least variable chemical family, but the model suggests that flares steadily convert atomic nitrogen to N_2.

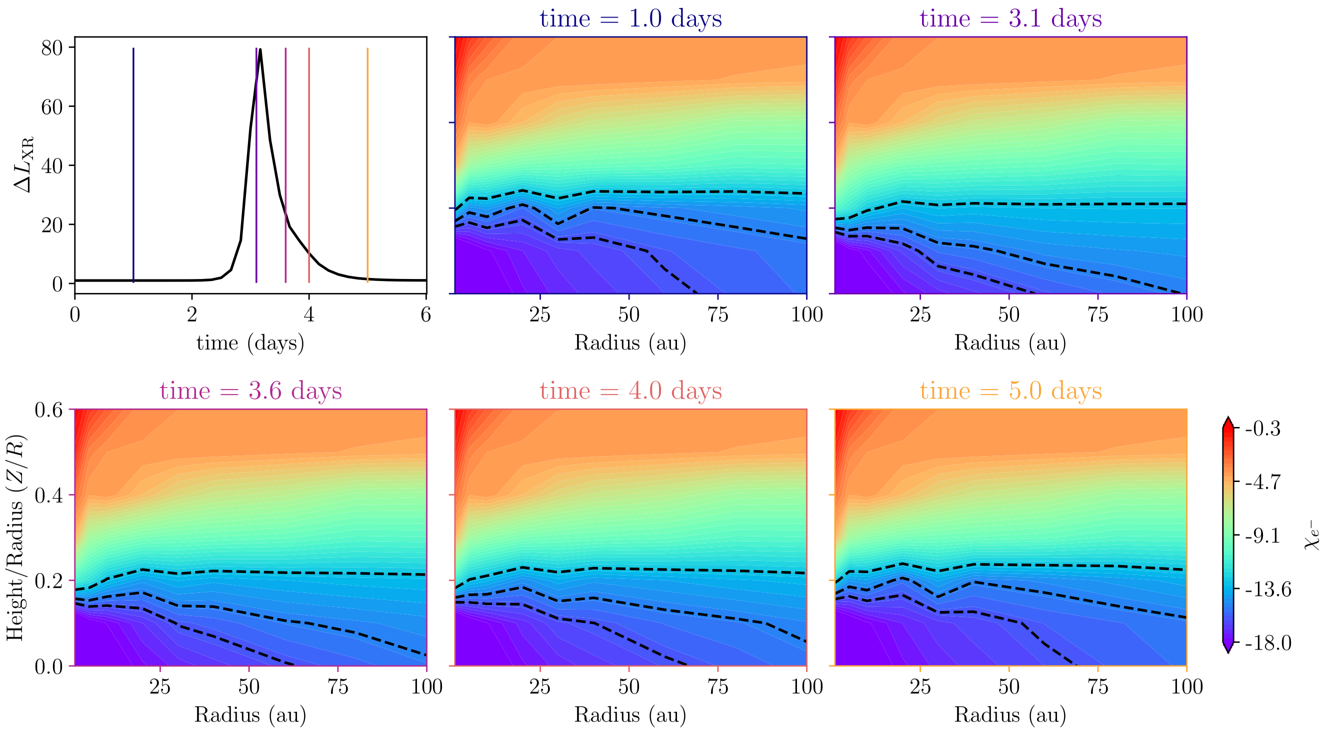

Figure 3.13 Fractional electron abundance (χ_{e^-}) with respect to total H in response to an X-ray flare. An X-ray flare with a peak $\Delta L_{XR} = 80$ (top left) temporarily enhances χ_{e^-} below $Z/R = 0.2$ during the flare ($t = 3.1$ and 3.6 days). After the flare has ended ($t = 5.0$ days), χ_{e^-} returns to its pre-flare abundance ($t = 1.0$ day). The colors of the axes denote the time steps labeled by the vertical lines in the top left panel. Within each sub-panel of electron abundance, the black contour line indicates $\chi_{e^-} = 10^{-16}$, 10^{-15}, and 10^{-13}, for reference.

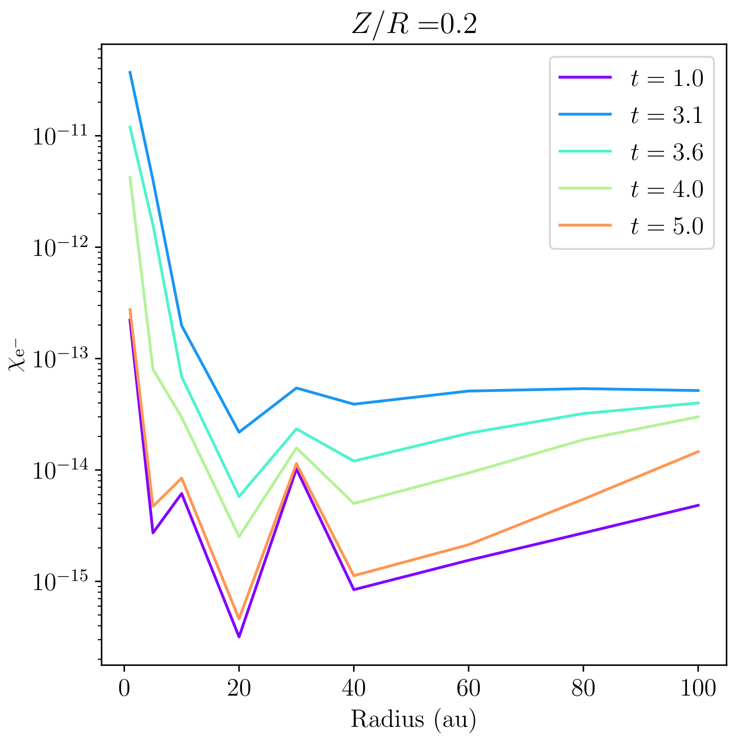

Figure 3.14 Fractional electron abundance with respect to H (χ_{e^-}) along the vertical height $Z/R = 0.2$ for the flare shown in Figure 3.13. Times are plotted in days at the same steps as shown in Figure 3.13. The flare peak occurs at $t = 3.1$ days. Electron abundance increases by more than an order of magnitude as a result of the flare. χ_{e^-} returns to its pre-flare abundance once the flare had ended.

are variable similarly to C-bearing species, we note that N-bearing species typically have lower number densities ($N_{tot} = 7 \times 10^{-5}$ w.r.t. H_{tot}, $C_{tot} = 1 \times 10^{-4}$ w.r.t. H_{tot}). Therefore, the relative variability naturally reports larger than for more abundant species. Gas-phase N reacts with CN and NO (see Figure 3.12), resulting in the formation of N_2. Both CN and NO are increased in abundance in response to individual flaring events, thus temporarily increasing N_2 production during flares. Nitrogen is then locked up in N_2, and over the course of the 500 year model CN, NO, and N have a decreasing average abundance over time due to cumulative flares. While the percent change in disk integrated abundance of nitrogen bearing species is small, we note that these are also relatively abundant species.

3.4.5 Electron Density

The disk-integrated number of electrons ($\mathcal{N}_{e^-} = 7.8 \times 10^{47}$) is relatively constant throughout the 500 year model ($\sigma < 0.01$, $\mathcal{C}< 1\%$) [1]. However, the fractional electron abundance with respect to total H (χ_{e^-}) in the warm molecular layer appears to be sensitive to discrete flaring events. We find that photoionization from both X-rays and fluoresced UV photons is the main mechanism behind electron enhancement. Dissociative recombination with positively charged molecular ions was found to be the primary mechanism that brings electrons back to their pre-flare abundance. Figure 3.13 shows the time variable χ_{e^-} in the disk before a flare, near the end of a flare, and after the flare. While χ_{e^-} in the upper disk surface and mid-plane are constant ($\Delta\chi_{e^-} \approx 1$) during a flare, electron abundance at intermediate heights ($Z/R < 0.2$) can be temporarily enhanced by several orders of magnitude, as shown in Figure 3.14. The surface is less susceptible since the electron abundance is dominated by UV photo-ionization. The midplane is also less susceptible due to the impact of flares

[1] Note that the disk overall remains "charge neutral" as required by the model.

dropping closer to the dense, X-ray attenuated midplane. Additionally, enhancement lasts for longer time scales at large radii, since dissociative recombination timescale scales with ion density. Therefore, more ionized regions, such as those close to the central star, typically have faster recombination rates. Recombination scales with respect to HCO^+ chemistry are explored more in depth in Cleeves et al. (2017).

The local electron abundance is sensitive to individual flares, but the disk integrated electron abundance remains effectively constant throughout the model. Therefore, there does not seem to be a long-term cumulative impact of flares on disk ionization.

3.4.6 Significance of Specific Flare History

To test our results' dependence on the specific history of stochastic flares, we ran five additional 100 year models to compare chemical responses to different light curves (Figure 3.15a-e). Each model was run with identical parameters, save for the randomly generated light curve, where each model was given a different random number seed. The five light curves are in agreement with the target energy distribution and frequency, as described in Section 3.3.1.

The standard deviation and relative change of chemical species for all five models are cross compared in Figure 3.15f. We find that the standard deviation and the relative change in abundance for each species are consistent across the five models within $\lessapprox 5\%$ of each other. We find that across the five models when examined over the full simulation timeframe, highly variable species are always highly variable, non-responsive species are always non-responsive, and so on. This suggests that when examined over longer time scales (e.g., 100 yrs), the general behavior of X-ray flare driven chemistry is not dependent on the history of the light-curve, so long as the flare energy distribution and flare frequency of the star are consistent.

3.5 Discussion

3.5.1 Flare Driven Chemistry

The majority of chemical responses to X-ray flares can be traced back to the ionization of H_2 or He, where the immediate byproducts (e.g., $\gamma_{\rm UV,fl}$, H_3^+, CH_3^+, C^+ shown in Figure 3.7) are responsible for causing most chemical variability in the disk. In general, X-ray flares are most likely to have a significant impact on small, less abundant ($\mathcal{N} < 10^{40}$, or a fractional abundance $< 10^{-16}$ w.r.t. $H_{\rm tot}$) cations, but it is possible that any species directly related to H_2 and He ionization is susceptible to variable X-ray ionization rates. More abundant species ($\mathcal{N} > 10^{45}$, or a fractional abundance $> 10^{-11}$ w.r.t. total hydrogen) and neutral species typically have a lower global response to flares. However, these species can have strong responses to flares at individual disk locations, as demonstrated by Waggoner & Cleeves (2019) in the case of water.

For the most part, oxygen bearing species, sulphur bearing species, and carbon bearing species are the most flare susceptible species seen in the model (Table 3.3). Flare driven variability in S-bearing species is directly dependent on variability on the carbon chemical network, so chemical variability in the disk can be broadly categorized as stemming from the oxygen chemical network or the carbon chemical network.

3.5.2 Application to the Missing Sulphur Problem

Sulphur bearing species are the second most responsive chemical family in the network. This behavior is tied to carbon cation chemistry. Small S-bearing species slowly react with flare enhanced carbon cations to form larger organosulphur compounds. The most notable conversion is from atomic sulphur ($\mathcal{C}_{\rm S} = 0.99$) to C_4S ($\mathcal{C}_{\rm C_4S} = 1.02$), as shown in Figures 3.6e and 3.11. Sulphur abundances are known to

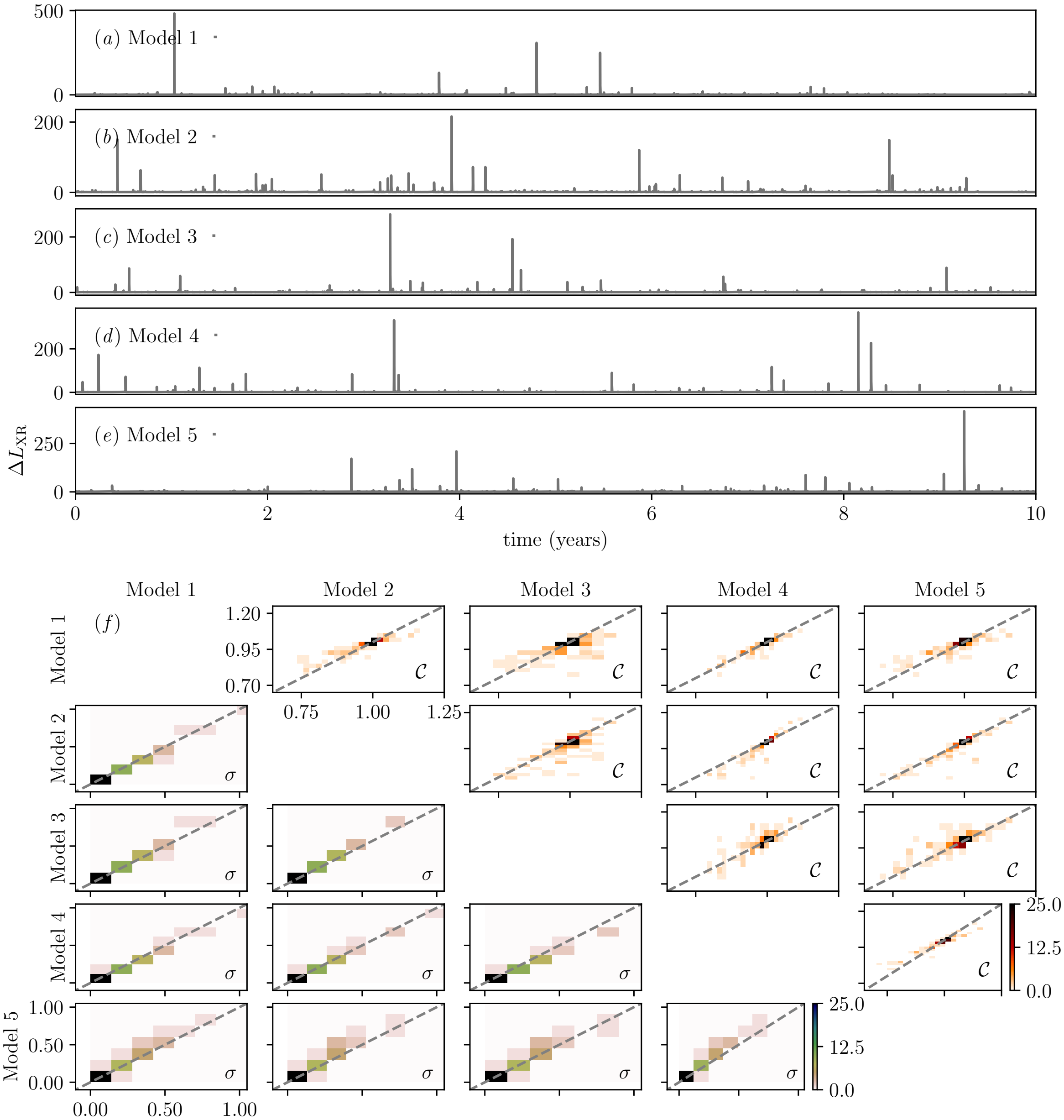

Figure 3.15 (*a*-*e*) The first ten years of the X-ray light curve for all five 100 year light-curve models. (*f*) A comparison plot of standard deviation (σ, bottom left plots) and relative change in abundance ($\mathcal{C}$, top right plots) for each combination of model seeds. All abundant molecules are plotted as a "heat map" where the density of species within a point are indicated by the color bar. The different seeds give similar chemical behavior, falling along the indicated one-to-one correspondence line (dashed), indicating that the history of individual flares is not the primary driver of the variations found in the models.

be low in disks, and the lower the abundance the more susceptible a species can be to having its abundance altered by flaring events. This result is significant, because observations suggest there is a 'missing sulphur problem' in the interstellar medium, and disks specifically (e.g. Ruffle et al., 1999; Kama et al., 2019; Le Gal et al., 2019). Recent literature has suggested that sulphur is locked up in larger and more difficult to detect species in protoplanetary disks and/or frozen out in ices (e.g. Laas & Caselli, 2019; Shingledecker et al., 2020). The results presented in this work are significant, because they suggest that X-ray flaring events impact the abundance of organosulphur species.

We note that the results in this section are speculative, and should not be taken as definitive. To better constrain the importance of flares on the long-term sulphur chemical network, more comprehensive models will need to be run. For example, this model is initialized with a reduced sulphur abundance to take into account refractory sulfur forms (10^{-9} per H_{tot}) compared to the Sun and ISM

3.5.3 Disk Ionization

Small, gas-phase cations are the most flare susceptible species in the network. Flares enhance the abundance of specific cations both temporarily (i.e., in response to a single flare) and for the duration of the simulation (i.e., reaching a new steady state). However, the disk integrated number of electrons and number of anions is relatively unaffected by flares. While the disk integrated number of electrons ($\mathcal{N}_{e^-} = 7.8 \times 10^{47}$ at 0.5 Myr) is equal to the disk integrated number of *total* cations in the disk, $\mathcal{N}_{e^-}$ is several orders of magnitude higher than the even most abundant individual cation species in the disk ($\mathcal{N}\sim 10^{43}$ at 0.5 Myr). Since variability reported in this work is measured by a *relative* change in abundance, cations tend to have higher reported variability than electrons due to their lower individual abundances. The model, by construction, remains "charge neutral" when considering all positively and negatively charged species.

While the disk integrated number of electrons is relatively constant in time, electron abundance does not respond to flares uniformly at all locations. For example, the electron density is relatively constant in the disk surface and mid-plane, but electron abundance can be temporarily enhanced in the warm molecular layer of the disk as a result of a strong flare (i.e., $\Delta L_{\mathrm{XR,peak}} > 70$). Figure 3.13 demonstrates that such a flare can increase the fractional electron abundance with respect to H by up to several orders of magnitude along the warm molecular layer. For example, Figure 3.14 shows that χ_{e^-} can increase from 10^{-15} to 10^{-13} during a flare. The lack of change closer to the surface is likely because ionization and electron production there is dominated by UV photolysis of species like carbon, which is approximately two orders of magnitude faster than the X-ray ionization. So, even when X-ray ionization rates are increased by flaring events, UV ionization still dominates at the surface. Similarly, cosmic rays dominate ionization in the disk mid-plane, where gas densities are high enough to block X-ray photons (see Figure 3.5).

A fractional electron abundance of $\chi_{e^-} = 10^{-14}$ has been linked to the minimum ionization required to couple magnetic fields to neutral gas (Igea & Glassgold, 1999). Once coupled, magnetic fields aid in disk accretion via processes such as magnetorotational instability (MRI; Balbus & Hawley, 1991). While further modeling is required to confirm this, it is possible that disk accretion rates through the molecular layer could be temporarily increased during X-ray flaring events.

Previous modeling by Ilgner & Nelson (2006d) has explored this idea, demonstrating that X-ray flares increase electron column density in magnetically active zones. The focus of that work differs compared to this work in that they analyze the impact of flares on the magnetohydrodynamic evolution of the disk rather than the chemical evolution. Moreover, they focus their modeling between radii of 0.1 au to 10 au. They found that an X-ray flare 100 times the characteristic X-ray ionization rate is seen to increase the electron abundance by a factor of ~ 10 at a radial distance of 1 au at the vertical "transition region" (where the magnetic Reynolds number is 100) for a model assuming low metal abundances. Our models show that the vertical transition occurs around $z \sim 0.18$ au, and at this location, a factor of ~ 100 flare can change the electron abundance by significantly more, over $400\times$ from a baseline of $\chi(e^-) = 7 \times 10^{-15}$. The main reason for this difference is most likely a differing underlying model for the disk and for the X-ray ionization. Their model contains 20% less mass than ours inside of 10 au, and solves directly for hydrostatic equilibrium, resulting in a vertically "puffier" disk with lower line of sight column densities to the midplane. These two factors make their model more transparent to X-rays, and would result in a higher baseline electron abundance in their model compared to ours. We also include Monte Carlo X-ray transport (including scattering) while they consider line of sight absorption of X-rays only (Ilgner & Nelson, 2006a). They do not explicitly report their baseline electron abundance, but these factors point to their disk being more ionized than ours, resulting in smaller relative changes for similar flare energies. This comparison suggests that the specifics of the impact of flares on magnetically active regions in disks will depend on a number of factors, including but not limited to the disk model itself and the treatment of X-rays (see also the detailed discussion of Ilgner & Nelson, 2006d), but together make it clear that flares have the potential to impact MRI through variable disk ionization fraction, and should be further explored.

3.5.4 "Permanently" altered species

An individual flare seems to result in a temporary change in disk-chemistry, but given sufficient time, the system tends to return to the pre-flare chemical state. This suggests that a single flare is unlikely to have a long term impact for global chemistry. However, when the system is exposed to multiple stochastic flares over centuries or longer, the chemical system is unable to fully return to the pre-flare steady state. We find that the cumulative impact of many flares drives some species to a "new pseudo steady state" in disk chemistry if the formation or destruction timescales are much longer than the timescales between significant flares. For example, if a species' formation is enhanced as a result of a flare-produced product, but the destruction timescale (via photons or reactions) is greater than the timescales between significant flares, then the system will not have time to relax before the next flare occurrence. The exact timescales will depend sensitively on the molecule of interest and the local physical conditions. While the results from our model generally suggest that most *long-term* impacted species have a relative change in $\mathcal{N}$ of a few percent or less, some of the impacted species do not appear to reach a plateau by the end of the 500 year model. Therefore it is possible that the full extent of flares in driving chemical change may be much greater.

Examples of species exhibiting the latter behavior are O and O_2, where neither O or O_2 reach a pseudo-steady-state after flares are initiated. O is slowly converted to O_2 (Section 3.4.4) at disk positions of $R \geq 20$au and $0.4 \leq Z/R \leq 0.5$. The O_2 to total gas-phase oxygen ratio (O_2/O_{tot}) increases by 0.004% (at $t = 0$, $O_2/O_{tot} = 0.289\%$), while the O to total gas-phase oxygen ratio (O/O_{tot}) decreases by 0.01% (at $t = 0$, $O/O_{tot} = 2.15\%$). This conversion may seem insignificant, but if the conversion continues linearly for 1 Myr in extension to the modeled 500 years, then O_2/O_{tot} will increase by $\sim 8\%$, and O/O_{tot} will decrease by $\sim 20\%$. However, linear extrapolation is an extreme case; in reality the O to O_2 conversion rate may slow down or reach a new steady state prior to 1 Myr. Previous work has shown that O_2 abundance in comets 67P/Churyumov-Gerasimenko (Bieler et al., 2015) and 1P/Halley (Rubin et al., 2015) is significantly higher than laboratory and modeling predictions (e.g. Taquet et al., 2016; Eistrup & Walsh, 2019). While further modeling is required to know the extent at which flares enhance O_2, it is possible that flares could contribute to the unusually high O_2 abundances seen in comets.

Species other than O and O_2, such as C_4S and S (see Section 3.5.2), are seen to exhibit a similar behavior in the model. Table B.1 in Appendix B contains the top 30 species with the highest $\mathcal{C}$ values.

3.6 A Closer Look at Sulphur

This section is not a part of the original paper. This section was researched by and written by Claire Thilenius, who I advised during the Fall 2022 semester. Claire performed a study on C_4S and other sulphur bearing species, similar to the study I performed on water in Chapter 2. I include this section because Claire's results are consistent with my results presented in this chapter. Additionally, I wanted to highlight Claire's hard work and effort during this semester.

Claire wrote the following in her end of semester report. C_4S was analyzed in the inner disk area at five different radii (R) at three different vertical height ratios (Z/R). These points sample the inner disk, mapping out the change in abundance of C_4S, HC_4S^+ , and HCO^+ in response to the X-ray Flare events. C_4S proved to be a very interesting molecule within the disk. At a $R = 1.0$ au and a Z/R of 0.3, the abundance experienced a short term decrease. This was an unexpected result, the major formation pathway from C_4S is a dissociative recombination with HC_4S^+ ;

$$C_4SH^+ + e \rightarrow C_4S + H \tag{3.25}$$

$R = 1.0$ au is very near the star, it will be warm ($\sim$ 100K) and highly irradiated with UV photons, which ionize H_2 and making this region very electron dense, thus allowing dissociative recombination reactions, like Equation 3.27, to readily occur (Agúndez et al., 2018). Therefore observing a decrease in the rate of formation for the C_4S after a flare was initially unexpected.

A rate analysis was done to determine the major paths of formation and destruction. The rates of both the major destruction and formation pathways decreased. The rate of formation remained higher than the rate of destruction throughout the flare, so the major cause to the reduced abundance is not an increase in the destruction, but a significant decrease in formation. The main mechanism for formation at this location is shown in Equation 3.27 , a dissociative recombination, to give C_4S and free hydrogen. Electrons should be very abundant in this dense region very close to the star after a flaring event, so there must be a significant decrease in the abundance of HC_4S^+ that is limiting the rate of this reaction. To determine what causes C_4S flare dependence, HC_4S^+ was further analyzed. The major formation and destruction paths of HC_4S^+ were calculated. Like C_4S, both rates of the major destruction and formation mechanisms decreased, indicating that the cause of HC_4S^+ depletion occurs due to a reduction in the reactants of the formation pathway. The major formation pathway resulted from an ion-molecule reaction between S^+ and C_4H_2;

$$S^+ + C_4H_2 \rightarrow HC_4S^+ + H \tag{3.26}$$

An analysis of S^+ and C_4H_2 yields that rate of S^+ destruction at this time significantly increases due to increased OH;

$$S^+ + OH \rightarrow SO^+ + H \tag{3.27}$$

The rate of S^+ destruction increases by almost an order of magnitude, on an already very high rate of reaction. The rate of formation of S^+ also increases at this location, however, the destruction dominates, lowering its abundance at this point. In the rate analysis of C_4H_2 both destruction and formation rates decrease, following the same trend as C_4S and HC_4S^+. Therefore, the significant decrease in HC_4S^+ and by extension C_4S originates from the destruction of S^+ by OH. When an X-ray flare occurs the abundance of OH will significantly increase in this region, as further explained in Waggoner & Cleeves (2022). The outer surface of the disk will be highly irradiated, ionizing large amounts of H^+ 3 . The hydrogen will react with the abundant oxygen (O) in the disk beginning the process to form neutral OH, pathway to form OH from H^+ 3 is described in Waggoner & Cleeves (2022). Thus, the decreases in abundance of C_4S and HC_4S^+ in this region are flare dependent based on the destruction of S^+ by OH.

3.7 Conclusions

We present the first study of the impact of stochastic X-ray flaring events on the long term (500 year) chemistry of a protoplanetary disk. The disk chemistry was modeled at disk locations ranging from the mid-plane to the disk surface ($0 \leq Z/R \leq 0.6$) and from radii spanning $R = 1\,\mathrm{au}$ to $R = 100\,\mathrm{au}$. We find that X-ray flares have the following impact on disk chemistry:

1. X-ray flares can cause a variety of changes to molecular abundances, including

short-term (days to weeks), long-term (centuries), or no change on different species in the disk.

2. The majority of species strongly impacted by flares are of relatively low abundance. Abundant species and commonly observed species, such as CO, HCN, HNC, C_2H, CN, etc., are only impacted up to $\leq 1\%$ by flares.

3. Small, gas-phase cations are impacted significantly more than neutral species and ices. Cations are the most likely to be impacted by individual flaring events (i.e., experience short-term variability). This suggests that detections of gas-phase cations (e.g., HCO^+, N_2H^+) will be more reliable if observed multiple times.

4. Gas-phase oxygen bearing species are the most variable chemical family seen in the model, followed by sulphur bearing species and carbon bearing species. This suggests that X-ray flares may play a role in the formation of more complex biologically relevant molecules. However, further modeling including a more extensive chemical reaction network is required to know the extent of this result.

5. The cumulative impact of many flares over hundreds of years appears to drives a new chemical 'steady-state' for certain species in the network, and in other cases, the impact never levels out, at least over the duration of the models. Further modeling is required to know the extent of X-ray flare driven chemistry over the disk life time (millions of years), since this model was computationally limited to 500 years.

6. In addition, we present a new observationally-motivated X-ray light curve generator, XGEN. XGEN is able to generate a stochastic light curve based on an observed energy distribution and flare frequency, along with a user specified flare

shape. Given commonalities between stellar flares across the age spectrum, we have made the code publicly available for use in a variety of applications beyond disk chemistry.

Among the chemical species that have been detected in protoplanetary disks (McGuire, 2018), we find that only HCO^+ and N_2H^+ are likely to be observed in a flare enhanced state (i.e., $\Delta\mathcal{N} > 1.20$). There is a 15.3% and a 1.4% chance to randomly observe HCO^+ and N_2H^+ in a flare-enhanced state, respectively. However, these values only consider variability in disk integrated abundance. Some species may be observably variable in local parts of the disk, as discussed in Waggoner & Cleeves (2019) on H_2O.

While the observational implications for individual flares may seem low, we note that only ∼24 species (excluding isotopes) have been detected in protoplanetary disks at this time. Our findings indicate $\gtrsim$ 10% of known species are flare susceptible. As additional species are observed, or unexpected abundance patterns are seen between species, flare effects, especially on gas-phase cations, should be considered.

3.8 Chapter Acknowledgements

We thank the anonymous referees who provided insightful feedback on this paper. A.R.W. acknowledges support from the Virginia Space Grant Consortium and the National Science Foundation Graduate Research Fellowship Program under grant No. 1842490. Any opinions,findings, and conclusions or recommendations expressed in this material are those of the author(s)and do not necessarily reflect the views of the National Science Foundation. L.I.C. acknowledges support from the David and Lucille Packard Foundation, Johnson & Johnson WISTEM2D, and NASA ATP 80NSSC20K0529. We also are grateful for the use of the Hydra Computing Cluster at the University of Virginia, on which the modeling for this work was carried out.

Chapter 4

Variable $H^{13}CO^+$ Emission in the IM Lup Disk: Observational Evidence for Flare Driven Chemistry

"Have you ever known me to make an inflammatory ridiculous statement without providing an equally ridiculous explanation to substantiate it?"

Brandon Sanderson

4.1 Background and Motivation

This project uses data from my first successful telescope proposal as a PI. Co-investigators include L. Ilsedore Cleeves, Sean Andrews, Ryan Loomis, Karin Öberg, Chunhua Qi, and David Wilner. This chapter will be converted to a paper that will be submitted to the Astrophysical Journal.

Abstract: In 2017, Cleeves et al. reported that the flux of the $H^{13}CO^+$ $3-2$ line effectively doubled (flux increased by 28σ) compare to previous observations. Cleeves et al. report that the most likely source of enhancement was an X-ray flare from the central star. This work uses data taken by the SMA to determine if the $H^{13}CO^+$ $3-2$ line flux is still enhanced or if the line has returned a non-enhanced flux. These data will help constrain the origins or the enhancement, which will also constrain whether or not enhancements can occur other disk systems. We find that the line flux has returned to a 'quiescent' state, indicating that the enhancement was short lived (<years), which is consistent with the X-ray flare theory proposed by Cleeves et al. (2017). Additionally, we report the HCN $3-2$ spectrum is consistent with previous observations (Guzmán et al., 2021), and we report the HCO^+ $3-2$ spectrum in IM Lup for the first time.

4.2 Introduction

Ionization is one the strongest forces of gas-phase chemical reactions in astronomical environments. This is especially true in protoplanetary disks, which are abundant in both external (such as galactic cosmic rays) and internal (such as stellar radiation) sources of ionization. While UV photons are efficient at ionizing small molecules, such as CO, X-ray photons are powerful enough to directly ionize hydrogen gas.

$$H_2 + \gamma_{XR} \rightarrow H_2^+ + e^-, \tag{4.1}$$

after which H_2^+ proceeds to react with an additional H_2 molecule to form H_3^+:

$$H_2^+ + H_2 \rightarrow H_3^+ + H \tag{4.2}$$

This process is particularly efficient in protoplanetary disks, since X-rays are abundantly produced by stellar radiation. In fact, T Tauri stars are typically NUMBER times brighter than the modern Sun in X-ray light, thus enriching the chemical evolution in the planet forming disk surrounding the star.

Radiation from T Tauri stars is not constant in time. These systems commonly undergo flaring events, which increases light emission across the electromagnetic spectrum and X-ray light in particular. Recent work has suggested that individual flaring events can temporarily increase the abundance of gas-phase cations and even some neutral species (Waggoner & Cleeves, 2019). Gas-phase cations like HCO^+ are particularly sensitive to X-ray flares, since HCO^+ is formed when the X-ray product H_3^+ protonates CO

$$H_3^+ + CO \rightarrow HCO^+ + H_2. \tag{4.3}$$

While a single flare is unlikely to impact disk chemistry on time scales relevant to the disks' life time, the cumulative impact of thousands of flares over hundreds of years may aid in the advancment of chemical complexity Waggoner & Cleeves (2022). However, at this time there is no direct observational evidence proving that X-ray flares alter disk chemistry.

Waggoner et al. (2023) searched for flare-driven variations in the HD 163296, MWC 480, IM Lup, GM Aur, and AS 209 protoplanetary. They imaged the HCO^+ $1-0$ line using individual epochs taken over a ∼year to determine if the spectrum was constant in time or not in all five disks. They report tentative spectral variability ($< 3\sigma$), indicating that it is unlikely that any of the observation epochs overlapped with an X-ray flare. However, this is not a surprising result. Flares strong enough to enhance the abundance of HCO^+ (and therefore flux) are relatively rare (Getman et al., 2005; Wolk et al., 2005; Caramazza et al., 2007), and there is less than a 5% chance of observing significant flare driven HCO^+ enhancement during any single observation (based on flare statistics for T Tauri stars, Waggoner & Cleeves (2022)).

In fact, Cleeves et al. (2017) is the only work to present strong observational evidence of flare driven chemical enhancement. They observed the $H^{13}CO^+$ $3-2$ line on three separate days, 17/July/2014, 29/Jan/2015, and 13/May/2015. On the first to epochs, the disk integrated $H^{13}CO^+$ $3-2$ flux was approximately the same with a peak flux of $\sim 0.2\,$Jy kms^{-1}. However, on the third and final epoch the peak flux nearly doubled to $\sim 0.4\,$Jy kms^{-1}, or by 28σ. This type of variability has been seen before in systems undergoing an accretion outburst (examples) due to dramatically enhanced UV ionization rates and disk temperatures. However, the IM Lup continuum emission remained constant even when the $H^{13}CO^+$ flux doubled, thus indicating that the increase in flux could not have been caused by an an accretion outburst. Instead, they find that the most likely source was an increased $H^{13}CO^+$ abundance due to an X-ray flaring event.

While IM Lup dust continuum and molecular gas has been observed in the years since Cleeves et al. (2017), none of these observations have followed up on the $H^{13}CO^+$ $3-2$ line. We have done just this. We report follow up observations of the $H^{13}CO^+$ $3-2$ line for the first time since its reported enhancement in 2015. If $H^{13}CO^+$ is still enhanced, then the X-ray flare theory must be ruled out, and the ionization structure of IM Lup will need to be further explored. If $H^{13}CO^+$ has returned to a peak flux of ~ 0.2 Jy kms^{-1}, then we have further evidence of flare driven chemical variability in disks.

4.3 Observations

4.3.1 Observational Setup

SMA observations were carried out on two separate epochs 29 days apart (2020B-S041) in a compact configuration spanning baselines 8 to 70 m with six antennas. Epoch one was observed on 15/May/2021 with 6 hours on source, and epoch two was observed on 13/Jun/2021 with 4 hourson source. Traditionally images would only be created by combining the two separate observations, but for the purpose of this study we produced images for the first observation day (15/May/2021), the second observation day (13/June/2021), and the combined observations. We refer to data produced the 'traditional' way as the time-integrated data.

Sentence on the calibrators, but I need to confirm what Charlie did when he calibrated this data. Weather was dry and stable for both epochs with precipitable water vapor between 0.6 and 0.8 mm on 15/May/2021 and between 0.7 and 1.2 mm on 13/Jun/2021.

The same spectral setup was used for both observations, which covered frequency windows ranging from 240 to 290 GHz with a frequency resolution of 139 kHz (0.16 km/s). We were able to simultaneously observe the $H^{13}CO^+$, HCO^+, HCN, and $HC^{15}N$ J=3-2 lines (see Table 4.1 for transition frequencies). These lines were chosen for the following reasons. $H^{13}CO^+$ $3-2$ was the line previously observed to be enhanced in Cleeves et al. (2017), and we sought to determine the line was still enhanced. HCO^+ $3-2$ has not been previously observed in IM Lup (by ALMA or

Molecule	Transition	Frequency (GHz)	Beam size ('','')
HCO^+	$3-2$	267.55762590	$(3.96 \pm 0.12, 2.20 \pm 0.05)$
$H^{13}CO^+$	$3-2$	260.25533610	$(4.16 \pm 0.23, 2.41 \pm 0.08)$
HCN	$3-2$	265.88643430	$(3.98 \pm 0.13, 2.22 \pm 0.04)$
Continuum		260	

Table 4.1 The lines and frequency targeted in these observations. $HC^{15}N$ is not included, since it was a non-detection. The reported beam covers the range of beam sizes across all three data sets.

inclination[1]		47.5
position angle[1]		144.5
M_*[2]	(M_{sun})	1.1
distance[3]	(kpc)	158.0
system velocity[4]	(km/s)	4.8×10^3
target resolution[5]	('')	$4.0, 4.5^*$
dvq[5]		-2.0

Table 4.2 keplerian mask parameters [1]Huang et al. (2018a) [2]Teague et al. (2021) [3]Gaia Collaboration et al. (2018) [4]Pinte et al. (2018b) [5]found to best fit the data $^*HCO^+$ was imaged with a target resolution of 4.0 and HCN mask was generated with a target res of 4.5.

SMA), and the HCO^+ to $H^{13}CO^+$ ratio will constrain optical depth. HCN $3-2$ has been previously observed by ALMA and is not expected to be sensitive to flares. This line provides a constraint to determine if the $H^{13}CO^+$ SMA data can be easily compared to ALMA data. $HC^{15}N$ was a 'bonus' line not necessary to complete our science goals, but would allow us to constrain HCN optical depth if detected.

The typical beam size is near (4.0'',2.3''), see Table 4.1 for details. Images were not smoothed to generate a uniform beam size since the science goal is to determine whether $H^{13}CO^+$ flux was still enhanced. Since the science goals for this data did not include classifying minute spectral variations, we find that using images with approximately the same beam size suffice.

4.3.2 Imaging Process

We used the python routine keplerian_mask[1] to generate two Keplerian masks centered on the HCO^+ and HCN $3-2$ lines (parameters are listed in Table 4.2). We attempted to image $H^{13}CO^+$ and HCN with the Keplerian masks; however, the final images and spectra were noisy since the $H^{13}CO^+$ and $HC^{15}N$ lines are exceptionally fainter than HCO^+ and HCN, Instead, $H^{13}CO^+$ and $HC^{15}N$ masks were generated by clipping the keplerian HCO^+ and HCN masks to 5σ. Assuming that the isotopologues trace each other, this method conservatively masks regions where emission is expected to occur and produces a more resolved spectrum. Channel maps and masks for detected line transitions are shown in Appendix C.

We used the task `tclean` in `CASA` v6.20.124 to image the four lines. HCO^+ and HCN lines were cleaned using a briggsbwtaper of 0.5 with a spectral resolution of of 0.161 kms^{-1} (resolution of the observations). The more rare isotopes were imaged with a robust value of 1.0 and a spectral resolution of three times the natural resolution (0.483 kms^{-1}). All lines were cleaned to a signal to noise (SN) of 2.

Continuum images were generated by using the `CASA` task `uvcontsub` to extract continuum data from the 260 GHz spectral windows. Continuum data was then cleaned with the hogbom deconvolver and a robust value of 0.25 to a SN of 0.5.

Spectra, moment zero maps, integrated line and continuum fluxes, and errors are found using the same methodology as Waggoner et al. (2023) and will not be repeated here.

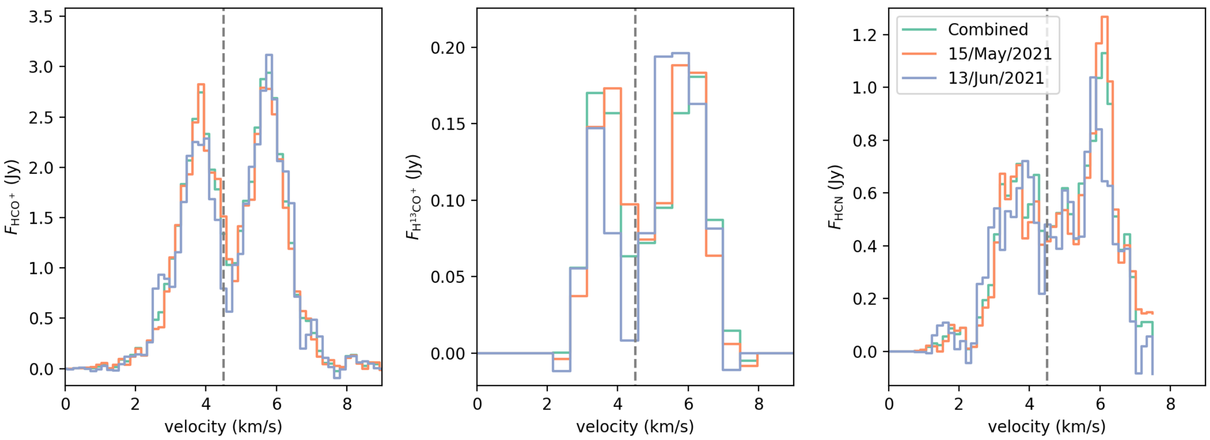

Figure 4.1 Line spectra for HCO^{+}, H^{13}CO^{+}, and HCN 3−2 lines. The dashed grey line indicates the accepted IM Lup source velocity (4.5 kms^{-1}, Pinte et al., 2018a). Note that the spectra for each observing day and the integrated spectrum are consistent within error (see Section C.1).

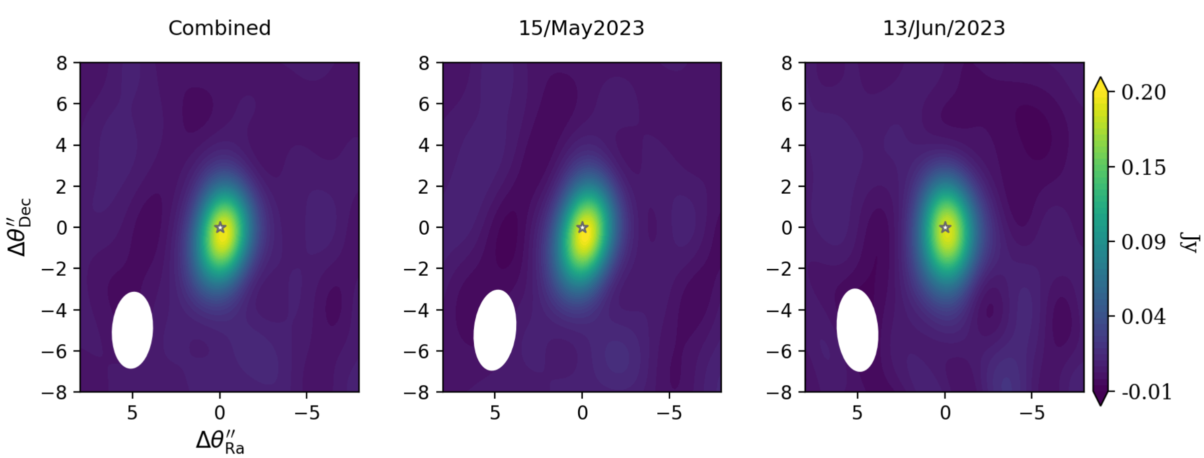

Figure 4.2 260 GHz continuum images for each of the observations and the integrated image. The continuum remained effectively constant across both observations.

Date	Disk Integrated $H^{13}CO^+$ $3-2$ (Jy kms-1)	Disk Integrated Continuum (Jy)
17/July/2014*	0.466 ± 0.032	0.286 ± 0.003
29/Jan/2015*	0.590 ± 0.020	0.308 ± 0.001
13/May/2015*	1.254 ± 0.019	0.307 ± 0.001
15/May/2021	0.297 ± 0.030	0.198 ± 0.010
13/Jun/2021	0.186 ± 0.046	0.185 ± 0.020

Table 4.3 Integrated line and continuum flux for each of the five observation epochs. The flux was approximately doubled on 13/May/2015, and is approximately the same on the other four epochs. Notably, the last two observations are slightly lower than the first two, but this is likely due to SMA and ALMA flux sensitivity differences.
* indicates data from Cleeves et al. (2017)

4.4 Spectra and Continuum Images

We found that a source velocity of $\sim 4.8\,\mathrm{kms}^{-1}$ resulted in the best fit masks, but the the accepted source velocity of IM Lup is $4.5\,\mathrm{km}^{-1}$ (Pinte et al., 2018b). This velocity shift is most likely caused by cloud contamination in the foreground, which is consistent with previous observations of the CO $3-2$ and $2-1$ lines.

The HCO^+, $H^{13}CO^+$, and HCN $3-2$ lines were all clearly detected in both observation epochs, as shown in Figure 4.1; however $HC^{15}N$ was not detected. Both HCO^+ and $H^{13}CO^+$ spectra are consistent with a symmetrical 'double-horn' spectrum, which is caused by the Keplerian rotation of the disk. The HCN line also has features consistent with the double-horn spectrum, but the line is broadened and asymmetrical. This is likely caused by unresolved hyperfine lines. The detected lines spectra and continuum flux (Figure 4.2) are consistent across both observations within 1σ, as further discussed in Appendix C.

[1]Developed by Richard Teague and publicly available on github at https://github.com/richteague/keplerian_mask

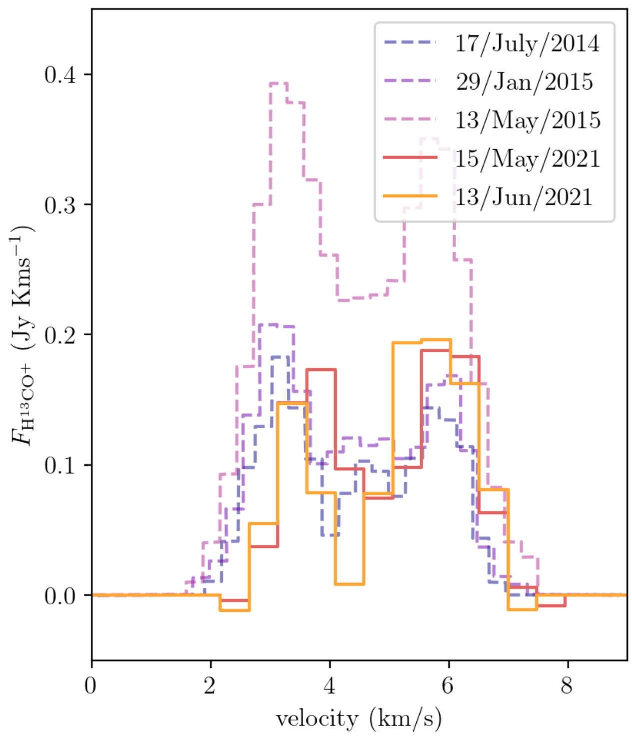

Figure 4.3 $H^{13}CO^+$ $3-2$ spectra observed on five separate days. Data collected on 17/July/2014, 29/Jan/2015, and 13/May/2015 (indicated by dashed lines) were collected by ALMA and reported in Cleeves et al. (2017). Data taken on 15/May/2021 and 13/Jun/2021 were taken with the SMA. The line flux is approximately doubled on 13/May/2015 compared to all other observations.

4.5 Conclusions

We present SMA observations of the HCO^+, $H^{13}CO^+$, and HCN J=3-2 line transitions in the IM Lup protoplanetary disk. These observations were a follow up of ALMA observations of $H^{13}CO^+$ $3-2$ reported in Cleeves et al. (2017). Cleeves et al. observed the $H^{13}CO^+$ $3-2$ flux to approximately double on one observation day compared to two previous epochs while continuum flux (and therefore disk temperature) remained constant.

We re-observed the $H^{13}CO^+$ $3-2$ line for the first time since it's reported enhancement and found that the line has returned to its 'quiescent', non-enhanced flux with a peak at ~ 0.18Jy. Additionally, we find that the HCN $3-2$ line flux is consistent with previous observations (Guzmán et al., 2021), and we report the HCO^+ $3-2$ line for the first time.

Notably, the SMA data reported here has significantly lower *uv* coverage compared to the previous ALMA observations in Cleeves et al. (2017). As discussed in Section include, telescope configuration and baseline coverage affect the final images. However, the non-overlapping *uv* coverage considered here corresponds to longer baselines achievable by ALMA but not the SMA. Since both telescope facilities have sufficient *uv* coverage at shorter baselines, we consider any loss or variations introduced by varying visibilities to be insignificant within error.

When combined with previous observations, our data supports the X-ray flare theory proposed by Cleeves et al. (2017); this theory states that a X-ray flaring event from the young, central star enhanced the abundance of gas-phase cations, like HCO^+. While we cannot constrain the exact duration of enhancement, since the data has been taken over course of several years, we have confirmed that the enhancement was short-lived when compared to other astrophysical events.

These are the first set of observations that directly support the theory that X-ray flares can temporarily increase the abundance of gas-phase cations. Although the theory cannot be confirmed, since there were no X-ray observations at the time the flare would have occurred, these data are the inspiration and motivation behind a multi-wavelength campaign designed to constrain flare driven physics and chemistry. These observations are discussed in further detail in Chapter 7.

4.6 Chapter Acknowledgements

This chapter makes use of the following SMA data: 2020B-S041.

Chapter 5

MAPS: Constraining Serendipitous Time Variability in Protoplanetary Disk Molecular Ion Emission

"If you're always on time, it implies that you never have anything better you should be doing."

Brandon Sanderson, *Mistborn*

5.1 Abstract

This chapter was originally published by Waggoner et al. (2023) in the Astrophysical Jounral with the co-authors L. Ilsedore Cleeves, Ryan A. Loomis, Yuri Aikawa, Jaehan Bae, Jennifer B. Bergner, Alice S. Booth, Jenny K. Calahan, Gianni Cataldi, Charles J. Law, Romane Le Gal, Feng Long, Karin I. Öberg, Richard Teague, and David J. Wilner.

Abstract: Theoretical models and observations suggest that the abundances of molecular ions in protoplanetary disks should be highly sensitive to the variable ionization conditions set by the young central star. We present a search for temporal flux variability of HCO^+ J$= 1 - 0$, which was observed as a part of the Molecules with Atacama Large Millimeter/submillimeter Array (ALMA) at Planet-forming Scales ALMA Large Program. We split out and imaged the line and continuum data for each individual day the five sources were observed (HD 163296, AS 209, GM Aur, MWC 480, and IM Lup, with between three and six unique visits per source). Significant enhancement ($> 3\sigma$) was not observed, but we find variations in the spectral profiles in all five disks. Variations in AS 209, GM Aur, and HD 163296 are tentatively attributed to variations in HCO+ flux, while variations in IM Lup and MWC 480 are most likely introduced by differences in the uv coverage, which impact the amount of recovered flux during imaging. The tentative detections and low degree of variability are consistent with expectations of X-ray flare-driven HCO^+ variability, which requires relatively large flares to enhance the HCO^+ rotational emission at significant ($> 20\%$) levels. These findings also demonstrate the need for dedicated monitoring campaigns with high signal-to-noise ratios to fully characterize X-ray flare-driven chemistry.

5.2 Introduction

Molecular abundances within protoplanetary disks have traditionally been expected to evolve over tens to hundreds of thousands of years or longer (Henning & Semenov, 2013; Öberg & Bergin, 2021, and references therein). However, young pre-main sequence stars at the center of disks are active in the X-ray regime on timescales of days to weeks (e.g. Getman et al., 2005; Wolk et al., 2005; Getman et al., 2022b,a). Due to an unstable dynamo, young stars regularly undergo magnetic reconnection events which result in a larger burst of X-ray photons commonly known as an X-ray flare (Güdel, 2004, and references therein), which can temporarily increase the X-ray flux and disk ionization rates (Ilgner & Nelson, 2006d). Flares can range in strength, increasing the flux by a factors of a few to several hundred times the baseline flux (Getman et al., 2005; Getman & Feigelson, 2021)

Flare-driven variable ionization rates drive variability in chemical species in disks. This variation largely stems from time variability in the ionization of H_2 and He, which play a major role in driving cold molecular chemistry (Maloney et al., 1996). For example, a single strong flare (i.e., 100 times stronger than the baseline luminosity) can temporarily increase the abundance of H_2^+ by up to a factor of ~ 70. H_2^+ then forms H_3^+, which enhances the formation of gas-phase species, such as H_2O, near the disk surface (< 100 au from the central star Waggoner & Cleeves, 2019). Gas-phase cations are especially sensitive to flares, where some species, such as HCO^+ and N_2H^+, can be increased by several orders of magnitude for days or weeks depending on the strength of the flare. For example, Waggoner & Cleeves (2022) found that a single strong flare can increase the disk integrated abundance of HCO^+ and N_2H^+ by ~ 4 and ~ 3, respectively. Additionally, the cumulative effect of thousands of flares aids in the advancement of chemical complexity over the course of hundreds of years by marginally ($\sim 1\%$ change) increasing the production of carbon chains and organosulphides (Waggoner & Cleeves, 2022).

While this study is motivated specifically by flare-driven variable ionization rates, it is important to note that other processes can drive variability. For example, accretion outbursts are known to increase UV flux and disk temperature. Observations and models indicate that outbursts evaporate ices and increase gas density, which in turn drives chemical reactions (e.g., Molyarova et al., 2018; Kóspál et al., 2021; Leemker et al., 2021; Ruíz-Rodríguez et al., 2022; Fischer et al., 2022; Tobin et al., 2023).

Significant enhancement in the flux of a gas-phase cation has been reported previously by Cleeves et al. (2017) in observations of the $H^{13}CO^+$ J=3 − 2 line with the Atacama Large Millimeter/submillimeter Array (ALMA). Cleeves et. al observed $H^{13}CO^+$ J=3 − 2 in the IM Lup protoplanetary disk on three separate days: July 2014, January 2015, and May 2015. In July 2014 and January 2015, the $H^{13}CO^+$ flux was effectively constant, but in May 2015 the flux doubled (an increase by 28σ). They concluded that enhancement was not caused by an increase in temperature, as the continuum emission remained constant, thus ruling out an outburst or similar type event. IM Lup, like most young stars, is known to be X-ray variable (Cleeves et al., 2017). Indeed, the most likely source of $H^{13}CO^+$ enhancement was due to an X-ray flaring event.

In fact, the detection in IM Lup was serendipitous and is currently the only source with reported variability. Espaillat et al. (2022) searched for variations in CO millimeter emission in GM Aur; however no significant variability was seen. This result was somewhat expected, since chemical models in Espaillat et al. (2022) and in Waggoner & Cleeves (2022) indicate that the robust CO molecule is not sensitive to variable X-ray and UV ionization rates.

This work seeks evidence of flare driven chemistry by searching for variability of the HCO^+ J=1 − 0 line in the five disks, HD 163296, AS 209, GM Aur, MWC 480, and IM Lup, observed as a part of Molecules with ALMA at Planet-forming Scales (MAPS) ALMA Large Program (Öberg et al., 2021), which fortuitously was observed at multiple dates spanning about a year. Section 5.3 describes the observational set up, sources, and line selection. Section 6.3 describes the `CLEAN`ing strategy, methodology, and error analysis. The results are presented in Section 6.4, where the degree of variability is constrained. In Section 5.6, we discuss the presence/absence of variability, along with possible connections to X-ray flaring events and/or related variable ionization rates. Section 5.7 provides a summary of this work along with concluding remarks.

5.3 Observations

The data used in this work were taken as a part of the MAPS ALMA Large Program (2018.1.01055.L, Öberg et al., 2021). MAPS observations included five sources: the IM Lup, GM Aur, AS 209, HD 163296, and MWC 480 protoplanetary disks. Table 5.1 includes the coordinates, systemic velocity, and additional observation details for each disk. MWC 480 and HD 163296 are both Herbig Ae systems, while the other three are T Tauri systems. These five disks were selected because they are bright and chemically rich, thus allowing for more in-depth observations (Öberg et al., 2021, Section 2.1 for more details).

HCO^+ J=1−0 observations were carried out between October 2018 and September 2019, where short-baseline data were collected in October and December 2018 and long-baseline data were taken in August and September 2019. Table 5.2 provides the baseline coverage and integrated observation time for each observation of each disk. A detailed description of data collection and the data reduction analysis is provided

Source	R.A. (J2000)	Decl.	Sys Vel (LSRK, km s^{-1})	Num of Obs.	Min Baseline (m)	Beam ”	BPA
IM Lup	15 : 56 : 09.186780	−37.56.06.58091	4.5[6]	3	60	2.0	63.8
GM Aur	04 : 55 : 10.981558	+30.21.58.87742	5.6[4]	5	55	2.0	8.6
AS 209	16 : 49 : 15.293780	−14.22.09.09404	4.6[3]	5	50	2.0	62.4
HD 163296	17 : 56 : 21.277330	−21.57.22.63945	5.8[1,2]	6	70	2.0	76.3
MWC 480	04 : 58 : 46.274800	+29.50.36.47709	5.1[2,5]	5	50	2.2	16.7

Table 5.1 The right ascension, declination, systemic velocity, number of unique observations days, minimum baseline used for imaging, and beam size for each of the five MAPS disks. For each disk, the beam was tapered and smoothed to be circular and the same across all epochs. The minimum baseline is the smallest baseline coverage used in the imaging process. (1) Teague et al. (2019) (2) Teague et al. (2021) (3) Huang et al. (2017) (4) Huang et al. (2020) (5) Piétu et al. (2007) (6) Pinte et al. (2018a)

Source	Date	uv (m)	time (s)
IM Lup	29 Oct 2018	13.5-1258.6	2470.90
	20 Aug 2019	35.7-3188.1	3751.49
	21 Aug 2019	39.2-3506.6	3698.02
GM Aur	13 Dec 2018	12.7-667.3	2372.98
	15 Dec 2018	12.0-687.8	2345.52
	31 Aug 2019	22.7-3143.7	3976.56
	02 Sep 2019	24.4-3141.3	8548.70
	04 Sep 2019	25.7-2904.0	4218.82
AS 209	26 Oct 2018	14.3-1394.8	2520.43
	23 Aug 2019	39.9-3396.5	3660.77
	24 Aug 2019	31.6-3330.3	3612.77
	03 Sep 2019	70.5-3118.4	3666.29
	04 Sep 2019	27.7-3627.5	3641.57
HD 163296	22 Oct 2018	12.7-1347.6	2511.17
	23 Aug 2019	56.7-2742.3	3503.42
	24 Aug 2019	30.3-3335.1	3499.78
	25 Aug 2019	39.1-3389.0	3519.79
	04 Sep 2019	34.6-3071.5	3508.90
	05 Sep 2019	73.0-3637.1	3527.23
MWC 480	13 Dec 2018	12.0-671.2	2974.51
	15 Dec 2018	12.1-691.7	2931.70
	31 Aug 2019	23.0-3143.8	4141.15
	02 Sep 2019	24.7-3142.6	8573.71
	04 Sep 2019	26.1-2884.5	4245.26

Table 5.2 The baseline coverage (uv) and total observation time spent on source for each observation day for each disk. Each unique observation day was a single ALMA execution block, except 02/Sep/2019 in MWC 480 and GM Aur, which contain two execution blocks.

in Öberg et al. (2021) and Czekala et al. (2021), respectively.

For the most part, there was only a single execution per observation day, with the exception of MWC 480 and GM Aur. Both of these sources were observed twice on 02/Sep/2019. A one day separation was found to be the optimal time to split the data based on: 1. timing of the execution blocks, 2. optimizing the signal to noise ratio of the data, and 3. providing the maximum number of distinct observations possible to search for variability.

For this work, we chose to limit the data to HCO^+ $1-0$ taken as a part of MAPS. There are previous observations of HCO^+ emission lines and its various isotopes in the MAPS sources. However, by limiting the analysis to MAPS data the analysis is much more homogeneous and allows for a more robust comparison between observations.

5.3.1 Line Selection

We use Band 3 data of HCO^+ J=$1-0$ (89.188525 GHz) for each of the five MAPS disks. HCO^+ was found to be the most likely candidate to trace variable disk chemistry based on models used in Waggoner & Cleeves (2022), as gas-phase cations have been shown to be the most susceptible to variable ionization rates. Aikawa et al. (2021) found that the optical depth (τ) of the HCO^+ line is ~ 1 for each of the MAPS disks. While a more optically thin line would be more ideal for this study, HCO^+ $1-0$ is the only gas-phase cation that is sufficiently bright to allow splitting into individual images for each observation block.

We investigated whether a similar analysis was possible for neutral species observed simultaneously with HCO^+; however, the C_2H and HCN lines were too weak to split into individual observations. A search for minor spectral changes was not feasible due to low signal to noise ratios.

All data used in this work are publicly available directly on the ALMA archive or through the interactive MAPS website[1] (See also Section 3.5 in Öberg et al., 2021). The line measurement set, line mask, and line plus continuum measurement set can be downloaded directly from the MAPS website. Continuum masks were hand drawn for each disk.

5.4 Methods

5.4.1 CLEANing Strategy

The line and continuum are imaged using the same process starting with the measurement sets (described in Section 5.3) using `CASA` version 6.2, where the line is flagged from the line plus continuum measurement set to generate the continuum image. Line images are produced using the `briggsbwtaper` weighting with a robust value of 0.5. `briggsbwtaper` is new to `CASA` as of version 6.2 and handles gridding more accurately than the commonly used `briggs` weighting. All images are `CLEAN`ed to 3σ, where σ is the rms measured in the dirty image. The imaging process proceeds as follows:

1. Data for each observation day is split into a new measurement set using the function `split` in `CASA`. Data taken on individual days was not further split because sensitivity would drastically decrease. Additionally, a day was found to be sufficient time for a flare to occur between epochs (for flare statistics see Wolk et al., 2005).

2. A dirty image is generated to determine the `CLEAN`ing threshold and dirty beam size.

[1]alma-maps.info

3. A *uv* taper is estimated from

$$\mathrm{b}_{\mathrm{tap}} = \left(\frac{\mathrm{b}_{\mathrm{dirty}}^{-1} - \mathrm{b}_{\mathrm{des}}^{-1}}{(\mathrm{b}_{\mathrm{dirty}}^{-2} - \mathrm{b}_{\mathrm{des}}^{-2})^{0.5}} \right)^{-1}, \tag{5.1}$$

   where $\mathrm{b}_{\mathrm{tap}}$ is the *uv* taper, $\mathrm{b}_{\mathrm{dirty}}$ is the dirty beam, and $\mathrm{b}_{\mathrm{des}}$ is the desired beam size. The taper is unique for each observation execution, but the same taper is used for both line and continuum imaging. The taper is essential to generate a uniform, approximately circular beam size (the 'target beam', Table 5.1) for each disk. Without a uniform beam, images for individual days could not be directly compared.

4. The lower resolution images made by applying the taper to the visibilities were `CLEAN`ed using the MAPS mask pre-smoothed to a larger beam to encompass all of the line emission. The MAPS mask is used to select the `CLEAN`ed region; however, the mask is pre-smoothed to the new, larger beam to encompass the full flux of the lower resolution line image. Smoothing is carried out with the `CASA` function `imsmooth`.

5. The `CLEAN`ed beam is nearly circular from the *uv* taper, but not perfectly. The final image is then smoothed using `imsmooth` to generate a uniform beam size and shape for each disk (listed in Table 5.1).

The `CLEAN`ing scripts are available upon request from A.R.W.

Figure 5.1 shows the moment zero maps for all observations, which shows integrated line emission. In this case, the moment zero maps were generated by integrating flux across frequency space across the entire image cube. Maps were generated without use of the mask. Figure 5.2 shows the continuum images for each observation.

5.4.2 Flux and Error Analysis

The integrated flux for the continuum emission was determined by integrating all emission within the hand-drawn mask in the continuum image (Figure 5.2). The integrated flux was found by integrating all channels with significant flux. Channels containing the line were defined as any channel that contain data emission greater than 3σ, where σ was the standard deviation of the unmasked data in each channel.

The error for the integrated line flux ($F_{\mathrm{HCO^+}}$) was determined as follows. First, the mask was randomly shifted to 40 different locations off source. The error of the integrated flux was then found by taking the standard deviation of the integrated flux within the off source locations. The error for the integrated continuum flux (F_{cont}) was found in a similar manner. This sampling method was used, rather than shifting the mask to line free channels, due to the limited number of channels available in the MAPS products' measurement sets. The flux calibration error is $< 20\%$ for all sources, with the assumption that the continuum flux should be constant across all observations (Figures 5.3-5.7). Flux calibration error $\sim 10\%$ or greater is consistent with the ALMA technical handbook (Cortes et al., 2022).

To ensure that any changes in HCO^+ emission were not due to changes in source brightness or temperature, the line flux to continuum flux ratio ($F_{\mathrm{HCO^+}}/F_{\mathrm{cont}}$) was used to compare line brightness for individual observation days. The continuum is expected to be constant, just as it was observed to be in for the IM Lup disk in Cleeves et al. (2017).

5.4.3 Baseline Coverage

Interferometrically measured flux is inherently sensitive to the baseline coverage of the observation. Shorter baselines are known to probe flux better, while being

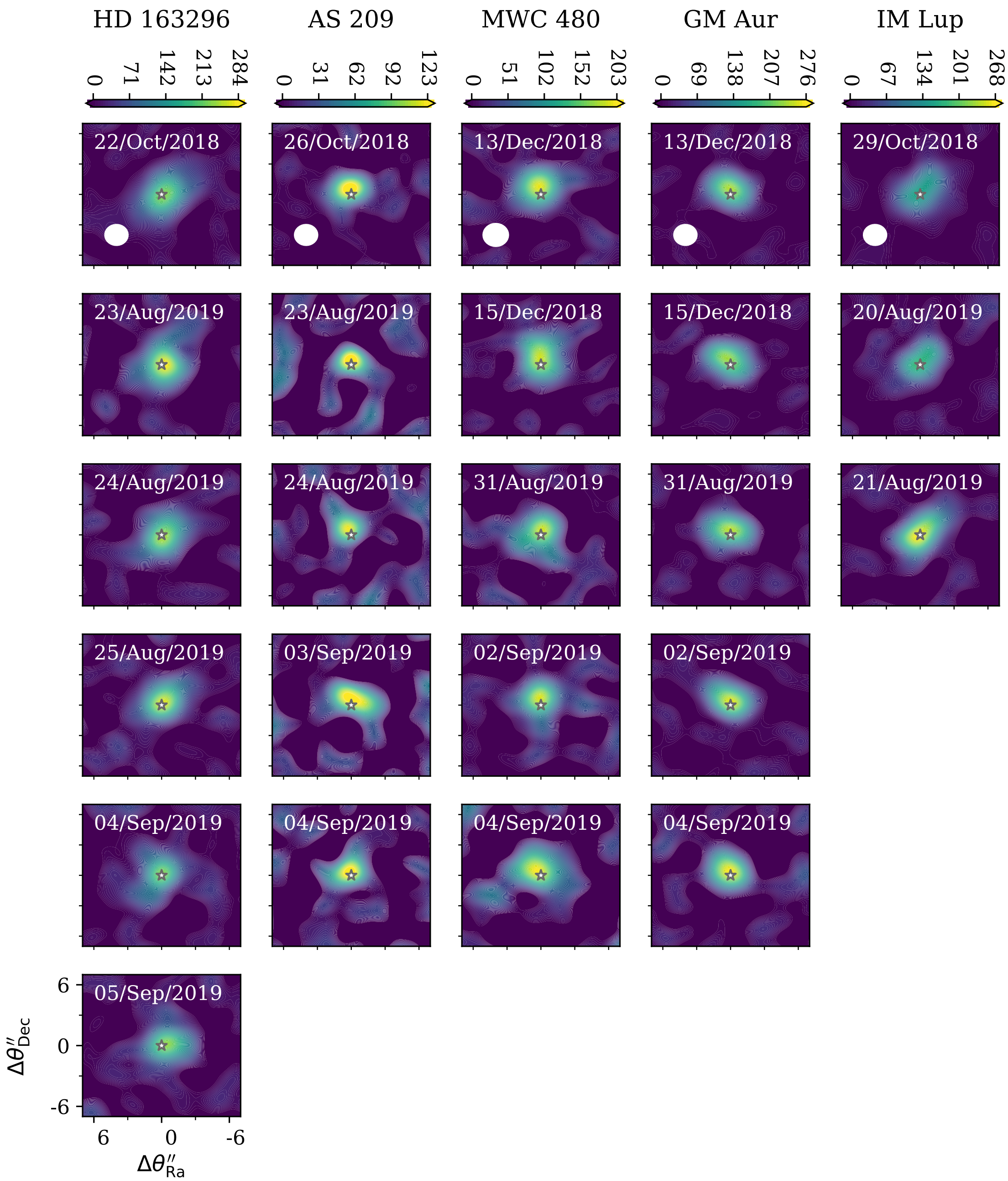

Figure 5.1 The moment zero map of HCO^+ $1-0$ for each observation execution for each disk. Each column corresponds to a different disk, while each row represents a separate observation day. The date of observation is shown in the top of each plot. Each disk has a unique own color bar with units in mJy. The beam for each disk is shown in white in the bottom left of the top row of images.

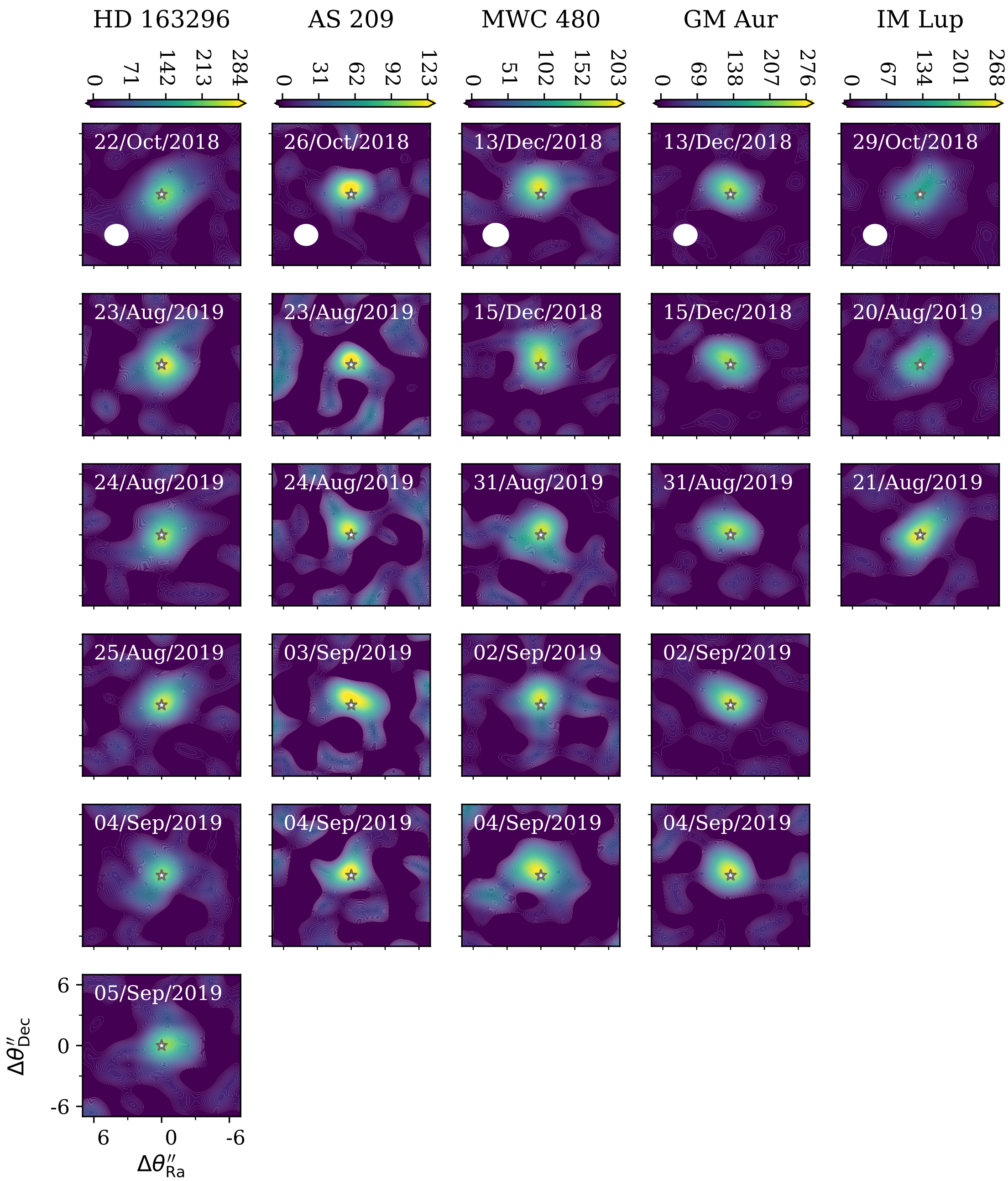

Figure 5.2 The 90 GHz continuum emission for each observation execution for each disk. Each column corresponds to a different disk, while each row represents a separate observation day. The date of observation is shown in the top of each plot. Each disk has a unique own color bar with units in mJy. The beam for each disk is shown in white in the bottom left of the top row of images.

less sensitive to structure, and longer baselines probe structure well, while being less sensitive to flux (for example see Chapter 5 in Thompson et al., 2017). The MAPS observations utilized multiple ALMA configurations to optimize the baseline coverage to include both short and long baselines. While this method is incredibly useful in generating a complete picture of the disk across multiple scales, varying telescope configurations adds an additional challenge to compare flux on different observation days.

Observations with longer baseline coverage, i.e., fewer short baselines, miss flux on larger scales (Thompson et al., 2017). A minimum baseline distance was set for each disk to ensure that long baseline observations do not have an artificially lower flux than images with thorough short baseline coverage. Even though the most "flux sensitive" baselines were removed, there is still sufficient *uv* sampling across all epochs to cross compare them. A range of minimum baseline values was examined, and we selected values that preserved as many short baselines as possible consistently across different epochs without cutting out too many short baselines that would introduce imaging artifacts (listed in Table 5.1). On average there was a $22\% \pm 12$ loss in flux as a result of this process based on comparisons between the clipped data and the full measurement set.

To further ensure that any detected variability was not artificially introduced by the varying baseline coverage, the `PYTHON` routine `vis_sample`[2] was used to create 'mock' data sets for each observation of each disk. The mock data was generated by first imaging the time integrated images of HCO^+ J$= 1-0$ (i.e., the complete observation set), as was done by Aikawa et al. (2021). The time integrated image is considered to be the 'ground truth' to generate the mock data set. Synthetic ALMA

[2] `vis_sample` is publicly available under the MIT license at https://github.com/AstroChem/vis_sample and described in further detail in Loomis et al. (2018)

observations were created by running the time integrated image through `vis_sample` for each of the observation days. This generated a synthetic observation using the same visibility effects as the actual observation. Mock images were created by imaging the synthetic observations using the same `CLEAN`ing process used for the real data (described above). This process helps constrain variability in HCO^+ or continuum emission introduced by visibility (i.e., *uv* sampling) effects, but the possibility of visibility effects is still considered in the results.

5.4.4 AS 209

AS 209 is the faintest source in HCO^+ $1-0$ of the five disks (Figure 5.3). Previous observations have revealed a cold molecular cloud in the foreground of AS 209, and the cloud absorbs cold emission from AS 209 at select velocities in CO gas (Öberg et al., 2011; Huang et al., 2016; Favre et al., 2019) and in HCO^+ gas (Law et al., 2021). In this source, HCO^+ $1-0$ is considered to be tentatively variable over the MAPS observations.

5.5 Results

5.5.1 General Behavior

A variable source is defined as any source with at least one observation where there is a $\geq 3\sigma$ change in disk integrated $F_{\mathrm{HCO^+}}/F_{\mathrm{cont}}$. A tentatively variable source is defined as a source with at least one observation day that has variability in the HCO^+ J= $1-0$ intensity spectrum. Spectral variability is defined on a case by case basis in the following sections. In this work, all changes in spectral shape are considered tentative due to (relatively) low signal to noise ratios (S/N). A tentatively variable source does not display variations in the disk integrated $F_{\mathrm{HCO^+}}$, F_{cont}, and $F_{\mathrm{HCO^+}}/F_{\mathrm{cont}}$, i.e. all integrated flux values are within 3σ of each other. All tentative

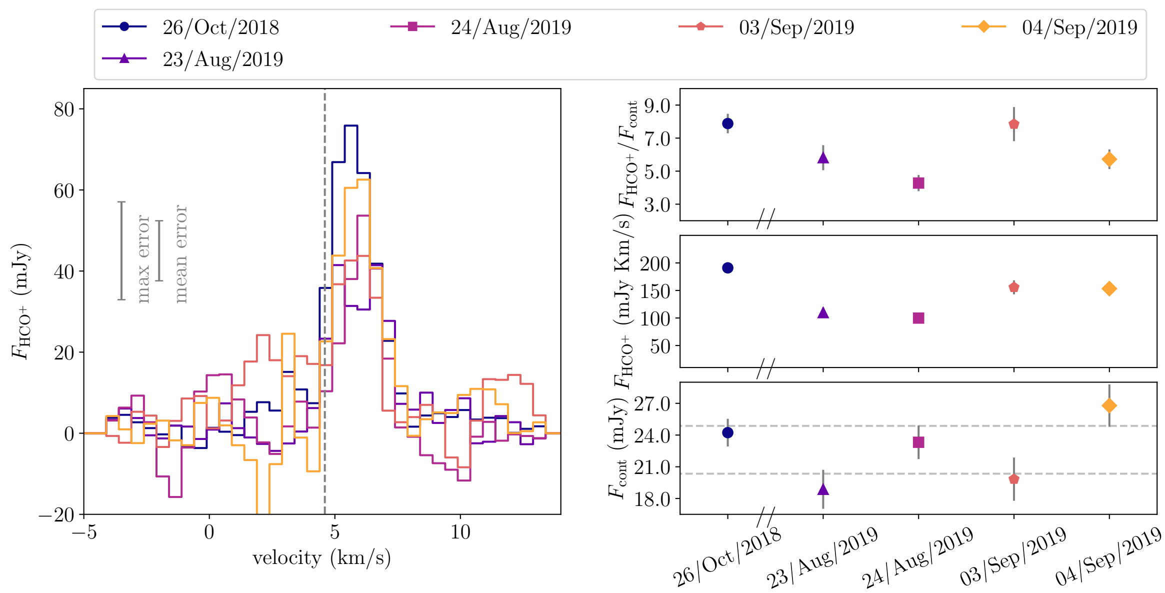

Figure 5.3 *Left*: The HCO$^+$ J=1−0 spectra in the AS 209 disk for each unique observation day. The grey bars one the left represent the maximum and mean error (standard deviation) for all channels across all observations. *Right*: The disk integrated continuum flux (F_{cont}, bottom), disk integrated HCO$^+$ $1-0$ flux ($F_{\mathrm{HCO^+}}$, middle), and normalized line flux with respect to the continuum ($F_{\mathrm{HCO^+}}/F_{\mathrm{cont}}$, top) for each day HCO$^+$ $1-0$ was observed in AS 209. Units for $F_{\mathrm{HCO^+}}/F_{\mathrm{cont}}$ are mJy km s^{-1} mJy^{-1}. Error bars indicate 1σ. Grey dashed lines in bottom plot indicate $\pm 10\%$ the average continuum flux.

variability occurs on a channel by channel basis.

None of the five disks were found to be variable on a disk-integrated basis in HCO^+ J$= 1-0$ emission during the MAPS observations, as is clear in the moment zero maps (Figure 5.1) which are constant within the error bars across nearly all epochs. On 03/Sep/2019, the disk integrated HCO^+ line flux observed in the AS 209 disk has more of an oval shape compared to the other epochs, which are more circular. This morphological difference appears to be a result of a small excess of blue shifted emission on 03/Sep/2019 compared to the other days (discussed further in Section 5.4.4). On 21/Aug/2019, HCO^+ emission in IM Lup is brighter than the other epochs. However, our analysis suggests the brighter line flux is likely caused by differences in baseline coverage (discussed further in Section 5.5.5).

While the disk integrated flux remained constant within the error bars for all disks, we report tentative variability in three of the five disks: AS 209, GM Aur, and HD 163296. Each of these disks feature some form of variability or shift in the HCO^+ spectral shape, as further discussed below (Sections 5.4.4, 5.5.3, and 5.5.4). MWC 480 also displays a shift in the HCO^+ spectral shape, but this shift is at the level of the noise (Section 5.5.6). IM Lup has a brighter peak at 6.8 km s^{-1} than other observation days, but the higher flux is most likely caused by baseline coverage (Section 5.5.5). Noise on a channel by channel basis is further discussed in Appendix D.2.

As discussed in Section 5.4.3 and Appendix D.1, we investigate if the differences in baseline coverage impact the measured flux. A "known flux" model was created using `vis_sample`. The analysis suggests that the tentative HCO^+ spectral variability in AS 209, GM Aur, and HD 163296 was unlikely to be introduced by differences in baseline coverage at the level of the noise in the data. However, IM Lup and MWC 480 appear to have been impacted by these effects.

5.5.2 Continuum

There are no significant and distinguishable differences in the continuum images taken as a part of the MAPS observation set (Figure 5.2). For each disk, disk integrated F_{cont} values (taking into account RMS uncertainty) were within 10 $\sim 20\%$ of each other. This magnitude of variation is consistent with the acceptable level of flux calibrator uncertainty reported for ALMA (Francis et al., 2020; Cortes et al., 2022). Therefore, all observations of continuum emission are constant within error for all disks.

While a clear ($> 3\sigma$) change in integrated flux is not seen, the spectral peak at 6.1 km s^{-1} relative to the source velocity is $\sim 62\%$ higher on 26/Oct/2018 compared to the other observation days. Additionally, the emission peak shifts towards the source velocity by ~ 5.1 km s^{-1}, or by one channel, on 26/Oct/2018. Notably, October 2018 has the best short baseline coverage, and the increase in emission and peak shift could be attributed to higher sensitivity to extended emission on this date.

There is also some variability in the wings, notably on 3/Sep/2019 where a higher flux is is seen at 12.1 and 1.6 km s^{-1}. Emission at 1.6 km s^{-1} is significant, since this is the only day that blue shifted emission is detected for any of the observed dates. While it is difficult to say with certainty, there is a slight elongation in the moment zero maps (Figure 5.1) on this day compared to the other dates. The channel maps showed that the excess emission was centrally peaked.

Changes in the spectrum are considered tentative, and a higher S/N is required to confirm if the general variable behavior of this source is indeed real or a noise artifact.

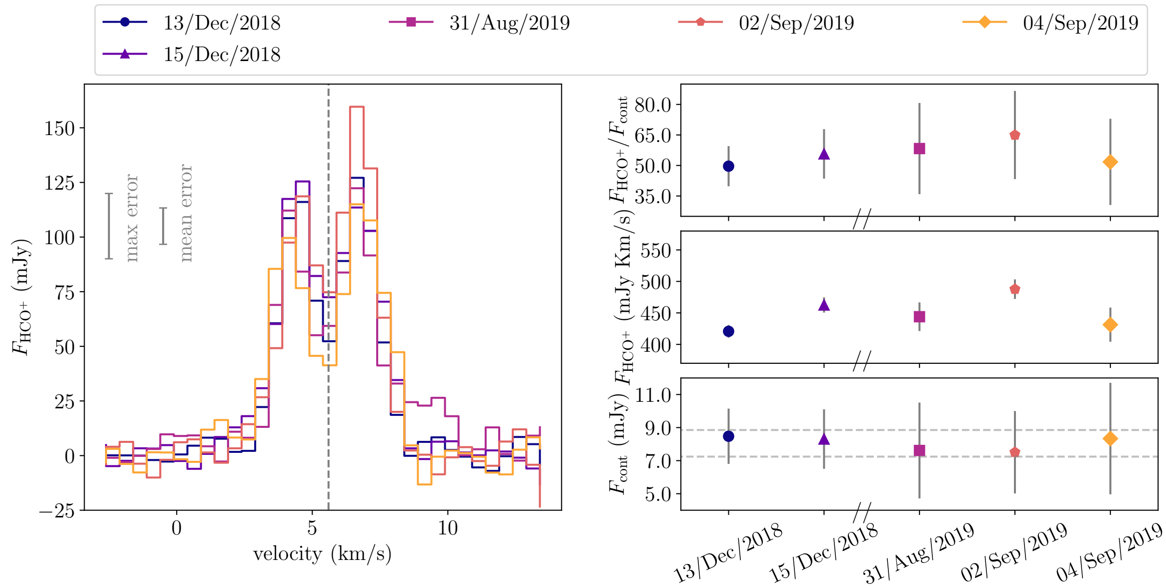

Figure 5.4 Same figure description as Figure 5.3, but for GM Aur.

5.5.3 GM Aur

HCO^+ $1-0$ is considered tentatively variable in GM Aur due to slight variations on 31/Aug/2019 (Figure 5.4). On this day, peak F_{HCO^+} at 6.6 km s^{-1} is $\sim$ 25% higher than the other epochs. The peak at 4.6 km s^{-1} remains constant across all observations. On 2/Sep/2019 a shoulder is visible at 9.6 km s^{-1} that is not seen on the other observation days.

Notably, both occurrences of variability are asymmetric, where channels within the red shifted portion of the spectrum are enhanced while the blue-shifted side of the spectrum remains constant. The complex substructure observed in GM Aur may be the force behind asymmetric variations. As a flare propagates through the disk light could be asymmetrically scattered due to spiral arms, which were seen in ^{12}CO gas emission (Huang et al., 2021). However, spiral arms were not seen in HCO^+ emission, which indicates that the substructure of GM Aur is complex. Without

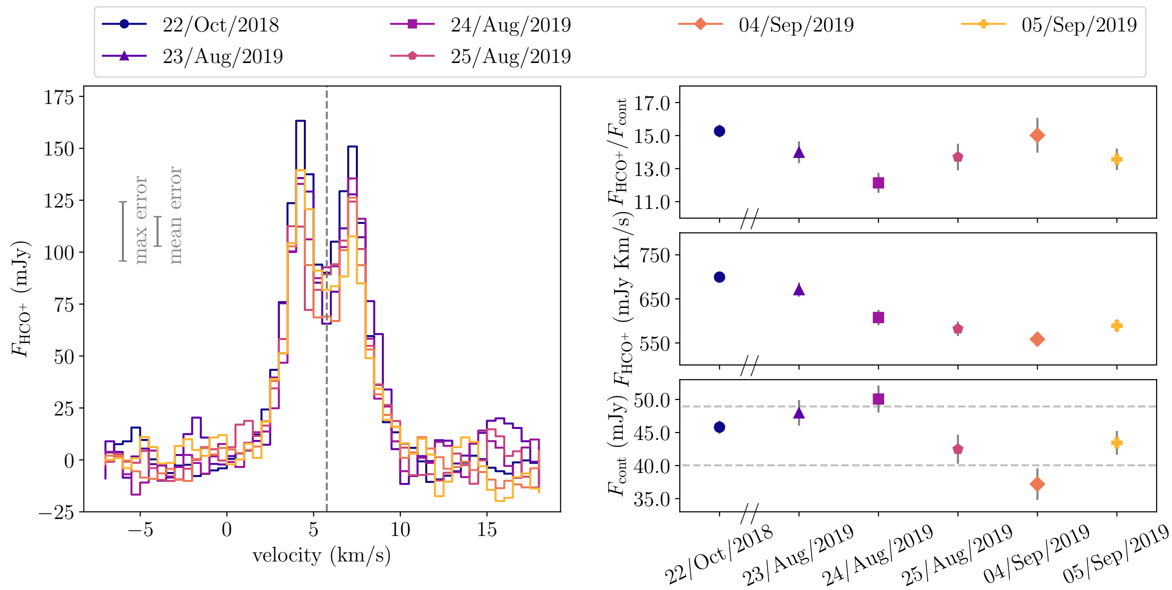

Figure 5.5 Same figure description as Figure 5.3, but for HD 163296.

further modeling it is uncertain how exactly the spiral arms would influence flare propagation or chemical changes.

5.5.4 HD 163296

HD 163296 is considered tentatively variable in HCO^+ $1-0$ emission (Figure 5.5). On 22/Oct/2018 (the first epoch) the double peaks are symmetrically $\sim$ 15% higher than the following observations. This change is small, symmetric, and only occurs on one day, so calibration or baseline effects could have introduced the variation. While steps were taken to minimize variations introduced by baseline coverage (Section 5.4.3), the October 2018 observation has more complete low baseline coverage than the later observations. While steps were taken to minimize variations introduced by baseline coverage, this epoch was the most impacted by flux loss. There was a 42% loss of flux on this day when small baselines were removed, which indicates that the October 2018 observation was strongly impacted by visibility effects. This sensitivity indicates that the enhancement could be caused by unaccounted visibilities. Even though our investigation of flux recovery did not suggest this to be true (Figure D.1c), the possibility is not ruled out.

5.5.5 IM Lup

Though significant variability was seen in $H^{13}CO^+$ $J = 3-2$ in previous observations (Cleeves et al., 2017), the HCO^+ $1-0$ flux is observed to be relatively constant in this data set (Figure 5.6). The spectral peak at 6.8 km s^{-1} is $\sim$ 26% higher on 21/Aug/2019 compared to other observations, which is also seen in the moment zero maps (Figure 5.1). However, the fluctuation may be due to baseline coverage. Flux retrieval on a model of known flux (using `vis_sample`) shows the same spectral variation, suggesting that the increase in emission is introduced by differences in uv-coverage (Figure D.1d).

IM Lup has slightly better low baseline coverage than the other four sources, with 90% of baselines being $\geq$ 280m for IM Lup and $\geq$ 310m for all other sources. Additionally, IM Lup is the most extended source (gas emission up to $\sim$ 750 au; Panić et al., 2009; Avenhaus et al., 2018) in the sample, thus the large scale emission area is more sensitive to shorter baselines.

5.5.6 MWC 480

The disk integrated HCO^+ $1-0$ line flux in MWC 480 is effectively constant during the MAPS observations (Figure 5.7). The line shape is a symmetric double horned peak and the emission remains constant in flux and shape on all observation days except 4/Sep/2019. On this day, the spectral shape becomes symmetrically singly peaked at the source velocity (5.1 km s^{-1}). The data from this day are noisier with a lower S/N (see Appendix D.2), therefore the single peak profile may be due to noise.

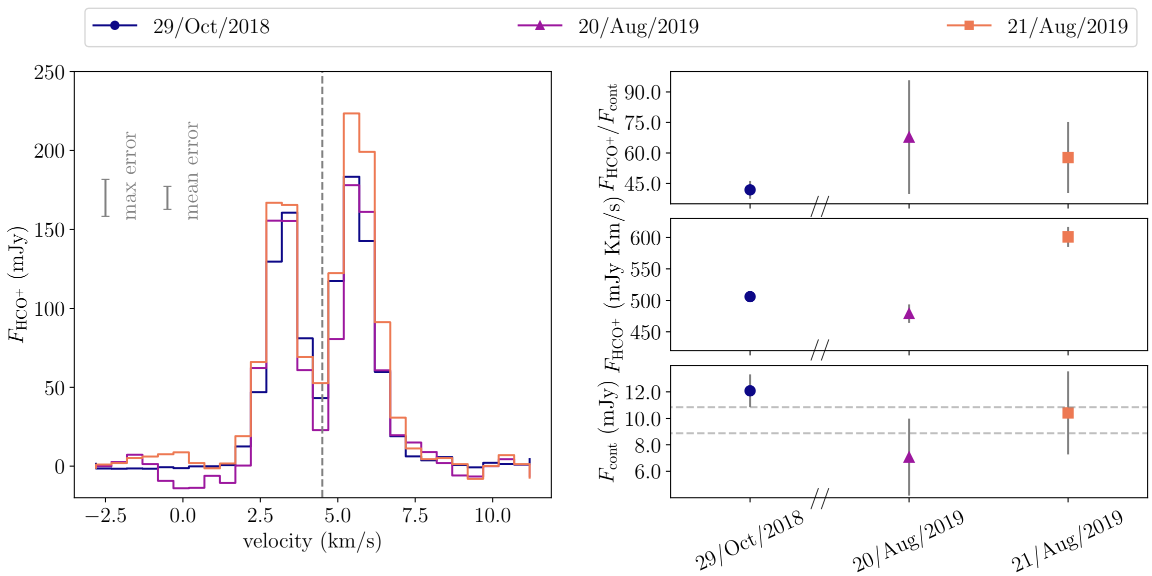

Figure 5.6 Same figure description as Figure 5.3, but for IM Lup.

There is also a small blue-shifted peak of emission at -2.4 km s^{-1} only seen on 4/Sep/2019. The emission is present across two channels and has a peak significance of $\sim 5\sigma$ in disk-integrated line flux. Interestingly, a blue-shifted peak was also seen in earlier observations of HCO^+ $3-2$ as a part of the Disk Imaging Survey of Chemistry with SMA (DISCS) survey (Öberg et al., 2010). At this time the origin of this tentative enhancement in emission at -2.4 km s^{-1} is unclear, although it could be due to a jet (Grady et al., 2010) or other similar phenomena.

5.6 Discussion

This work was motivated by models (Waggoner & Cleeves, 2019, 2022) and observations (Cleeves et al., 2017) that suggest flare driven variable X-ray ionization rates result in variable gas-phase cation abundances. In each of the five MAPS disks, some degree of spectral variation was seen in their HCO^+ $1-0$ emission. However, generally the variations were small ($\lesssim 3\sigma$), and occurred within discrete parts of the

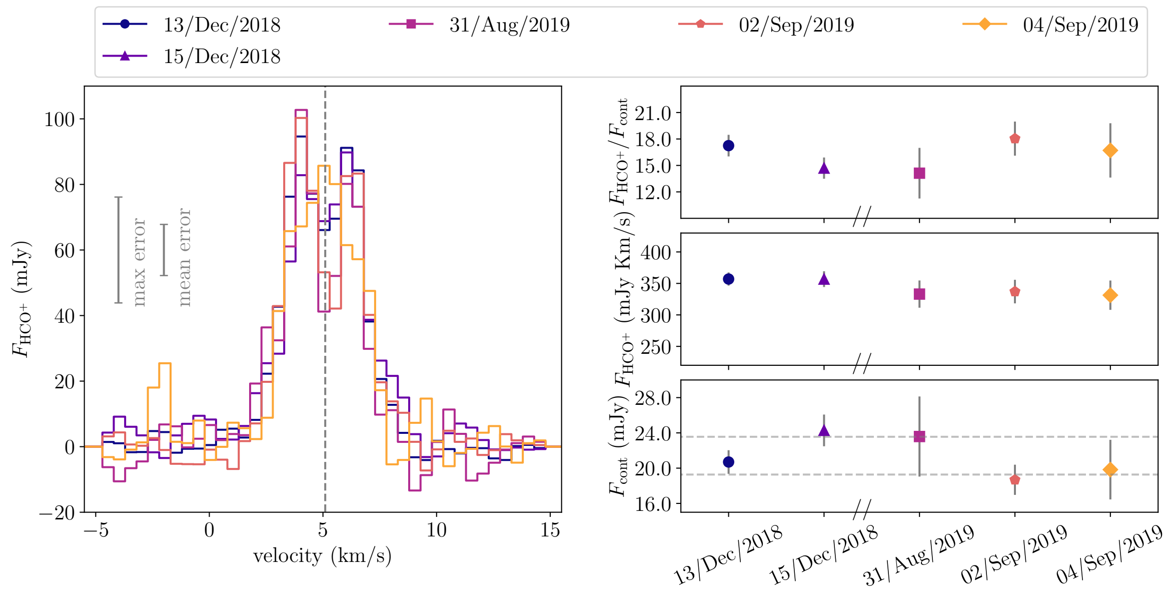

Figure 5.7 Same figure description as Figure 5.3, but for MWC 480.

spectrum rather than an overall increase in emission.

5.6.1 Possible Sources of Spectral Variability

The two most likely scenarios that could explain spectral variations seen in this work are as follows. First, observed changes in flux could be astrophysical, i.e., real variations in HCO^+ emission. Second, the changes in measured line emission could be non-astrophysical and instead introduced as a result of the observing and/or imaging process. In this section, we discuss the possibility of both scenarios, and the observational consequences of each scenario.

Possible Astrophysical Origins of Variability

In this discussion we classify possible variability sources, but it should be noted that ‘types’ of variability may not (and are likely not) exclusive to one another. In reality variability in astronomical sources is incredibly dynamic, where bursts, flares, and other similar phenomena occur across the electromagnetic spectrum and can even include cosmic rays. For example, accretion outbursts increase both UV ionization rates and temperature (Molyarova et al., 2018), and X-ray flares are often associated with coronal mass ejections (Benz & Güdel, 2010). Increased ionization rates driven by radiation are the most likely sources of the spectral changes we report.

X-ray flares are one possible source of variability in the HCO^+ spectra. Waggoner & Cleeves (2019, 2022) indicate that changes in abundance scale directly with flare strength, where larger flares result in a higher and longer increase in HCO^+ abundance than smaller flares. Relatively large X-ray flares (i.e., flares that increase the baseline X-ray luminosity by tens or hundreds) can increase the abundance of HCO^+ by factors of 2 or more. Relatively small flares, also known as nano- or micro-flares (i.e. flares that increase baseline X-ray luminosity by a factors of a few Pearce & Harrison, 1988; Feldman et al., 1997), result in a relatively small HCO^+ enhancement. Radiative transfer models are required to know precisely how flares of varying strengths impact the HCO^+ flux, so for the purpose of this discussion we assume that flux scales directly with HCO^+ abundance.

According to Waggoner & Cleeves (2022), if a relatively large X-ray flare had occurred a clear and distinguishable change would have been seen in the HCO^+ spectra. Previous observations of $H^{13}CO^+$ in the IM Lup protoplanetary disk support this, where the $H^{13}CO^+$ flux roughly doubled (28σ Cleeves et al., 2017) in one observation compared to two others. Since all instances of (tentative) variation seen in this work are relatively small ($< 3\sigma$) a strong flare is unlikely to be the source of variation. However, a relatively small flare, such as a nano- or micro-flare, would drive relatively small increases in the HCO^+ spectrum. Therefore, if the spectral changes reported in this work were caused by an X-ray flare, they are most likely to have been caused by a relatively small flare.

T Tauri stars, such as AS 209, GM Aur, and IM Lup are known to be X-ray bright and variable (Güdel et al., 2003), thus suggesting that, if the fluctuations are true changes in HCO^+ emission, they are most likely to be caused by X-rays. Herbig stars, such as MWC 480 and HD 163296 have bright photospheric UV emission, thus the chemistry of these disks may be more sensitive to the stellar UV radiation field, and any associated variations (such as accretion or jet variability, Mendigutía et al., 2013; Francis et al., 2020; Rich et al., 2020). Unfortunately, with low degrees of observed variability and without concurrent X-ray or UV observations we are unable to directly confirm the origin of the observed spectral variations.

Variations in the observed line emission could also be caused by changes in disk temperature instead of a change in molecular abundance. However, we find that the disk temperature - at least that in the mid-plane - remains constant to within the flux and RMS error, as indicated by the continuum measurements. Additionally, if there was a change in disk temperature the spectra would be universally and symmetrically scaled (assuming the flare uniformally impacts the disk, e.g. Favata et al., 2005) and the majority of variations in this work were found to occur asymmetrically on a channel by channel basis. Assuming that the HCO^+ $1-0$ gas and continuum trace the same temperature regime, then spectral variations would most likely be due to changes in HCO^+ abundance, rather than temperature.

Possible non-Astrophysical Origins of Variability

Alternatively, the observed changes can be a product of how the disks were observed. Some examples include the following. *a)* By splitting out data on an day-to-day basis, the data is naturally noisier than the final time integrated image. Lower signal to noise, as is the case in the MWC 480 spectra, makes assessing low level variability challenging.

b) We minimized the effect of baseline coverage as much as possible (see Sections

5.4.3 and Appendix D.1); however, baseline effects cannot be ruled out for HD 163296, the shift in AS 209 emission peak, or in IM Lup, since these instances of variability occurred when ALMA was in a compact configuration. Our flux recovery tests indicate that the variability in IM Lup was likely caused by spatial filtering, but HD 163296 and AS 209 variability likely has a different source.

c) Flux calibrators are ideally considered to be constant on observationally relevant time scales, but this is not always the case. In reality, minor changes in flux calibrator luminosity do occur. If a flux calibrator varied in brightness, a symmetric and uniform change would be introduced in the HCO^+ spectra and continuum. The variations reported here are asymmetric and non-uniform (except HD 163296). Therefore, we find that the changes in flux calibrator are an unlikely source of variability. For a complete list of flux calibrators used in this work, see Öberg et al. (2021).

5.6.2 Tentative First Detection of Spatial Variability in Disks

AS 209 and GM Aur are the first protoplanetary disks with potential spatial variability, as indicated by a shift in the spectral peak and variations in the line wings of the spectra. The physical origin of the peak shifts and fluctuations in spectral wings (if real) cannot be confirmed due to the timing and limit of observation windows, but a reasonable explanation is that the shift was caused by an X-ray flare propagating through the disk. This discussion assumes an enhancement of HCO^+ immediately (within minutes) traces the flare, as indicated by Waggoner & Cleeves (2022).

Light produced by large X-ray flares (i.e., a flare that increases the characteristic luminosity by $> 10\times$) will symmetrically propagate through the disk (due to the large size of the X-ray emitting region compared to the physical size of the star, e.g. Favata et al., 2005). If a disk were to be observed immediately after a flare occurs, i.e., after the flare hits the inner disk but has not yet reached the outer disk (hours after the flare), then an increase in inner disk HCO^+ emission would be seen. This effect would primarily be seen in the high velocity spectral wings, as seen on 03/Sep/2019 for AS 209 and on 31/Aug/2019 for GM Aur.

If the disk were to be re-observed after the flare has propagated through the entire disk (over a timescale longer than the light crossing time, ∼days), then a uniform increase in the spectrum would be seen. A uniform enhancement occurred for HCO^+ in HD 163296 in this work and $H^{13}CO^+$ in IM Lup in Cleeves et al. (2017), suggesting that these observations occurred several days after the flare occurred.

After the flare has propagated through the entire disk, inner disk HCO^+ molecules will rapidly dissociate via electron recombination to H and CO, while the outer disk HCO^+ abundance remains enhanced for a longer period due to a lower level of free electrons. If HCO^+ rotational emission were observed during this time, the spectrum closer to the source velocity, including the peaks, would be enhanced while the wings would be quiescent. The spectra observed on 26/Oct/2018 for AS 209 and on 02/Sep/2019 for GM Aur are consistent with this interpretation. How flares change the chemistry as a function of radius and time is described further in Waggoner & Cleeves (2022), who report the same phenomena in models of HCO^+ column density throughout a flaring event (see Figure 7 in Waggoner & Cleeves, 2022).

Large X-ray flares originating within extended stellar coronae are expected to uniformly illuminate the disk, changing the HCO^+ abundance across the entire azimuthal range. But this is not consistent with the type of variations seen in AS 209 and GM Aur. Since only half of the AS 209 spectrum is visible due to cloud obstruction, we are unable to determine if the spectral changes were indeed spectrally (and spatially) symmetric. Future observations targeting warmer HCO^+ lines, which are expected to be less impacted by foreground absorption, are necessary to explore symmetric variations, as shown by Öberg et al. (2011) and Huang et al. (2017). GM Aur has a known ^{12}CO spiral structure (Huang et al., 2021). When a flare occurs in this system, X-ray light would still uniformly propagate outward. Instead of uniformly impacting the disk and enhancing HCO^+, the flare could first impact the closest arm, thus causing an asymmetric increase in the HCO^+ spectrum. This cannot be confirmed without additional chemical modeling including 3D structure; however, both cases where $F_{\mathrm{HCO^+}}$ increased in GM Aur only occurred in the red-shifted portion of the spectrum.

5.6.3 Tentative First Detection of Variability in a Herbig System

We report the first tentative detection of HCO^+ variability in a Herbig protoplanetary disk system, HD 163296. Unfortunately, the peak HCO^+ emission occurred during the first observation window, and the following observation windows did not occur until a year later. If HD 163296's enhancement was real, the duration and behavior are unknown since it was not re-observed for 9 months. Thus it is challenging to determine the exact cause of HCO^+ variability in this source. While the source of variability could be an X-ray flare, it is also possible that a fluctuation of UV radiation could have led to the higher HCO^+ emission observed in October 2018.

Fluctuations in UV flux may be a more likely origin than X-rays in HD 163296, as Herbig stars are more massive and hotter than solar mass T Tauri stars. Stellar spectrum for Herbig star emission peaks in the UV range, resulting in much lower relative contributions from X-ray emission than T Tauri stars. Therefore, Herbig disk ionization may instead be driven by a variable UV flux. Since HCO^+ is sensitive to disk ionization rates, which is connected to both UV and X-ray flux (e.g. Seifert et al., 2021), it is impossible to determine the exact origin of variability in HD 163296 without further multi-wavelength monitoring observations.

5.6.4 Comparison to X-ray Flare Models

How does the degree of HCO^+ variability compare with that predicted by chemical models including X-ray flares? Of the five sources observed by MAPS, none showed strong variability at the level previously seen in IM Lup as reported in Cleeves et al. (2017). X-ray flares are known to occur on a regular basis (varying by factors of 4 to 10 about once a week for T Tauri stars, Wolk et al., 2005). Stronger flares are rarer; they occur only every few months (varying by factors greater than 10.)

We can compare this lack of strong chemical variability with disk models reported in Waggoner & Cleeves (2022). Based on the typical uncertainty in the measured disk integrated flux, a minimum change of *at least* 100% in disk integrated $F_{\mathrm{HCO^+}}$ is required to confidently detect enhancement ($> 3\sigma$). A smaller change may be detectable in a disk with a higher signal to noise ratio, but this discussion uses the typical flux and uncertainties in this work. Flare models predict a 2.2% chance of observing the disk-integrated HCO^+ enhanced by a factor of at least 100% when observed one time on any given day. Each of the MAPS disks was observed between 3 and 6 times, so we can estimate the probability that they are observed to be enhanced during at least one of these observations.

In total, 24 separate observations were executed. If this entire data set is considered, then there is a 41% chance of observing clear and distinguishable variability. If Herbig (observed 11 times) and T Tauri systems (observed 13 times) are considered separately, then there is only 22% and 25% chance of observing enhancement, respectively. For the HD 163296 disk (observed six times), there was a 12.5% chance of observing HCO^+ to be enhanced by 100% or greater at least one time. For the disks observed five times, AS 209, GM Aur, or MWC 480, there was a 10.5% chance of observing them with elevated HCO^+. Finally, IM Lup was only observed three times, thus 6.5% chance of observing variability in IM Lup.

Note that the theoretical probabilities discussed here are likely an overestimate of the chance of detecting a flare, since many of the MAPS observations occurred within several days with each other, while the modeled statistics are derived from a 500 year window and assume observations are independent. This discussion also assumes HCO^+ emission increases linearly with an increase in abundance, which is only true if the line is optically thin and the emitting conditions are constant. Additionally, these statistics are true for X-ray flares produced by T Tauri stars, and the probability of observing X-ray or UV driven variability in a Herbig star is likely different.

5.7 Conclusions

Fluctuations in ionization, such as an X-ray flaring event, have been shown to temporarily increase the abundance of gas-phase cations, which results in time variable emission. In this work we searched for variability in HCO^+ $J=1-0$ in the HD 163296, AS 209, GM Aur, MWC 480, and IM Lup protoplanetary disks using data from the MAPS ALMA Large Program. While disk integrated F_{HCO^+} remained constant within the uncertainty across all observations, low level spectral variability was seen in all five disks.

- AS 209: On 26/Oct/2018 the HCO^+ spectral peak is increased and shifted blueward toward the source velocity. While this particular shift could be impacted by baseline coverage, there is also variation in the spectral wings and an increase in blue shifted emission is also seen on 03/Sep/2019.

- GM Aur: There is an asymmetric increase in peak emission on 02/Sep/2019, and enhancement in the red-shifted wing is also seen on 31/Aug/2019. The asymmetric spectral shifts may be due to disk structural asymmetry, as GM Aur has spiral arms in ^{12}CO gas emission.

- HD 163296: The spectral peaks are slightly enhanced on 22/Oct/2018 compared to later observations. While this could be due to an increase in ionization rates, this fluctuation could also be due to varying baseline coverage.

- IM Lup: There is an asymmetric increase in emission for the red shifted peak on 21/Aug/2019, but this same phenomena occurs in data simulated using `vis_sample`. Therefore, the spectral variation in IM Lup is most likely introduced by differences in baseline coverage between observations.

- MWC 480: There is a change in spectral shape on 04/Sep/2019, where the spectrum has a single peak compared to two peaks on the other observation days. However, the change in shape can be attributed to higher levels of noise and is not conclusively astrophysical.

Our observations are consistent with the theory that a temporary increase in high energy stellar emission can drive changes in the abundance and flux of gas-phase cations in planet-forming disks (Waggoner & Cleeves, 2022).

Additionally, we show that substantial serendipitous fluctuations in disk-integrated flux as was seen in IM Lup (Cleeves et al., 2017) are rare. In order to confidently detect flare driven chemistry and constrain spectral variation, a dedicated time domain campaign, optimizing high S/N, is required. A designated time domain observing program is necessary to measure variable gas-phase cation emission. Such a program will be scientifically useful, as it could result in measurements of electron abundances and information about magnetic fields, magnetorotational instability (MRI), and disk accretion (e.g. Balbus & Hawley, 1991; Glassgold et al., 1997; Ilgner & Nelson, 2006b).

5.8 Chapter Acknowledgements

We thank the anonymous referees for their insightful comments on this work. We thank the entire MAPS collaboration for all the hard work that went into data collection and reduction. This paper makes use of the following ALMA data: ADS/JAO.ALMA#2018.1.01055.L. ALMA is a partnership of ESO (representing its member states), NSF (USA) and NINS (Japan), together with NRC (Canada), MOST and ASIAA (Taiwan), and KASI (Republic of Korea), in cooperation with the Republic of Chile. The Joint ALMA Observatory is operated by ESO, AUI/NRAO and NAOJ. The National Radio Astronomy Observatory is a facility of the National Science Foundation operated under cooperative agreement by Associated Universities, Inc. A.R.W. acknowledges support from the Virginia Space Grant Consortium and the National Science Foundation Graduate Research Fellowship Program under grant No. 1842490. Any opinions, findings, and conclusions or recommendations expressed in this material are those of the author(s)and do not necessarily reflect the views of the National Science Foundation. Support for F.L. was provided by NASA through the NASA Hubble Fellowship grant #HST-HF2-51512.001-A awarded by the Space Telescope Science Institute, which is operated by the Association of Universities for Research in Astronomy, Incorporated, under NASA contract NAS5-26555. Y.A. acknowledges support by NAOJ ALMA Scientific Research Grant code 2019-13B and Grant-in-Aid for Transformative Research Areas 20H05847. L.I.C. acknowledges support from the David and Lucille Packard Foundation, Research Corporation for Science Advancement, NASA ATP 80NSSC20K0529, and NSF grant no. AST-2205698. K.I.Ö. acknowledges support from the Simons Foundation (SCOL #321183), an award from the Simons Foundation (#321183FY19), and an NSF AAG Grant (#1907653).

Chapter 6

Improving Undergraduate Astronomy Students' Skills with Research Literature via Accessible Summaries

"The purpose of a storyteller is not to tell you how to think, but to give you questions to think upon."

Brandon Sanderson, *The Way of Kings*

6.1 Abstract

This chapter is a part of collaborative study with Astrobites. This work is currently in peer review with Physical Review Physics Education Research. As a Co-PI I am second author on this paper, and Briley Lewis (Co-PI) is the first author. My primary role in this project was data collection, anonymization, and organization, but I was also an active member in the data analysis and writing.

Abstract: Undergraduate physics and astronomy students are expected to engage with scientific literature as they begin their research careers, but reading comprehension skills are rarely explicitly taught in major courses. We seek to determine the efficacy of lesson plans designed to improve undergraduate astronomy (or related) majors' perceived ability to engage with research literature by using accessible summaries of current research written by experts in the field. During the 2022-2023 academic year, twelve faculty members incorporated lesson plans using accessible summaries from Astrobites into their undergraduate astronomy major courses, surveyed their students before and after the activities, and participated in follow-up interviews with our research team. Quantitative and qualitative survey data clearly show that students' perceptions of their abilities with jargon, identifying main takeaways of a paper, conceptual understanding of physics and astronomy, and communicating scientific results all improved with use of the tested lesson plans. Additionally, students show evidence of increased confidence of their abilities within astronomy after exposure to these lessons, and instructors valued a ready-to-use resource to incorporate reading comprehension in their pedagogy. This case study with Astrobites-based lesson plans suggests that incorporating current research in the undergraduate classroom through accessible literature summaries may increase students' confidence and ability to engage with research literature, as well as their preparation for participation in research

and applied careers.

6.2 Introduction

Research experience is an integral part of modern STEM undergraduate education, especially for students who plan to continue on to graduate study in the field, and undergraduates are often highly encouraged to get involved in research early in their careers. Exposure to research during undergraduate education also provides a number of benefits, including helping students build research skills, providing a basis for career planning, and encouraging students to develop scientific mindsets (Seymour et al., 2004). Exposure to current research in the classroom is also known to have a positive impact on undergraduate learning experiences, as current literature directly shows students what questions they can answer in their future studies and provides real-world motivation for course content (Donohue et al., 2021; Wooten et al., 2018). Recent work exploring Course Based Undergraduate Research Experiences (CUREs) in physics and astronomy further supports the positive benefits of including research in the classroom (Rector et al., 2019; Werth et al., 2022; Oliver et al., 2023; Werth et al., 2023; Hewitt et al., 2023).

However, scientific research requires the ability to comprehend the literature of a field, and jargon and niche topics used in scientific literature are often a significant barrier for budding scientists. This barrier can be particularly high for underrepresented students who may not have the support or experience needed to parse dense and jargon-heavy papers (Barthelemy et al., 2022; James et al., 2020; Kricorian, Katherine and Seu, Michelle, and Lopez, Daniel and Ureta, Elsie and Equils, Ozlem, 2020). Reading comprehension skills are also rarely explicitly taught in the higher education science classroom, despite the fact that research shows that interventions focused on discipline-based reading and writing skills are beneficial to students–for example, these interventions can empower students to better contextualize their work and engage in scientific discourse, making them more effective, culturally-aware, and well-rounded scientists (Duncan & Arthurs, 2012; Sørvik & Mork, 2015; Szymanski, 2014; Pelger & Nilsson, 2016; Lewis et al., 2022)–and correlate with success in STEM courses (Akbasli et al., 2016). The recent Phys21 report from the Joint Task Force on on Undergraduate Physics Programs from the American Physical Society, National Science Foundation, and American Association of Physics Teachers further emphasized the need for literature and communication skills as preparation for 21st century careers, and the lack of existing preparation for said skills; for example, they state, "Unless they write a senior thesis, undergraduates are also not often called upon to search the literature; read, analyze, evaluate, interpret, and cite technical articles; and make specific use of the scientific and engineering information therein, despite the fact that graduates are likely to be called upon to do so whether they pursue graduate study or enter the workforce" (Heron et al., 2019). Reading and writing skills may be neglected due to a number of reasons: lack of priority in an already content-packed curriculum (Williams, 2020), lack of awareness of current education research and methods (Van Schaik et al., 2018; Shkedi, 1998; Young et al., 2022), lack of preparation for teaching these skills (Adler-Kassner & Estrem, 2007), and a lack of time and resources to implement new lessons (Henderson & Dancy, 2007; Dancy & Henderson, 2010). Despite these challenges, there already exist natural opportunities to explicitly introduce reading and writing skills into physics and astronomy curricula, e.g. via lab courses and CUREs.

Some prior work on reading comprehension in the science classroom has been completed in physics, including the use of metacognition and question formulation for improving reading skills (Koch & Eckstein, 1991; Koch, 2001); however, this research is generally limited, hyper-focused on a specific reading strategy, and not involving authentic research literature. The available literature on reading comprehension in astronomy-specific courses is even more limited (e.g. one study on reading for introductory non-major courses (Garland & Ratay, 2007)), and the unique culture and demographic of each STEM sub-field prevents us from blindly extrapolating from the research of other disciplines, such as biology or chemistry where research comprehension has been more commonly studied with findings that support the importance of these skills (e.g. (Susiati et al., 2018).

However, teaching reading comprehension skills for research literature is only one way to tackle this problem; research literature can also be made more accessible via simplified summaries written by experts in the field (Kohler et al., 2018; Young et al., 2022). Accordingly, we propose that offering easy-to-implement, readily available plans featuring both reading comprehension skills and accessible summaries of recent literature will be beneficial to student skills and confidence with research literature, as well as the uptake of educators actually implementing these lesson plans. To this end, we have developed four astronomy-focused lesson plans to improve students' skills and confidence with research literature via hands-on experiences with scientific articles, The concept of using accessible summaries (specifically "science bites") articles for reading comprehension exercises in the classroom was originally presented in Sanders et al. (2012), and practical infrastructure, in the form of sample lesson plans, are provided in Sanders et al. (2017). Building from these works, this investigation aims to to gauge the efficacy of interventions focused on reading comprehension and communication skills involving simplified current literature summaries in achieving the following goal: improving student confidence with and comprehension of research literature.

We use lesson plans from the Astrobites website[1] as an example of such inter-

[1] astrobites.org

ventions, making this a case study from which further research can build to more generalizable conclusions. These lesson plans harness existing accessible summaries of research literature hosted on the well-known Astrobites platform supported by the American Astronomical Society. This website provides accessible daily summaries of recent research in the field intended for an undergraduate audience, as well as other professional development and education resources for astronomers. In this work, we distributed the aforementioned lesson plans and oversaw their incorporation into undergraduate astronomy courses during the 2022-2023 academic year. Although existing Astrobites resources can be adapted for a variety of educational levels, this study focuses on the applications of these lesson plans to undergraduates who are enrolled in an astronomy or related major [2].

In Section 6.3, we describe the study population, further details on the lesson plans used, and the design of the surveys and other assessments used in this case study. In particular, we seek to evaluate the effects of the lessons on their perceived ability to engage with astronomy literature (particularly with respect to parsing jargon, understanding the main takeaways of a paper, their conceptual understanding/intuition, and their ability to communicate about science) and their perceptions of their broader ability and belonging in the field of astronomy. In Section 6.4, we discuss the effects of these lesson plans on students' perceived abilities, as well as instructor and student feedback on these lesson plans. Finally, in Section 6.5, we further explore the impacts of these lesson plans as shown in our results, and suggest future uses and investigations inspired by our findings.

[2]Related majors include physics, astrophysics, biology, math, geology, engineering, chemistry, computer science, planetary science, and undeclared majors

6.3 Methods

6.3.1 Lesson Plans

The Astrobites lesson plans can be summarized as follows:

1. **Periodic Reading Assignments:** Students are assigned Astrobites articles and an associated list of guided questions which evaluate their conceptual understanding and reading comprehension.

2. **Student Research Project:** Students use Astrobites articles to carry out a research project (delivered as a paper and/or presentation) on an astronomy topic of their choice.

3. **Student Writing Assignment:** Students select a research paper and write an Astrobites-like article summarizing the context, content, and key conclusions.

4. **Student Presentation:** Students deliver an in-class presentation based on an Astrobites interview post and paper by the interviewee.

Each lesson plan involves reading about current research topics, whether via an Astrobites article and/or original research literature. More detailed descriptions can be found in Appendix E.3, and further detail about Astrobites more generally is provided in Appendix E.1. Each participating instructor corresponded with the research team to implement one or more of the lesson plans of the instructor's choice in their classroom. All instructors were required to participate in a pre-intervention meeting to ensure knowledge of study protocols (including how to distribute student survey assessments) and a post-intervention meeting to gather information on their experience incorporating the lesson plans in their classes. Research team members only advised the instructor, answered questions and did not have any direct contact with the students themselves. Instructors notified the study team of any deviations from the lesson plan as provided. Some instructors were allowed to implement multiple lessons or repeat a lesson multiple times, although the analysis of "dosing effects" from exposure to multiple lessons is not included in this work.

6.3.2 Assessment Design & Study Population

Student surveys were administered by participating instructors before and after implementing their chosen lesson plan in the form of a Google Forms survey. The survey contained both Likert-scale quantitative questions and open-ended written response questions, probing student perceptions of ability over six categories: parsing jargon, understanding main takeaways, conceptual understanding/intuition, science communication ability, broad ability within astronomy, and feelings of belonging within astronomy. Since the survey did not directly assess student ability, only their *perceptions* of their ability, we cannot make strong claims about changes in their actual abilities or skills, only their confidence. Post-intervention surveys also included direct questions about lesson plan itself. Student responses were not anonymous, but identifying information was only used to match pre- and post-survey responses and categorize students to their instructor to note the lesson plan they completed. Additionally, instructors participated in post-lesson interviews to gather qualitative information about the efficacy of the lesson plans and avenues for future improvements. All study protocols and assessments described within were approved by both UCLA and University of Virginia's Institutional Review Boards (UCLA IRB#22-001473 and UVA IRB#5514). Full text of the assessment questions is available in Appendix E.2.

202 students from 13 courses for astronomy-related majors taught by twelve faculty instructors across nine institutions participated in this study from Fall 2022 to

Winter and Spring 2023. Student participants were undergraduates with an intention to major in astronomy or a related subject, and were either taking the course featuring the Astrobites lesson plan for major or minor credit, or intending to pursue an astronomy-related career. Six of the host institutions (hosting eight of the courses) were R1 universities, while three were liberal arts colleges (hosting five of the courses).

Lesson Plan (LP) 1 was taught in eight courses; LP 2 in two courses; a combination of LPs 1 and 2 in one course; a combination of LPs 2 and 3 in one course; a combination of LPs 2, 3, and 4 in one course. Out of these 202 students, 82 responded to both the pre-lesson and post-lesson surveys; all instructors who completed their participation in the study confirmed distributing the surveys as we instructed, so we suspect the lower response rate in the post-lesson surveys, leading to the smaller sample size, is due to an increase in student responsibilities at the end of the school term when these were often administered. Of the 82 students who participated in both surveys, 51 were part of Lesson Plan 1, 7 students were in LP 2, and 16 students were in LP 4. A further 8 students had a combination of Lesson Plan 1 and 2. No students in both surveys were part of LP 3, neither on itself or in combination with other LPs.

The qualitative and quantitative data collection for this study took place in parallel. Students responded to both types of questions in a single survey. The investigation is a convergent mixed-methods study, wherein qualitative and quantitative data are analyzed separately and then synthesized to provide a broader view of the problem; as stated in Ponce & Pagán-Maldonado (2015), "The quantitative approach measures the objective aspects of the problem and the qualitative phase enters the subjective aspects of the problem or the experiences of the participants." A consistency analysis was also completed between the results of the qualitative and quantitative data collected, as described in Appendix E.6.

All questions, both qualitative and quantitative, were designed specifically for this study. Assessments were developed in collaboration with UCLA's Center for the Integration of Research, Teaching, and Learning (CIRTL), and drew on established assessments from education research literature as inspiration to create the surveys (Bartlett et al., 2018; Elby, 2001; Estrada et al., 2011; Espinosa et al., 2019). The assessments were pilot tested with astronomy graduate students, who likely have an experience level intermediate to the undergraduates experiencing the lessons and the instructors administering them, to ensure the question text was interpreted reliably and as expected (Litwin & Fink, 1995; Taherdoost, 2016).

6.3.3 Data Analysis

Quantitative Analysis

The data set for quantitative analysis consists of 82 complete pre- and post-survey responses to the 35 Likert-scale questions listed in Appendix E.2. We summarize the change in the responses to each question with the 95% confidence interval ('CI95%') for the mean of the pre-post survey differences in student responses. Using the statistics package `Pingouin` Vallat (2018), we perform a paired t-test for each question by pairing pre- and post-survey responses for individual students. For each question, the p-value was determined using the canonical significance threshold of 0.05 (Bakan, 1966). The effect size is measured by Cohen's d Cohen (1988), with values above $d = 0.5$ classified as 'moderate,' values around $d = 0.2$ as 'small', and smaller values as 'very small.' The Bayes factor in favor of the alternative hypothesis ('BF10') (e.g., Bartoš & Wagenmakers (2023)) is computed and describes how many times more likely the observed data are under the alternative hypothesis, 'H1': that student perceptions changed. The survey questions are designed to fit into six conceptual categories: jargon, main takeaways, conceptual, communication, ability, and belonging (Table 6.1). Each question in a category is designed to probe a similar underlying concept; Figure 6.1 shows the degree to which the questions are related to each other based on student responses. We also analyzed changes within these six categories; the same statistical analyses performed with responses to individual questions were applied to each of the conceptual categories. "Reversed" Likert scale questions were adjusted [3] by reversing the Likert scale for these responses prior to performing any group calculations. We also performed an analysis of second-order correlations, described in Appendix E.7.

Table 6.1 The numbers of questions included in each of the conceptual categories. The text of each question can be found in Section E.2.

Category	Question numbers in category
Jargon	1-5
Main Takeaways	6-11
Conceptual	12-18
Communication	19-24
Ability	25-29
Belonging	30-35

Qualitative Analysis

We explored student responses to open-ended survey questions regarding perception of ability (Questions 35 through 39, 41, and 44 in Appendix E.2) through reflexive thematic analysis (Clarke et al., 2015). Codes and sub-codes were determined inductively, based on the content of student responses. All responses were read before creating codes, and then responses were re-read several times to refine the initial set of themes/codes. After collective creation of a set of thematic categories by the study team (referred to herein as codes, and summarized in Table 6.2), five raters (authors

[3] For quantitative questions 2 and 5, low Likert scores (disagreement) represent *greater* confidence. This is the opposite of the majority of the questions, for which higher Likert scores indicate greater confidence.

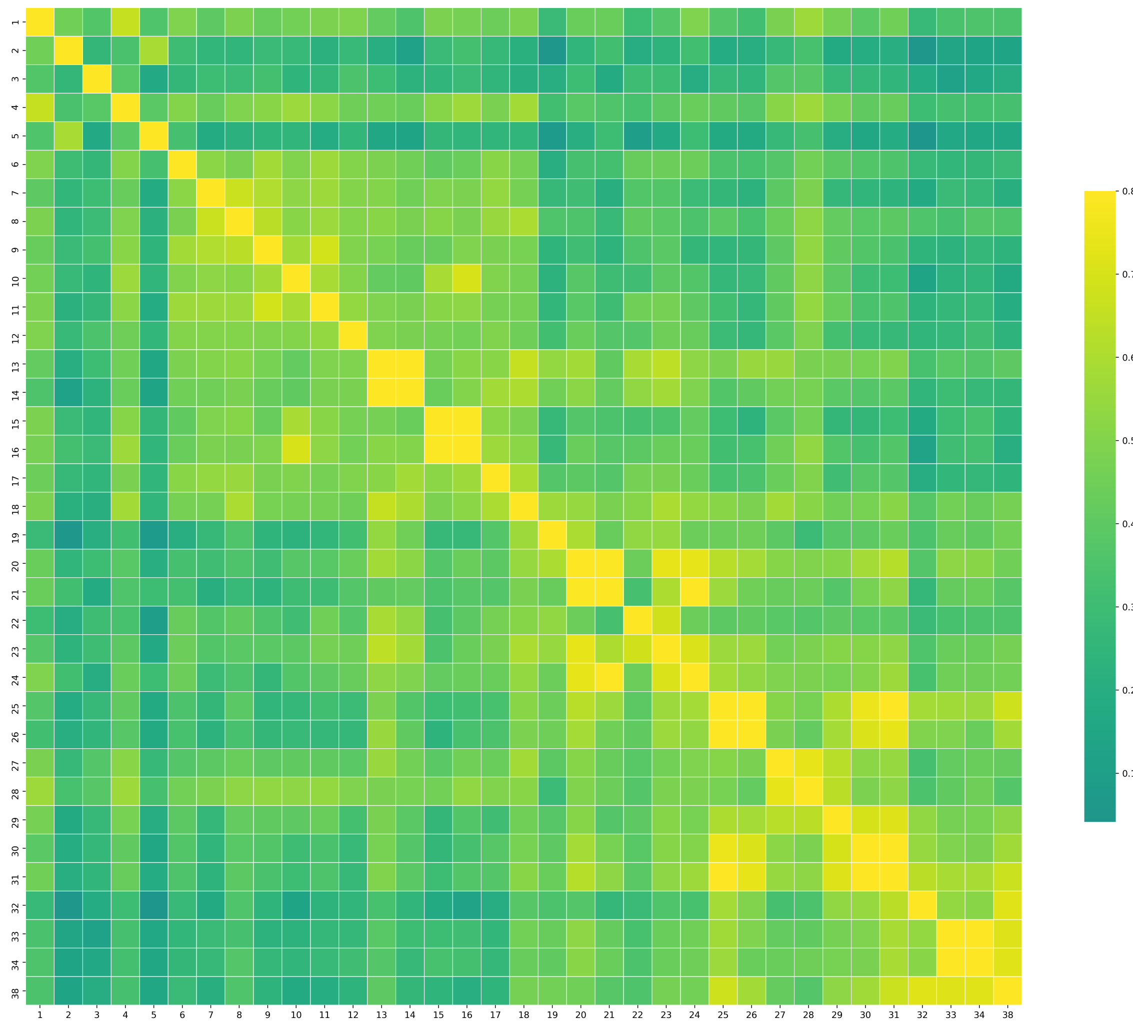

Figure 6.1 Correlation plot showing how survey items are related to each other; broadly, items in the same category appear to be more closely related. As described in Table 6.1, Questions 1-5 aim to probe ability with jargon, 6-11 for main takeaways, 12-18 for astronomy concepts, 19-24 for communication skills, 25-29 for perception of ability, and 30-35 for feelings of belonging.

BLL, GMD, SH, RL, and IM) independently assigned codes to each response. Codes applied by a majority of raters were included as the final set of identified codes for each response, essentially determining the interpretation of the response by consensus; codes applied by ≤ 2 raters were not included, which was relatively uncommon ($\leq 5\%$ of codes were rejected).

We do not compute inter-rater reliability scores here, instead following the philosophy that coding is a flexible and organic process that cannot be separated from the perspectives of the researchers themselves, and there is no single "accurate" coding of a qualitative data set (Yardley, 2015; Clarke et al., 2015). It is worth noting that some students left questions blank, or provided responses that were illegible or unable to be matched to a code. These responses have all been excluded from the analysis, and as a result, the number of respondents per question varies; this is accounted for by reporting percentages instead of raw counts. Responses to student survey feedback (Questions 40, 42, and 43 in Appendix E.2) and instructor interviews are read holistically instead of coded and their broad themes summarized in Section 6.4.2.

Qualitative response codes were tallied, and the percentage of responses in each main code category (e.g., not including sub-codes) was compared between pre- and post-lesson surveys. We report the percent change between pre- and post-lesson in each relevant category and the tallies of post-lesson responses in Section 6.4, Figures 6.3 and 6.4, respectively.

6.4 Results

6.4.1 Observed Changes in Student Attitudes

Summaries from the quantitative analysis are shown in Table 6.3 for the conceptual categories and Table 6.4 for selected individual questions displaying particularly

Table 6.2 Open-ended student survey questions probing perceptions of ability, belonging, and learning from the lesson plans, along with the codes used to categorize them by theme. Sub-codes are indicated with brackets and examples are given in parenthesis.

Survey Question	Codes
How do you feel about reading scientific research papers?	**Intimidation (Int)** (intimidated, daunting, overwhelmed, confused, not comfortable); **Require effort (E)** (time-consuming, tedious, read multiple times); **Worthwhile (W)** (rewarding, useful, necessary); **Unprepared (U)** (lacking knowledge, not taken enough classes, "not ready yet"); **Improved (Imp)** (e.g., "better now"); **Confidence (Co)** (comfortable, good, "like I can do it"); **Cause of feelings (C) [jargon (j), figures (f), writing style (s), audience (a)]**; **Enjoyment (En)** (interesting, fun, enjoy)
What comes to mind when you think of astronomy research?	**Topics (T)** (cosmology, astrobiology, stars, galaxies, exoplanets, etc.); **Perceptions of Research (P) [difficult (d), interesting (i), fun (f), tedious (t), requires preparation (p)** (professors, competence, education)], **Skills (S) [coding (c)** (computers, plotting, data analysis), **observation (o)** (telescopes, observing), **math (m)**, **reading papers (r)**, writing (w)], **Career desires (C)** (e.g. "want to be a part of it"), **Scientific process/discovery (D)**
Do you think you are capable of being an astronomer (or related scientist)? Why or why not?	**Yes (Y); No (N); Maybe (M)** (depends, yes and no); **Confident (C)** (good at it, previous or current experience, have what it takes, success in classes); **Insecure (I)** (no, maybe, unsure, grades, imposter syndrome, doubt); **Passion (P)** (life long interest, plans for graduate school); **Barriers (B) [learning disorder (d), mental health (h), minority (m)]**
Do you feel like you belong in astronomy? Why or why not?	**Yes (Y); No (N); Maybe (M); Motivation (Mo)** (motivation, passion, interest); **Experience (E)** (classes, research, academic success); **Community (C)** (welcoming, representation, role models, friends + peers); **Toxicity (T)** (toxic, unwelcoming, lack of representation); **Self-doubt (S)** (imposter syndrome, negative comparison to peers, don't feel smart, lack of academic success, feel overwhelmed)
What is your main takeaway from this activity?	**Astronomy knowledge (K)** (topics, interpreting plots, data); **Understanding of field (U)** (breadth of topics, better, how papers written, programming, statistics, visuals); **Confidence (C)** (boost, more capable, more confident, less daunting, more daunting, decreased); **Accessibility (A)** (more accessible, digestible, resources); **Motivation (M)**
How have your feelings about astronomy research changed as a result of this activity, if at all?	**Improved (I)** (more capable, less daunting, more confident); **Enjoyment (E)** (appreciation for sci. comm., more inspired to do astro., more excited to read papers); **Meta-knowledge of field (M)** [Resources (r) (e.g. better knowledge of resources available), **Options (o)** (better idea of possibilities), **Appreciation (a)** (appreciation for what goes into research)]; **No change (Nc)**

strong evidence for change: p-value < 0.05, the largest effect sizes (measured by Cohen's d), and moderate to extreme evidence for change (measured by BF10). Histograms and statistical summaries for all of the questions are shown in Figure E.1 and Table E.1 in Appendix E.5.

All questions but one showed positive mean of differences, indicating an increase in Likert score, corresponding to an average increase in perceived abilities between the pre- and post-surveys. The exception is Question 26, "I am capable of succeeding in my astronomy courses," which had a mean difference of zero and nonsignificant p-value. The histogram of pre- and post- responses for this question (Figure E.2) demonstrates that the majority of students perceived themselves as capable of succeeding in astronomy courses both before and after the intervention.

The analysis for the conceptual categories of questions, as summarized in Table 6.1 and provided in full in Section E.2, is shown in Table 6.3. Every category showed significant change from pre- to post-lesson. The effect sizes were small as measured by Cohen's d, but BF10 provided evidence in favor of change for all groups. Notably, there is extremely strong evidence for change in the groups perceived ability with jargon and main takeaways. There is strong or very strong evidence for perceived ability with conceptual understanding/intuition, perception of science communication ability, and perceived ability within astronomy. Evidence for changes in feelings of belonging within astronomy were only anecdotal. This lack of change in feelings of belonging may be related to Question 26, as described above.

Results from the qualitative coding are summarized in Figures 6.3 and 6.4. In response to the question "How do you feel about reading research papers?", responses citing intimidation lowered by 13.6%, unpreparedness by 6.8%, and enjoyment/fun increased by 6.8%. Additionally, 6.8% more responses described the importance of reading research papers. In response to "What comes to your mind when you think of

Table 6.3 Student perceptions for the groups of questions as described in Section 6.1. CI95% is the 95% confidence interval of the mean change, Cohen's d measures the effect size, and BF10 is the Bayes factor of the alternative hypothesis, as described in Section 6.3.3.

Group	p-value	CI95%	Cohen's d	BF10	BF10 interpretation	power
Jargon	8.64×10^{-5}	[0.12 0.34]	0.155	118	extreme	0.87874
Main Takeaways	5.42×10^{-7}	[0.16 0.37]	0.218	1.35×10^{4}	extreme	0.99799
Conceptual	1.40×10^{-4}	[0.09 0.27]	0.142	64.1	very strong	0.92311
Communication	7.72×10^{-4}	[0.07 0.25]	0.120	14.0	strong	0.75953
Ability	2.95×10^{-4}	[0.1 0.33]	0.163	37.3	very strong	0.91009
Belonging	5.37×10^{-3}	[0.04 0.25]	0.102	2.40	anecdotal	0.61747

Table 6.4 Selected questions with statistically significant p-values and moderate to extreme evidence for changes. CI95% is the 95% confidence interval of the mean change, p is the p-value, and BF10 is the Bayes factor of the alternative hypothesis as described in Section 6.3.3.

Question	CI95%	p ($\times 10^{-4}$)	Cohen's d	d interp.	BF10	BF10 interp. for H1	Text
1	[0.25 0.75]	1.27	0.456	small	158	extreme	I am able to define technical terminology that appears in scientific literature.
4	[0.09 0.55]	78.2	0.259	small	3.83	moderate	I am able to understand the technical details of a scientific study.
6	[0.3 0.79]	0.256	0.428	small	698	extreme	After reading a paper, I can summarize it well to a classmate in a science course.
24	[0.22 0.71]	3.51	0.324	small	62.1	very strong	I can explain astronomy concepts to my science instructors.
28	[0.18 0.72]	14.5	0.347	small	17.2	strong	I am able to use scientific literature to guide my studies in astronomy.

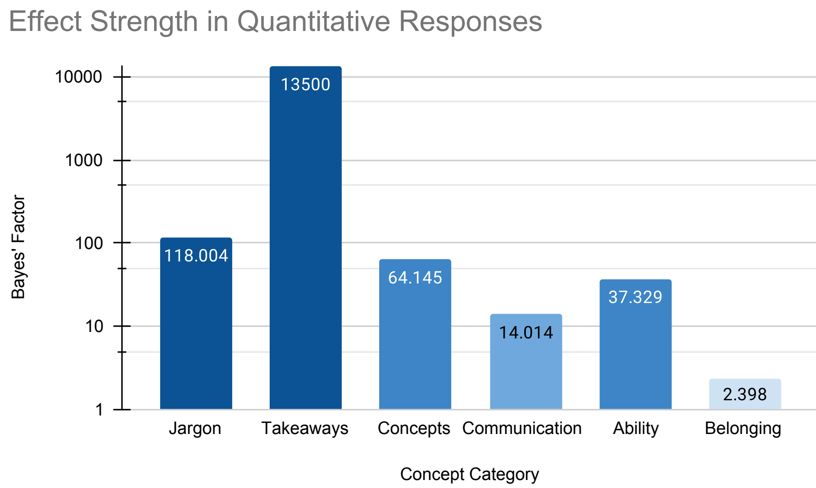

Figure 6.2 Visualization of effect strength across the six categories of concepts probed in the survey assessment, as presented in Table 6.3. Effects are colored by their "strength" of the Bayes' Factor interpretation, from anecdotal (lightest blue) to extreme (darkest blue).

research?", all categories show small or no change; students overwhelmingly responded with the topics and skills needed (e.g., coding, observing/telescopes, math, etc.) more than their feelings about it. In response to "Do you think you are capable of being an astronomer?", responses coded as confident were reduced by 6.5%, but responses coded as insecure were also reduced by ∼11%. Other codes for this question only show small change, if any. In response to "Do you feel like you belong? Why or why not?", yes responses slightly increased while no slightly decreased, and maybe responses increased by 4%. Responses citing motivation, experience, and community decreased by ∼4-5%, while self-doubt also decreased by 2%. All codes for this question show small change, and such minute differences should be interpreted with caution.

Two questions were available on the post-lesson survey only. For the question "What is your main takeaway?", 44% of responses described an increased understanding of the field, 25% described an understanding of accessibility (e.g., resources, science communication), 23% claimed increased confidence, 15% described furthering their knowledge of astronomy, and a small number reported increased motivation or decreased confidence. In response to "How have your feelings changed?", 50% of responses described no change, 27% said their feelings were "improved" in one way or another, 12% cited further enjoyment (e.g., appreciation for science communication, more inspired to do astronomy, more excited to read papers), and 11% described increased meta-knowledge of the field (e.g., how to find resources, appreciation for the work involved, career options). Our consistency analysis, described in detail in Appendix E.6, shows that open-ended responses tend to track Likert scores for each question; however, the Spearman correlation coefficient is smaller in the post-survey than in the pre-survey. When looking at the changes in individual students, students with initially low scores generally improved, students with initially medium scores generally showed no change or a slight benefit, and students with initially high scores generally stayed the same, but a small number decreased, as summarized in the Sankey diagram in Figure 6.5.

6.4.2 Direct Feedback on Lesson Plans

Both students and instructors were asked to provide direct feedback on the lesson plans, including their enjoyment, what they found most useful, and what they found most confusing. Below is a summary of their responses on the lesson plans.

Students had an overwhelmingly positive sentiment towards the lesson plans when asked, "Did you enjoy this activity with Astrobites?". 103/119 (86.6%) said they enjoyed the lessons, with 12/119 (10%) indifferent and 4/119 not enjoying (3.4%). (Note: for direct feedback, we included responses from students who did not take the pre-lesson survey, making the sample size 119 instead of the 82 for analysis of pre-post pairs.) The four who did *not* enjoy the activity cited an instructor's addition

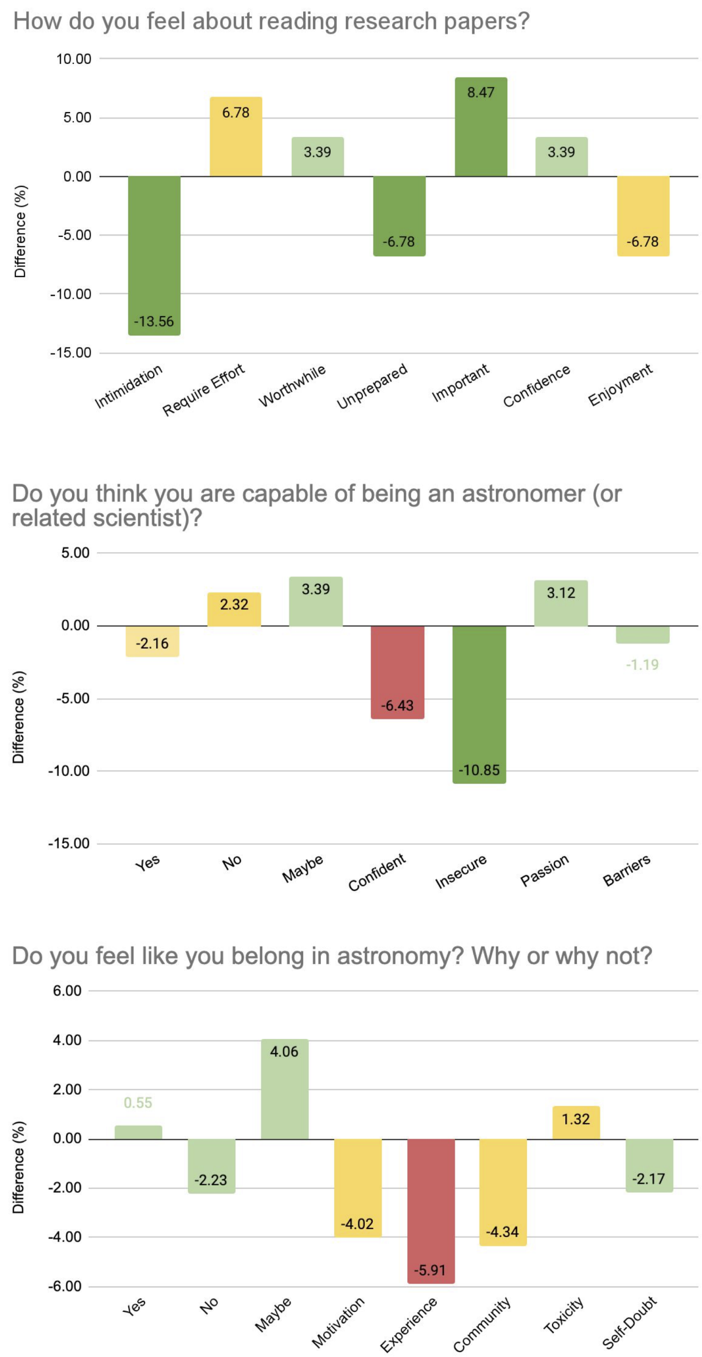

Figure 6.3 Percent changes in number of responses coded as each thematic category between students' pre- and post-lesson survey responses. Changes that match our expected learning outcomes are colored in green, that require further investigation are in yellow, and that contradict our expected learning goals in red. See Table 6.2 for a full description of code categories.

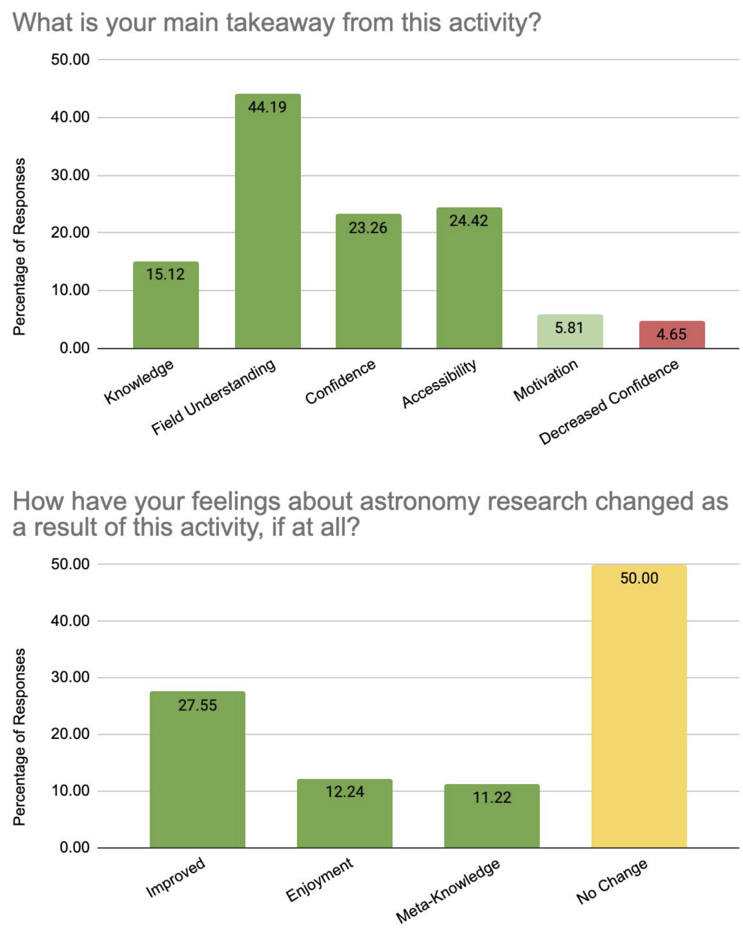

Figure 6.4 Student responses to post-survey only questions by percent in each coded category. Changes that match our expected learning goals are colored in green, that require further investigation are in yellow, and that contradict our expected learning goals in red. See Table 6.2 for a full description of code categories.

to the lesson, personal preference to not read long articles, the lesson plans not being challenging enough, or wanting more freedom to choose which paper they read (versus one assigned by their instructor).

Students found the lessons useful because of the real-world applications of the assignment, increased engagement and discussion in class facilitated by the activities, the opportunity to practice science writing and communication, and the opportunity to get a better sense of career options and role models in the field, as expressed in the below quotes from student responses. The most common response regarding usefulness, though, was the exposure to research literature and practice reading papers provided by the lesson plans; five students explicitly cited Astrobites itself as a useful resource they're glad to have learned about. Finally, one student encapsulated their main takeaways as follows, going into detail on how this lesson plan benefited them:

> "The main takeaway from this activity if that when you take things step by step, they aren't as daunting as they seem. Learning about the scientist, then a major concept they are involved with, and lastly a paper they partook in was surprisingly easy to understand. I feel accomplished for my understanding of all this new material in less then two weeks and I feel like this information will stick with me for the long run."

When asked what was most confusing about the lesson plans, students overwhelmingly cited plots and jargon from the papers–exactly what we'd expect for students just learning how to engage with scientific literature, as quoted below. Students did not provide any actionable feedback on the lesson plan itself.

> "The scholarly article was the most difficult and confusing, but I am really glad I overcame that and learned what all of that research had offered me. Amazing."

All instructors said the lesson plan was well-received in their class, and mentioned the following benefits of the lesson plans (with illustrative quotes below): helping to get students reading papers, exposing them to what kind of research exists in the field, increased engagement in class, increases in student confidence, awareness of Astrobites as a resource, and a change of pace from a normal routine (e.g., problem sets).

Instructors nearly unanimously stated the most useful aspect of the lesson plan was simply that it exists; structured/pre-made lesson plans connecting to current research that can be easily slotted into a course are an extremely beneficial resource for already over-committed educators. The resource of Astrobites in particular, as described by one educator, enables connections to literature that may not be possible otherwise for an introductory course:

> "With an Astrobites post, it's been since simplified enough that we can cover it in one class, but they still get a lot of the same benefits they get from working directly with the article."

Instructors additionally provided helpful feedback and suggestions for improvement, which we will take under consideration next time we revise the lesson plan resources. These improvements include: incorporating "classic" (e.g., foundational or historical) papers for their pedagogical value and fundamental roles in the field, adding a structured option to do Lesson Plan 1 (readings) as a recurring activity, and adding a reflection component for the presentations (e.g., "What made you choose this scientist?"). One instructor also requested a forum for sharing Astrobites lesson plans and resources between instructors, which we hope to implement on our website in the near future. Additional illustrative quotes from responses are available in Appendix E.4.

6.5 Discussion

Both students and educators expressed positive feelings towards the Astrobites lesson plans in their direct feedback, and our data show positive change in all major categories probed by the quantitative survey questions (see Tables 6.1), as summarized in Section 6.4.1. The strongest effect sizes were measured for ability with jargon and main takeaways. The majority of students participating in the study experienced Lesson Plan 1 (Reading Assignments), where the learning goals are expressly focused on reading comprehension and jargon. When broken down by lesson plan, the data clearly show that the group experiencing Lesson Plan 1–which had the most participants, and directly focused on reading comprehension skills–was driving the extreme evidence for improvement with main takeaways. Additionally, qualitative responses such as "I generally find it interesting, especially now that I have a base of knowledge to understand the key concepts" and "usually is a daunting task but Astrobites makes it manageable" highlight the usefulness of these lesson plans and the accessible summaries for students' literature-reading skills.

The amount of students whose scores began and remained high (as shown in Figure 6.5) highlights a limitation in our analysis: students whose initial responses lay to one extreme or another (the "floor and ceiling effects" (Wang et al., 2008)), i.e., students whose initial averages in a category were close to 1 or 7. A student with an initial average of 2 could not exhibit a decrease of more than -1 after experiencing the lesson plans, while a student with an initial average of 6 could not exhibit an increase of more than 1. It is also possible that the use of Astrobites may have confused initially high-scoring students, leading to the small number of decreases in scores, suggesting that the existing Astrobites lesson plans may be good for introducing students to a topic but less effective for delving into it further. Alternatively, it is important to

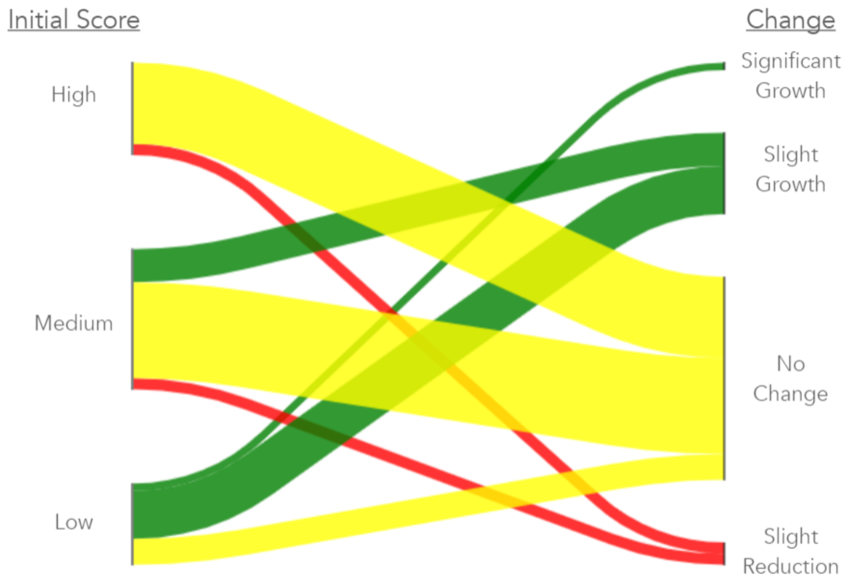

Figure 6.5 A Sankey diagram showing how the scores of students in each range of pre-activity scores changed over the course of the study. This diagram maps the flow of scores for the "understanding" category. "Low" corresponds to a range of 1 to 5, "medium" to a range of 5 to 6, and "high" to a range of 6 to 7. The changes correspond to the following intervals (measured as average score post-activity minus average score pre-activity): significant reduction – (-7, -2); slight reduction – (-2, -0.5); no change – (-0.5, 0.5); slight growth – (0.5, 2); significant growth – (2, 7). The width of the bars represents the number of students in that flow.

note we only completed the treatment once, and it make take repeated exposures (i.e. more practice with the lesson plans) for benefits to be realized.

Qualitative responses from students showed a more mixed and nuanced view of their development from before to after experiencing the lesson plans. Feelings of belonging were largely improved in the qualitative responses, although their reasons for their responses varied unpredictably. In response to questions about feelings while reading research, students less often mentioned feelings of intimidation and unpreparedness after the lesson, while mentioning more often that papers feel important/worthwhile and they are confident in their abilities. However, they also more often cited papers as requiring effort, and less often as enjoyable after the lesson; we interpret this as students having a more realistic understanding of the task at hand, for better or worse, while also being better equipped to handle it. Similarly, students reported fewer feelings of insecurity when asked about their ability to be a scientist, but also fewer feelings of confidence. Decreases in confidence may also be attributed to the fact that students' "measuring stick" for themselves has changed since the beginning of the course, as they have gained knowledge and practice (Hiebert et al., 2012; Kanevsky, 2016).

For a majority of students, as shown in Figure 6.4, the main takeaway from the lesson was a greater understanding of the field of astronomy, e.g. how research works, what scientists do, how research publications come to be. Nearly all students' takeaways were positive and in line with the learning objectives from the lesson plans, including increased content knowledge, increased confidence with course material, and a greater awareness of resources and the need for accessibility in science. Although 50% of students claim their feelings about astronomy have not changed as a result of the activity, those who do claim to have changed are remarkably all positive in some way.

Students were generally consistent in their qualitative and quantitative responses for the pre-survey, but this is not the case in the post-survey. We argue that the greater nuance available in written responses meant that students were more likely to express a mix of positive and negative feelings — with our qualitative scoring model for consistency analysis, this could translate to more neutral or negative scores, even if their overall feelings (as reflected through a collection of Likert scale questions) showed positive change.

Additionally, students and instructors were largely consistent in their feedback – instructors reported feeling that their students had gained understanding and perspective from the lessons, and most students reported either improved or reinforced senses of belonging and understanding in astronomy. Feedback also supported that our lesson plans were addressing their intended learning goals, which vary slightly across the four available activities; from post-implementation interviews with the instructors, those who used Lesson Plan 1 (reading assignments) commented more on the usefulness of exposing students to literature, while those who used Lesson Plan 4 (presentations from Astrobites interviews) commented about belonging, diverse role models, and career options.

6.6 Conclusions and Recommendations

Overall, our results show that the Astrobites lesson plans were largely successful at their main goal–increasing student comfort and ability with research literature–plus other beneficial effects, such as increasing student knowledge about the field of astronomy and the process of research. In particular, our reading-intensive intervention (Lesson Plan 1) significantly improved student ability and confidence with parsing jargon and understanding the main takeaways of an article. Our results, therefore, also show strong evidence for the positive benefits of reading comprehension assignments featuring accessible summaries of current literature more generally; as such, we identify a recommendation for instructors to use such assignments and a need for further research work in this area to fully maximize the benefits and understand the mechanisms at play in student learning.

Open-ended responses from participants also indicate that the accessible summary was a key component of the lesson plans' success in increasing student confidence with literature; scaffolding steps have long been shown to improve student outcomes (Van de Pol et al., 2010), and our work indicates a similar phenomenon for the task of reading complex scientific articles. Scaffolding scientific research articles can often be difficult, as the available alternatives to cover the content (namely science journalism) often reduce the complexity to the point of being an entirely different, non-technical genre that likely cannot target the same skills of reading technical literature. Astrobites and similar efforts represent the creation of a third writing type in the field, the accessible summary, intended for beginner technical audiences such as the students in this study population. Our results indicate that this type of writing is strongly beneficial for students as they enter the realm of scientific research.

As the sample in this paper focused on reading research papers, however, there is still significant work to be done to explore how writing lessons (e.g. Lesson Plan 3) impact students in STEM classrooms; we envision this as complimentary work to the reading comprehension interventions we studied, especially as reading is the first step to writing (Barger, 2017). Additionally, as mentioned previously, it is yet unclear how students' gains will change with repeated exposure to these lessons, e.g., if the majority of change is in the first exposure or if they grow substantially with practice; future work will need to test these "dosing effects" to determine the optimal usage of these lessons.

Accessible summaries show significant promise for bridging the gap between students' entry points and the difficult task of reading scientific literature. Additionally, it is important to note that instructors were appreciative of the existence of pre-made resources to use=, as opposed to starting from scratch to incorporate reading in their courses; future efforts in this area should similarly work to provide instructors with usable lessons to encourage uptake of reading/writing-focused activities in astronomy courses. We strongly encourage further work on integrating reading comprehension exercises and research literature into the classroom, especially through accessible summaries as in the Astrobites lesson plan models shown herein to positively benefit students.

6.7 Chapter Acknowledgements

B.L.L. acknowledges support from the National Science Foundation Graduate Research Fellowship under Grant No. 2021-25 DGE-2034835. A.R.W. acknowledges support from the Virginia Space Grant Consortium and the National Science Foundation Graduate Research Fellowship Program under grant No. 1842490. Any opinions, findings, and conclusions or recommendations expressed in this material are those of the author(s)and do not necessarily reflect the views of the National Science Foundation.

Support for C.J.L. was provided by NASA through the NASA Hubble Fellowship grant No. HST-HF2-51535.001 awarded by the Space Telescope Science Institute, which is operated by the Association of Universities for Research in Astronomy, Inc., for NASA, under contract NAS5-26555. RRL is supported by the Deutsche Forschungsgemeinschaft (DFG, German Research Foundation) in the form of an Emmy Noether Research Group – Project-ID 445674056 (SA4064/1-1, PI Sander). This work was partially funded by the American Astronomical Society Education and Professional Development (EPD) mini-grant program.

This study was conducted with a UCLA IRB Exemption Certificate IRB#22-001473 and UVA IRB Approval Certificate IRB#5514. B. Lewis would like to thank the UCLA CIRTL TAR program for their guidance and mentorship, especially her CIRTL co-authors on this paper, Rachel Kennison for serving as faculty sponsor for UCLA IRB, and Graham Read. Thank you to Nicholas Young for valuable feedback on this manuscript, Jessie Thwaites and Haley Wahl for participating in talk-throughs as part of the survey design process, to Luna Zagorac for proofreading, to Nathan Sanders for his unwavering support of Astrobites' education initiatives, to Huei Sears for her support of grant proposals to fund this work, and to the rest of the Astrobites collaboration for their support of this project.

Chapter 7

Conclusions and Future Work

"Books can store information better than we can – what we do that books cannot is interpret. So if one is not going to draw conclusions, then one might as well just leave the information in the texts."

Brandon Sanderson, *The Way of Kings*

7.1 Relevance to the Field

Until recently, chemical and disk models ignored stellar variability on relatively short time scales (compared to the star's lifetime), but I have established astrochemistry in protoplanetary disks as a new time-domain science. I have shown that we can use the incredibly dynamic ionization levels in T Tauri disks to guide us to a more comprehensive picture of the chemical history of planets. In this thesis, I have established the theory behind flare driven chemical variability; I have developed methodology most likely to lead to successful observations; I have created adaptable models capable of simulating variable ionization beyond just X-rays.

7.2 Future Work

Today, we still don't have a complete picture of time variable chemistry. In this section, I highlight three projects that will be completed in the future to test the limits of stellar driven ionization and chemistry. I will 1) search for direct observational evidence of X-ray driven HCO^+ enhancement; 2) create a more realistic flare model to explore the impact of flares on biologically relevant molecules; 3) develop the first disk chemical model to include time variable coronal mass ejections, which reaches chemical species deep in the disk mid-plane where planets form.

My future work will not only help us better understand the chemical origin of life, but this research will also help constrain the types of planet formation processes that can occur. Magneto-rotational active and inactive zones have been shown to lead to two different types of planet formation, core accretion and gravitational instability, respectively. Based on my previous work, flares (and likely CMEs by extension) can increase gas-phase electron abundance enough to temporarily activate magneto-rotational instability (electron abundance $> 10^{-14}$ w.r.t. H, Igea & Glassgold, 1999).

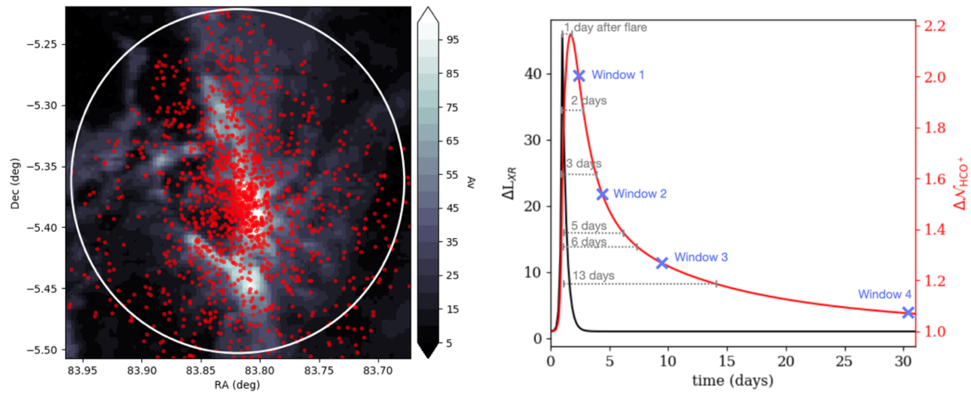

Figure 7.1 *Left:* An image of the Orion Nebular Cluster, represented by visual extinction. The *Chandra* field of view is represented by the white circle. Each red point corresponds to a star previously observed in the X-ray regime. Each was a potential candidate for our observations. *Right:* An X-ray flare ($\Delta L_{XR} \sim 45\times$ the quiescent flux) more than doubles the amount of disk integrated abundance of HCO+ (ΔHCO+).

7.2.1 Flare-driven HCO^+ Variability in the Orion Nebula Cluster

There is no direct evidence of flare driven chemical variability at this time. While an X-ray flare is the most likely source of $H^{13}CO^+$ $3-2$ enhancement in IM Lup (as discussed in Chapter 4), there are not coordinated X-ray observations to prove that a flare is the source of enhancement. Unfortunately, there is $< 5\%$ chance of catching observationally significant variability in HCO^+ serendipitously, and Cleeves et al. (2017) were exceptionally fortuitous in observing the disk almost immediately after what was likely an X-ray flare. Indeed, the best way to prove that X-ray flares can temporarily increase ionization levels, and therefore gas-phase ion abundance, is via a coordinated multi-wavelength observation campaign. I am a leading member in a collaboration that provides has done just this.

Chandra (a space-based X-ray telescope) surveyed hundreds of stars (Represented in Figure 7.1) in the Orion Nebula Cluster (ONC). Our team then identified which stars are actively undergoing a flaring event from a list of previously observed stars as a part of the COUP survey (Getman et al., 2005). Once candidates were selected, we triggered observations from ground-based telescopes including the Very Long Baseline Array (VLBA), the Hobby-Eberly Telescope, and ALMA. I then determined which of the flaring stars have an observed cold sub-mm emission (i.e., have a gaseous disk) through previous disk surveys (Ballering et al., 2023; Boyden & Eisner, 2023). I selected four separate disk systems, and each was successfully observed four times within the predetermined windows (described below). At this time, it appears that the observing campaign was successfully executed. We are still processing data, so this work was not included as an individual chapter.

Our observations will reveal how flares impact the chemistry and physics of protoplanetary disks, which will have potentially profound implications for disk evolution and planet formation. The suite of observations aims to measure surface magnetic field enhancements (via near-infrared line Zeeman broadening), coronal mass ejections (via milliarcsecond radio continuum detection), and ionization chemistry of protoplanetary disks (via the $H^{13}CO^+$ $J = 3-2$ transition). This coordinated effort is only able to occur because of high levels of collaboration between observation coordinators from around the world. [1]

As the PI of the accepted ALMA proposal, I was responsible for all scheduling and communication in the execution of these observations. $H^{13}CO^+$ wasobserved five times after the flare occurs, where we hope to catch HCO^+ enhancement directly

[1] I'd like to give a special shout out to Konstatine Getman and Eric Feigelson for actively identifying flaring stars as *Chandra* data was still being taken. They worked for several days straight to ensure that we were able to follow up with ALMA observations within *a single day* of the first *Chandra* epoch. Thanks are also given to Antonio Hayes, who was our contact ALMA scientist. Antonio ensured that our ALMA observations were observed within the designated windows. He even responded to my emails well past midnight.

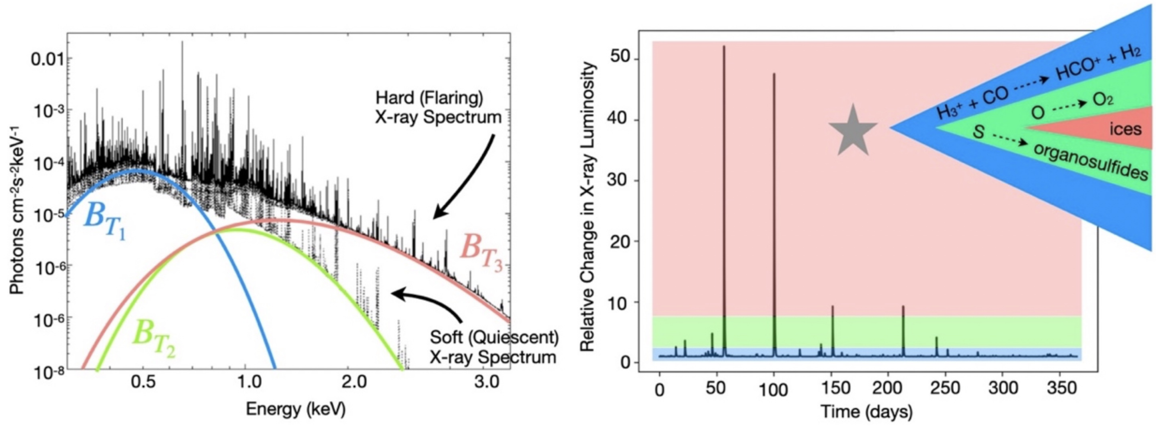

Figure 7.2 Higher energy X-ray photons, or "hard" photons, are produced in higher excess during an X-ray flare. These photons reach further into the disk. *Left*: X-ray spectra modeled by XSPEC. The grey spectrum is the 'quiescent' spectrum, created by black bodies B_{T_1} and B_{T_2}, and the black spectrum is a hard spectrum created by blackbodies B_{T_1} and B_{T_3}. *Right*: X-ray light curve simulated using XGEN. Larger flares (red) result in harder spectra, which penetrate further into the protoplanetary disk. The quiescent flux (blue) are strongest in the disk surface. A disk graphic is overlaid to demonstrate that B_{T_3} photon penetration is greater than B_{T_2} penetration, which is greater than B_{T_1} penetration. Representative X-ray driven chemical processes are shown in each layer.

after the flare and then monitor the decay in HCO^+, as demonstrated in Figure 7.1. To analyze the observed data, I will use reaction kinematics to calculate the electron abundance through the decay of HCO^+ flux. As the dominant destruction mechanism for HCO^+ is dissociative recombination, $HCO^+ + e^- \rightarrow CO + H$, the relative change in HCO^+ abundance is approximately equal to the relative change in electron abundance. Electron abundance has never been measured in a protoplanetary disk system, so my results will give us never before seen information on ionization and magneto-rotational instability, which guides the types of planet formation that can occur.

7.2.2 Does X-ray Hardening Magnify Molecular Complexity?

My X-ray flare model, XGEN , simulates an X-ray light curve based on observed flare statistics. I have incorporated XGEN into a chemical disk model, where X-ray flares are simulated by uniformly scaling disk X-ray ionization rates with respect to relative flare strength. This process effectively uniformly scales the X-ray spectrum when a flare happens, but in reality a process known as spectral hardening occurs, where more 'hard' photons (>1keV) are produced with respect to 'soft' photons ($\sim$ 1 keV), as demonstrated in Figure 7.2. Hardening occurs as a result of magnetic reconnection, which increases plasma temperatures on the stellar surface (Feigelson et al., 2007).

During the fellowship, I will upgrade XGEN to include spectral hardening to more realistically model flaring events. Hardening will be incorporated by modeling an X-ray spectrum as a two-component black body using XSPEC , where the soft and hard spectral components are treated as separate black bodies. The softest, or coolest, black body, B(T_{soft}), will be held constant over time, while the second black body B(T_{hard}), will have a variable temperature, based on the strength of the X-ray:

$$E_{tot} = \int B(T_{soft}) + B(T_{hard}) dv = 2hc^{-2} \int v^3 (e^{\frac{hv}{kT_{soft}}} - 1)^{-1} + v^3 (e^{\frac{hv}{kT_{hard}}} - 1)^{-1} dv \quad (7.1)$$

Hardening statistics will be based on surveys of T Tauri stars observed as a part of the Chandra Orion Ultra-deep Project (COUP, Getman et al., 2005; Wolk et al., 2005) and statistics reported in (Getman & Feigelson, 2021). By incorporating hardening into XGEN, and therefore into the chemical disk model, photons will penetrate further into the disk, reaching the regions where I found that O_2, organics, and organosulfides were enhanced by X-ray flares in my 2022 paper (Chaper 3). A more realistic model of flare energy will likely produce life-sustaining molecules in an even higher abundance, meaning that flares could aid in the formation of habitable planets. I will also include an upgraded sulfur network, which is currently being developed by UVa undergraduate student Becky Williams.

Additionally, I will include new, experimentally motivated X-ray driven ice reactions. Recent laboratory work has shown that X-ray photons can cause ice processing and further chemical reactions. For example, ices that contain oxygen (e.g., CO, H_2O, CH_3OH) have been shown to form complex organic molecules (carbon bearing molecules with six or more atoms) in the presence of X-ray photons (Dupuy et al., 2018; Basalgète et al., 2023). However, at this time X-ray ice processing has not yet been included in a complete chemical network. My model, with an updated sulfur chemical network and with new X-ray ice processing, will provide a new perspective on chemical evolution of cold gasses and ices, which can be implemented in a future JWST proposal.

7.3 Coronal Mass Ejections: Can They Increase Ionization Deep in the Disk?

Flaring events are often associated with coronal mass ejections (CMEs), which emit energetic particles commonly referred to as stellar cosmic rays (CRs). Stellar CRs are significantly less energetic than galactic CRs (produced by supernovae), so they are often considered to be a minor contribution to chemical reactions. However, there is increasing evidence that stellar CRs may play a key role in disk ionization rates. For example, Cleeves et al. (2013, 2015) and Seifert et al. (2021) sought to constrain ionization rates in several disks by using the HCO^+/N_2H^+ ratio. This ratio

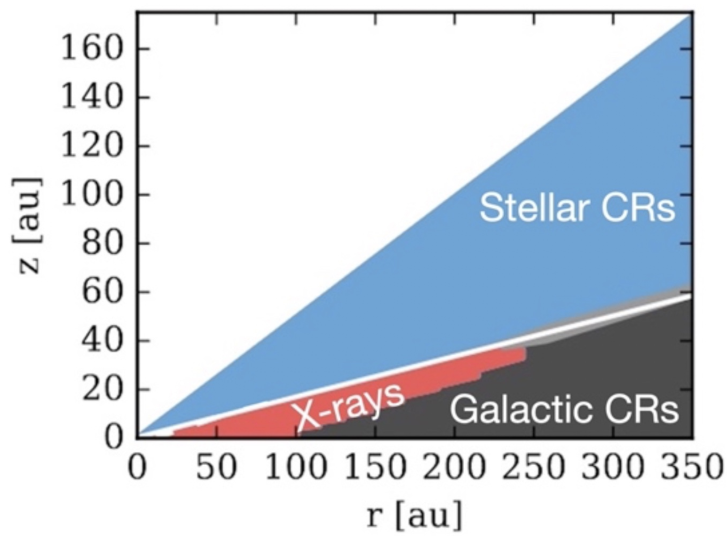

Figure 7.3 Dominate ionization rates throughout a typical T Tauri disk. Note that this particular model indicates that stellar CRs are the dominant form of ioniza@on in the disk. During a CME, stellar CRs will dominate even deeper in the disk. Figure adapted from Rab et al. (2017).

is commonly used to trace gas ionization, as both species are incredibly sensitive to ionization and dependent on CO abundance. In order to understand disk ionization levels, and therefore how gas evolves during the planet formation process, we must be able to constrain this ratio. The HCO^+/N_2H^+ ratio observed in the previously cited papers could only be explained by the presence of a cosmic ray gradient (i.e., higher CR ionization rates in the disk surface than in the disk mid-plane). One possible way to create a CR gradient is to introduce stellar CRs, particularly variable stellar CRs associated with CMEs (Rab et al., 2017). During this fellowship, I will use my chemical disk model, which is already optimized for variable ionization rates, to determine if CME driven stellar CR enhancement increases ionization rates where planets form (Figure 7.3).

I will develop the first chemical disk model to include time-variable stellar CR ionization rates. Previous models have simulated this phenomenon by including a constant 'enhanced' stellar CR rate (Rab et al., 2017), but my models will be the first to use astrophysically representative stochastic CR ionization rates. At this time, it is unknown if variable CR ionization rates will impact chemistry; however, CR ionization is fundamentally similar to X-ray ionization (e.g., Öberg & Bergin, 2021), and I have already shown that variable X-ray ionization aids in molecular complexity. This project seeks to determine if variable stellar CR emission could trigger chemical reactions in ices on dust grains that will later form planets. This project will use the same version of (Fogel et al., 2011) that I adapted for stochastic X-ray flares, where a variable CR ionization rate is introduced. The frequency and energetics of the stellar CRs will be motivated by previous CME modeled statistics described in Rab et al. (2017) and Brunn et al. (2023).

This project is particularly relevant in modern astronomy thanks to JWST, which allows us to observe ices in protoplanetary disks like never before. With an influx of JWST ice data, theorists will need to adapt our models to best match and explain observational results. I plan to extend this work by submitting JWST proposals to determine if there is a relationship between HCO^+/N_2H+ ratios and ice abundance. These proposals will monitor ice in disks with well constrained HCO^+/N_2H+ ratios, which can then be compared to my variable stellar CR models to determine if stellar CRs shape pre-planetary chemistry.

Appendix A

Additional Information for Chapter 2

A.1 Protoplanetary Disk Physical Conditions

Within a protoplanetary disk, gas and dust density is highest along the mid-plane and near the central star, and density decreases as the disk surface is approached and radial distance from the star increases as a natural consequence of the viscous motion of the gas (Lynden-Bell & Pringle, 1974). Temperature, X-ray ionization rate, and UV flux are highest along the disk surface and decrease with increasing radial distance from the star. Figure A.1 plots these physical conditions in the IM Lup protoplanetary disk, , which are the physical conditions used in the present study. Points whose chemistry is modeled are represented by red dots in Figure A.1. The exact physical condition values used for all 35 modeled points are presented in Table A.1.

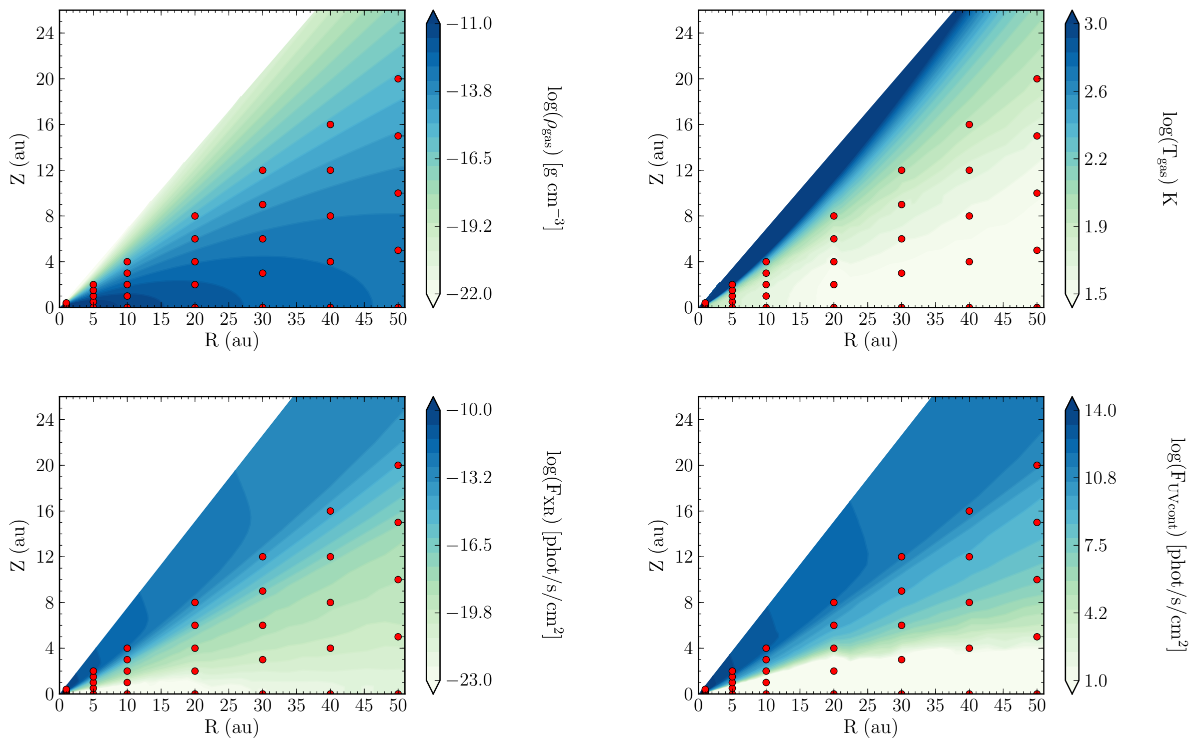

Figure A.1 These plots represent density, temperature, X-ray ionization rate, and UV flux in the IM Lup protoplanetary disk, a disk encircling a solar-mass young star. Red dots indicate the 35 locations modeled and analyzed in this paper.

Table A.1 Model locations and parameters.

R au	Z au	ρ gcm^{-3}	T_{gas} K	T_{dust} K	UV Flux $\gamma s^{-1} cm^{-2}$	X-ray Ionization $s^{-1} H_2^{-1}$
1.0	0.0	1.07×10^{-9}	134.3	134.3	0.0	1.0×10^{-30}
1.0	0.1	2.49×10^{-10}	132.2	133.2	0.0	1.06×10^{-30}
1.0	0.2	7.03×10^{-12}	168.4	167.8	3.37×10^{10}	5.64×10^{-16}
1.0	0.3	7.29×10^{-15}	662	342.5	4.50×10^{14}	3.19×10^{-11}
1.0	0.4	1.98×10^{-18}	4200	341.1	5.82×10^{14}	1.63×10^{-10}
5.0	0.0	3.45×10^{-11}	60.9	61.0	0.0	1.0×10^{-30}
5.0	0.5	1.39×10^{-11}	60.8	61.0	0.0	3.53×10^{-22}
5.0	1.0	9.15×10^{-13}	75.3	75.8	3.50×10^{8}	1.55×10^{-17}
5.0	1.5	2.09×10^{-14}	145.9	141.5	4.06×10^{11}	1.88×10^{-14}
5.0	2.0	1.26×10^{-16}	820.5	164.9	2.54×10^{13}	5.854×10^{-12}
10.0	0.0	7.26×10^{-12}	43.9	44.0	0.0	7.66×10^{-27}
10.0	1.0	3.48×10^{-12}	44.4	44.3	0.0	2.91×10^{-22}
10.0	2.0	3.84×10^{-13}	52.9	52.9	2.41×10^{7}	2.73×10^{-18}
10.0	3.0	1.80×10^{-14}	90.2	88.5	3.58×10^{10}	1.23×10^{-15}
10.0	4.0	2.86×10^{-16}	259.1	121.1	5.76×10^{12}	7.40×10^{-13}
20.0	0.0	1.45×10^{-12}	26.1	26.1	0.0	2.41×10^{-25}
20.0	2.0	8.00×10^{-13}	27.3	28.0	0.0	1.60×10^{-21}
20.0	4.0	1.86×10^{-13}	32.3	34.0	9.25×10^{4}	2.82×10^{-19}
20.0	6.0	1.12×10^{-14}	53.7	56.0	4.58×10^{9}	7.91×10^{-17}
20.0	8.0	3.92×10^{-16}	117.4	90.2	7.90×10^{11}	3.95×10^{-14}
30.0	0.0	5.43×10^{-13}	19.0	19.2	0.0	4.50×10^{-23}
30.0	3.0	3.21×10^{-13}	28.8	29.2	5.37	1.05×10^{-20}
30.0	6.0	8.84×10^{-14}	37.4	38.2	1.07×10^{7}	2.73×10^{-19}
30.0	9.0	7.38×10^{-15}	53.6	55.2	2.21×10^{9}	2.21×10^{-17}
30.0	12.0	3.80×10^{-16}	101.4	87.9	2.48×10^{11}	8.27×10^{-15}
40.0	0.0	2.62×10^{-13}	16.3	16.3	2.51×10^{-29}	1.01×10^{-22}
40.0	4.0	1.62×10^{-13}	27.4	27.3	1.86×10^{2}	9.96×10^{-21}
40.0	8.0	4.96×10^{-14}	34.2	34.8	9.97×10^{6}	1.80×10^{-19}
40.0	12.0	5.10×10^{-15}	50.6	50.3	1.25×10^{9}	9.75×10^{-18}
40.0	16.0	3.37×10^{-16}	87.3	79.5	1.09×10^{11}	3.20×10^{-15}
50.0	0.0	1.42×10^{-13}	14.5	14.6	4.41×10^{-19}	2.51×10^{-22}
50.0	5.0	9.07×10^{-14}	26.9	25.9	2.43×10^{3}	1.09×10^{-20}
50.0	10.0	3.02×10^{-14}	32.2	32.6	$1.48\mathrm{E}\times10^{7}$	1.19×10^{-19}
50.0	15.0	5.18×10^{-15}	44.2	43.4	5.16×10^{8}	1.64×10^{-18}
50.0	20.0	4.59×10^{-16}	74.0	70.5	2.00×10^{10}	7.23×10^{-16}

Appendix B

Additional Information for Chapter 3

B.1 Most variable species

Table B.1 presents the most chemically impacted species in the model. As can be seen, cations are by far the most strongly impacted molecules in the network.

Table B.1 Left column: The thirty most stochastically variable chemical species in the network. Right column: The thirty species that are most changed when compared to a model without flares after 500 years of chemical evolution.

Highest σ			Highest $\mathcal{C}$		
	σ	$\mathcal{C}$		σ	$\mathcal{C}$
SO_2^+	4.51	1.00	$H_2S_2^+$	0.37	1.25
H_2^+	4.39	0.99	$HOCS^+$	0.31	1.25
O_2H^+	4.36	1.06	HSO_2^+	0.37	1.24
H_3^+	3.24	0.99	N^+	0.42	1.22
HeH^+	1.03	1.18	He^+	0.13	1.21
CO_2^+	0.70	1.01	HSO^+	0.23	1.21
$C_5H_2^+$	0.64	1.00	H^+	0.24	1.20
H_3O^+	0.51	1.08	HeH^+	1.03	1.18
N_2^+	0.46	1.10	$COOCH_4^+$	0.23	1.17
N_+	0.42	1.22	HC_3O_+	0.28	1.17
HCO^+	0.40	1.07	$CH_2O_2^+$	0.05	1.17
HNO^+	0.38	1.03	O^+	0.20	1.16
HSO_2^+	0.37	1.24	$C_2H_5OH^+$	0.11	1.16
$H_2S_2^+$	0.37	1.25	O_2H	0.07	1.13
$C_6H_5^+$	0.32	1.11	$C_3H_3N^+$	0.05	0.87
$HOCS^+$	0.31	1.25	HNS^+	0.22	1.13
CH_4^+	0.28	1.12	CH_4^+	0.28	1.12
HC_3O^+	0.28	1.17	H_2CS^+	0.16	1.12
H^+	0.24	1.20	$H_3S_2^+$	0.17	1.11
HSO^+	0.23	1.21	$C_6H_5^+$	0.32	1.11
$COOCH_4^+$	0.23	1.17	$C_7H_4^+$	0.02	1.10
HNS^+	0.22	1.13	N_2^+	0.46	1.10
$C_7H_2^+$	0.22	0.99	$C_6H_4^+$	0.05	1.09
O^+	0.20	1.16	$CH_3O_2^+$	0.12	1.09
$C_3H_4^+$	0.19	1.02	$C_2H_6^+$	0.10	1.09
$H_3S_2^+$	0.17	1.11	$C_4H_4N^+$	0.04	0.92
N_2H^+	0.17	1.00	$C_7H_5^+$	0.02	1.08
H_2CS^+	0.16	1.12	$C_4H_5^+$	0.02	1.08
He^+	0.13	1.21	H_3O^+	0.51	1.08
$C_4H_7^+$	0.12	1.06	HCO^+	0.40	1.07

Appendix C

Additional Information for Chapter 4

C.1 Spectra with Error Bars

Both observation epochs for HCO^+, $H^{13}CO^+$, and HCN were had similar spectral shape and flux, indicating that there were no variations in line flux between the two observations. The line spectra were within 1σ of each other for each observation epoch, as shown in (Figure C.1).

C.2 Channel maps

A Keplerian mask was generated for HCN and HCO^+ $3-2$, as shown in Figures C.2 and C.3. The $H^{13}CO^+$ $3-2$ line was too faint to generate a Keplerian mask, so channel averaging was done to improve sensitivity, then a mask was generated by clipping the HCO^+ $3-2$ Keplerian mask to 5σ.

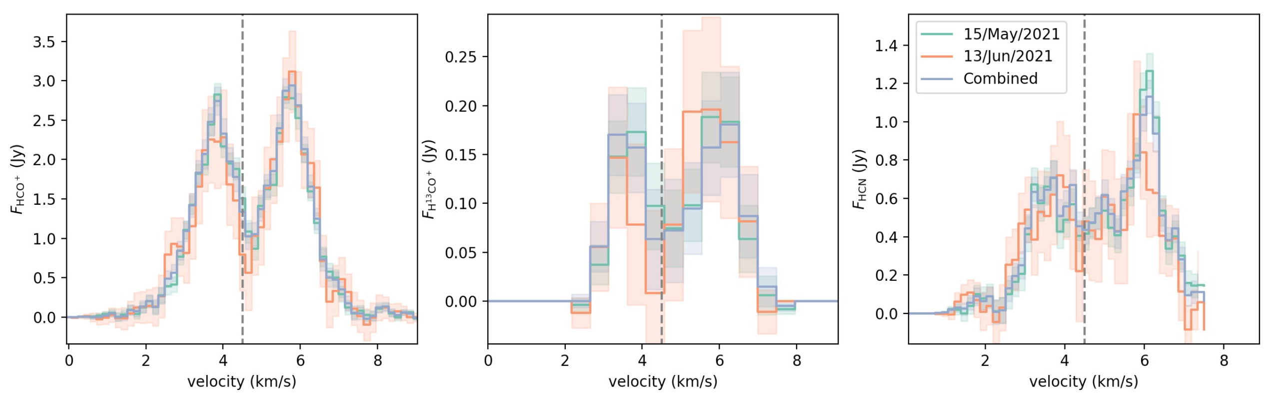

Figure C.1 HCO^+, $H^{13}CO^+$, and HCN J$= 3-2$ line emission for IM Lup with error bars. Each error bar indicates $\pm 1\sigma$. Spectra observed on different days consistent with each other within error.

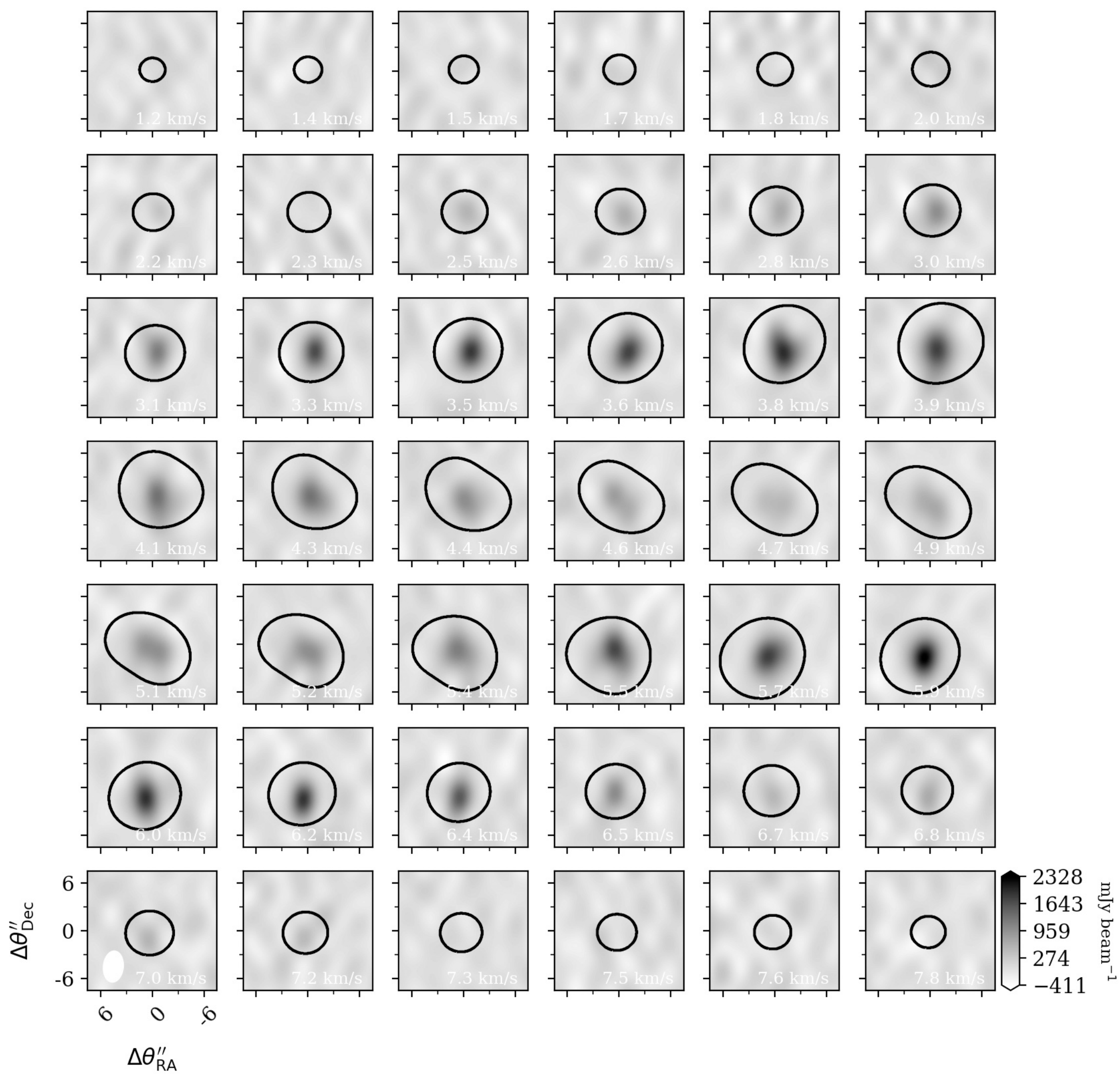

Figure C.2 Channel map and keplarian generated mask for HCO^+ $3-2$. Channels are produced by combined observation dates.

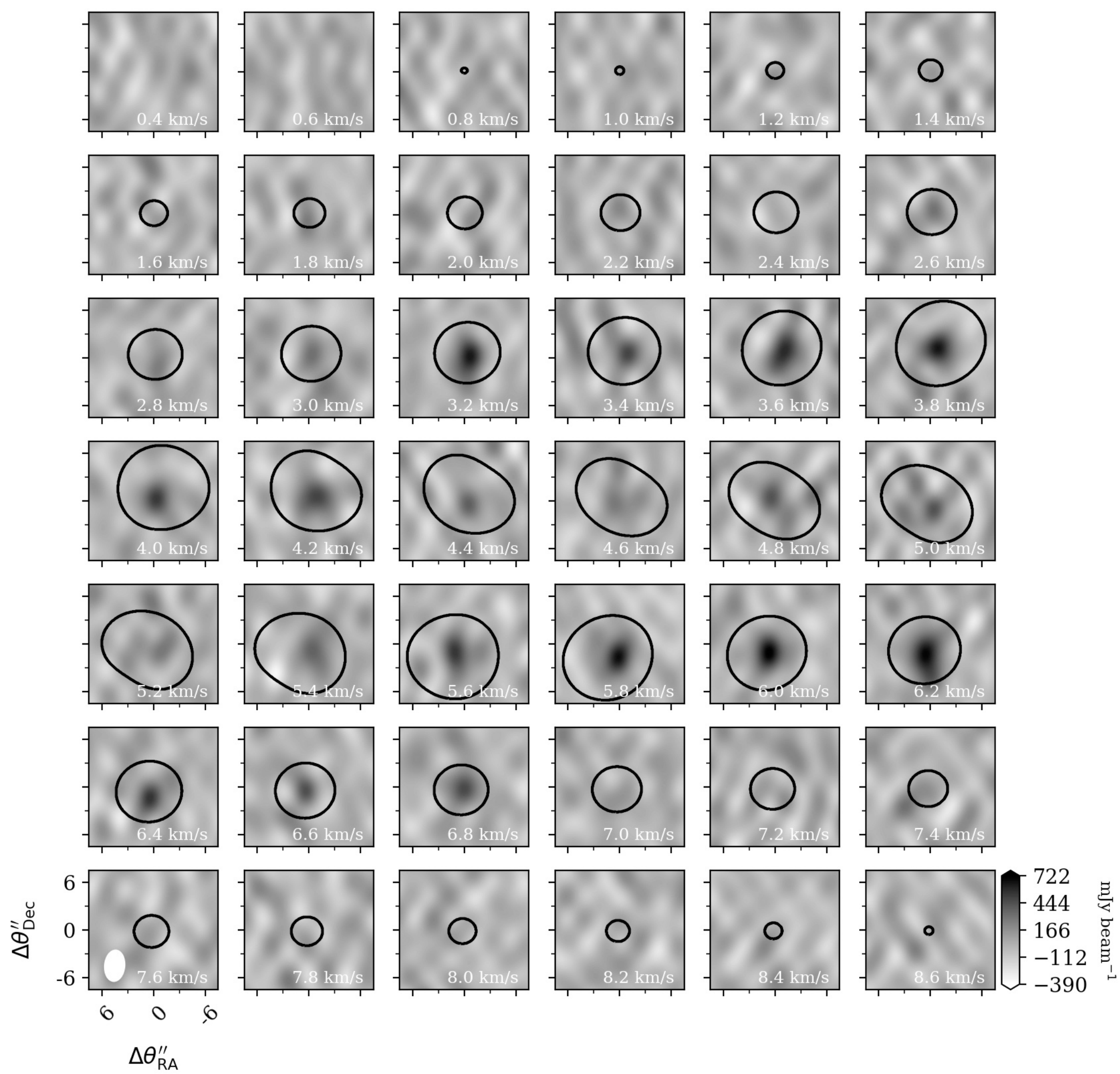

Figure C.3 Channel maps and keplerian generated mask for HCN $3-2$.

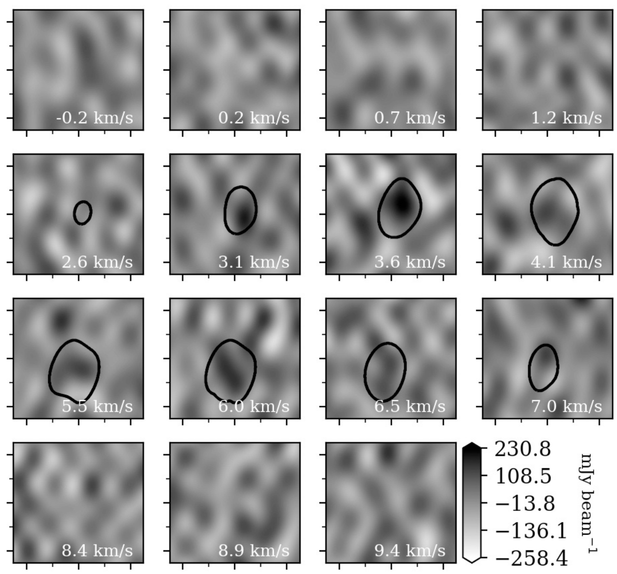

Figure C.4 Channel map of $H^{13}CO^+$. Mask was generated by clipping the keplerian HCO^+ to 5σ. This image is created from the combined data.

Appendix D

Additional Information for Chapter 5

D.1 Visibility Effects on HCO^+ Emission

To ensure that any detected variability was not artificially introduced by varying telescope configurations, the python function `vis-sample` was used to generate 'mock' data (as described in Section 5.4.3). These data are produced using the exact same `CLEAN`ing method as the real data. Therefore, the mock data reveal any variability that would have been introduced by varying baseline coverage from different telescope configurations.

IM Lup is the only system with a clear baseline effect in the mock data. $F_{\mathrm{HCO^+}}$ on 21/Aug/2019 is higher than the other observations, despite the fact that all mock observations were modeled using the same initial measurement set. This same effect is seen in the real data (Figure 5.6), and is attributed to baseline coverage.

There are several scenarios where observations with more complete short baseline coverage (i.e., those taken in October 2018) yield slightly higher $F_{\mathrm{HCO^+}}$ values

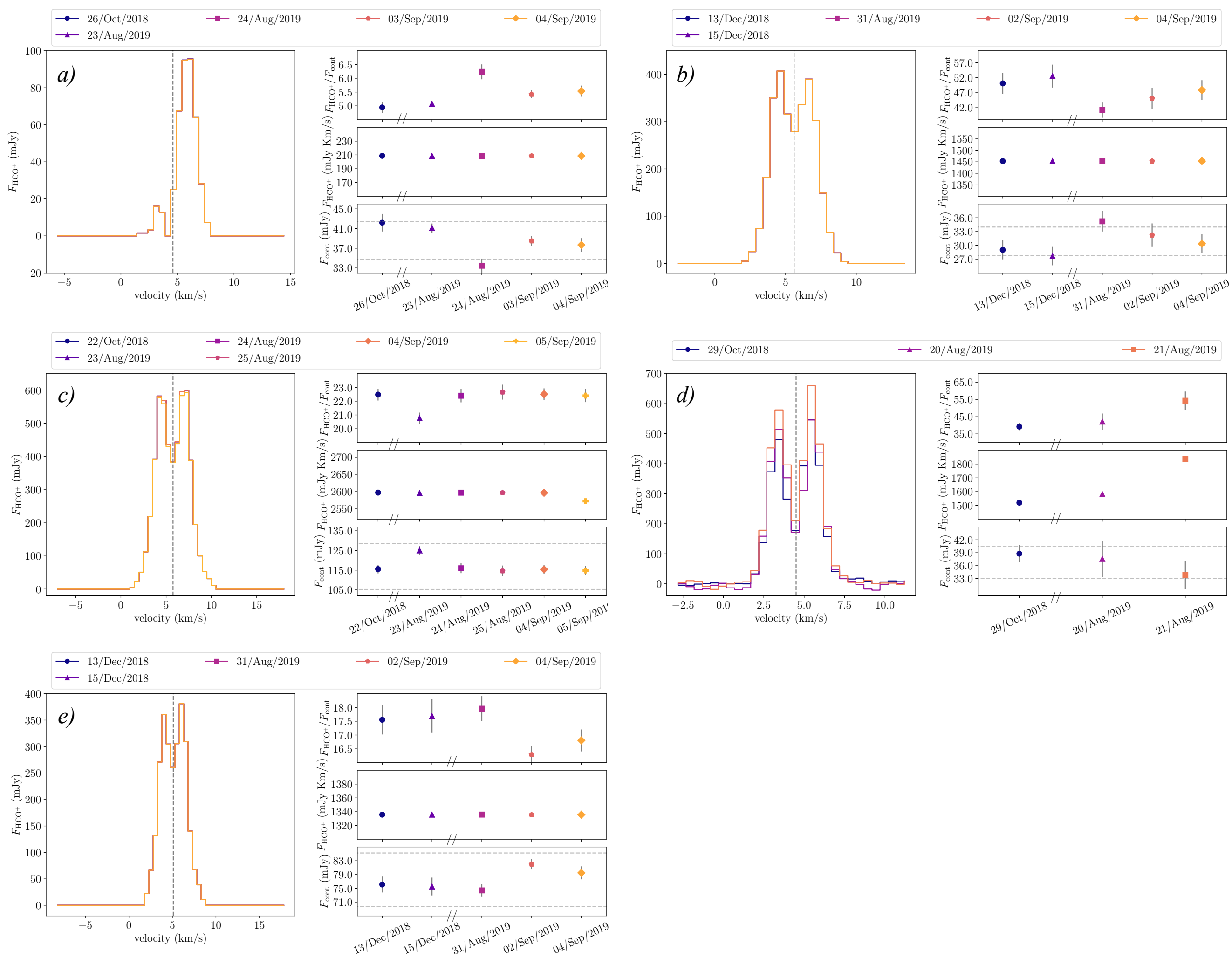

Figure D.1 Synthetic spectra ("mock data") produced using the `vis-sample` routine on the time-integrated HCO^+ $1-0$ cubes. These models reveal any spectral or flux fluctuations that would have been introduced by varying baseline coverage for each source's unique spatial emission structure. Each sub-figure shows the analysis for: *a)* AS 209; *b)* GM Aur; *c)* HD 163296; *d)* IM Lup; *e)* MWC 480. For each panel, *Left:* mock HCO^+ $1-0$ spectrum, and *Right:* mock disk integrated continuum, line, and continuum normalized line emission. Note that the spectra overlap.

(HD 163296, AS 209). In the disks where this effect occurs, no significant variations were seen in the mock line or continuum flux. There are variations in the disk integrated flux values, most notably in F_{cont}. This variation is attributed to RMS uncertainty, since all F_{cont} values are with $\pm 10\%$ of each other (See Section 5.5.2).

Changes in flux are unlikely caused by baseline coverage.

D.2 Channel Error Bars on Spectra

All spectral changes reported in this work are considered tentative, since no change is $> 3\sigma$. However, there are a number of spectral variations greater than the level of noise, as shown in Figure D.2 and defined as follows.

- AS 209: The peak at 6.1 km s^{-1} is enhanced and shifted toward source velocity on 26/Oct/2018. The 6.1 km s^{-1} peak appears to also be shifted and enhanced on 04/Sep/2019, but not above the level of noise, so it is not considered a change in emission in this work. On most observation days little to no blue shifted emission is seen, except on 03/Sep/2019.

- GM Aur: The peak at 6.6 km s^{-1} is enhanced on 26/Oct/2018, and a shoulder is visible at 9.6 km s^{-1} on 2/Sep/2019.

- HD 163296: Both central peaks are enhanced on 22/Oct/2018 compared to the following observations.

- IM Lup: The peak at 6.8 km s^{-1} is enhanced on 21/Aug/2019 compared to the other two observations.

- MWC 480: An unknown emission peak is seen on 04/Sep/2019 at km s^{-1} km/s and not on any other observation day. There may be a shift in spectral shape on 04/Sep/2019, but the change is below the level of noise and not considered in this work.

For more information on error calculations, see Section 5.4.2.

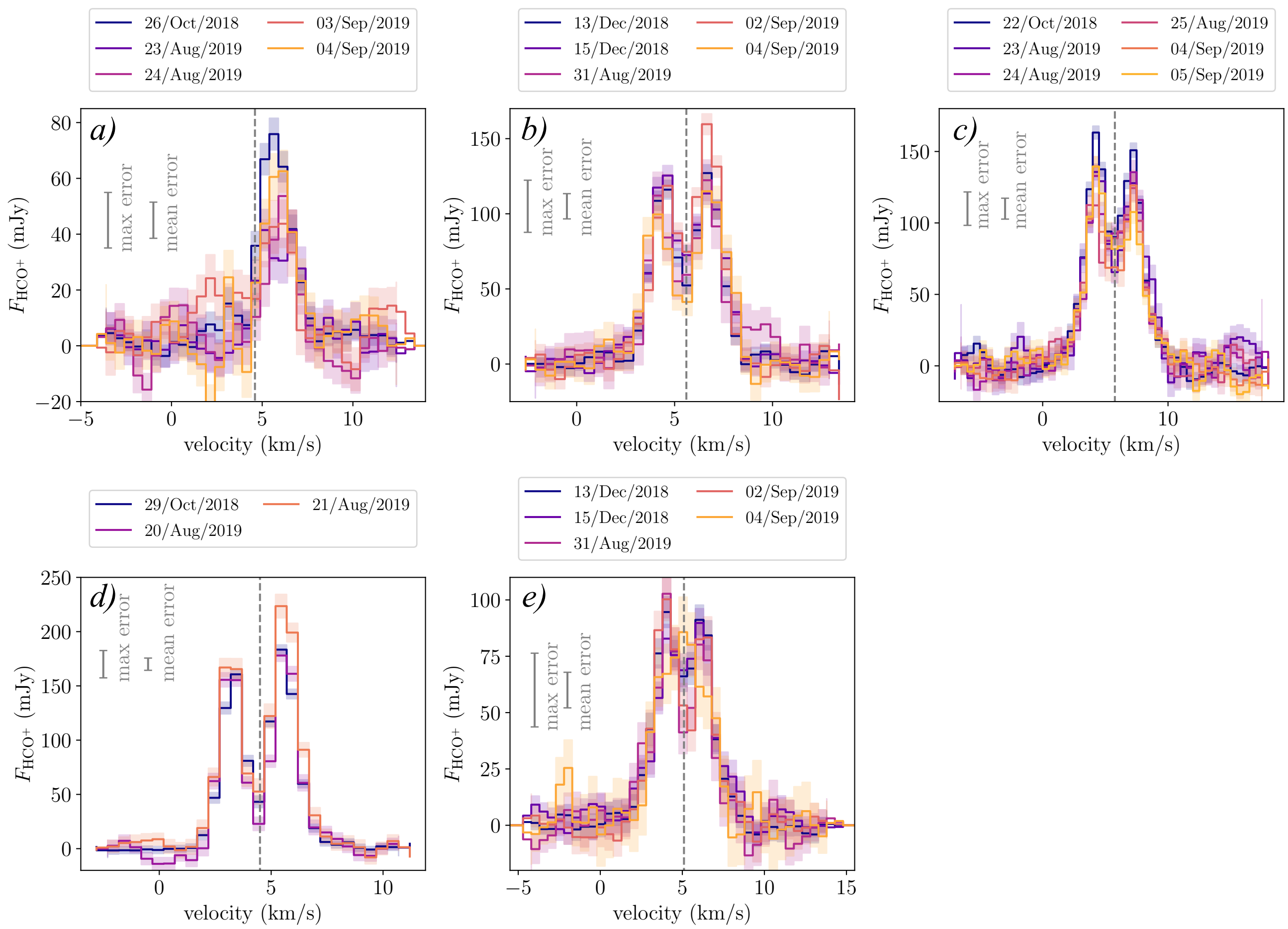

Figure D.2 HCO^+ J= $1-0$ spectra for each of the MAPS disks with error bars for each channel. The grey error bars represent the max and mean error bar (standard deviation) for all channels. *a)* AS 209; *b)* GM Aur; *c)* HD 163296; *d)* IM Lup; *e)* MWC 480.

Appendix E

Additional Information for Chapter 6

E.1 About Astrobites

The Astrobites collaboration is a group of volunteer graduate students in astronomy and related fields who publish daily blog-style posts summarizing current astronomy research papers. Astrobites also publishes guides to specific topics and other resources relevant to career development and equity/inclusion. While Astrobites content is primarily targeted towards undergraduate astronomy majors, its audience has grown to include everyone from hobbyists to emeritus professors since our founding in 2011.

A central focus of Astrobites' mission is to further efforts for inclusion and equity in astronomy. We impact accessibility by addressing the inaccessibility and technical language of research articles through summaries, and our host of "guides" to different aspects of astronomy and academic professional development. Astrobites articles are also an excellent way for students to explore differences in audience between various forms of science writing, and for students–both undergraduates reading the articles and graduate students serving as regular writers–to practice writing skills, which are increasingly critical for becoming a successful scientist. Astrobites has also taken an active role in incorporating its pedagogical content, wide topical coverage, and scaffolded contextual resources into formal education (Sanders et al., 2012, 2017).

All content on Astrobites – including the education resources used in this study – is free and open access, publicly available on astrobites.org. Similar websites (known as "Science Bites" sites) are available in other disciplines.

E.2 Full Assessment Text

Questions not designated as "interview" or "open-ended" were answered on a Likert scale from 1 to 7, where 1 indicates strong disagreement, 4 is neutral, and 7 is strong agreement.

Perceived ability with jargon

1. I am able to define technical terminology that appears in scientific literature.
2. Technical terms are a major barrier to my understanding of scientific literature. [Reversed]
3. I am able to use outside resources to help define technical terminology.
4. I am able to understand the technical details of a scientific study.
5. I find technical vocabulary in astronomy papers daunting. [Reversed]

Perceived ability with main takeaways

6. After reading a paper, I can summarize it well to a classmate in a science course.
7. I can understand the motivation behind a scientific paper.

8. I can understand how a given scientific paper contributes to the field at large.

9. I am able to figure out the main takeaways / key ideas of a scientific paper.

10. I am able to interpret the data on a plot and extract the key takeaway from it.

11. I know what the most important pieces of information are after reading a scientific research paper.

<u>Perceived ability with conceptual understanding/intuition</u>

12. I can see how concepts learned in class feature in astronomy papers.

13. I am able to understand astronomy concepts.

14. I am able to relate different astronomy concepts to each other.

15. I could evaluate whether the data on a plot seems reasonable given the scenario it represents.

16. I can interpret what the data on a plot is telling me about a concept.

17. I am able to draw analogies between concepts discussed in astronomy literature and concepts prevalent in everyday life.

18. I have a strong intuition for concepts in astronomy.

<u>Perception of science communication ability</u>

19. I feel comfortable discussing astronomy with my friends.

20. I feel comfortable discussing astronomy with my science classmates.

21. I feel comfortable discussing astronomy with my science instructors.

22. I could explain basic astronomy concepts to a non-scientist.

23. I can explain astronomy concepts to a classmate in a science course.

24. I can explain astronomy concepts to my science instructors.

Perceived ability within astronomy

25. I have what it takes to be an astronomer.

26. I am capable of succeeding in my astronomy courses.

27. I am able to use technical astronomy skills (tools, instruments, and/or techniques).

28. I am able to use scientific literature to guide my studies in astronomy.

29. I am capable of working on astronomy research.

Feelings of belonging within astronomy

30. I see myself as someone who can contribute to science.

31. I see myself as someone who can contribute to astronomy.

32. I could see myself becoming an astronomer as my career.

33. I feel a part of the group when I am with other astronomers.

34. I have a strong sense of belonging to the community of astronomers.

35. I feel like I belong in the field of astronomy.

Open-Ended Questions

36. How do you feel about reading scientific research papers?

37. What comes to mind when you think of astronomy research?

38. Do you think you are capable of being an astronomer (or related scientist)? Why or why not?

39. Do you feel like you belong in astronomy? Why or why not?

40. Did you enjoy this activity with Astrobites? Why or why not? [Post-Lesson Survey Only]

41. What is your main takeaway from this activity? [Post-Lesson Survey Only]

42. What did you find most useful about this activity? [Post-Lesson Survey Only]

43. What was most confusing about this activity? [Post-Lesson Survey Only]

44. How have your feelings about astronomy research changed as a result of this activity, if at all? [Post-Lesson Survey Only]

Instructor Interview Questions

- Which Astrobites lesson plan did you implement, and did you make any changes to it?

- Overall, how do you think this lesson went in your classroom?

- How do you think this activity / lesson plan impacted your students?

- Do you think your students are more prepared to engage with scientific research literature after this lesson? Why or why not?

- Do you think your students enjoyed this activity with Astrobites? Why or why not?

- What did you find most useful about this lesson plan?

- What suggested changes do you have for this lesson plan?

E.3 Further Information on Lesson Plans

Astrobites currently maintains four lesson plans based on our prior published work (Sanders et al., 2017). These lesson plans provide four pathways to engage students with Astrobites materials—guided reading assignments, student research projects, a student writing assignment, and student presentations—and are available in this linked document. For each lesson plan, we provide an overview of the learning objectives, an outline of how the plan can be adapted for different course levels, sample handouts for presenting the assignment to students, and a potential grading rubric.

The first lesson plan (Lesson Plan 1: Periodic Reading Assignments), which features a series of guided reading assignments, is designed to grow students' reading comprehension and strengthen their conceptual understanding of course material in the broader context of active research. Students build familiarity and confidence in their ability to monitor and keep pace with recent developments in the astronomy literature by reading a series of Astrobites articles and testing their understanding through directed questions. This lesson can be easily adapted to different course levels by varying the frequency of assignments and altering the style of the associated questions (e.g., asking more directed questions for lower-division undergraduates compared to open-ended questions for graduate students).

In the second lesson plan (Lesson Plan 2: Student Research Project), students select a topic and prepare a paper or presentation using Astrobites articles to guide their research. Students synthesize concepts and interpret figures and data from different articles for their report. Students build confidence in developing techniques to tackle new concepts by using Astrobites articles to identify technical terminology (jargon) with which they are unfamiliar. Students then define jargon by creating a glossary. This lesson plan is meant to teach students how to engage with full research articles in the future.

For the third lesson plan (Lesson Plan 3: Student Writing Assignment), students read one or more papers and write an Astrobites-like summary. Much as with the second lesson plan, students practice synthesizing information from multiple sources. However, they additionally develop valuable science communication and composition skills by compiling information into a bite-sized article. Additionally, students actively practice reading the scientific literature directly. By scaffolding the assignment—e.g., having students present drafts and outlines along the way—instructors can help students settle into the reading and writing process more smoothly.

Finally, in the fourth lesson plan (Lesson Plan 4: Student Presentation), students deliver an in-class presentation featuring a profile of an astronomer who has been interviewed by Astrobites and a summary of a paper by the interviewee. While also incorporating the reading comprehension and communication skills that appear in the other lesson plans, the focus of this lesson plan is to support students' career preparation and develop a sense of belonging in the field. By sharing presentations describing the career trajectory and advice of successful astronomers hailing from diverse backgrounds, students are able to see that astronomy is for everyone, while also identifying and discussing important steps on the way to becoming a professional astronomer. For example, one study of the importance of role models for career preparation and aspiration of young Black British people is presented in Archer et al.ARCHER et al. (2015) and summarized in Astrobites in 2020.

E.4 Additional Response Quotes from Students and Educators

Student comments on the usefulness of the Astrobites lesson plans:

> "The activity helped me to understand the findings of a research paper at my level of knowledge. It wasn't too technical, and wasn't too 'dumbed-down' either."

> "While the stuff we learn in class is important, I felt like this activity took we learned in class and made us do something 'practical' with it."

> "I learned more about other astronomers and their contributions (no matter how big or small) to astronomy."

> "I found the length of the Astrobites less daunting to read about and made the experience more enjoyable."

Instructor comments on the utility of the Astrobites lesson plans:

> "I think it gave them something to chew on when I was doing lectures...Students were definitely engaged with the literature in a way that seemed positive."

> "A student was like I just wanted to say that I really appreciated that there was a person there like working hard on accessibility and disabilities, and it's something that we don't see a lot of. And I was like, wow, these students are seeing themselves in accomplished astronomers. And that was cool for me as the instructor to witness."

> "[Astrobites] enabled the possibility to connect to the paper, because the paper was so inaccessible for the current know-how of the students."

> "I do [think they are more prepared] because they told me. But then from my perspective, I could see what they were writing asking deeper questions...I saw it [the improvement] in their work."

> "I noticed when students would do presentations, they would reference the results from their classmates previous Astrobites presentations. And I feel like that is one indicator of being able to interact more strongly with the literature, is recalling the results from previous works and incorporating that into their own presentation."

E.5 Further information on quantitative analysis

This appendix includes histograms (Figure E.1) and a table of statistical summaries (Table E.1) for all of the Likert response questions individually, supplementary to Section 6.4.1.

E.6 Consistency Analylsis

When performing a mixed methods study such as this, it is good practice to compare results obtained through multiple questions covering the same themes. One way to conduct such a comparison involves assigning numerical scores to qualitative questions Caracelli & Greene (1993); Onwuegbuzie & Combs (2010). Here, we identified three qualitative questions (Questions 36, 38, and 39 in Appendix E.2) for which there are Likert scale questions that address similar themes. We determined which qualitative response codes denoted positive, neutral, and negative feelings toward the three questions, and assigned each student a qualitative "score" for that question based on the prevalence of each type of code in their response. The related Likert questions

Figure E.1 Histograms for the differences between post- and pre-survey Likert responses for the quantitative questions in Section E.2. Vertical black dashed line marks the mean change. 95% confidence intervals for the mean are given in E.1.

Table E.1 Statistics and effect size interpretations for pre-post differences for all quantitative questions (Sample size = 82). Q is the question number, CI95% is the 95% confidence interval for the difference in pre and post means, 'cohen-d' is the value of Cohen's d, 'd interp' is the interpretation of Cohen's d value, BF10 is the Bayes factor of the alternative hypothesis, 'BF10 interp' gives the interpretation of BF10 value, power=1-type II error.

Q	CI95%	p	cohen-d	d interp	BF10	BF10 interp	power
1	[0.25 0.75]	1.27×10^{-4}	0.456	small	157	extreme for H1	0.983
2	[-0.39 0.17]	0.439	0.0702	very small	0.163	moderate for H0	0.0962
3	[-0.08 0.39]	0.184	0.156	very small	0.288	moderate for H0	0.286
4	[0.09 0.55]	7.82×10^{-3}	0.259	small	3.83	moderate for H1	0.638
5	[-0.58 0.15]	0.236	0.131	very small	0.242	moderate for H0	0.217
6	[0.3 0.79]	2.56×10^{-5}	0.428	small	698	extreme for H1	0.969
7	[-0.07 0.46]	0.149	0.175	very small	0.337	anecdotal for H0	0.348
8	[-0.17 0.34]	0.502	0.0688	very small	0.152	moderate for H0	0.0944
9	[-0.05 0.44]	0.114	0.175	very small	0.412	anecdotal for H0	0.347
10	[0.02 0.57]	0.0373	0.232	small	1.01	anecdotal for H1	0.547
11	[0.03 0.53]	0.0267	0.245	small	1.33	anecdotal for H1	0.591
12	[0.05 0.53]	0.0177	0.290	small	1.89	anecdotal for H1	0.737
13	[-0.03 0.39]	0.0874	0.179	very small	0.506	anecdotal for H0	0.361
14	[-0.11 0.36]	0.305	0.107	very small	0.203	moderate for H0	0.160
15	[-0.05 0.47]	0.113	0.150	very small	0.413	anecdotal for H0	0.267
16	[-0.08 0.44]	0.163	0.156	very small	0.314	moderate for H0	0.287
17	[-0.23 0.32]	0.726	0.0359	very small	0.129	moderate for H0	0.0619
18	[-0.03 0.47]	0.0803	0.160	very small	0.540	anecdotal for H0	0.298
19	[-0.05 0.46]	0.110	0.158	very small	0.422	anecdotal for H0	0.294
20	[-0.13 0.32]	0.386	0.0749	very small	0.176	moderate for H0	0.103
21	[-0.19 0.31]	0.625	0.0413	very small	0.137	moderate for H0	0.0658
22	[-0.09 0.31]	0.274	0.0987	very small	0.218	moderate for H0	0.143
23	[-0.18 0.23]	0.813	0.0198	very small	0.125	moderate for H0	0.0536
24	[0.22 0.71]	3.51×10^{-4}	0.324	small	62.1	very strong for H1	0.827
25	[-0.11 0.33]	0.332	0.0889	very small	0.193	moderate for H0	0.125
26	[-0.22 0.22]	1.00	0.00	very small	0.122	moderate for H0	0.05
27	[-0.07 0.48]	0.135	0.151	very small	0.361	anecdotal for H0	0.273
28	[0.18 0.72]	1.45×10^{-3}	0.347	small	17.2	strong for H1	0.873
29	[0. 0.58]	0.0479	0.223	small	0.821	anecdotal for H0	0.513
30	[-0.16 0.33]	0.489	0.0695	very small	0.154	moderate for H0	0.0954
31	[-0.11 0.35]	0.295	0.104	very small	0.208	moderate for H0	0.153
32	[-0.18 0.31]	0.622	0.0418	very small	0.137	moderate for H0	0.0662
33	[-0.1 0.37]	0.262	0.0902	very small	0.225	moderate for H0	0.127
34	[-0.17 0.37]	0.472	0.0634	very small	0.157	moderate for H0	0.0875
35	[0.08 0.68]	0.0142	0.237	small	2.28	anecdotal for H1	0.562

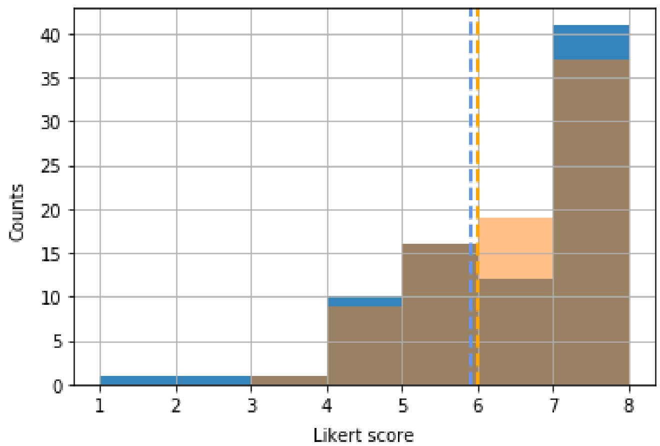

Figure E.2 Histogram of pre (blue) and post (orange) response Likert scores to the statement “I am capable of succeeding in my astronomy courses," the only question which did not show pre-post change. Pre- and post- response means are indicated by the vertical dashed lines. Student perceptions were overwhelmingly positive in both the pre- and post- surveys.

and positive, neutral, and negative codes considered for each of the three qualitative questions used in this comparison are listed in Table E.2.

For each student response to each of these three questions, we took the average of related Likert scale questions to find their “Likert score” (quantitative). To assign a student’s “written score” (qualitative) on a topic, we assigned +1 to every positive code applied to their response to that question, −1 to every negative code, and 0 to every neutral code. By adding these values, we found a total score — if this total score was positive (negative), we assigned the student a written score of 1 (−1) for that question; if the total score was 0, we left it as 0. For each of the three qualitative questions selected, we compared each student’s Likert and written scores, as well as the score change for each student from pre- to post-survey.

Note that not every Likert question was used in this analysis, and several Likert questions were considered in relation to more than one qualitative question. We only considered codes applied by a majority of raters, as in the general qualitative

Table E.2 Details of qualitative-quantitative consistency analysis. Question 36: "How do you feel about reading scientific research papers?" Question 38: "Do you think you are capable of being an astronomer (or related scientist)? Why or why not?" Question 39: "Do you feel like you belong in astronomy? Why or why not?" In figures showing results of this consistency analysis, these are referred to as "Papers," "Capable," and "Belonging." Full text of Likert questions can be found in Section E.2, and code descriptions can be found in Table 6.2.

Open-Ended Question	Codes considered	Related Likert questions
36 (Papers)	Int(−), U(−), E(−), Co(+), W(+), En(+)	1, 2, 3, 4, 5, 7, 8, 9, 11, 28
38 (Capable)	Y(+), N(−), M(0)	14, 18, 25, 26, 27, 28, 29, 30, 31, 32
39 (Belonging)	Y(+), N(−), M(0)	32, 33, 34, 35

analysis, and we considered the number of raters who applied a given code (e.g., if three scorers applied a positive code to a response but five applied a negative code, the response received a -2 and was scaled to a written score of -1). We experimented with taking the average value of the codes (e.g., the former example would yield a score of $(+3-5)/8=-0.25$), though we found that the correlation between Likert and written scores was not significantly impacted by this change in methodology. We proceeded to use the integer scores $(-1, 0, 1)$ in recognition of the inherent subjectivity of assigning numerical scores to qualitative responses based on response codes.

Written response scores tend to track Likert scores for each of the questions (Figure E.3); however, the correlation between the two scores, as computed with the Spearman correlation coefficient, is smaller in the post-survey than in the pre-survey. This is true for all three questions for which we performed consistency analysis. Many students show no change in written score from pre- to post-survey (Figure E.4), though many students, for each collection of Likert scale questions, exhibit a positive change after the activities.

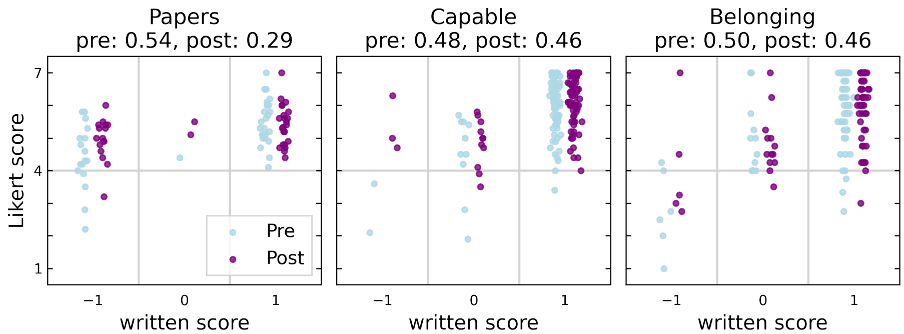

Figure E.3 Written and Likert score for each student in pre- (light blue) and post-survey (dark purple) responses to the three questions for which we performed consistency analysis. A small x-axis offset is applied to each data point for visualization purposes — each datum has a written score of -1, 0, or 1. Spearman correlation coefficients, which relate to consistency between written and Likert scores, are calculated separately for pre-survey and post-survey data and are reported above each subplot. The correlation between written and Likert scores in the pre-survey is stronger than that in the post-survey.

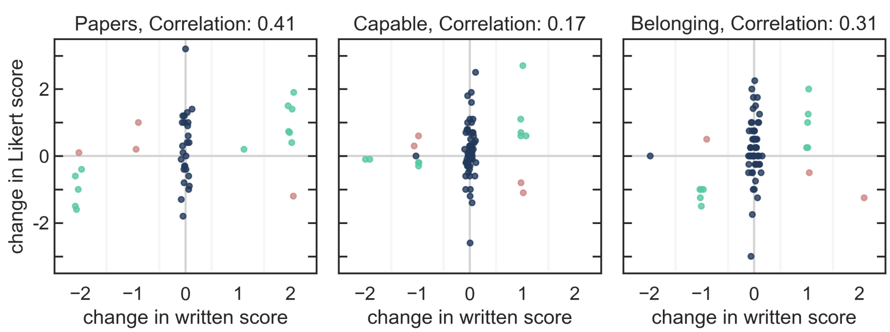

Figure E.4 Change in written and Likert score for each student from pre- to post-survey. As in Figure E.3, a small x-axis offset is applied to each data point for visualization purposes. Points are colored based on their quadrant — those for which Likert and written scores change in the same direction are in green, those for which the scores change in opposite directions are in orange, and those for which there was no change in one or both scores are in dark blue. Because relatively few written scores exhibited change, the correlations are weak.

E.7 Correlation Analysis

Quantitative survey questions were used to study second-order effects, how improvements or reductions in an ability to parse information correlate to changes in an ability to apply that knowledge. We divided the quantitative questions into four categories: one that represented understanding of information (“Understanding"), one that represented synthesizing that information into more abstract concepts (“Synthesizing"), one that represented discussing the material with others (“Communication"), and one that represented how students viewed themselves in the context of the field of astronomy and the degree to which they identified as being part of the astronomy community (“Self-Assessment").

Details of the makeup of each category are listed in Table E.3. Note that not all questions were used and that these categories are distinct from those used in the assessment design (the “conceptual catgeories”) as detailed in Section 6.3 and summarized in Table 6.1.

Table E.3 The numbers of questions included in each of the four skill categories for the second-order effects analysis. The text of each question can be found in Appendix E.2.

Category	Question numbers in category
Understanding	1, 3, 4, 7, 8, 9, 10, 13, 18
Synthesizing	11, 12, 13, 14, 15, 16, 17
Communicating	6, 19, 20, 21, 22, 23, 24
Self-assessment	25, 26, 27, 28, 29, 30, 31, 32, 33, 34, 35

For each student, we computed their initial score in each category by averaging their responses to questions in the category from the pre-lesson survey. We computed the student’s final score in the category the same way, using responses from the post-lesson survey. We then quantified changes in each category by taking the difference of the two scores. The correlations between category improvement or reduction were described quantitatively by the Spearman correlation coefficient. We choose to use the Spearman coefficient and not the Pearson correlation coefficient, because the Likert scale is ordinal, meaning that any relationships may not be linear, and it is possible that there are outliers due to, e.g., students choosing to not take the survey seriously. This combination makes the Spearman coefficient the better choice (De Winter et al., 2016).

In all categories, the majority of students showed no substantial net change, but students who did exhibit a change in skill largely improved. Figure 6.5 is a Sankey diagram of the "understanding" category showing the evolution of individual students, broken down by pre-activity score in that area. Sankey diagrams for the remaining three categories show similar trends. Students with low pre-activity scores generally exhibited slight growth; students with medium pre-activity scores generally exhibited no substantial change or slight growth; and students with high pre-activity scores generally exhibited no substantial change or slight reduction.

We found mild positive correlations between all four skill categories, with the strongest being between "Understanding" and "Synthesizing" (Spearman coefficient $r_s = 0.660$). No correlations were negative; for individual students, an increase in one area seldom corresponded with a decrease in another. Table E.4 displays the Spearman coefficients for each combination of skill categories.

Table E.4 The Spearman correlation coefficients for all pairs of skill categories. All values are close to 1/2, indicating moderate positive correlations.

Category	Understanding	Synthesizing	Communicating	Self-assessment
Understanding	N/A	0.660	0.487	0.540
Synthesizing	0.660	N/A	0.511	0.410
Communicating	0.487	0.511	N/A	0.416
Self-assessment	0.540	0.410	0.416	N/A

We hypothesized that changes in self-assessment scores may be a function of changes in the three learning categories (understanding, communicating, and synthesizing). To test this, we performed multiple linear regression to determine the coeffients for the following equation:

$$\begin{aligned}\Delta\text{Self} = \alpha &+ \beta_1(\Delta\text{Understanding}) \\ &+ \beta_2(\Delta\text{Communicating}) \\ &+ \beta_3(\Delta\text{Synthesizing})\end{aligned} \tag{E.1}$$

The variables showed moderate dependency on each other, displaying Variance Inflation Factors of 2-3. This is considered moderate dependency, and as such we perform standard multiple linear regression. Our results are shown in the following table:

Table E.5 The regression results for the hypothesis that changes in self-assessment scores can be related to changes in other learning categories. Only the changes in understanding (β_1) and communicating (β_2) have statistically significant results. The total regression has an adjusted $R^2 = 0.467$ and an F-statistic$= 25.58$ with a probability of 9.68×10^{-12}, suggesting the regression itself is statistically significant.

Coefficient	Value	Error	P-value
α	0.017	0.069	0.803
β_1	0.473	0.145	0.002
β_2	0.505	0.129	$leq 0.001$
β_3	-0.047	0.143	0.743

We find the relationships between self-assessment and the other three learning categories to be statistically significant, primarily the relationships between self-assessment, understanding, and communicating.

References

Ádámkovics, M., Glassgold, A. E., & Meijerink, R. 2011, The Astrophysical Journal, 736, 143

Adler-Kassner, L., & Estrem, H. 2007, Writing Program Administration, 31, 35

Agúndez, M., Marcelino, N., Cernicharo, J., & Tafalla, M. 2018, Astronomy and Astrophysics, 611, L1

Aikawa, Y., Momose, M., Thi, W.-F., et al. 2003, Publications of the Astronomical Society of Japan, 55, 11

Aikawa, Y., Umebayashi, T., Nakano, T., & Miyama, S. M. 1999, The Astrophysical Journal, 519, 705

Aikawa, Y., van Zadelhoff, G. J., van Dishoeck, E. F., & Herbst, E. 2002, Astronomy and Astrophysics, 386, 622

Aikawa, Y., Cataldi, G., Yamato, Y., et al. 2021, The Astrophysical Journal Supplement Series, 257, 13

Akbasli, S., Sahin, M., & Yaykiran, Z. 2016, Journal of Education and Practice, 7, 108

Andrews, S. M., Wilner, D. J., Espaillat, C., et al. 2011, The Astrophysical Journal, 732, 42

Andrews, S. M., Huang, J., Pérez, L. M., et al. 2018, The Astrophysical Journal Letters, 869, L41

ARCHER, L., DEWITT, J., & OSBORNE, J. 2015, Science Education, 99, 199

Ardila, D. R., Basri, G., Walter, F. M., Valenti, J. A., & Johns-Krull, C. M. 2002, The Astrophysical Journal, 567, 1013

Avenhaus, H., Quanz, S. P., Garufi, A., et al. 2018, The Astrophysical Journal, 863, 44

Bakan, D. 1966, Psychological bulletin, 66, 423

Balbus, S. A., & Hawley, J. F. 1991, The Astrophysical Journal, 376, 214

Ballering, N. P., Cleeves, L. I., Haworth, T. J., et al. 2023, The Astrophysical Journal, 954, 127

Barger, J. M. 2017, BAD IDEAS, 44

Barthelemy, R. S., Swirtz, M., Garmon, S., et al. 2022, Physical Review Physics Education Research, 18, 010124

Bartlett, S., Fitzgerald, M. T., McKinnon, D. H., et al. 2018, Journal of Astronomy & Earth Sciences Education (JAESE), 5, 1

Bartoš, F., & Wagenmakers, E.-J. 2023, Stat, 12, e600

Basalgète, R., Torres-Díaz, D., Lafosse, A., et al. 2023, Astronomy and Astrophysics, 676, A13

Benz, A. O., & Güdel, M. 2010, Annual Review of Astronomy and Astrophysics, 48, 241

Bergin, E. A., Aikawa, Y., Blake, G. A., & van Dishoeck, E. F. 2007, Protostars and Planets V, 751

Bernath, P. F. 2016, Spectra of Atomand and Molecules (Oxford University Press)

Bethell, T. J., & Bergin, E. A. 2011a, The Astrophysical Journal, 740, 7

—. 2011b, The Astrophysical Journal, 739, 78

—. 2011c, The Astrophysical Journal, 739, 78

Bieler, A. M., Altwegg, K., Balsiger, H. R., et al. 2015, in AGU Fall Meeting Abstracts, Vol. 2015, P33E–01

Boyden, R. D., & Eisner, J. A. 2023, The Astrophysical Journal, 947, 7

Brunn, V., Marcowith, A., Sauty, C., et al. 2023, Monthly Notices of the Royal Astronomical Society, 519, 5673

Burkhardt, A. M., Long Kelvin Lee, K., Bryan Changala, P., et al. 2021, The Astrophysical Journal Letters, 913, L18

Caracelli, V. J., & Greene, J. 1993, Educational Evaluation and Policy Analysis, 15, 195

Caramazza, M., Flaccomio, E., Micela, G., et al. 2007, Astronomy and Astrophysics, 471, 645

Carrol, B. W., & Ostlie, D. A. 2007, An Introduction to Modern Astrophysics (Pearson)

Chen, H., Zhan, Z., Youngblood, A., et al. 2021, Nature Astronomy, 5, 298

Clarke, V., Braun, V., & Hayfield, N. 2015, Qualitative psychology: A practical guide to research methods, 3, 222

Cleeves, L. I., Adams, F. C., & Bergin, E. A. 2013, The Astrophysical Journal, 772, 5

Cleeves, L. I., Bergin, E. A., & Adams, F. C. 2014a, The Astrophysical Journal, 794, 123

Cleeves, L. I., Bergin, E. A., Alexander, C. M. O. ., et al. 2014b, Science, 345, 1590

Cleeves, L. I., Bergin, E. A., & Harries, T. J. 2015, The Astrophysical Journal, 807, 2

Cleeves, L. I., Bergin, E. A., Öberg, K. I., et al. 2017, ArXiv e-prints, arXiv:1706.00833

Cleeves, L. I., Öberg, K. I., Wilner, D. J., et al. 2016, The Astrophysical Journal, 832, 110

Cohen, J. 1988, Statistical Power Analysis for the Behavioral Sciences (Lawrence Erlbaum Associates)

Cortes, P., Remijan, A., Carpenter, J., et al. 2022, ALMA Cycle 9 Technical Handbook (ALMA Doc. 9.3, ver. 1.0)

Czekala, I., Loomis, R. A., Teague, R., et al. 2021, The Astrophysical Journal Supplement Series, 257, 2

Dancy, M., & Henderson, C. 2010, American Journal of Physics, 78, 1056

De Winter, J. C. F., Godwin, S. D., & Potter, J. 2016, Psychological Methods, 273

Donohue, K., VanDenburgh, K., Reck, C., & Buck, G. 2021, Journal of College Science Teaching, 51, 46

Draine, B. T. 1947, Physics of the Interstellar and Intergalactic Medium (Princeton University Press)

Duncan, D., & Arthurs, L. 2012, Astronomy Education Research, doi:10.3847/AER2009067

Dupuy, R., Bertin, M., Féraud, G., et al. 2018, Nature Astronomy, 2, 796

Dutrey, A., Guilloteau, S., & Guelin, M. 1997, Astronomy and Astrophysics, 317, L55

Dutrey, A., Henning, T., Guilloteau, S., et al. 2007, Astronomy and Astrophysics, 464, 615

Eistrup, C., & Walsh, C. 2019, Astronomy and Astrophysics, 621, A75

Elby, A. 2001, American Journal of Physics, 69, S54

Espaillat, C. C., Macías, E., Wendeborn, J., et al. 2022, The Astrophysical Journal, 924, 104

Espinosa, T., Miller, K., Araujo, I., & Mazur, E. 2019, Phys. Rev. Phys. Educ. Res., 15, 010132

Estrada, M., Woodcock, A., Hernandez, P. R., & Schultz, P. 2011, Journal of educational psychology, 103, 206

Event Horizon Telescope Collaboration, Akiyama, K., Alberdi, A., et al. 2022, The Astrophysical Journal Letters, 930, L13

Favata, F., Flaccomio, E., Reale, F., et al. 2005, The Astrophysical Journal Supplement Series, 160, 469

Favre, C., Fedele, D., Maud, L., et al. 2019, The Astrophysical Journal, 871, 107

Fedele, D., van den Ancker, M. E., Henning, T., Jayawardhana, R., & Oliveira, J. M. 2010, Astronomy and Astrophysics, 510, A72

Feigelson, E., Townsley, L., Güdel, M., & Stassun, K. 2007, in Protostars and Planets V, ed. B. Reipurth, D. Jewitt, & K. Keil, 313

Feigelson, E. D., & Montmerle, T. 1999, Annual Review of Astronomy and Astrophysics, 37, 363

Feldman, U., Doschek, G. A., & Klimchuk, J. A. 1997, The Astrophysical Journal, 474, 511

Fischer, W. J., Hillenbrand, L. A., Herczeg, G. J., et al. 2022, arXiv e-prints, arXiv:2203.11257

Flaccomio, E., Damiani, F., Micela, G., et al. 2003, The Astrophysical Journal, 582, 398

Fogel, J. K. J., Bethell, T. J., Bergin, E. A., Calvet, N., & Semenov, D. 2011, The Astrophysical Journal, 726, 29

Francis, L., Johnstone, D., Herczeg, G., Hunter, T. R., & Harsono, D. 2020, The Astronomical Journal, 160, 270

Gaia Collaboration, Brown, A. G. A., Vallenari, A., et al. 2018, Astronomy and Astrophysics, 616, A1

Garland, C. A., & Ratay, D. L. 2007, Astronomy Education Review, 6

Getman, K. V., Akimkin, V. V., Arulanantham, N., et al. 2022a, Research Notes of the American Astronomical Society, 6, 64

Getman, K. V., & Feigelson, E. D. 2021, The Astrophysical Journal, 916, 32

Getman, K. V., Feigelson, E. D., Broos, P. S., Micela, G., & Garmire, G. P. 2008a, The Astrophysical Journal, 688, 418

Getman, K. V., Feigelson, E. D., & Garmire, G. P. 2021, The Astrophysical Journal, 920, 154

Getman, K. V., Feigelson, E. D., Garmire, G. P., et al. 2022b, The Astrophysical Journal, 935, 43

Getman, K. V., Feigelson, E. D., Micela, G., et al. 2008b, The Astrophysical Journal, 688, 437

Getman, K. V., Flaccomio, E., Broos, P. S., et al. 2005, The Astrophysical Journal Supplement Series, 160, 319

Glassgold, A. E., Feigelson, E. D., Montmerle, T., & Wolk, S. 2005, in Astronomical Society of the Pacific Conference Series, Vol. 341, Chondrites and the Protoplanetary Disk, ed. A. N. Krot, E. R. D. Scott, & B. Reipurth, 165

Glassgold, A. E., Najita, J., & Igea, J. 1997, The Astrophysical Journal, 480, 344

Grady, C. A., Hamaguchi, K., Schneider, G., et al. 2010, The Astrophysical Journal, 719, 1565

Güdel, M. 2004, , 12, 71

Güdel, M., Audard, M., Kashyap, V. L., Drake, J. J., & Guinan, E. F. 2003, The Astrophysical Journal, 582, 423

Gullbring, E., Hartmann, L., Briceño, C., & Calvet, N. 1998, The Astrophysical Journal, 492, 323

Guzmán, V. V., Bergner, J. B., Law, C. J., et al. 2021, The Astrophysical Journal Supplement Series, 257, 6

Haisch, Jr., K. E., Lada, E. A., & Lada, C. J. 2001, The Astrophysical Journal Letters, 553, L153

Hasegawa, T. I., Herbst, E., & Leung, C. M. 1992, The Astrophysical Journal Supplement Series, 82, 167

Hayes, C. R., Matthews, A. M., Song, Y., et al. 2020, Physical Review Physics Education Research, 16, 010131

Henderson, C., & Dancy, M. H. 2007, Physical Review Special Topics-Physics Education Research, 3, 020102

Henning, T., & Semenov, D. 2013, Chemical Reviews, 113, 9016

Herczeg, G. J., Wood, B. E., Linsky, J. L., Valenti, J. A., & Johns-Krull, C. M. 2004, The Astrophysical Journal, 607, 369

Heron, H., McNeil, L., & Co-chairs. 2019, Joint Task Force on Undergraduate Physics Programs. Phys21: preparing physics student for 21st-century careers, ,

Hewitt, H. B., Simon, M. N., Mead, C., et al. 2023, Physical Review Physics Education Research, 19, 020156

Hiebert, B., Bezanson, L., O'Reilly, E., et al. 2012, Ottawa: Ressources humaines et développement des compétences Canada

Huang, J., Öberg, K. I., & Andrews, S. M. 2016, The Astrophysical Journal Letters, 823, L18

Huang, J., Öberg, K. I., Qi, C., et al. 2017, The Astrophysical Journal, 835, 231

Huang, J., Andrews, S. M., Dullemond, C. P., et al. 2018a, The Astrophysical Journal Letters, 869, L42

—. 2018b, The Astrophysical Journal Letters, 869, L42

—. 2020, The Astrophysical Journal, 891, 48

Huang, J., Bergin, E. A., Öberg, K. I., et al. 2021, The Astrophysical Journal Supplement Series, 257, 19

Hudson, H. S. 1991, , 133, 357

Igea, J., & Glassgold, A. E. 1999, The Astrophysical Journal, 518, 848

Ilgner, M., & Nelson, R. P. 2006a, Astronomy and Astrophysics, 445, 205

—. 2006b, Astronomy and Astrophysics, 445, 223

—. 2006c, Astronomy and Astrophysics, 455, 731

—. 2006d, Astronomy and Astrophysics, 455, 731

James, W., Bustamante, C., Lamons, K., Scanlon, E., & Chini, J. J. 2020, Phys. Rev. Phys. Educ. Res., 16, 020111

Kama, M., Shorttle, O., Jermyn, A. S., et al. 2019, The Astrophysical Journal, 885, 114

Kanevsky, L. 2016, Post-pre surveys, Simon Fraser University

Koch, A. 2001, Science education, 85, 758

Koch, A., & Eckstein, S. G. 1991, International Journal of Science Education, 13, 473

Kohler, S., Collaboration, A., et al. 2018, Proceedings of the International Astronomical Union, 14, 524

Kóspál, Á., Cruz-Sáenz de Miera, F., White, J. A., et al. 2021, The Astrophysical Journal Supplement Series, 256, 30

Kricorian, Katherine and Seu, Michelle, and Lopez, Daniel and Ureta, Elsie and Equils, Ozlem. 2020, International Journal of STEM Education, 7, 7

Kwok, S. 2007, Physics and Chemistry of the Interstellar Medium (University Science Books)

Laas, J. C., & Caselli, P. 2019, Astronomy and Astrophysics, 624, A108

Law, C. J., Loomis, R. A., Teague, R., et al. 2021, The Astrophysical Journal Supplement Series, 257, 3

Le Gal, R., Öberg, K. I., Loomis, R. A., Pegues, J., & Bergner, J. B. 2019, The Astrophysical Journal, 876, 72

Leemker, M., van't Hoff, M. L. R., Trapman, L., et al. 2021, Astronomy and Astrophysics, 646, A3

Lewis, B., Waggoner, A., Clarke, E., et al. 2024, in American Astronomical Society Meeting Abstracts, Vol. 56, American Astronomical Society Meeting Abstracts, 345.08

Lewis, B. L., Supriya, K., Read, G. H., et al. 2022, arXiv preprint arXiv:2209.02852, doi:10.48550/arXiv.2209.02852

Litwin, M. S., & Fink, A. 1995, How to measure survey reliability and validity, Vol. 7 (Sage)

Loomis, R. A., Cleeves, L. I., Öberg, K. I., et al. 2018, The Astrophysical Journal, 859, 131

Lupi, J., Puzzarini, C., & Barone, V. 2020, The Astrophysical Journal Letters, 903, L35

Lynden-Bell, D., & Pringle, J. E. 1974, Monthly Notices of the Royal Astronomical Society, 168, 603

Mackey, J., Walch, S., Seifried, D., et al. 2019, Monthly Notices of the Royal Astronomical Society, 486, 1094

Maloney, P. R., Hollenbach, D. J., & Tielens, A. G. G. M. 1996, The Astrophysical Journal, 466, 561

McCall, B. J. 2006, Philosophical Transactions of the Royal Society of London Series A, 364, 2953

McGuire, B. A. 2018, The Astrophysical Journal Supplement Series, 239, 17

McGuire, B. A., Burkhardt, A. M., Loomis, R. A., et al. 2020, The Astrophysical Journal Letters, 900, L10

Meinert, C., de Marcellus, P., Le Sergeant D'Hendecourt, L., et al. 2011, Physics of Life Reviews, 8, 307

Mendigutía, I., Brittain, S., Eiroa, C., et al. 2013, The Astrophysical Journal, 776, 44

Molyarova, T., Akimkin, V., Semenov, D., et al. 2018, The Astrophysical Journal, 866, 46

Montmerle, T., & Casanova, S. 1996, in IAU Colloq. 153: Magnetodynamic Phenomena in the Solar Atmosphere - Prototypes of Stellar Magnetic Activity, ed. Y. Uchida, T. Kosugi, & H. S. Hudson, 247

Öberg, K. I., & Bergin, E. A. 2021, , 893, 1

Öberg, K. I., Guzmán, V. V., Furuya, K., et al. 2015, Nature, 520, 198

Öberg, K. I., Qi, C., Fogel, J. K. J., et al. 2010, The Astrophysical Journal, 720, 480

—. 2011, The Astrophysical Journal, 734, 98

Öberg, K. I., Guzmán, V. V., Walsh, C., et al. 2021, The Astrophysical Journal Supplement Series, 257, 1

Oliver, K. A., Werth, A., & Lewandowski, H. 2023, Physical Review Physics Education Research, 19, 010124

Onwuegbuzie, A., & Combs, J. 2010, Handbook of Mixed Methods in Social and Behavioral Research, 397

Panić, O., Hogerheijde, M. R., Wilner, D., & Qi, C. 2009, Astronomy and Astrophysics, 501, 269

Pearce, G., & Harrison, R. A. 1988, Astronomy and Astrophysics, 206, 121

Pelger, S., & Nilsson, P. 2016, Research in Science Education, 46, 439

Peres, G., Orlando, S., Reale, F., Rosner, R., & Hudson, H. 2000, The Astrophysical Journal, 528, 537

Piétu, V., Dutrey, A., & Guilloteau, S. 2007, Astronomy and Astrophysics, 467, 163

Pinte, C., Padgett, D. L., Ménard, F., et al. 2008, Astronomy and Astrophysics, 489, 633

Pinte, C., Ménard, F., Duchêne, G., et al. 2018a, Astronomy and Astrophysics, 609, A47

—. 2018b, Astronomy and Astrophysics, 609, A47

Pollack, J. B., Hubickyj, O., Bodenheimer, P., et al. 1996, , 124, 62

Ponce, O. A., & Pagán-Maldonado, N. 2015, International journal of educational excellence, 1, 111

Preibisch, T., & Feigelson, E. D. 2005, The Astrophysical Journal Supplement Series, 160, 390

Rab, C., Güdel, M., Padovani, M., et al. 2017, Astronomy and Astrophysics, 603, A96

Rahul, K. K., Ambresh, M., Sahu, D., et al. 2020, arXiv e-prints, arXiv:2008.10011

Rector, T. A., Puckett, A. W., Wooten, M. M., et al. 2019, in Astronomy Education, Volume 1: Evidence-based instruction for introductory courses (IOP Publishing Bristol, UK), 7–1

Rich, E. A., Wisniewski, J. P., Sitko, M. L., et al. 2020, The Astrophysical Journal, 902, 4

Rosén, L., Kochukhov, O., & Wade, G. A. 2015, The Astrophysical Journal, 805, 169

Rubin, M., Altwegg, K., van Dishoeck, E. F., & Schwehm, G. 2015, The Astrophysical Journal Letters, 815, L11

Ruffle, D. P., Hartquist, T. W., Caselli, P., & Williams, D. A. 1999, Monthly Notices of the Royal Astronomical Society, 306, 691

Ruíz-Rodríguez, D. A., Williams, J. P., Kastner, J. H., et al. 2022, Monthly Notices of the Royal Astronomical Society, 515, 2646

Sanders, N. E., Kohler, S., Faesi, C., Villar, A., & Zevin, M. 2017, American Journal of Physics, 85, 741

Sanders, N. E., Kohler, S., Newton, E., & Astrobites Collaboration. 2012, Astronomy Education Review, 11, 010201

Scerri, E. R. 2007, The Periodic Table Its Story and Its Significance (Oxford University Press)

—. 2015, Philosophical Transactions, 373(2037)

Seifert, R. A., Ilsedore. Cleeves, L., Adams, F. C., & Li, Z.-Y. 2021, arXiv e-prints, arXiv:2103.10971

Seymour, E., Hunter, A.-B., Laursen, S. L., & DeAntoni, T. 2004, Science Education, 88, 493

Shingledecker, C. N., Álvarez-Barcia, S., Korn, V. H., & Kästner, J. 2019, The Astrophysical Journal, 878, 80

Shingledecker, C. N., Lamberts, T., Laas, J. C., et al. 2020, The Astrophysical Journal, 888, 52

Shkedi, A. 1998, International Journal of Qualitative Studies in Education, 11, 559

Shu, F. H. 1982, The Physical Universe An Introduction to Astronomy (University Science Books)

Sipilä, O., Silsbee, K., & Caselli, P. 2021, The Astrophysical Journal, 922, 126

Smith, I. W. M., Herbst, E., & Chang, Q. 2004, Monthly Notices of the Royal Astronomical Society, 350, 323

Sørvik, G. O., & Mork, S. M. 2015, Nordic Studies in Science Education, 11, 268

Steinfeld, J. I. 1974, Molecules and Radiation an Introduction to Modern Molecular Spectroscopy (Dover Publications, Inc)

Strom, K. M., Strom, S. E., Edwards, S., Cabrit, S., & Skrutskie, M. F. 1989, The Astronomical Journal, 97, 1451

Susiati, A., Adisyahputra, A., & Miarsyah, M. 2018, Biosfer: Jurnal Pendidikan Biologi, 11, 1

Szymanski, E. A. 2014, Across the Disciplines, doi:10.37514/ATD-J.2014.11.2.06

Taherdoost, H. 2016, How to test the validation of a questionnaire/survey in a research (August 10, 2016), doi:10.2139/ssrn.3205040

Taquet, V., Furuya, K., Walsh, C., & van Dishoeck, E. F. 2016, Monthly Notices of the Royal Astronomical Society, 462, S99

Teague, R., Bae, J., & Bergin, E. A. 2019, Nature, 574, 378

Teague, R., Bae, J., Aikawa, Y., et al. 2021, The Astrophysical Journal Supplement Series, 257, 18

Thompson, A. R., Moran, J. M., & Swenson Jr, G. W. 2017, Interferometry and Synthesis in Radio Astronomy Third Edition (Gewerbestrasse 11, 6330 Cham, Switzerland: Springer International Publishing AG)

Thompson, A. Richard, M. J. M. S. G. W. 2017, Interferometry and Synthesis in Radio Astronomy (Springer)

Tielens, A. G. G. M. 2005, The Physics and Chemistry of the Interstellar Medium (Cambridge University Press)

Tobin, J. J., van't Hoff, M. L. R., Leemker, M., et al. 2023, Nature, 615, 227

Vallat, R. 2018, Journal of Open Source Software, 3, 1026

Van de Pol, J., Volman, M., & Beishuizen, J. 2010, Educational psychology review, 22, 271

Van Schaik, P., Volman, M., Admiraal, W., & Schenke, W. 2018, International Journal of Educational Research, 90, 50

Waggoner, A. R., & Cleeves, L. I. 2019, The Astrophysical Journal, 883, 197

—. 2022, The Astrophysical Journal, 928, 46

Waggoner, A. R., Cleeves, L. I., Loomis, R. A., et al. 2023, The Astrophysical Journal, 956, 103

Wakelam, V., Cuppen, H. M., & Herbst, E. 2013, ArXiv e-prints, arXiv:1309.7792

Walsh, C., Loomis, R. A., Öberg, K. I., et al. 2016, The Astrophysical Journal Letters, 823, L10

Wang, H., Bell, R. C., Iedema, M. J., Tsekouras, A. A., & Cowin, J. P. 2005, The Astrophysical Journal, 620, 1027

Wang, L., Zhang, Z., McArdle, J. J., & Salthouse, T. A. 2008, Multivariate behavioral research, 43, 476

Watanabe, N., & Kouchi, A. 2002, The Astrophysical Journal Letters, 571, L173

Werth, A., West, C. G., & Lewandowski, H. 2022, Physical Review Physics Education Research, 18, 010129

Werth, A., West, C. G., Sulaiman, N., & Lewandowski, H. 2023, Physical Review Physics Education Research, 19, 020151

Williams, D. 2020, ""

Williams, D., & Hartquist, T. 2013, The Cosmic-Chemical Bond Chemistry from the Big Band to Planet Formation (RSC Publishing)

Williams, J. P., & Cieza, L. A. 2011, Annual Review of Astronomy and Astrophysics, 49, 67

Wolfire, M. G., Vallini, L., & Chevance, M. 2022, Annual Review of Astronomy and Astrophysics, 60, 247

Wolk, S. J., Harnden, Jr., F. R., Flaccomio, E., et al. 2005, The Astrophysical Journal Supplement Series, 160, 423

Wooten, M. M., Coble, K., Puckett, A. W., & Rector, T. 2018, Physical Review Physics Education Research, 14, 010151

Yamamoto, S. 2017, Introduction to Astrochemistry Chemical Evolution from Interstellar Clouds to Star and Planet Formation (Springer)

Yardley, L. 2015, Qualitative psychology: A practical guide to research methods, 3, 257

Young, N. T., Lewis, B. L., Kerr, E., & Nair, P. H. 2022, arXiv preprint arXiv:2209.07627